AUG 5 1996

SANDIA REPORT

SAND94–0779 • UC–814
Unlimited Release
Printed July 1996

Yucca Mountain Site Characterization Project

Sensitivity of Hydrological Performance Assessment Analyses to Variations in Material Properties, Conceptual Models, and Ventilation Models

Steven R. Sobolik, Clifford K. Ho, Ellen Dunn
Thomas H. Robey, Walter T. Cruz

Prepared by
Sandia National Laboratories
Albuquerque, New Mexico 87185 and Livermore, California 94550
for the United States Department of Energy
under Contract DE-AC04-94AL85000

RECEIVED
AUG 15 1996
OSTI

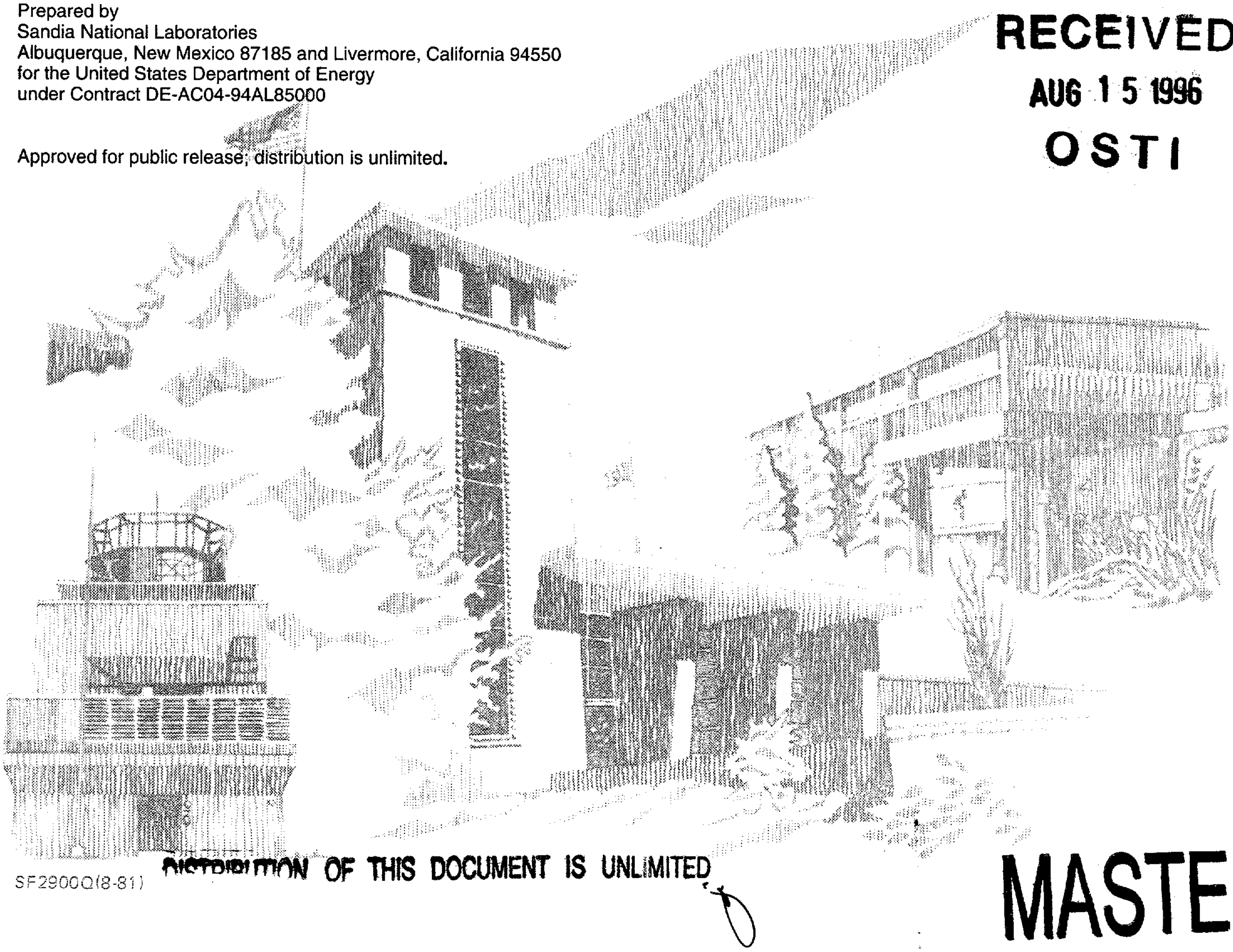

SF2900Q(8-81)

MASTER

"Prepared by Yucca Mountain Site Characterization Project (YMSCP) participants as part of the Civilian Radioactive Waste Management Program (CRWM). The YMSCP is managed by the Yucca Mountain Project Office of the U.S. Department of Energy, DOE Field Office, Nevada (DOE/NV). YMSCP work is sponsored by the Office of Geologic Repositories (OGR) of the DOE Office of Civilian Radioactive Waste Management (OCRWM)."

Issued by Sandia National Laboratories, operated for the United States Department of Energy by Sandia Corporation.

Printed in the United States of America. This report has been reproduced directly from the best available copy.

Available to DOE and DOE contractors from
Office of Scientific and Technical Information
PO Box 62
Oak Ridge, TN 37831

Prices available from (615) 576-8401, FTS 626-8401

Available to the public from
National Technical Information Service
US Department of Commerce
5285 Port Royal Rd
Springfield, VA 22161

NTIS price codes
Printed copy: A11
Microfiche copy: A01

SAND94-0779
Unlimited Release
Printed July 1996

Distribution
Category UC-814

Sensitivity of Hydrological Performance Assessment Analyses to Variations in Material Properties, Conceptual Models, and Ventilation Models

Steven R. Sobolik, Clifford K. Ho, and Ellen Dunn
Sandia National Laboratories
Albuquerque, New Mexico

Thomas H. Robey
Spectra Research, Inc.
Albuquerque, New Mexico

Walter T. Cruz
Universidad del Turabo
Gurabo, Puerto Rico, U.S.A.

ABSTRACT

The Yucca Mountain Site Characterization Project is studying Yucca Mountain in southwestern Nevada as a potential site for a high-level nuclear waste repository. Site characterization includes surface-based and underground testing. Analyses have been performed to support the design of an Exploratory Studies Facility (ESF) and the design of the tests performed as part of the characterization process, in order to ascertain that they have minimal impact on the natural ability of the site to isolate waste. The information in this report pertains to sensitivity studies evaluating previous hydrological performance assessment analyses to variation in the material properties, conceptual models, and ventilation models, and the implications of this sensitivity on previous recommendations supporting ESF design. This document contains information that has been used in preparing recommendations for Appendix I of the Exploratory Studies Facility Design Requirements document.

The work discussed in this report was performed under Yucca Mountain Project (YMP) WBS number 1.2.5.4.7. The QA controls applied to the work contained in this report are identified in QAGR 1.2.5.4.7 and Work Agreement WA-0089.

ACKNOWLEDGMENTS

The authors acknowledge the work of fellow coworkers who helped in the preparation of this report. Jack Gauthier, Eric Ryder, and Larry Costin reviewed the technical content of this document and offered corrections and ideas for improvement. Corinne Taylor provided valuable assistance in preparing the figures in this report.

CONTENTS

FIGURES

TABLES

1.0 Introduction

The Yucca Mountain Site Characterization Project (YMP) is studying Yucca Mountain in southwestern Nevada as a potential site for a high-level nuclear waste repository. Site characterization includes underground and surface-based testing. Underground testing will be facilitated by the construction of an Exploratory Studies Facility (ESF). Surface-based testing will require boreholes, test pits, and other similar surface activities. Water is being used during the construction and operation of surface and underground facilities for the ESF. Several previous performance assessment (PA) analyses have been performed to evaluate the impact of this additional water on waste isolation and site characterization; those analyses performed to support ESF and surface-based design activities are listed in Table 1.1. There is some potential for this water to affect repository performance, the proposed experiments in the ESF, and surface-based testing locations, such as boreholes. Recommendations in the form of restrictions used for facility design and operations have been implemented in the Exploratory Studies Facility Design Requirements (ESFDR) document (DOE-YMP, 1993b) based on the results of the analyses in Table 1-1.

Table 1-1: ESF PA Analyses Assessing Hydrological Issues

ESF PA Analysis No.	Analysis Description	Reference
1	Surface Construction Water Movement	SAND91-0790 (Fewell et al., 1992)
2	Construction Water Movement in Shafts and Drifts	SAND 91-0791 (Sobolik et al., 1991)
3	Sewage and Settling Pond Water Movement	SAND91-0792 (Sobolik and Fewell, 1992)
12	Underground Water Movement from Surficial Water Used Outside the Drift Perimeter Boundary	SAND92-2248 (Sobolik and Fewell, 1993)
13	Movement of Water Used in Underground Construction Activities in the ESF	SAND93-1182 (Dunn and Sobolik, 1993)

The results of the analyses in Table 1-1 rely on a variety of limitations and assumptions concerning the material properties of the various hydrogeological layers; these include the minimal amount of measured data which could be used to derive the hydrologic parameter values, the assumption of homogeneity and isotropy of hydrological properties within a stratigraphic layer, and the degree to which stratigraphic layers are discretized. The results of some of these analyses are also dependent upon the model chosen for the drying effects of underground ventilation, and the conceptual model used (e.g., equivalent continuum versus dual permeability, single-phase flow versus multi-phase, etc.). The purpose of the work described in this report is to investigate the sensitivity of hydrologic PA analyses to the variability of the parameters described above, and to assess the effect of this sensitivity on the recommendations provided by previous PA analyses.

The evaluations and computational analyses described in this report form the basis for ESF PA Analysis #14. A summary of this analysis and recommended controls based on the results of this analysis have been submitted for inclusion in Appendix I of the ESFDR. The calculations and analyses performed for ESF PA Analysis #14 were conducted as a quality-related activity in accordance with Sandia National Laboratories' (SNL's) implementation of the Yucca Mountain Project Quality Assurance Plan and were controlled by Work Agreement WA-0089 (SNL, 1994).

These calculations are based on available data and on the present conceptual understanding of the processes and mechanisms perceived to be active at Yucca Mountain. Because of limited knowledge of Yucca Mountain prior to site characterization, the hydrogeological conceptual models, other existing conceptual models of the physical processes, and the mathematical models used in these analyses are not validated. Recommendations based on the results of these analyses are intended to provide guidance for applying engineering judgment during the design, construction, and operation of the ESF and the conduct of surface-based activities. Therefore, they must provide relevant results to the architects and engineers who design the ESF. Refinement of the results is an ongoing and iterative process, which must complement site characterization. These calculations should be refined as better understanding evolves through site characterization and through additional analyses, which will address uncertainties and the sensitivity of the results to alternate conceptual models.

2.0 Approach

The purpose of ESF PA Analysis #14 is to estimate the sensitivity of hydrological PA analyses used to evaluate potential impacts on waste isolation to the selection of several parameters, and to assess the effect of this sensitivity on the recommendations provided by previous PA analyses. Calculations were performed to evaluate sensitivity to four parameters[1]:

- Sensitivity of Evaluation of Water Movement to Characterization of **Paintbrush Tuff (PTn) Hydraulic Parameters**
- Sensitivity of Evaluation of Water Movement to **Heterogeneity of Material Properties**
- Sensitivity of Evaluation of Water Movement to **Fracture/Matrix Characterization**
- Sensitivity of Evaluation of Underground Water Movement to Modeling of Rock Drying Effects Due to **Ventilation.**

The analyses described in Table 1-1 represent an initial attempt to perform PA analyses which assess the effect of construction and testing activities on the natural ability of the Yucca Mountain site to isolate waste. Performance assessment analyses are an iterative process requiring re-investigation given new site data, new information on the in situ physical processes, and improved or enhanced numerical models. These advancements require the gathering of field and laboratory data, as well as performing numerical experiments in parallel with these activities. This suite of sensitivity studies represents the first of several iterations in the performance assessment process. These studies were approached with the idea that they would not necessarily answer any old questions, but rather would introduce new questions about our knowledge of the physical processes active at Yucca Mountain, and the effects of human activities on those processes which could impact potential repository performance.

The analyses described in this report represent a number of firsts for quality-affecting performance assessment analyses. The calculations in Chapter 3 are the first parametric study of water flow through the nonwelded Paintbrush Tuff (PTn) unit, a layer of primarily nonwelded rock having highly variable porosity and fracture characteristics. In Chapter 4, heterogeneous material properties based on geostatistical representations of site data are attempted for the first time in a quality-affecting environment. The studies in Chapter 5 introduce the use of the dual porosity and dual permeability models in contrast to the equivalent continuum flow model used for previous analyses, and Chapter 6 implements a vapor-phase diffusion model to evaluate the tunnel dryout effects of ventilation.

Calculations of water movement in layered, fractured, unsaturated porous media using the currently accepted mathematical models are complex and require sophisticated computer codes. The computer program NORIA-SP (Hopkins et al., 1991) was used to perform the calculations listed in Table 1-1. NORIA-SP numerically solves the two-dimensional Richards' equation for single-phase flow (liquid water) in porous media using the equivalent continuum model (Peters and Klavetter, 1988), also known as the composite fracture/matrix porosity model. The van

---

[1] A fifth study, which was to study the sensitivity of one-dimensional modeling of surficial water addition to fracture/matrix characterization, was not performed because of time allocation problems, and was so noted in a letter included in the analysis file for WA-0089.

Genuchten model (van Genuchten, 1980) was implemented in NORIA-SP to describe the moisture characteristic curves for the matrix and fractures. Multi-phase and nonisothermal effects were not modeled in NORIA-SP. To test the sensitivity of previous ESF PA analyses to the parameters described above, additional codes are required. TOUGH2 (Pruess, 1991) is a multi-dimensional flow code which models Richards' equation for multi-phase (liquid water, water vapor, and air), nonisothermal flow, with the option of using one of several models for conceptualizing the relationship of flow between fractures and matrix. TOUGH2 has a long history of use for thermal-hydrological analyses both inside and outside the YMP. NORIA-SP and TOUGH2 have met the requirements of SNL's implementation of the YMP's criteria for software quality assurance. For these reasons, NORIA-SP and TOUGH2 were chosen to perform the sensitivity calculations described in this report.

3.0 Sensitivity of Evaluation of Water Movement to Characterization of PTn Hydraulic Parameters

(Sobolik, Cruz)

The nonwelded Paintbrush Tuff (PTn) is a highly porous, conductive tuff with variable material properties occurring throughout its many sublayers. Examples of variable properties in PTn include welded or nonwelded tuff, rock quality, pore size distribution, and in situ saturation. The range of variation of these properties brings into question the use of any set of homogeneous properties for PTn, particularly the set that has been used in previous analyses. ESF PA Analyses #3 (Sobolik and Fewell, 1992) and #12 (Sobolik and Fewell, 1993) estimated the movement of off-block surficial water used for pond storage and road watering, respectively. ESF PA Analysis #13 (Dunn and Sobolik, 1993) estimated the movement of water used for underground construction and operations. The hydrology code NORIA-SP (Hopkins et al., 1991), which employs the equivalent continuum model (ECM) for a two-dimensional, single-phase, isothermal flow, was used for these previous analyses. The calculations performed for these analyses used properties for PTn obtained from boreholes USW G-4 and USW GU-3 (Peters et al., 1984; Klavetter and Peters, 1986). These property values and the resulting in situ saturation calculated for PTn differ significantly from those cited in several versions of the Reference Information Base (RIB) (DOE-YMP, 1993a), as well as those from recent site investigations (e.g., Flint and Flint, 1990) and recent computational investigations (e.g., Barnard et al., 1992; Wilson et al., 1994).

Three new sets of calculations were performed to investigate the sensitivity of hydrologic PA analyses to the variability of parameters in PTn and to assess the effect of this sensitivity on the recommendations provided by the previous PA analyses listed above. The code NORIA-SP was used for this study, and the same hydrologic parameters for non-PTn units and the grid spacing was matched as closely as possible with the original NORIA-SP calculations. This chapter describes the calculations performed for pond water, road watering, and the underground water usage problems, with resulting conclusions applicable to the ESF design process, the conduct of performance assessment analyses, and other issues such as site characterization and model validation.

Many of the results of the calculations are presented in terms of the change of saturation from in situ conditions due to the movement of water through the rock. This change in saturation, called **Δsat**, indicates the extent of movement of the infiltrated water.

3.1 PTn Hydraulic Parameters

The hydraulic parameters that will be used to represent PTn for the calculations for this study are listed in Table 3.1-1. They have been obtained from several different YMP sources. This tabulation is certainly not an exhaustive list of all existing data on PTn, but the authors belived it to be representative of the range of values that have been documented thus far. Table A.1 in Appendix A lists the unit designations and the stratigraphy used for these calculations. Figures 3.1-1 and 3.1-2 plot the curve fit approximations using van Genuchten formulation for the characteristic curve given for Pah Canyon in Table 3.1-1; Figures 3.1-3 and 3.1-4 show the same curve fits used for the Yucca Mountain member.

Table 3.1-1: Hydraulic Properties Used for PTn in Sensitivity Calculations

		Matrix Properties						Fracture Properties	
Sample Name	Matrix Data Source	Porosity	K_{sat}, m/s	alpha, 1/m	beta	Resid. Sat.	Fracture Data Source	Porosity	K_{sat}, m/s
ESF3 (ESF Analysis #3: SAND91-0792; also ESF Analysis #12: SAND92-2248)	SAND84-1471 (Peters et al.), Sample GU3-7	0.4	3.90×10^{-7}	0.015	6.872	0.1	SAND84-2642 (Klavetter, Peters)	2.70×10^{-5}	6.10×10^{-4}
BT (Tpc-BT) - Bedded Tuff, high pumice	YMP/CC-0002 (RIB, Ver. 4, Rev.0), 4/13/92, Section 1.4.4, p 4-6	0.22	2.40×10^{-6}	0.016	10	0.1	RIB (no fractures in nonwelded units)	0	0
PAH (Pah Canyon Member)	USGS OFR 90-569, Sample 4-5H; see Figures 3.1-1 and 3.1-2	0.47	7.14×10^{-7}	0.40157	2.5206	0.2256	SAND84-2642 (Klavetter, Peters)	2.70×10^{-5}	6.10×10^{-4}
TM (Tpt-TM) - Moderately welded, highly fractured	YMP/CC-0002 (RIB, Ver. 4, Rev.0), 4/13/92, Section 1.4.4, p 4-6	0.1	2.00×10^{-11}	0.005	1.9	0.1	YMP/CC-0002 (RIB, Ver.4, Rev.0), 4/13/92, Section 1.4.4, p 4-6	3.00×10^{-5}	4.00×10^{-5}
TN (Tpc-TN) - Ash flow, nonwelded, high pumice	YMP/CC-0002 (RIB, Ver. 4, Rev.0), 4/13/92, Section 1.4.4, p 4-6	0.5	2.00×10^{-11}	0.004	1.5	0.15	RIB (no fractures in nonwelded units)	0	0
YM (Yucca Mountain Member)	USGS OFR 90-569, Sample IV; see Figures 3.1-3 and 3.1-4	0.436	1.75×10^{-7}	0.9	1.45	0.39	SAND84-2642 (Klavetter, Peters)	2.70×10^{-5}	6.10×10^{-4}
YMNF (Yucca Mountain Member, no fractures)	USGS OFR 90-569, Sample IV; see Figures 3.1-3 and 3.1-4	0.436	1.75×10^{-7}	0.9	1.45	0.39	RIB (no fractures in nonwelded units)	0	0
G4 (Well USW G-4, derived from SAND84-1471 (Peters et al.))	K_{sat}: YMP/93-02 (RIB, Rev. 1, 3/8/93), Section 1.4.3; all else, ESF3	0.4	5.00×10^{-10}	0.015	6.872	0.1	SAND84-2642 (Klavetter, Peters)	2.70×10^{-5}	6.10×10^{-4}

Figure 3.1-1: Moisture Retention Curve for Pah Canyon Member (Sample 4-5H, Flint and Flint, 1990)

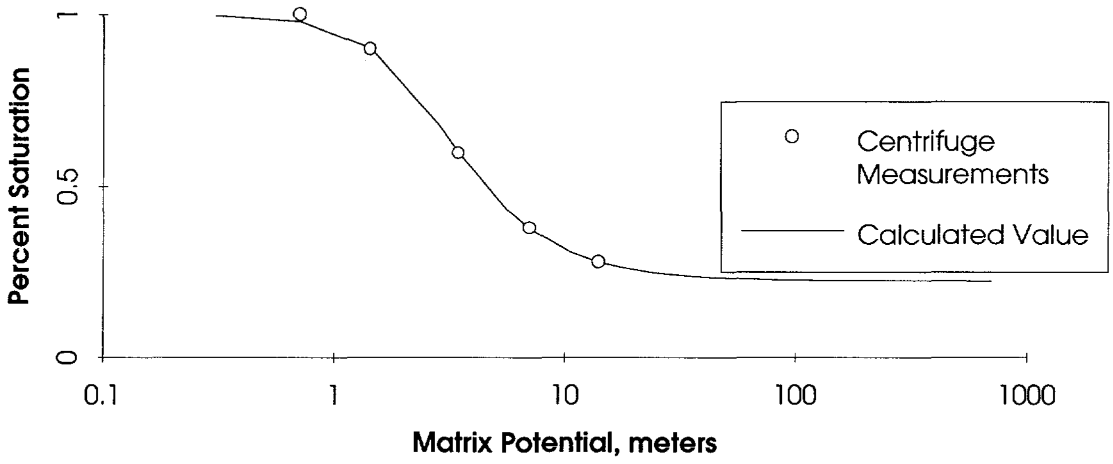

Figure 3.1-2: Relative Permeability Curve for Pah Canyon Member (Sample 4-5H, Flint and Flint, 1990)

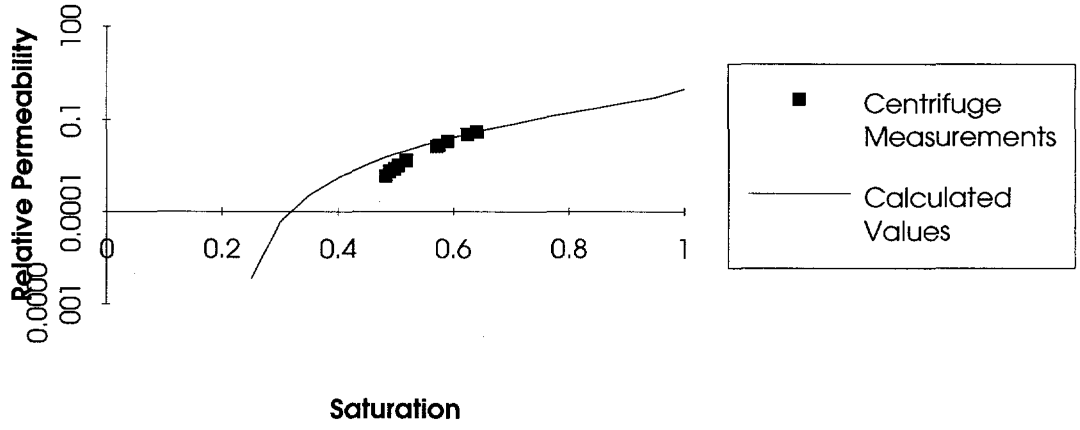

Figure 3.1-3: Moisture Retention Curve for Yucca Mountain Member (Sample IV, Flint and Flint, 1990)

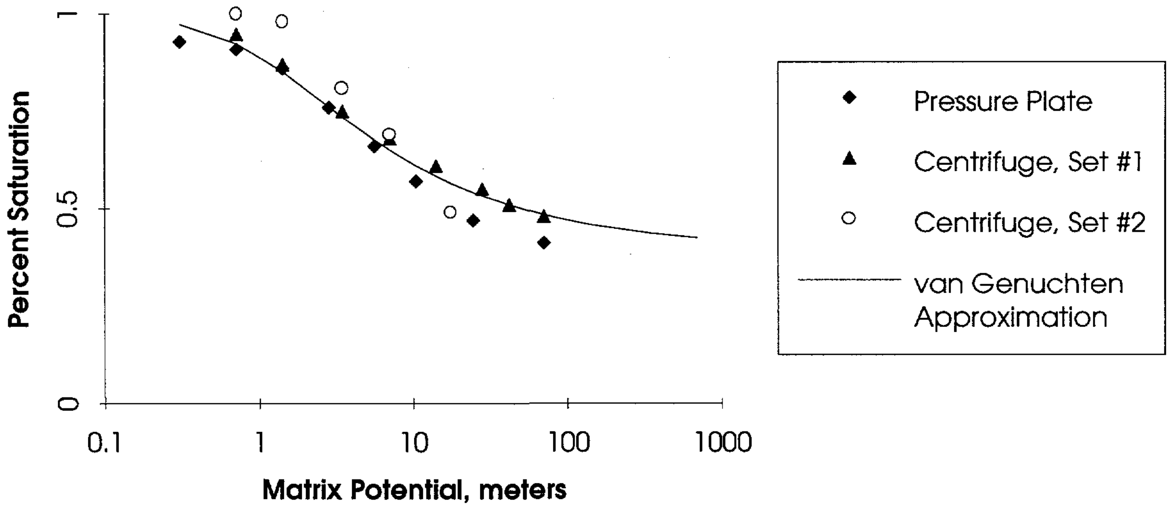

Figure 3.1-4: Relative Permeability Curve for Yucca Mountain Member (Sample IV, Flint and Flint, 1990)

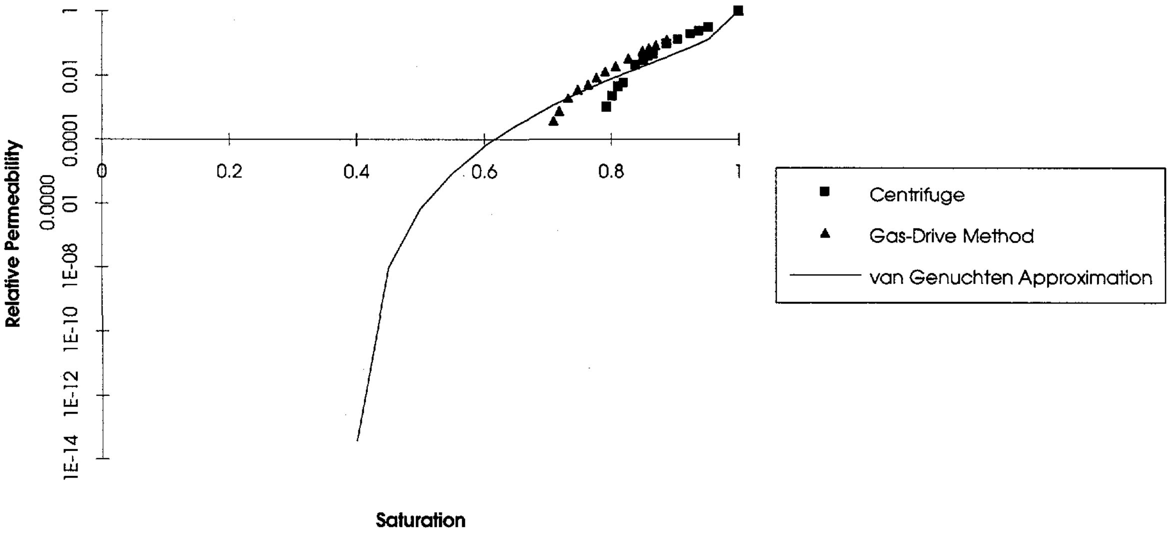

3.2 **Comparison with Pond Calculations of ESF PA Analysis #3**

The first set of calculations performed for this study evaluates the sensitivity of the results of ESF PA Analysis #3 (movement of pond water) to the choice of parameters for PTn. A full description of the assumptions used to formulate the original pond problem is in Sobolik and Fewell (1992); an abridged description is included for the new calculations.

3.2.1 Problem Definition

The problem is conceptualized as follows. The sewage pond design modeled for this analysis was assumed to hold waste water maintained at a constant depth during a five-year ESF construction and operation period as originally assumed in Sobolik and Fewell (1992). It was assumed that the water infiltrates the surface uniformly through the design area of the pond. The calculations are simplified to two dimensions by assuming radial symmetry for the infiltration process and that the stratigraphic layers are horizontal and parallel. As in Sobolik and Fewell (1992), the two-dimensional cross-section used to model the mountain is given initial saturation conditions that correspond to a uniform, steady-state infiltration of 0.01 mm/yr through the surface of the mountain. At "time zero," a pond of waste water is introduced at a constant depth of 1.83 m. This pond water will infiltrate the top of the mountain at a rate determined by the pressure head of the pond, while water continues to infiltrate the mountain through the remaining surface at 0.01 mm/yr. The pond is removed after five years, after which the infiltration into the entire surface is returned to a uniform 0.01 mm/yr. The movement of this pond water is followed over 10,000 years. The following additional assumptions are made for the analysis:

- Data for Well UE-25 a#1, which is in Version 2.002 (document number YMP/CC-0002) of the Reference Information Base, but not in the current RIB, are used for locating the boundaries between stratigraphic layers.
- The hydrologic properties previously used in Sobolik and Fewell (1992) are used for these calculations[2], with of course the exception of the properties to be used for PTn. Calculations were run for six other sets of properties for PTn, all based on different measured values. The additional six sets of properties used are shown in Table 3.1-1. An eighth set of calculations was performed using a different stratigraphy in the TCw-PTn-TSw1 region. This stratigraphy used the member interfaces first used in the PACE-90 calculations (Barnard and Dockery, 1991), which are listed in Table 3.2-1. The thermomechanical properties in each layer are assumed to be homogeneous and isotropic throughout the layer.
- The effects of evapotranspiration are not included in the analysis.
- The ground surface is the upper boundary, and the water table is the lower boundary for the computational domain. The surface area of the pond is 9,351 m^2. The sewage pond is assumed to be unlined; therefore, the upper boundary condition is as described above. One vertical boundary is the axis of symmetry through the center of the pond. The other vertical boundary is located at a radius of 600 m from the axis of symmetry. No-flux boundary conditions are imposed on both vertical boundaries.

---

[2] For the calculations performed for Sobolik and Fewell (1992), the material properties listed for TSw2 in Table A.4 were used as the material properties for TSw3. For ESF Analysis #12 (Sobolik and Fewell, 1993), the values listed for TSw3 were used for TSw3 (see Section 3.3).

Table 3.2-1: PACE90 Stratigraphy and Hydraulic Properties

Unit Name	Elevation at Base of Unit (m)	Source of Information
Surface	1199	Same as previous PA analyses
Alluvium	1190	Same as previous PA analyses
TCw	1137.7	SAND90-2726 (Barnard and Dockery, 1991) stratigraphy for UE25 a#1; same material properties as previous PA analyses
PTn (Tpc-TN)	1127.1	SAND90-2726 (Barnard and Dockery, 1991) stratigraphy for UE25 a#1; TN properties listed in Table 3.1-1
PTn (Tpc-BT)	1116.4	SAND90-2726 (Barnard and Dockery, 1991) stratigraphy for UE25 a#1; BT properties listed in Table 3.1-1
PTn (Tpt-TM)	1093.6	SAND90-2726 (Barnard and Dockery, 1991) stratigraphy for UE25 a#1; TM properties listed in Table 3.1-1
TSw1	871	Same as previous PA analyses
TSw2	815	Same as previous PA analyses
TSw3	798	Same as previous PA analyses
CHn3	730.6	Same as previous PA analyses

The results of the original calculations for ESF Analysis #3 (Sobolik and Fewell, 1992), with alluvium as the top layer, indicated that there would be no effect on experiments in the ESF or on potential repository performance because water movement from the sewage pond and the resulting changes in saturation would not penetrate to repository depth. These calculations were re-run for this analysis, and for convenience are referred to as ESF3. ESF3 results were used as the benchmark to which the other seven sets of results were compared. The results of these calculations are compared at three points: after 5 years of water infiltration from the surface pond; and after 100 and 10,000 years of movement of this water.

Figure 3.2-1 shows the portion of the computational grid in the location where the effects of the pond water primarily occur; the pond radius is 54.6 m and is included in the three left-most columns of elements. Figures 3.2-2 through 3.2-9 display the in situ saturation profiles calculated for each of the eight problems (ESF3, BT, PAH, TM, TN, YM, and YMNF, and PACE90, respectively). The first observation to be made here is that all the saturation profiles except PACE90 are identical beneath the PTn-TSw1 interface (385 m above the water table), and even the PACE90 results are the same beneath the top of its TSw1 section. This is because at a steady-state flux, the solution is only dependent on what material properties are below the point of interest. The two Yucca Mountain member cases (with and without fractures) are identical to each other. As expected, a wide range of values for in situ saturation in the PTn were calculated, ranging from 10% to 97%. There was also some significant variation in the saturation levels in the TCw. The level of saturation in the alluvium is essentially the same for all cases. The in situ water content of the cylindrical section of mountain modeled for these calculations is shown for each of the cases in Table 3.2-2; because of the high porosity assigned to PTn by many of the cases, the amount of in situ water is highly tied to the level of saturation in PTn.

Figure 3.2-1: Computational Grid for Pond Water Calculations

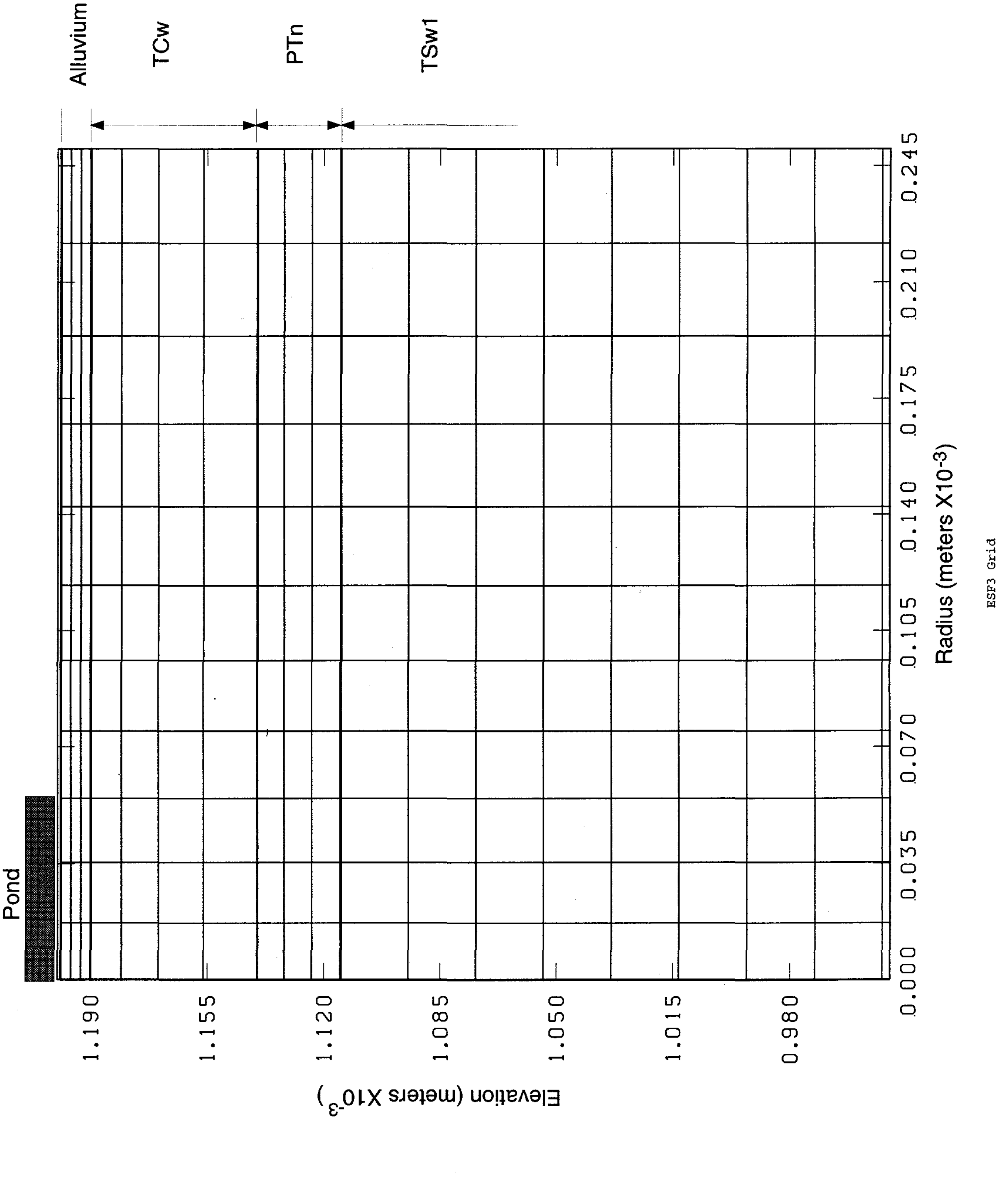

Figure 3.2-2: In Situ Saturation Profile, Pond Water Calculations
PTn Modeled Per ESF3

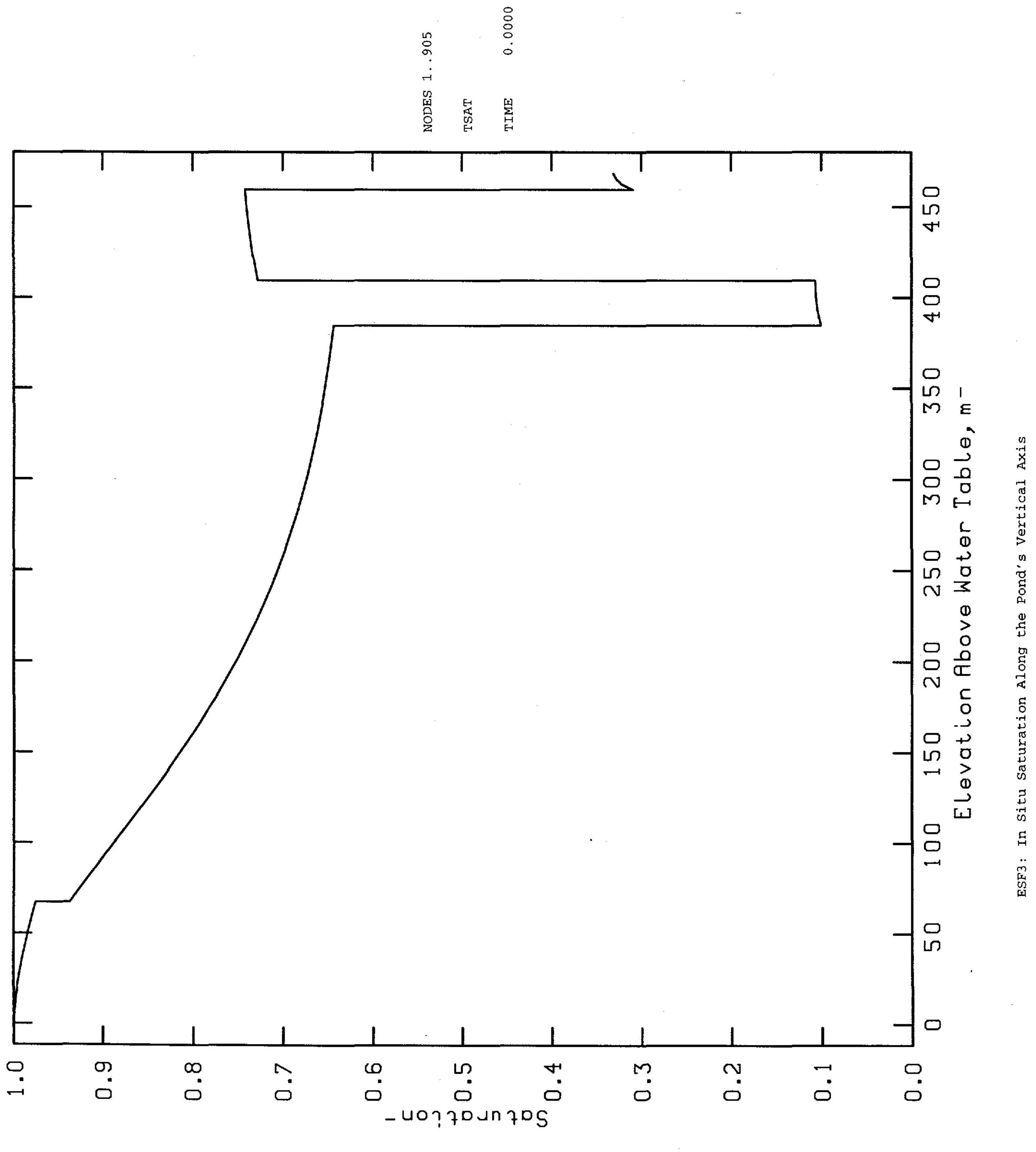

Figure 3.2-3: In Situ Saturation Profile, Pond Water Calculations PTn Modeled as Bedded Tuff

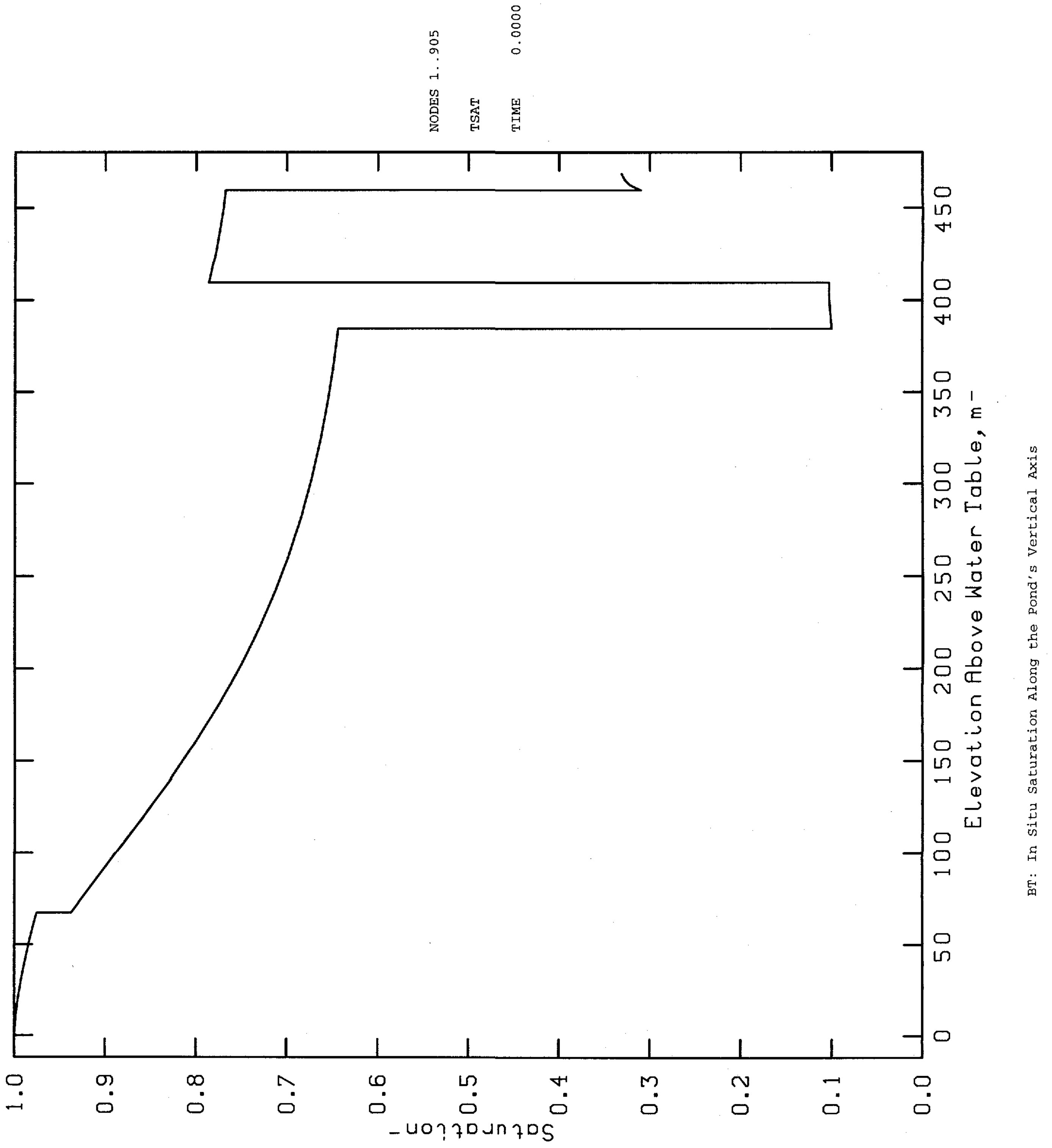

Figure 3.2-4: In Situ Saturation Profile, Pond Water Calculations
PTn Modeled as Pah Canyon Member

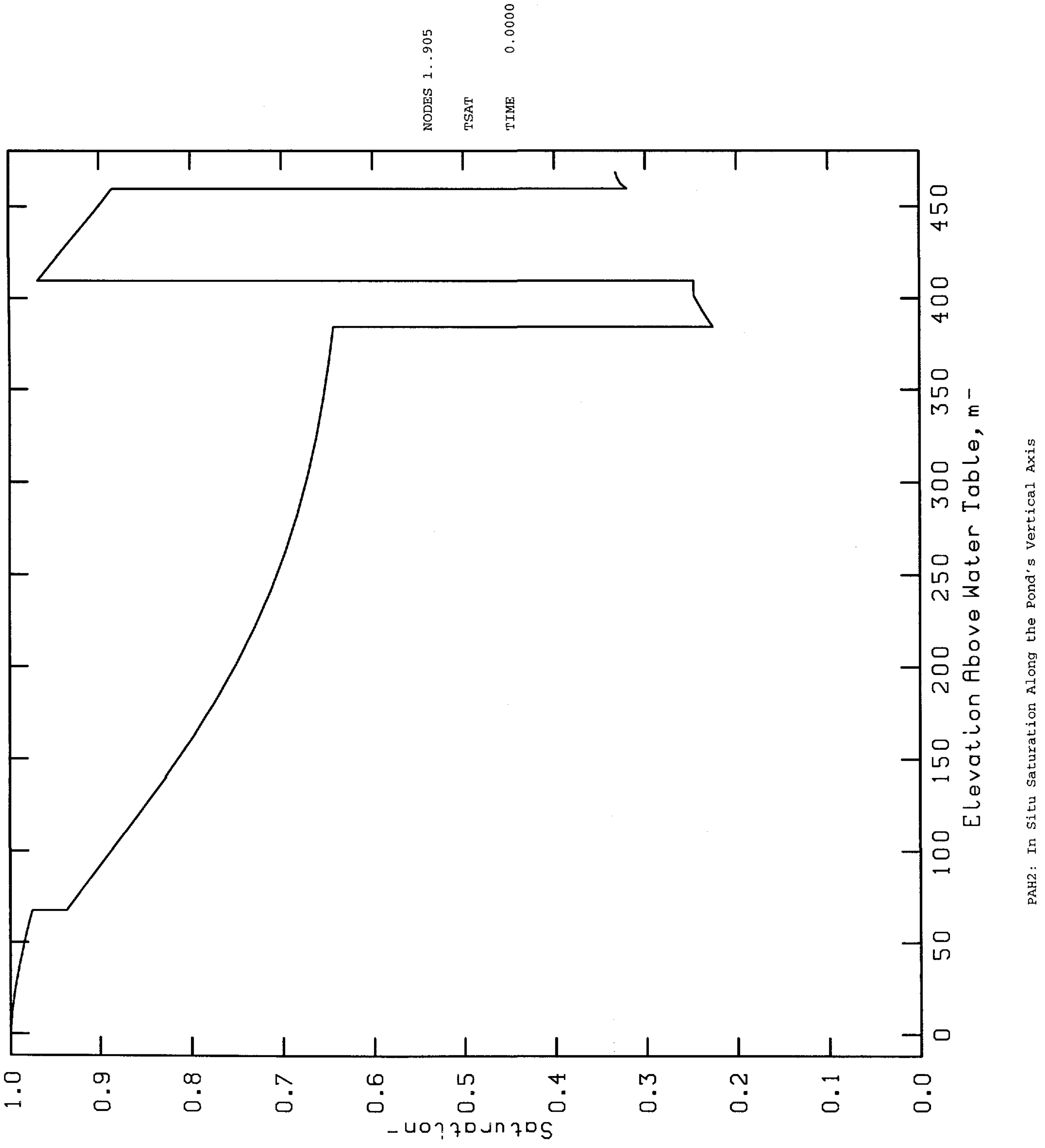

Figure 3.2-5: In Situ Saturation Profile, Pond Water Calculations
PTn Modeled as Tpt-TM

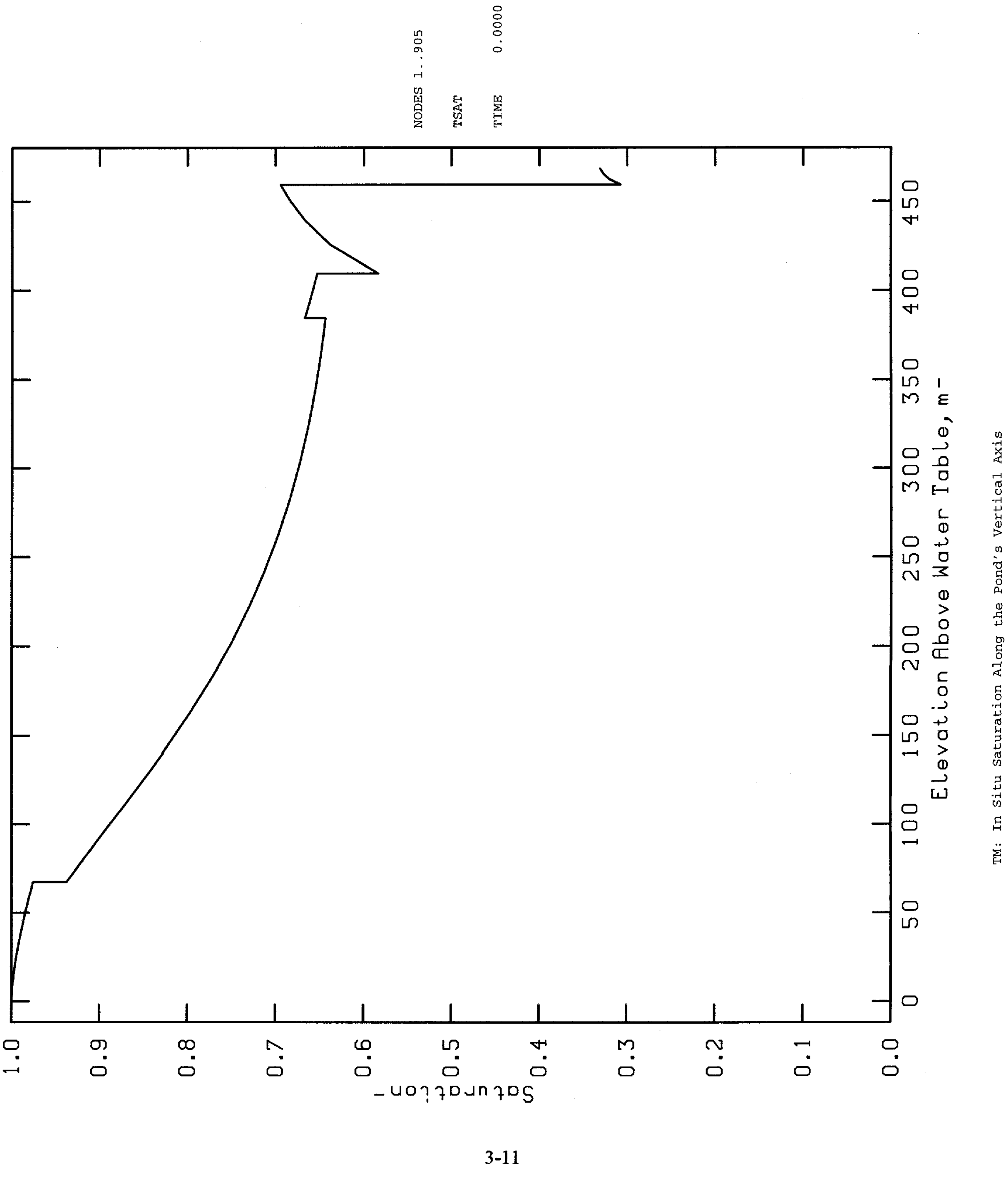

Figure 3.2-6: In Situ Saturation Profile, Pond Water Calculations PTn Modeled as Tpc-TN

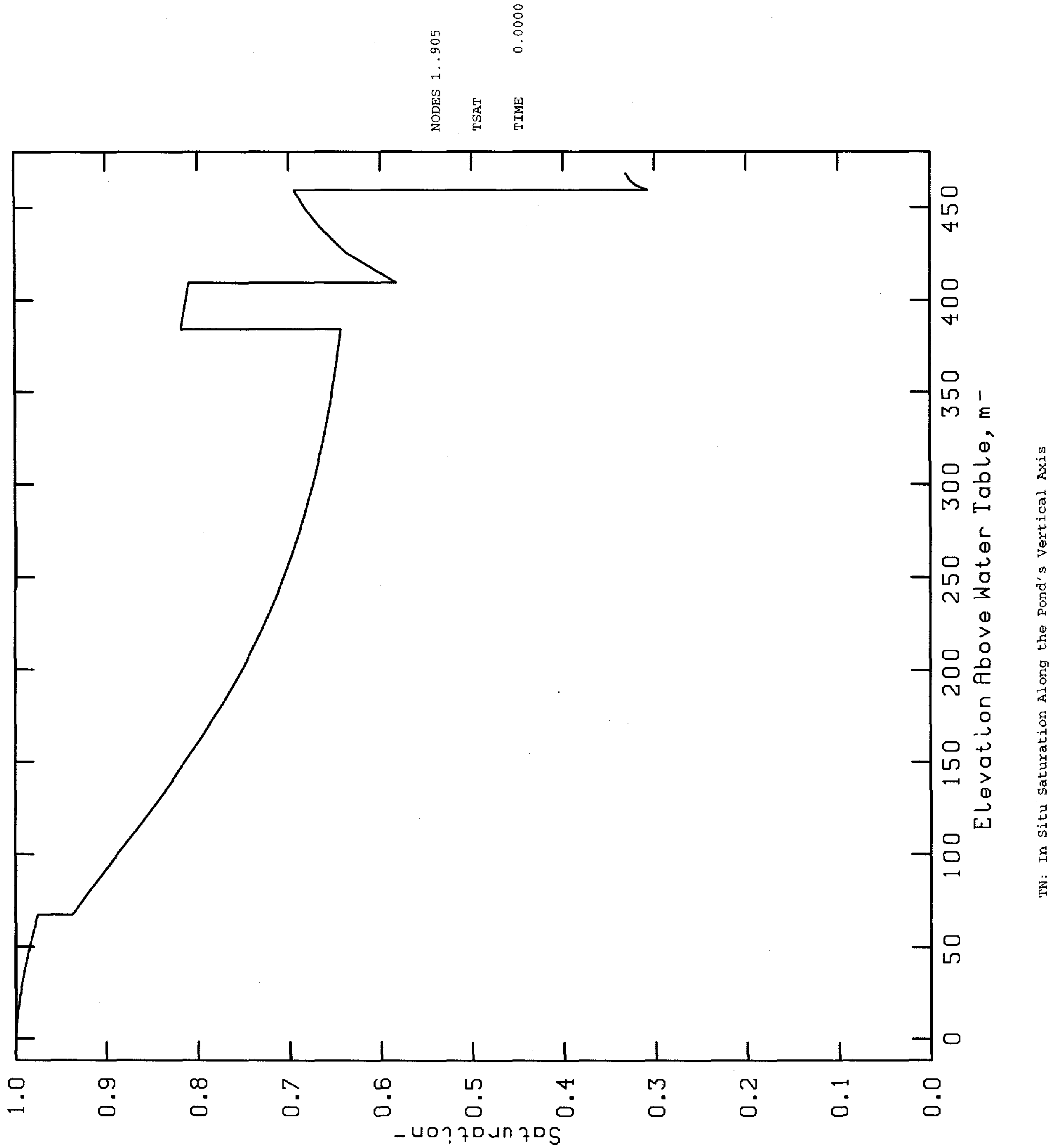

Figure 3.2-7: In Situ Saturation Profile, Pond Water Calculations PTn Modeled as Yucca Mountain Member

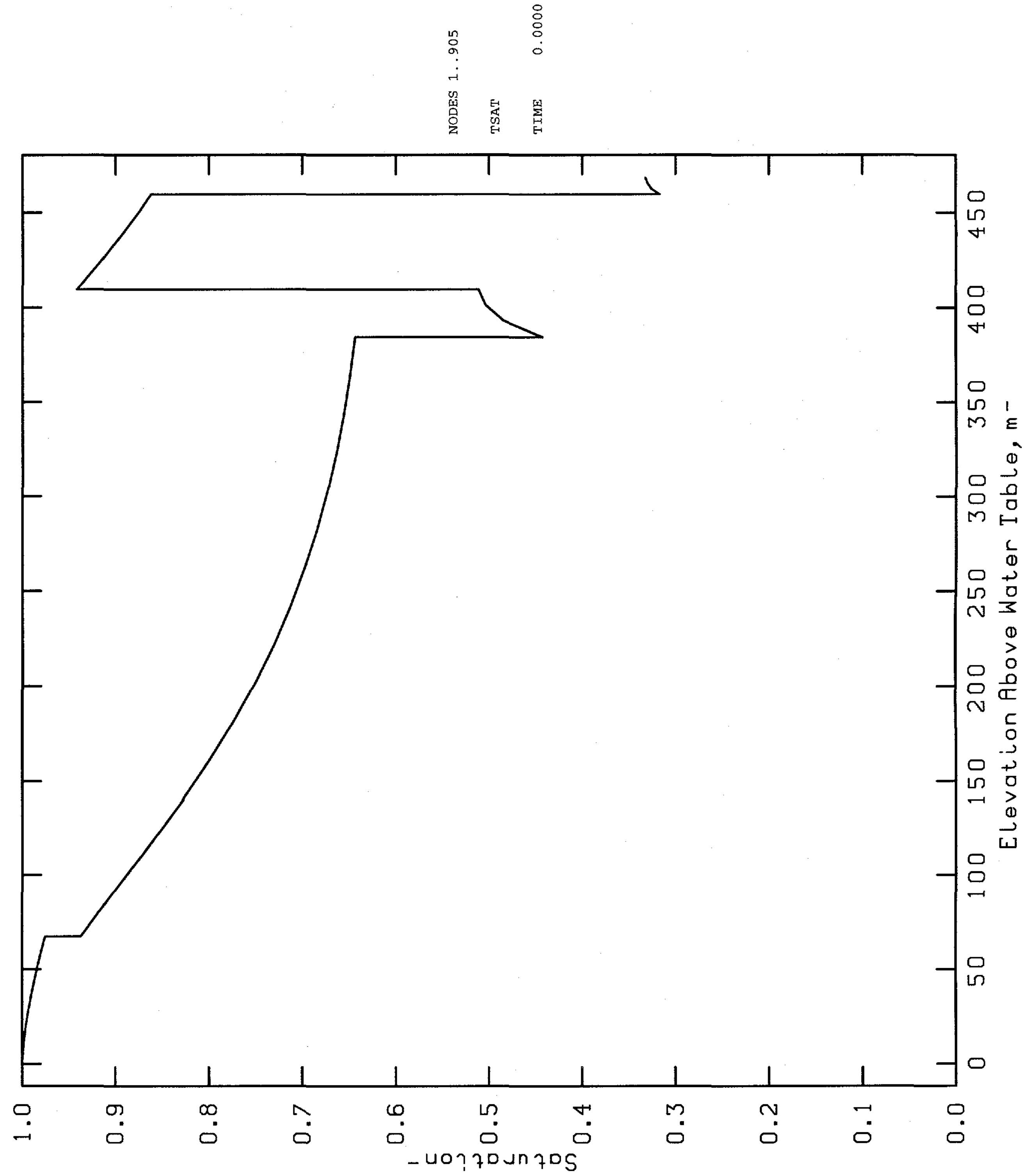

YM: In Situ Saturation Along the Pond's Vertical Axis

Figure 3.2-8: In Situ Saturation Profile, Pond Water Calculations PTn Modeled as Yucca Mountain Member (No Fractures)

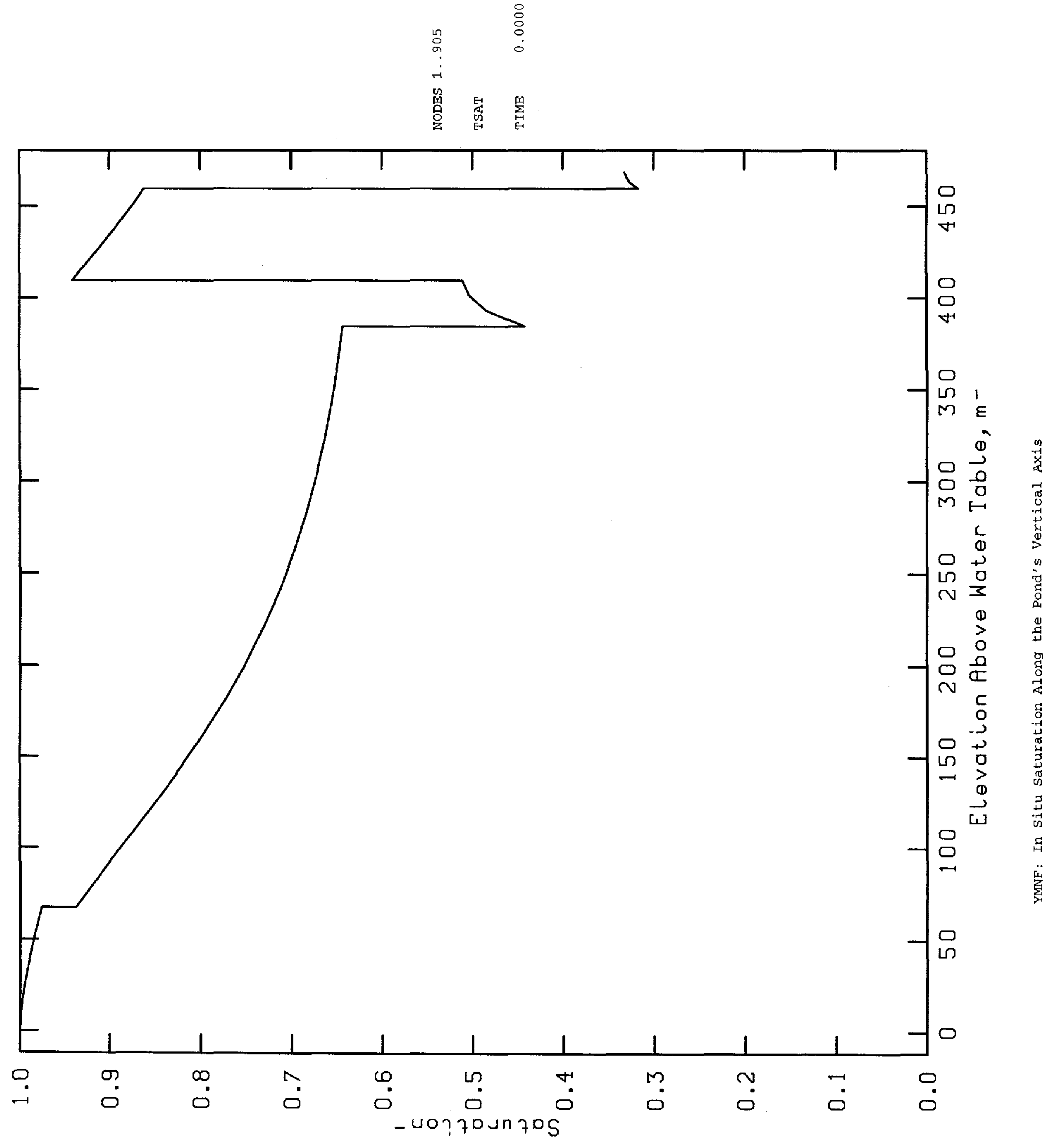

Figure 3.2-9: In Situ Saturation Profile, Pond Water Calculations PTn Modeled Per PACE-90

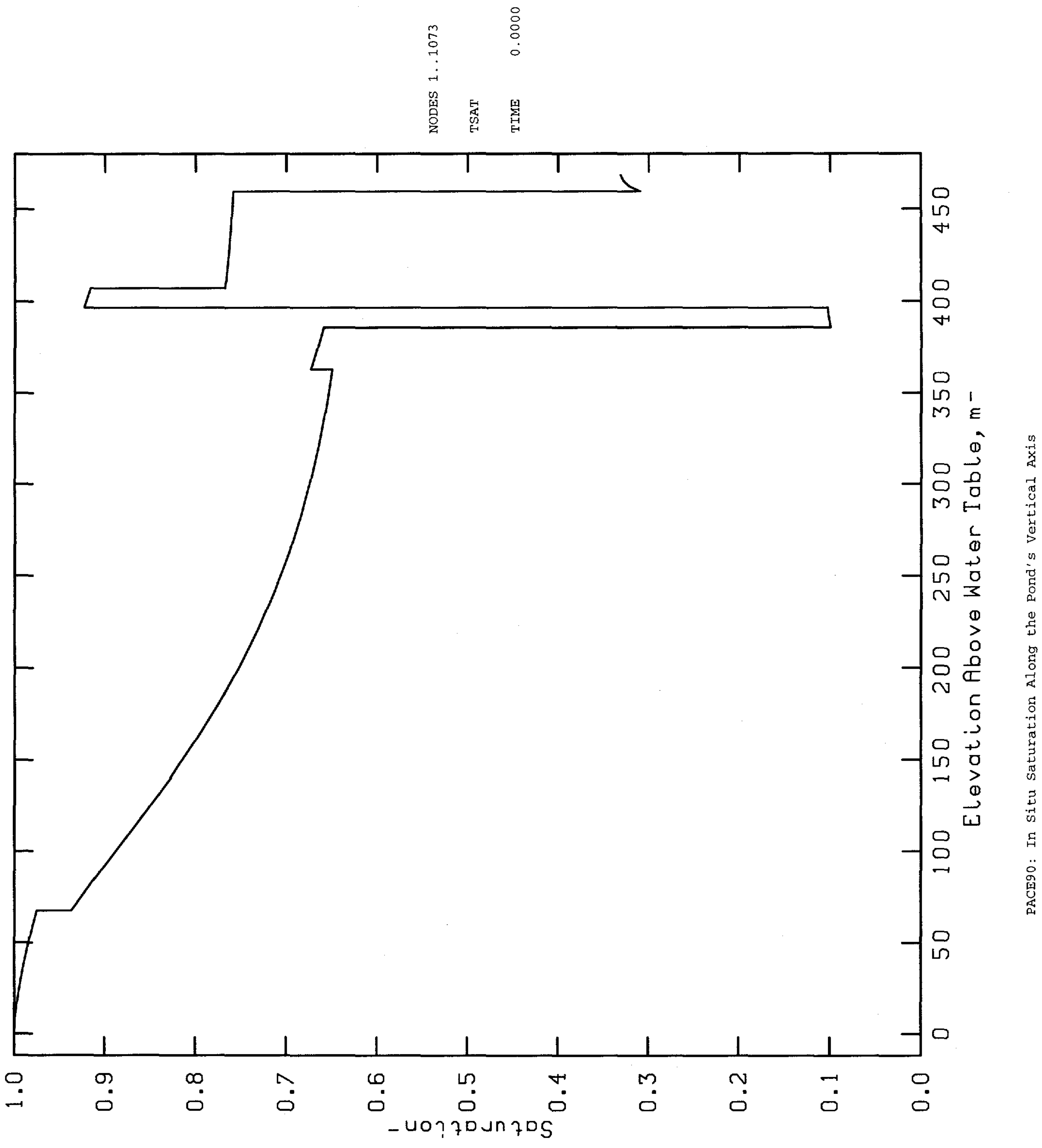

Table 3.2-2: Results of Pond Calculations

PTn Modeled as	In Situ Water Content (m^3)	PTn In Situ Saturation	TCw In Situ Saturation	Meters of head through pond surface after 5 years[3]	Radial Extent of Δsat=2% After 5 yr (m)	Bulk K_{sat} in PTn (m/s)	Matrix K_{sat} in PTn (m/s)	Matrix Porosity in PTn	Fractures in PTn
Tpc-TN	8.0356×10^7	81-82%	58-70%	9.96	162.4	2.00×10^{-11}	2.00×10^{-11}	0.5	no
Yucca Mtn.	7.4220×10^7	43-52%	86-95%	9.51	160.0	1.91×10^{-7}	1.75×10^{-7}	0.436	yes
Yucca Mtn. No Fractures	7.4220×10^7	43-52%	86-95%	9.50	160.0	1.75×10^{-7}	1.75×10^{-7}	0.436	no
Pah Canyon	7.2465×10^7	22-25%	89-97%	9.70	158.9	7.30×10^{-7}	7.14×10^{-7}	0.47	yes
ESF 3	6.7602×10^7	10-11%	72-74%	10.07	162.3	4.06×10^{-7}	3.90×10^{-7}	0.4	yes
Bedded Tuff	6.2141×10^7	10-11%	77-79%	10.10	162.2	2.40×10^{-6}	2.40×10^{-6}	0.22	no
PACE90	6.1163×10^7	92-93% (TN) 10-11% (BT) 66-68% (TM)	76-77%	10.08	162.1				
Tpt-TM	5.9416×10^7	66-68%	58-70%	9.97	162.4	1.22×10^{-9}	2.00×10^{-11}	0.1	yes

3.2.2 Results After 5 Years

Figure 3.2-10 is a contour plot of Δsat which shows the extent of water movement after 5 years for the original calculations (ESF3)[4]. Figures 3.2-11 through 3.2-17 are similar contour plots showing the extent of water movement when the calculations used BT, PAH, TM, TN, YM, and YMNF properties, and the PACE-90 stratigraphy, respectively, for PTn. The extent of lateral and vertical water movement is marked by the location of the outermost contours, which represent a Δsat of 5%. Qualitatively, in terms of the lateral and vertical extent of water movement, there is very little difference among the eight sets of results. Table 3.2-2 shows the lateral (i.e., radial) extent of values of Δsat of 2%; these values are referred to in Section 3.3. Most of the other sets of PTn properties produced approximately the same lateral extent of water movement along the alluvium-TCw interface as the original properties. The Pah Canyon (Figure 3.2-12) properties predicted the smallest extent of lateral water movement. The Pah Canyon and Yucca Mountain (Figures 3.2-15 and 3.2-16) properties predicted fairly significant penetrations of pond water into the PTn. Penetrations into PTn are also shown for the bedded tuff properties (Figure 3.2-11), but the small change in saturation and the low porosity signify a relatively minuscule amount of water penetration. It is important to note that water penetration into PTn seems to occur only where the TCw becomes nearly saturated; the high suction pressures predicted for less than ~90% saturation in TCw prevent water movement into PTn. The results from the Yucca Mountain member calculations with and without fractures are nearly identical. Table 3.2-2 shows the volume of water imbibed through the surface after 5 years for each of the eight sets of calculations. Again, there is no significant difference in the amount of imbibed water, with the

---

[3] "Meters of head through pond surface" = Volume of imbibed pond water / Area of pond.

[4] Figures 10 through 17 are plotted with the same contour values as Figure 11 in Sobolik and Fewell (1992) to allow direct comparison. Figure 10 was plotted from the same solution as was Figure 11 in Sobolik and Fewell (1992), but with a different plotting package (BLOT) which better captures the discontinuity in the change in saturation at the interfaces between geohydrologic units.

minor exception of Pah Canyon and Yucca Mountain properties, indicating that in areas of thick alluvial deposits the predicted amount of imbibed surficial water does not appear to be sensitive to the characterization of PTn.

3.2.3 Results After 100 Years

For each set of calculations, the water imbibed into the mountain after 5 years was allowed to migrate through 100 years. Figure 3.2-18 is a contour plot of Δsat which shows the extent of migration predicted by the original calculations; similarly, Figures 3.2-19 through 3.2-25 show the same for the other cases.

There are several interesting things to notice here. First, compare the values of Δsat in the TCw layers in Figures 3.2-18 through 3.2-25 to the values of in situ saturation in TCw in Table 3-2.2. At 100 years, all cases exhibit large areas in TCw which are nearly saturated (>95%). Also note that significant movement into the PTn has occurred for all cases after 100 years. Another similarity is that the lateral extent of water movement (as signified by the 2.5% Δsat contour at the alluvium-TCw interface) is approximately the same for all cases. All these examples indicate little sensitivity to the characterization of PTn.

There are significant differences in some of the results. Note that the shallowest penetration of additional water is predicted by the calculations using the TM (Figure 3.2-21) and TN (Figure 3.2-22) properties, and by those using the PACE-90 stratigraphy (Figure 3.2-25), which employs TM and TN as two of its layers. Also common among these three cases is that they had the lowest in situ saturation values in TCw, and they have the highest amounts of additional water remaining in TCw after 100 years. The presence of the lower permeability in the TM and TN layers keeps waters at the higher elevations longer. The presence of a bedded tuff section between TM and TN in the PACE-90 calculations seems to have little effect on moving water through the lower permeability units. In Figures 3.2-19 and 3.2-20, note the significant amounts of water allowed to penetrate into the Topopah Spring unit (TSw) through the bedded tuff and Pah Canyon member, respectively. The nearly saturated conditions in TCw at 5 years for these two cases hastened the flow of water to TSw.

3.2.4 Results After 10,000 Years

For each set of calculations, the water imbibed into the mountain after 5 years was allowed to migrate through 10,000 years. Figure 3.2-26 is a contour plot of Δsat which shows the extent of migration predicted by the original calculations; similarly, Figures 3.2-27 through 3.2-33 show the same for the other cases. Again, in terms of potential effects at the repository horizon, there is little significant difference between the various cases. The calculations using Pah Canyon properties show the greatest extent of vertical migration (signified by a value of Δsat of 1%) of all the calculations. The calculations using the bedded tuff, Pah Canyon, and Yucca Mountain properties (Figures 3.2-27, 3.2-28, 3.2-31, and 3.2-32, respectively), which at five years were the only calculations showing infiltration of surficial water into the PTn, display the smallest amounts of surficial water remaining in the TCw at 10,000 years. The lateral extent of water movement seems to be driven by the bulk conductivity of the PTn layer.

Figure 3.2-10: Change in Saturation After 5 Years, Pond Water Calculations PTn Modeled Per ESF3

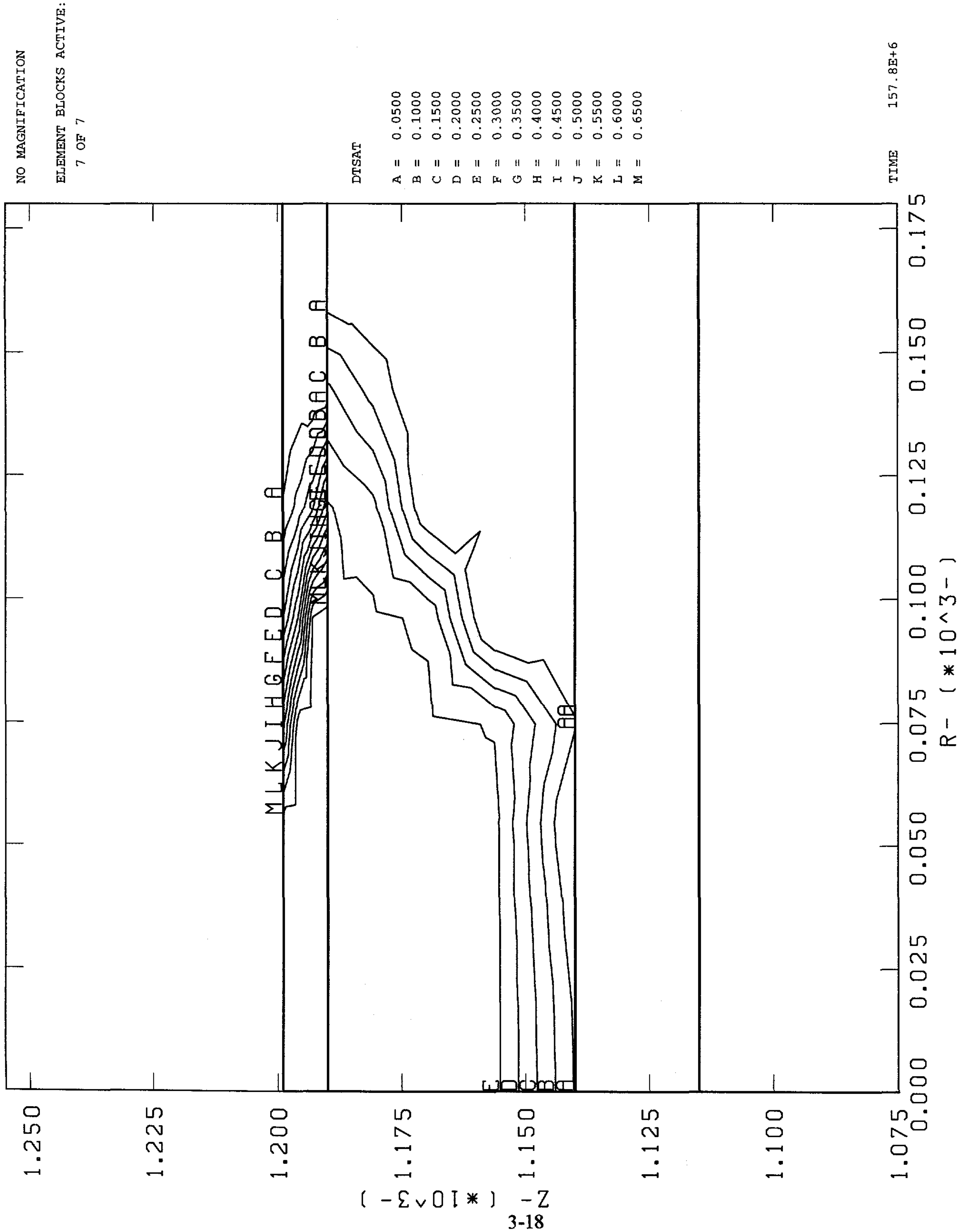

ESF3: Change from In Situ Saturation After 5 Years
(Compare with Figure 11, SAND91-0792)

Figure 3.2-11: Change in Saturation After 5 Years, Pond Water Calculations
PTn Modeled as Bedded Tuff

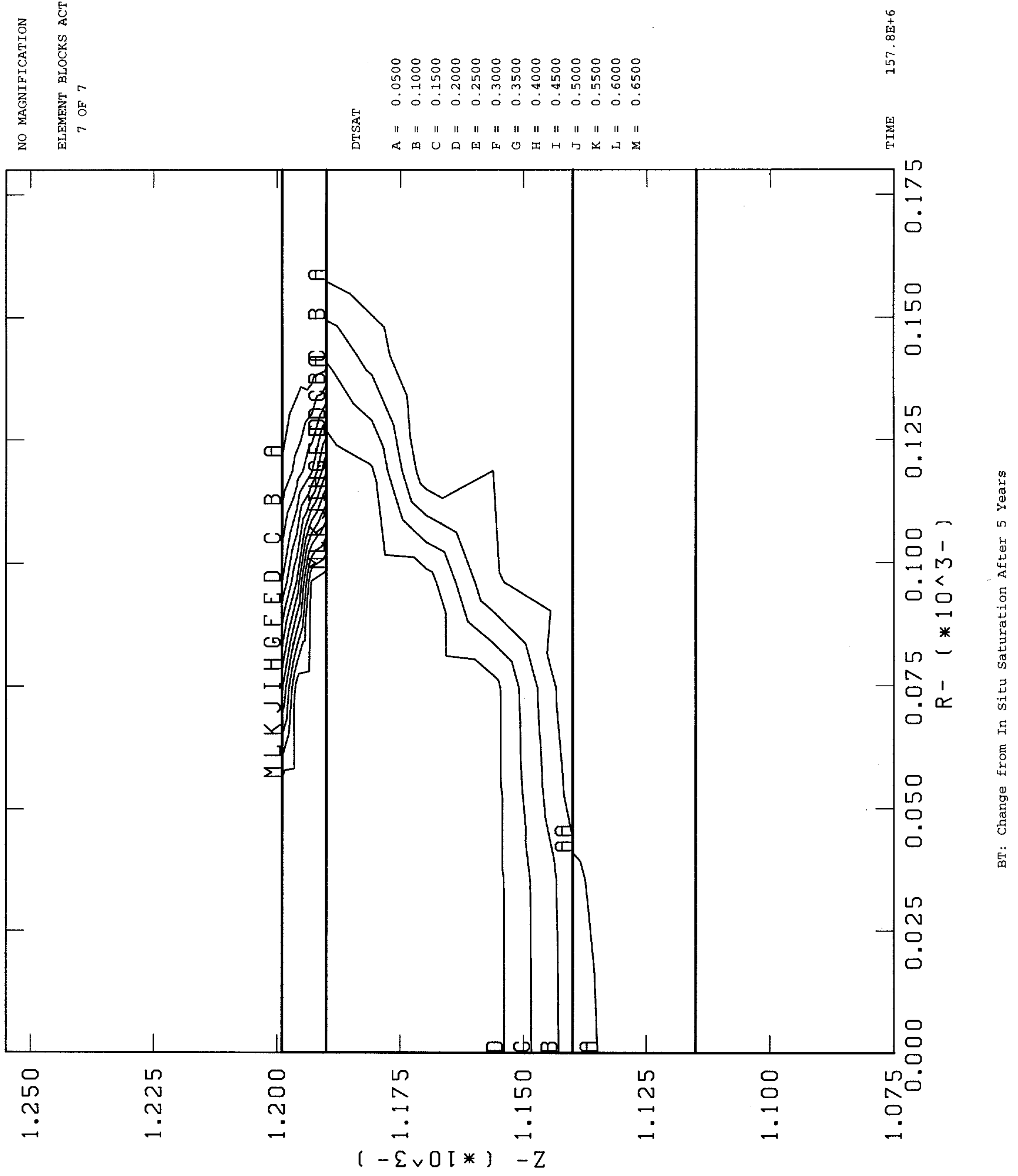

Figure 3.2-12: Change in Saturation After 5 Years, Pond Water Calculations
PTn Modeled as Pah Canyon Member

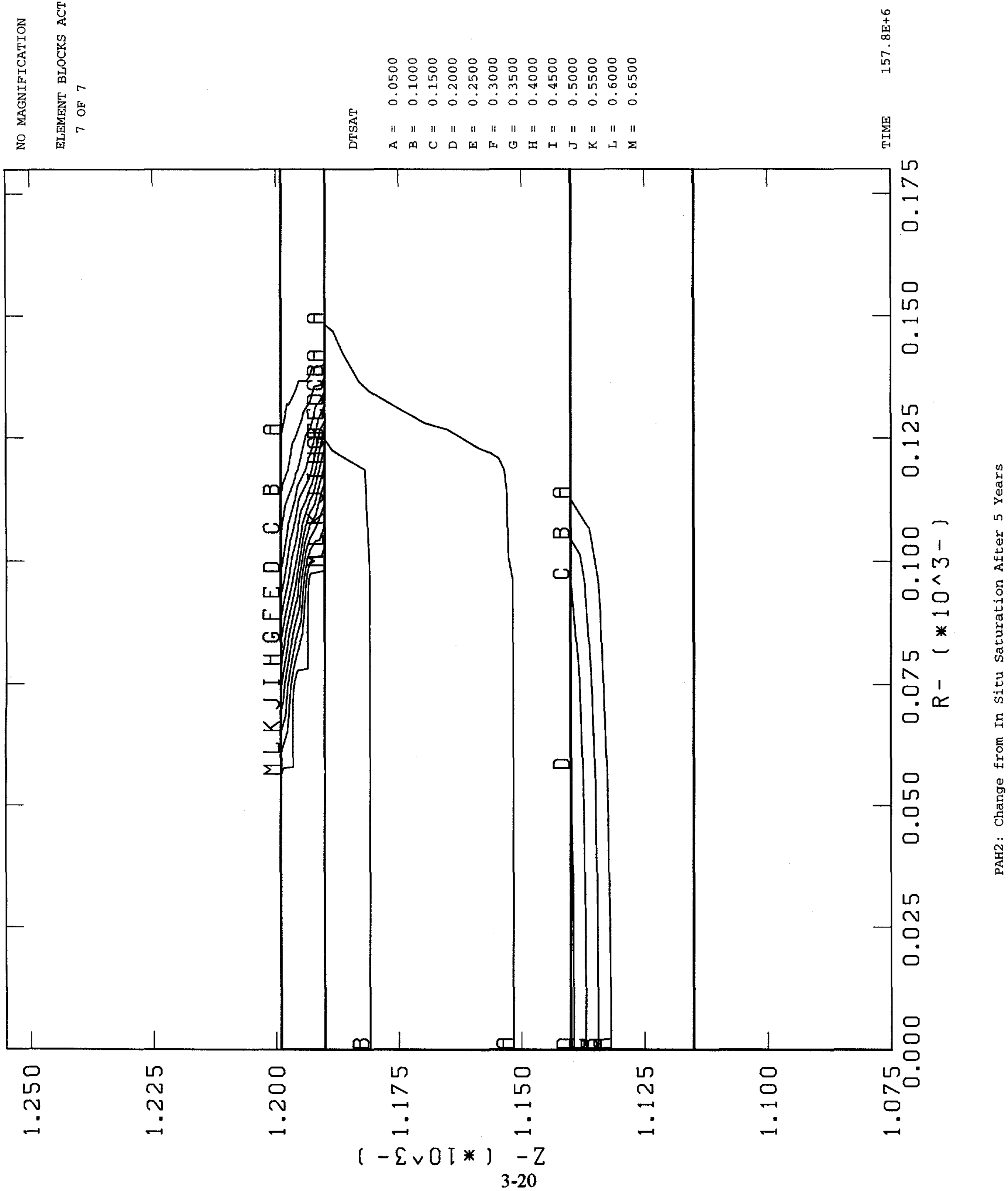

Figure 3.2-13: Change in Saturation After 5 Years, Pond Water Calculations PTn Modeled as Tpt-TM

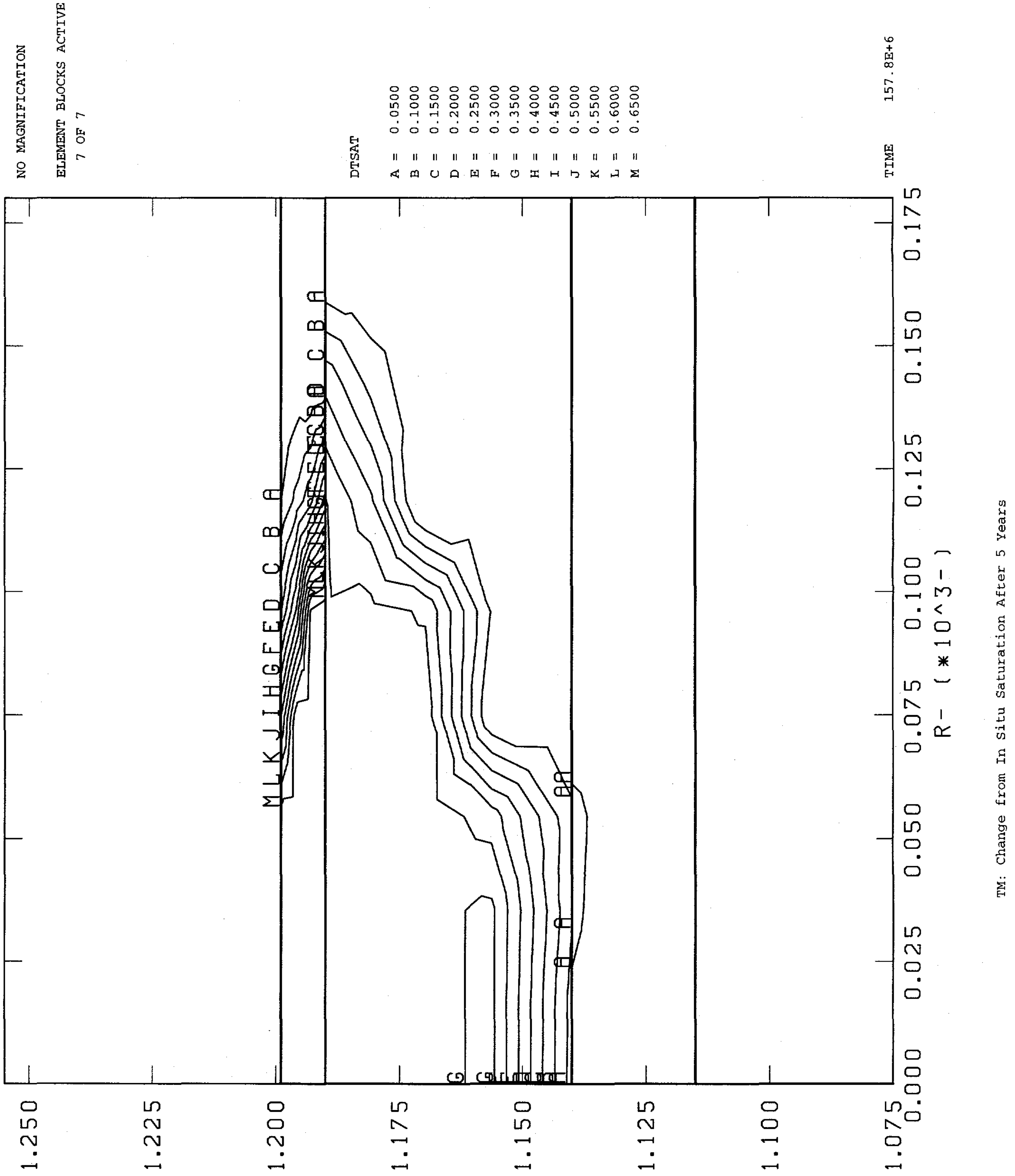

TM: Change from In Situ Saturation After 5 Years

Figure 3.2-14: Change in Saturation After 5 Years, Pond Water Calculations
PTn Modeled as Tpc-TN

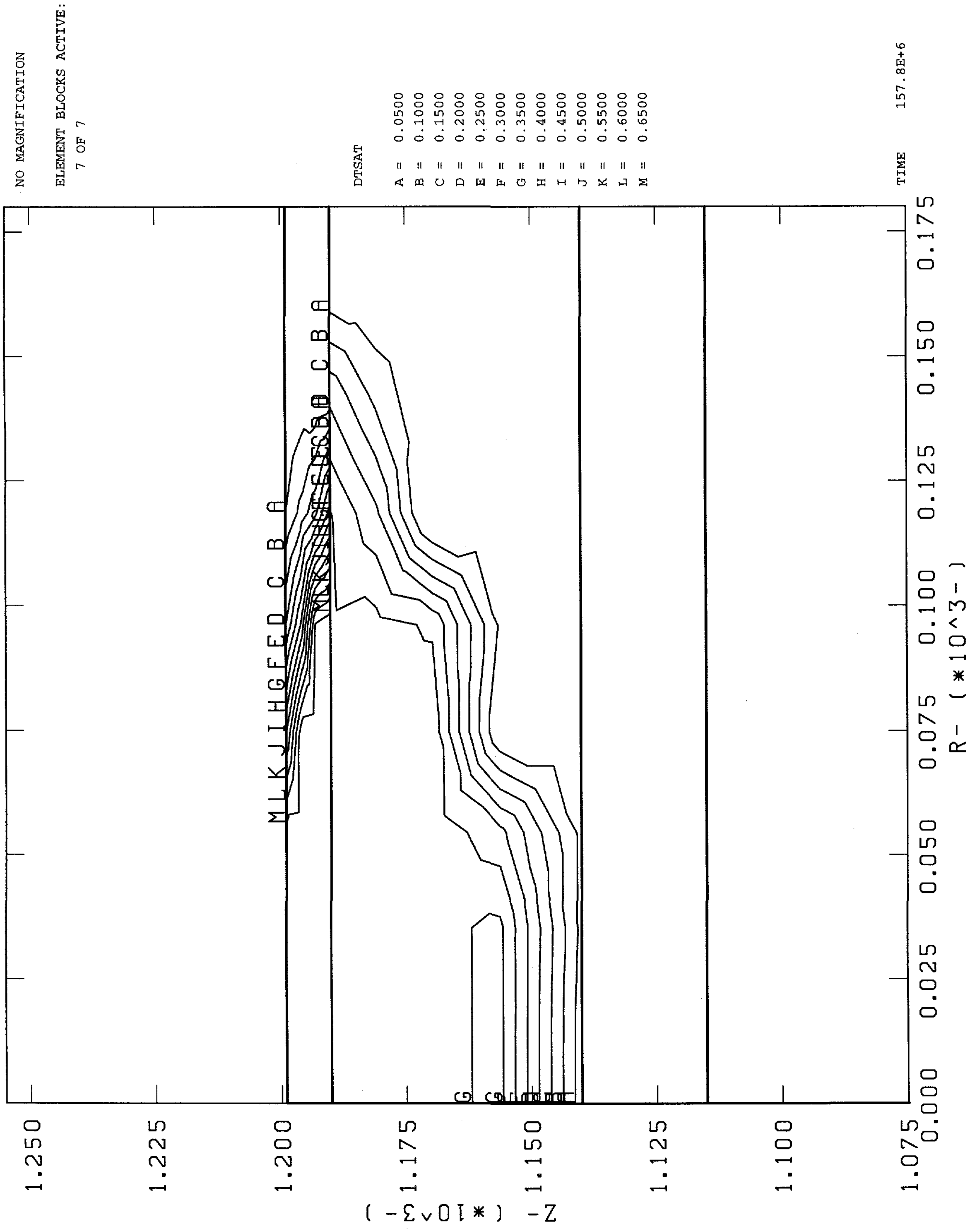

TN: Change from In Situ Saturation After 5 Years

Figure 3.2-15: Change in Saturation After 5 Years, Pond Water Calculations PTn Modeled as Yucca Mountain Member

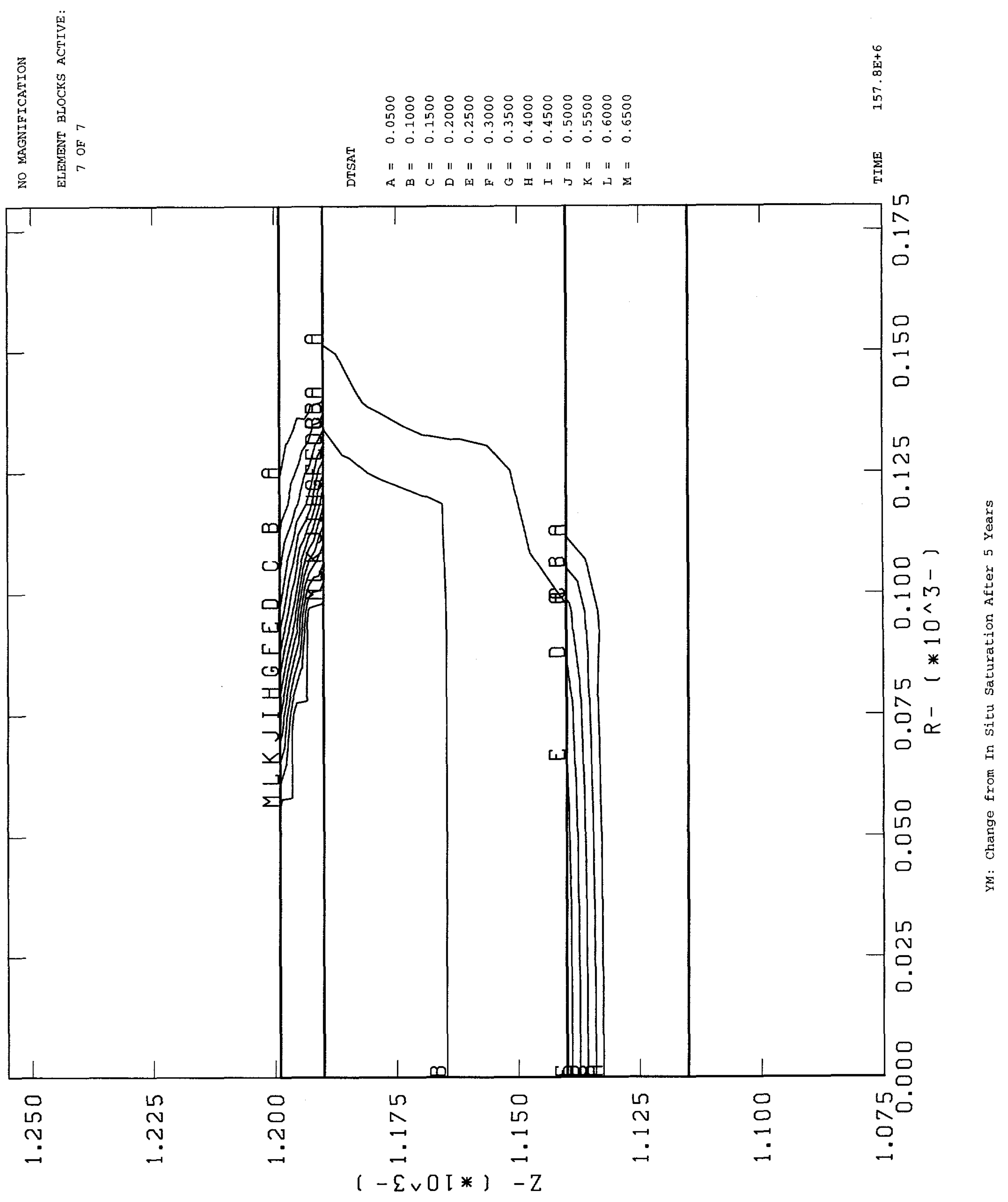

Figure 3.2-16: Change in Saturation After 5 Years, Pond Water Calculations PTn Modeled as Yucca Mountain Member (No Fractures)

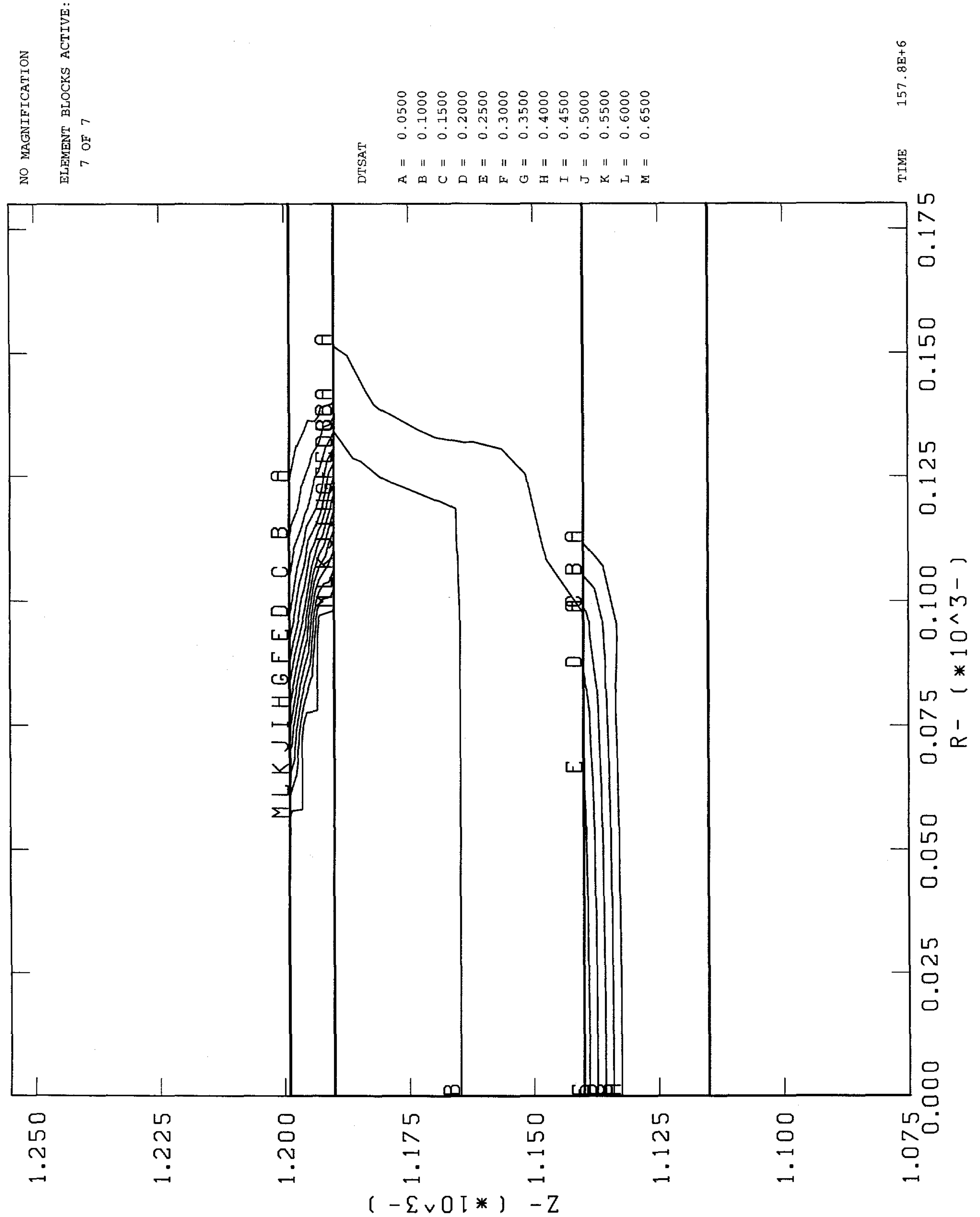

YMNF: Change from In Situ Saturation After 5 Years

Figure 3.2-17: Change in Saturation After 5 Years, Pond Water Calculations
PTn Modeled Per PACE-90

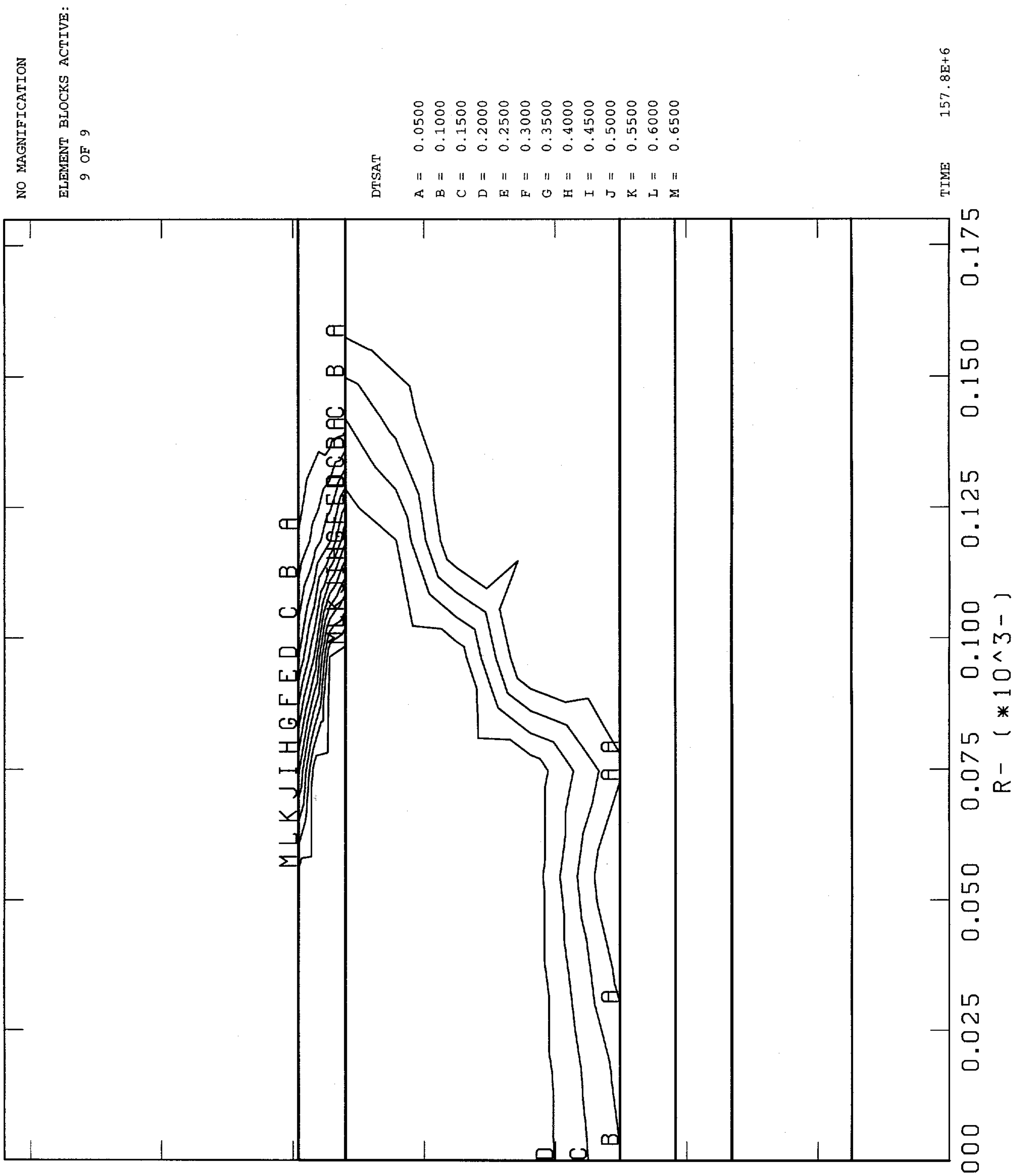

PACE90: Change from In Situ Saturation After 5 Years

Figure 3.2-18: Change in Saturation After 100 Years, Pond Water Calculations PTn Modeled Per ESF3

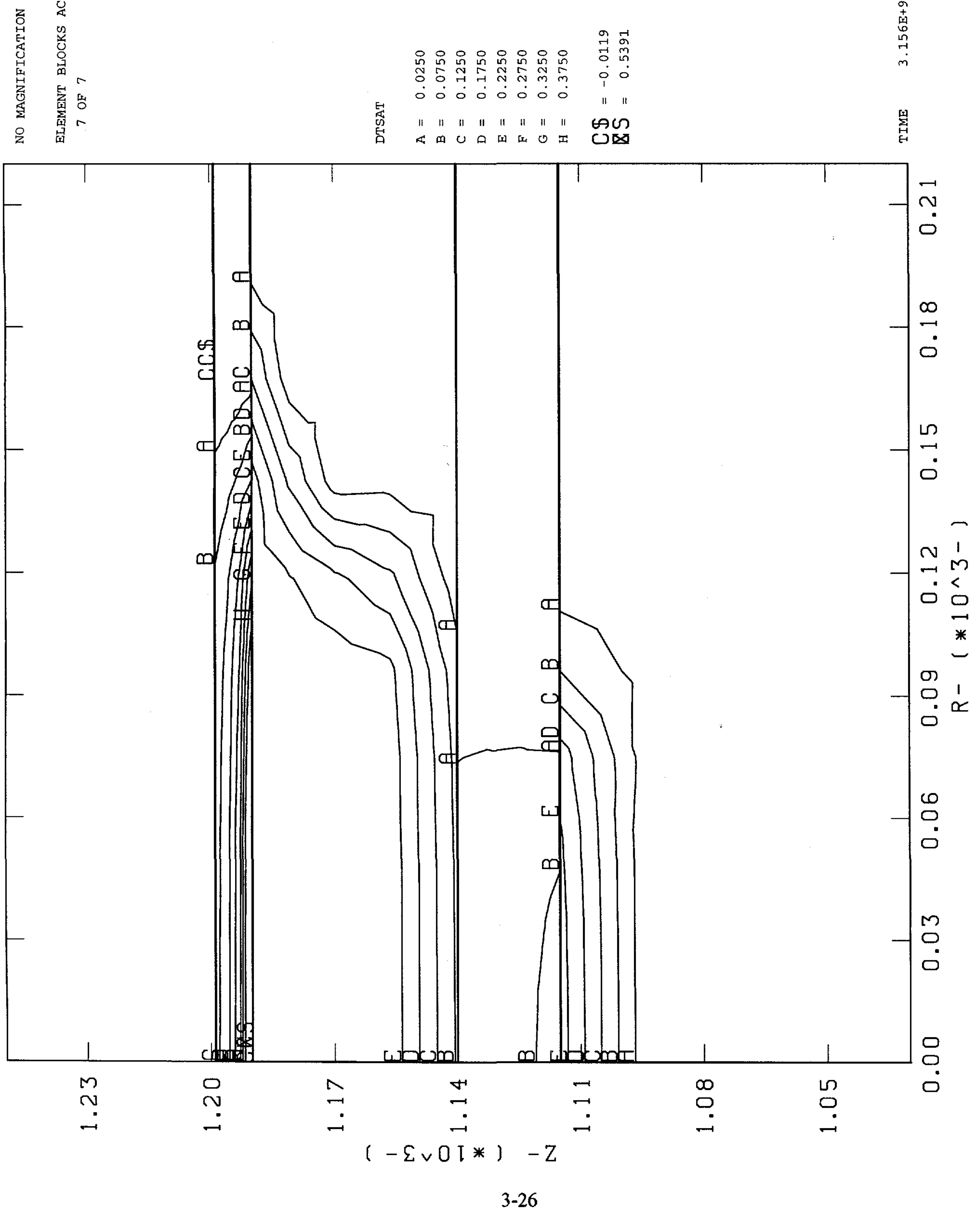

ESF3: Change from In Situ Saturation After 100 Years
(Compare with Figure 12, SAND91-0792)

Figure 3.2-19: Change in Saturation After 100 Years, Pond Water Calculations PTn Modeled as Bedded Tuff

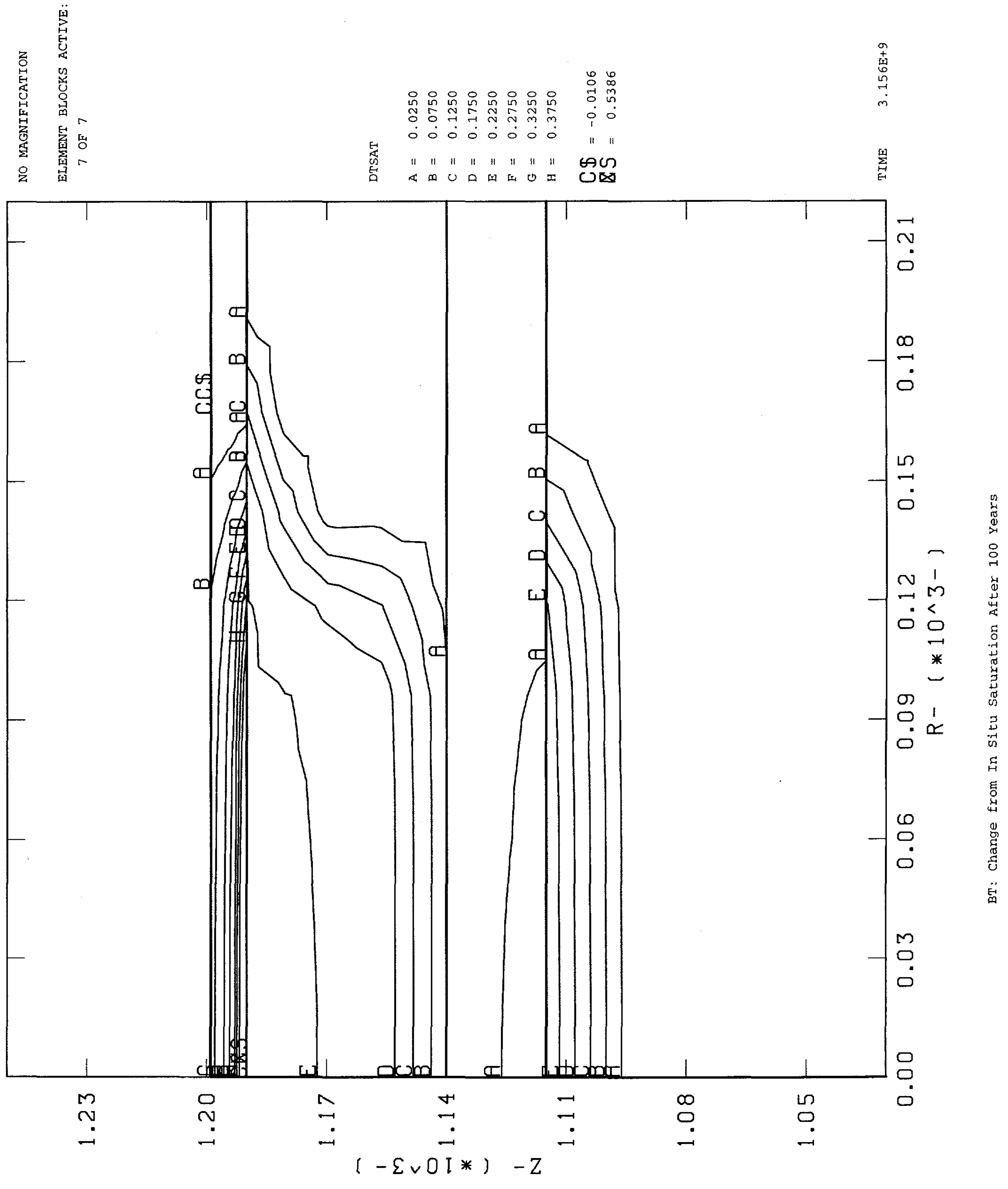

BT: Change from In Situ Saturation After 100 Years

Figure 3.2-20: Change in Saturation After 100 Years, Pond Water Calculations PTn Modeled as Pah Canyon Member

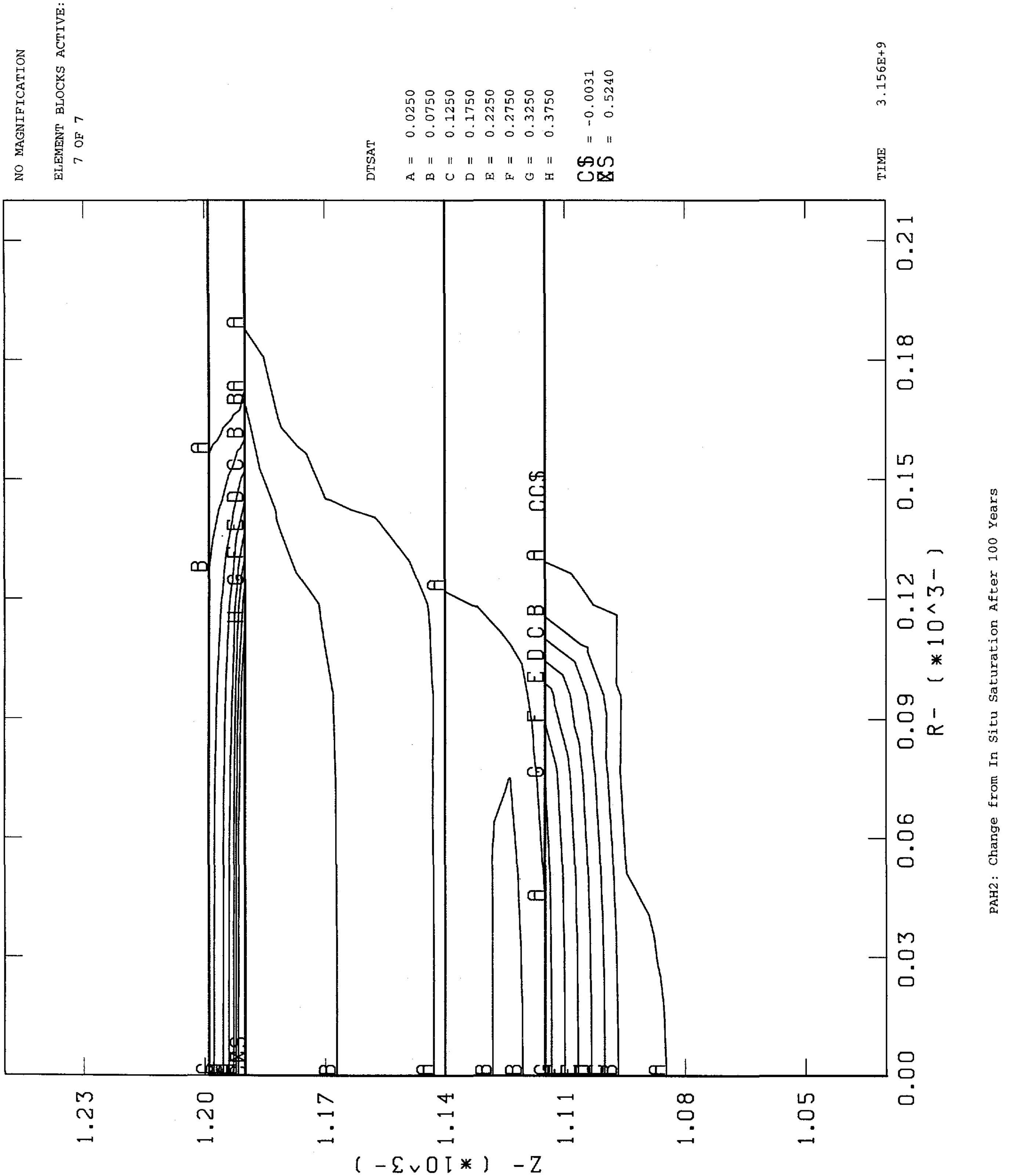

Figure 3.2-21: Change in Saturation After 100 Years, Pond Water Calculations
PTn Modeled as Tpt-TM

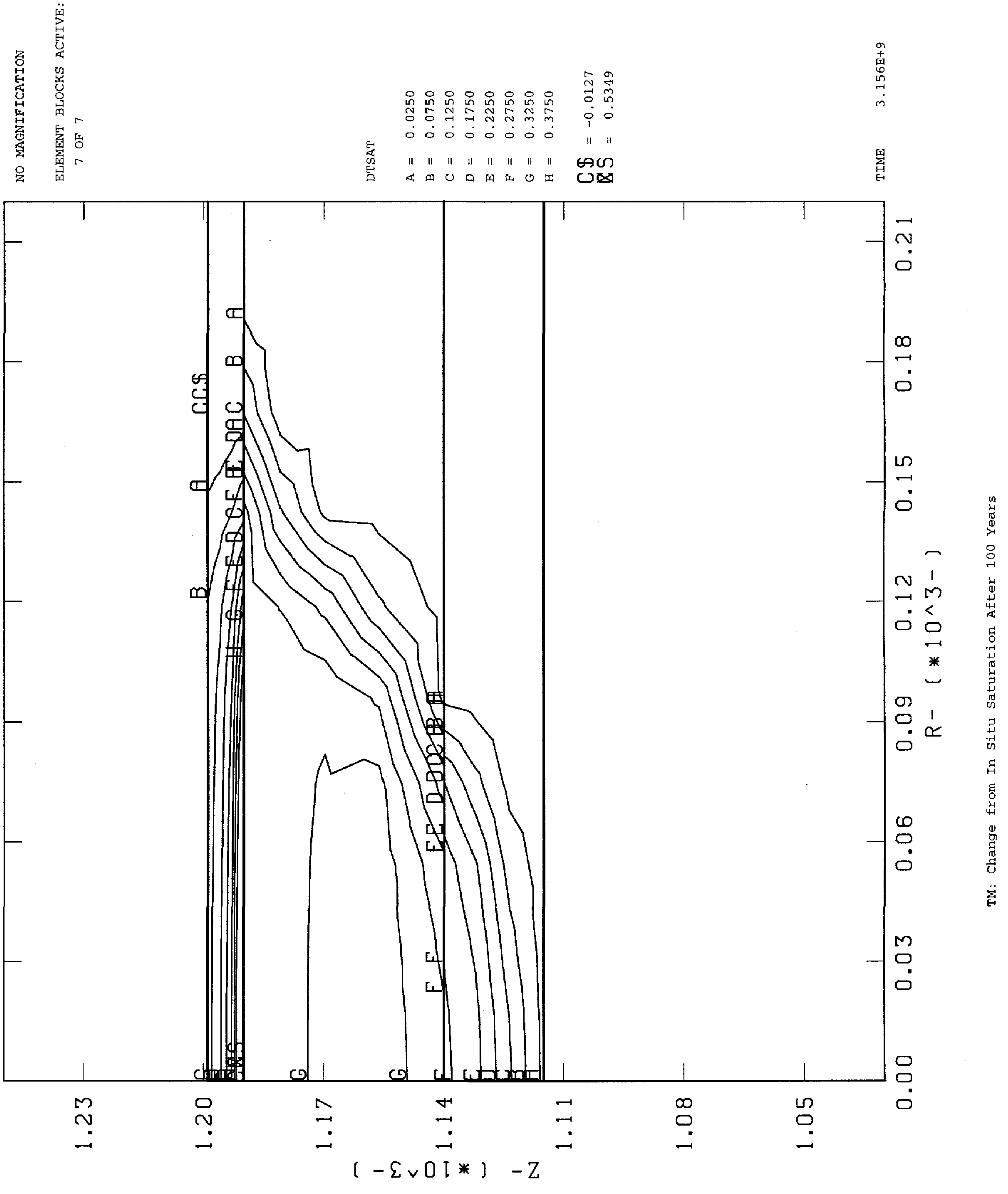

Figure 3.2-22: Change in Saturation After 100 Years, Pond Water Calculations
PTn Modeled as Tpc-TN

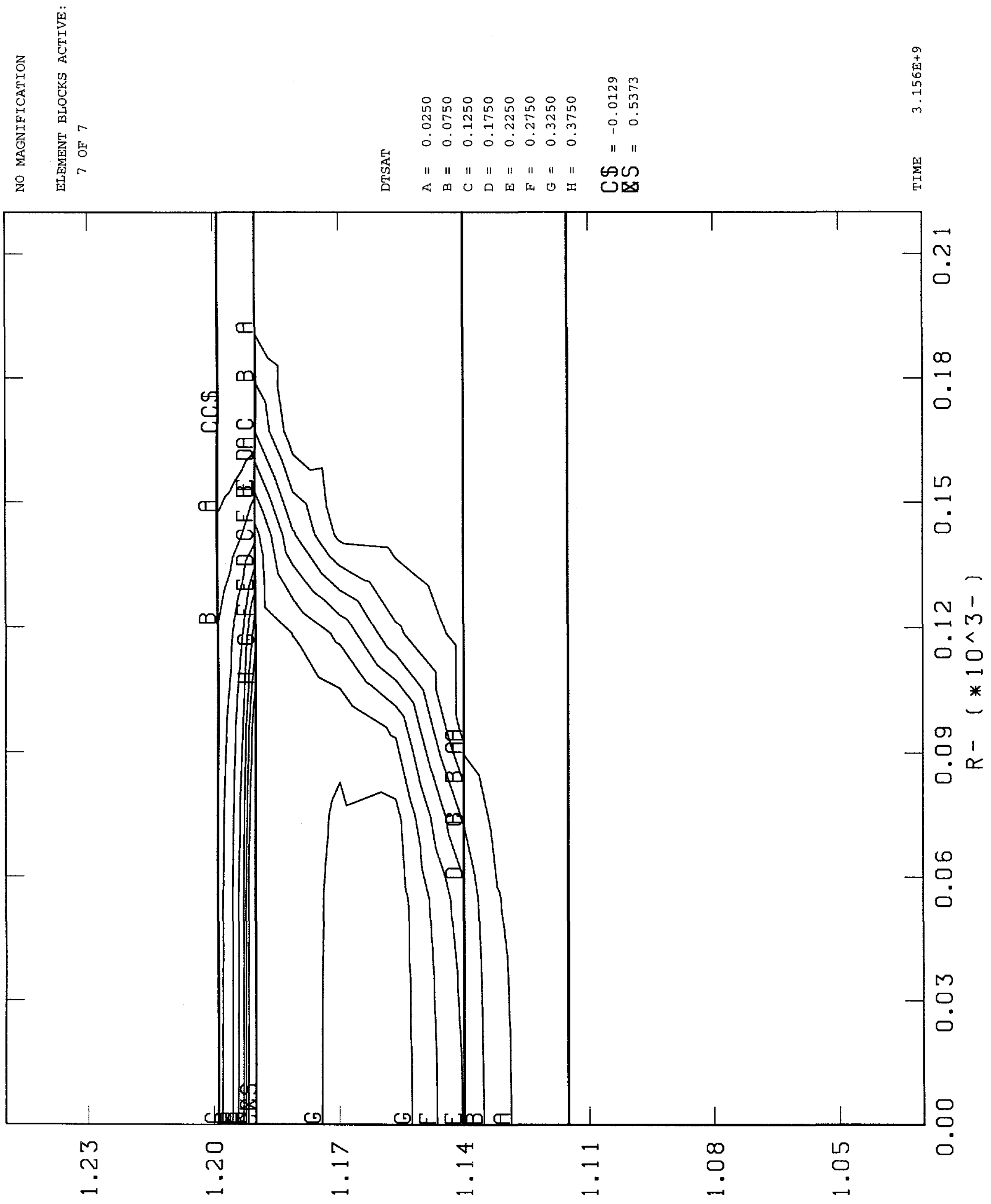

TN: Change from In Situ Saturation After 100 Years

Figure 3.2-23: Change in Saturation After 100 Years, Pond Water Calculations PTn Modeled as Yucca Mountain Member

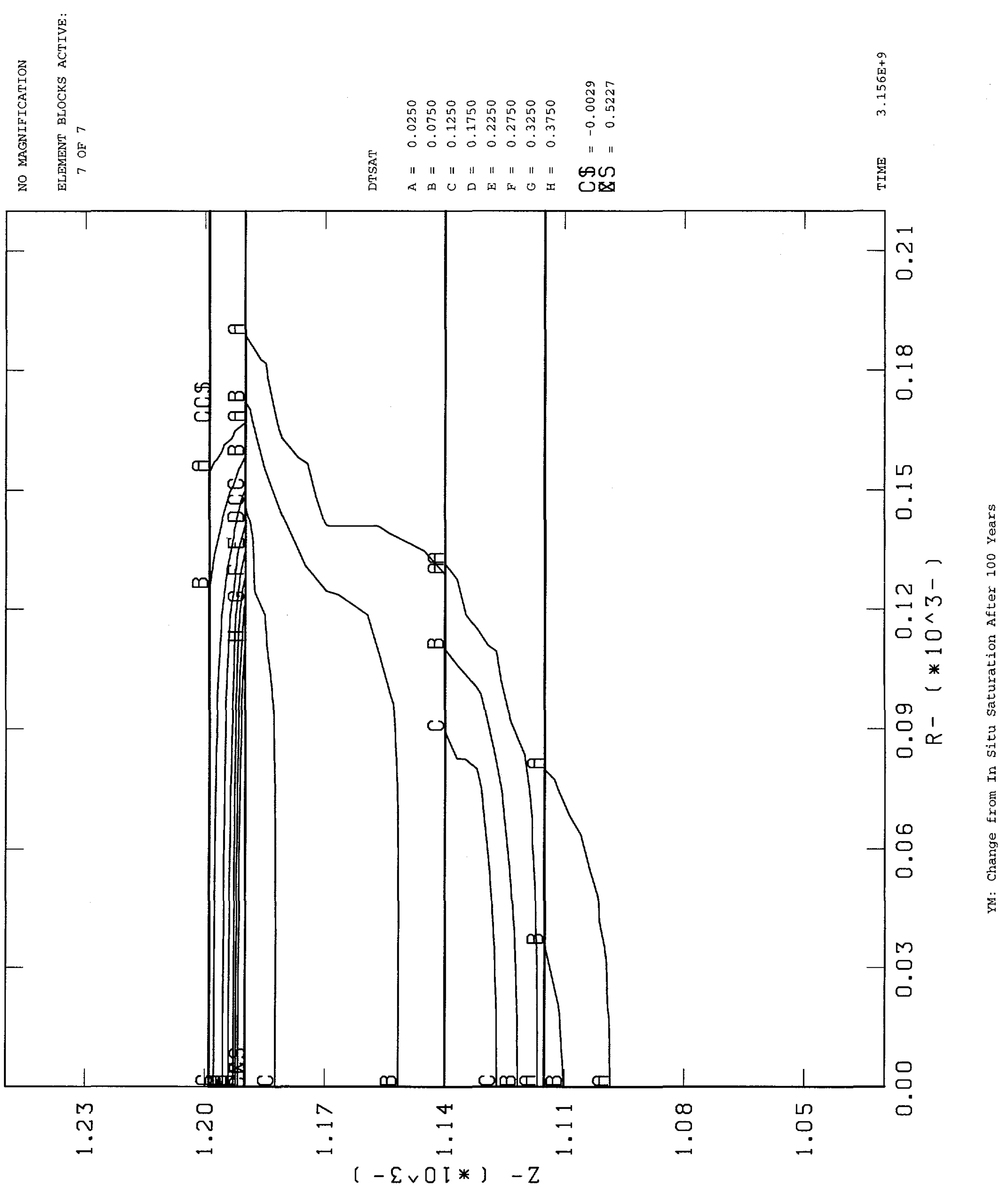

Figure 3.2-24: Change in Saturation After 100 Years, Pond Water Calculations PTn Modeled as Yucca Mountain Member (No Fractures)

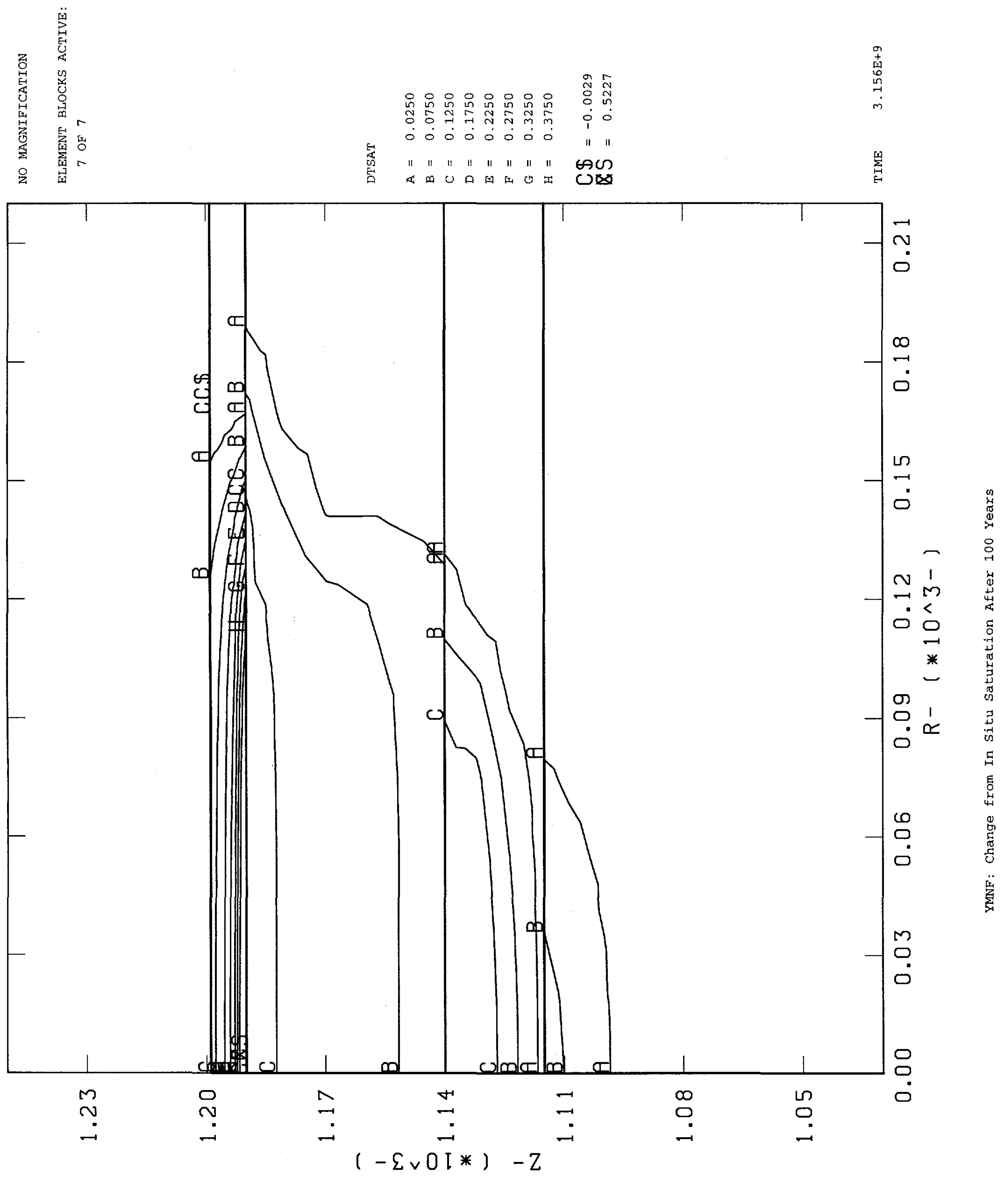

Figure 3.2-25: Change in Saturation After 100 Years, Pond Water Calculations
PTn Modeled Per PACE-90

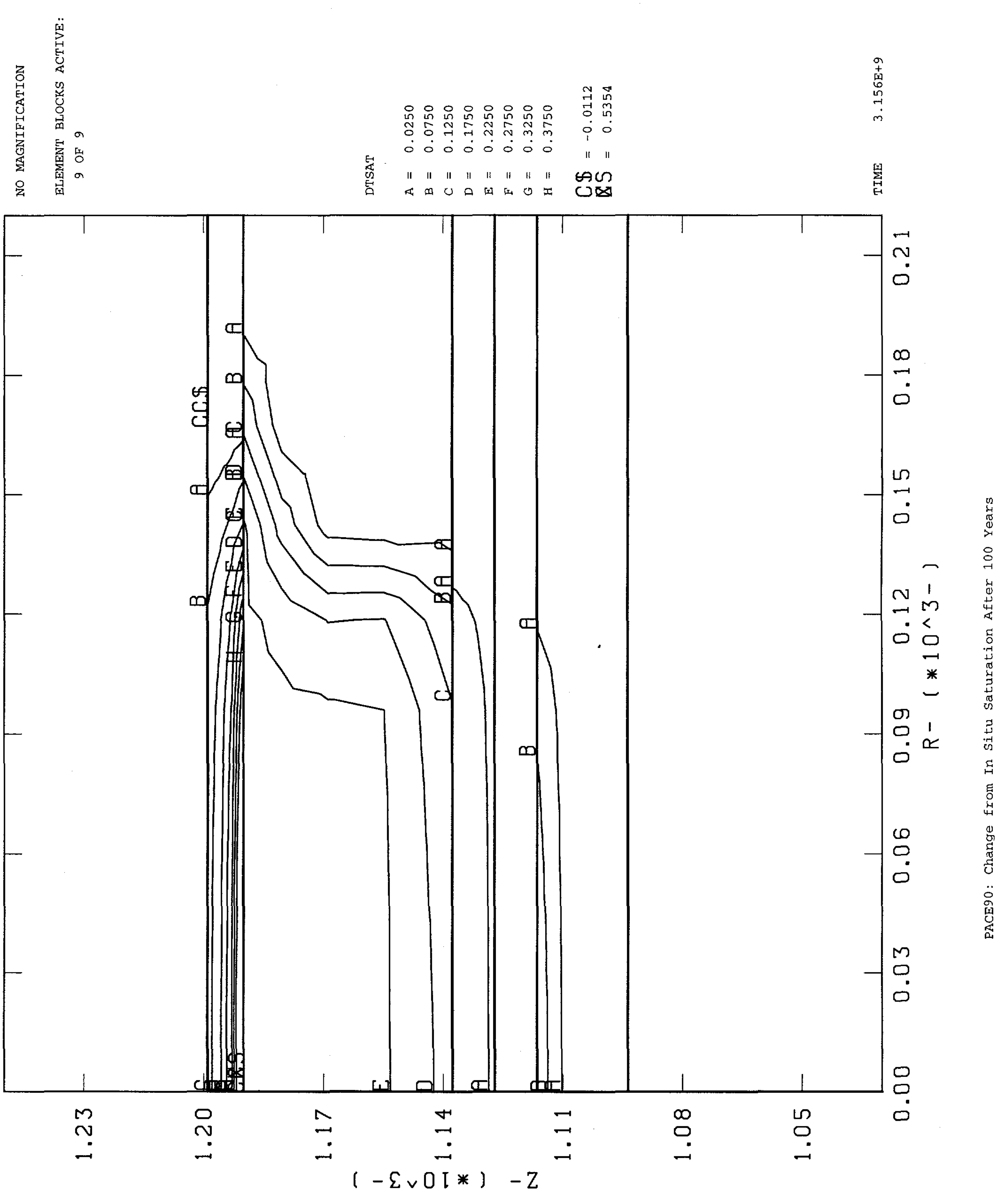

Figure 3.2-26: Change in Saturation After 10,000 Years, Pond Water Calculations PTn Modeled Per ESF3

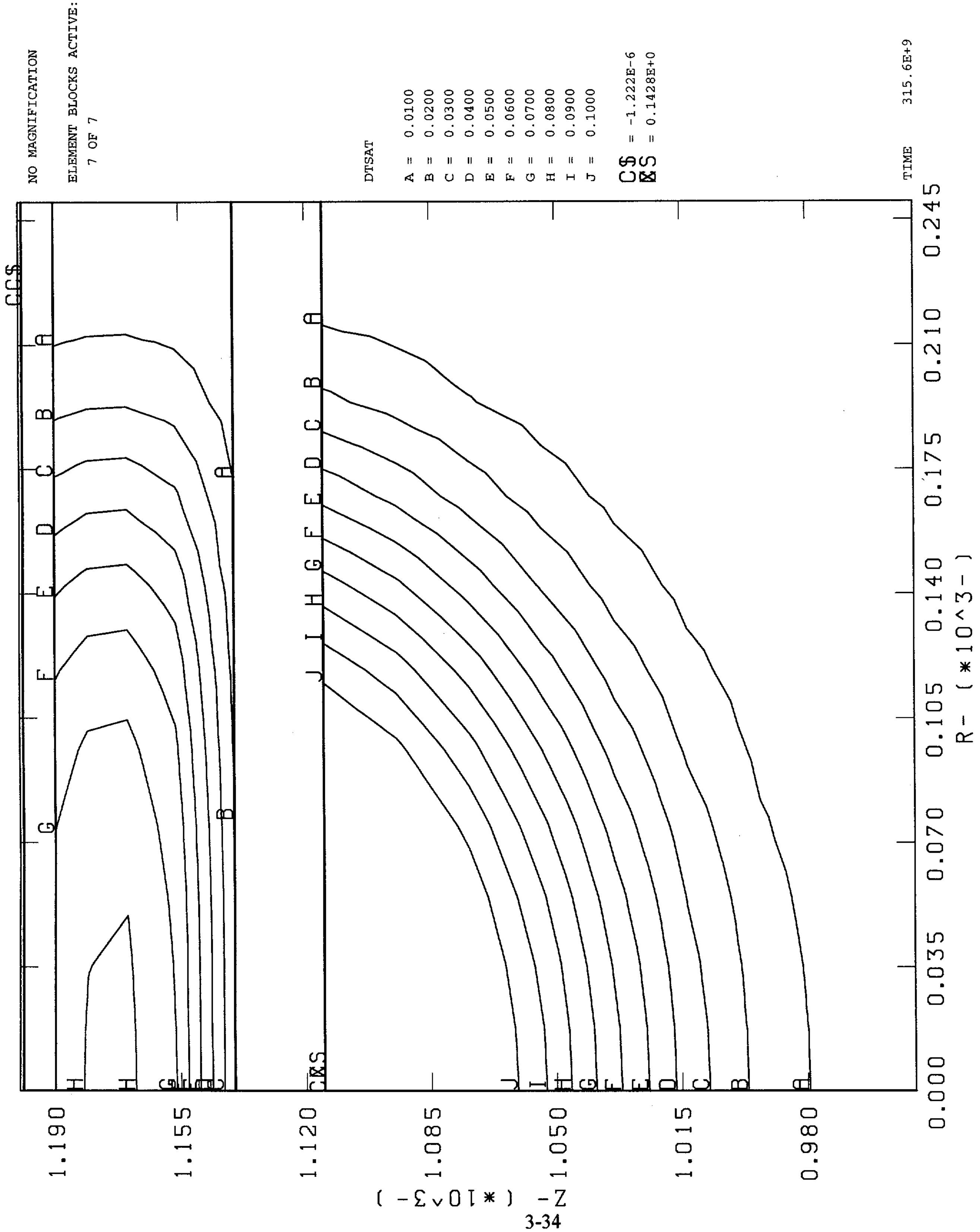

ESF#: Change from In Situ Saturation After 10,000 Years
(Compare with Figure 13, SAND91-0792)

Figure 3.2-27: Change in Saturation After 10,000 Years, Pond Water Calculations PTn Modeled as Bedded Tuff

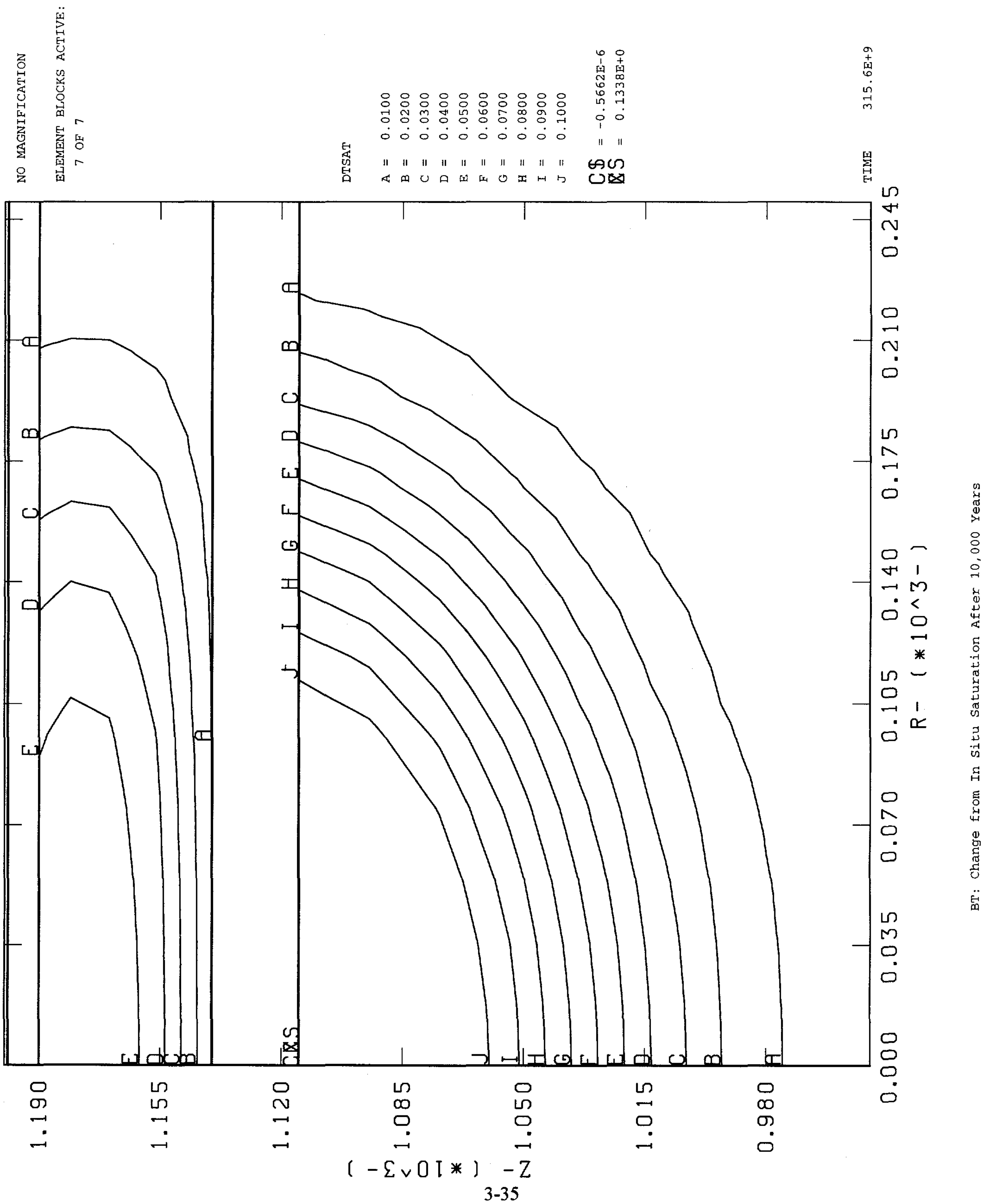

Figure 3.2-28: Change in Saturation After 10,000 Years, Pond Water Calculations
PTn Modeled as Pah Canyon Member

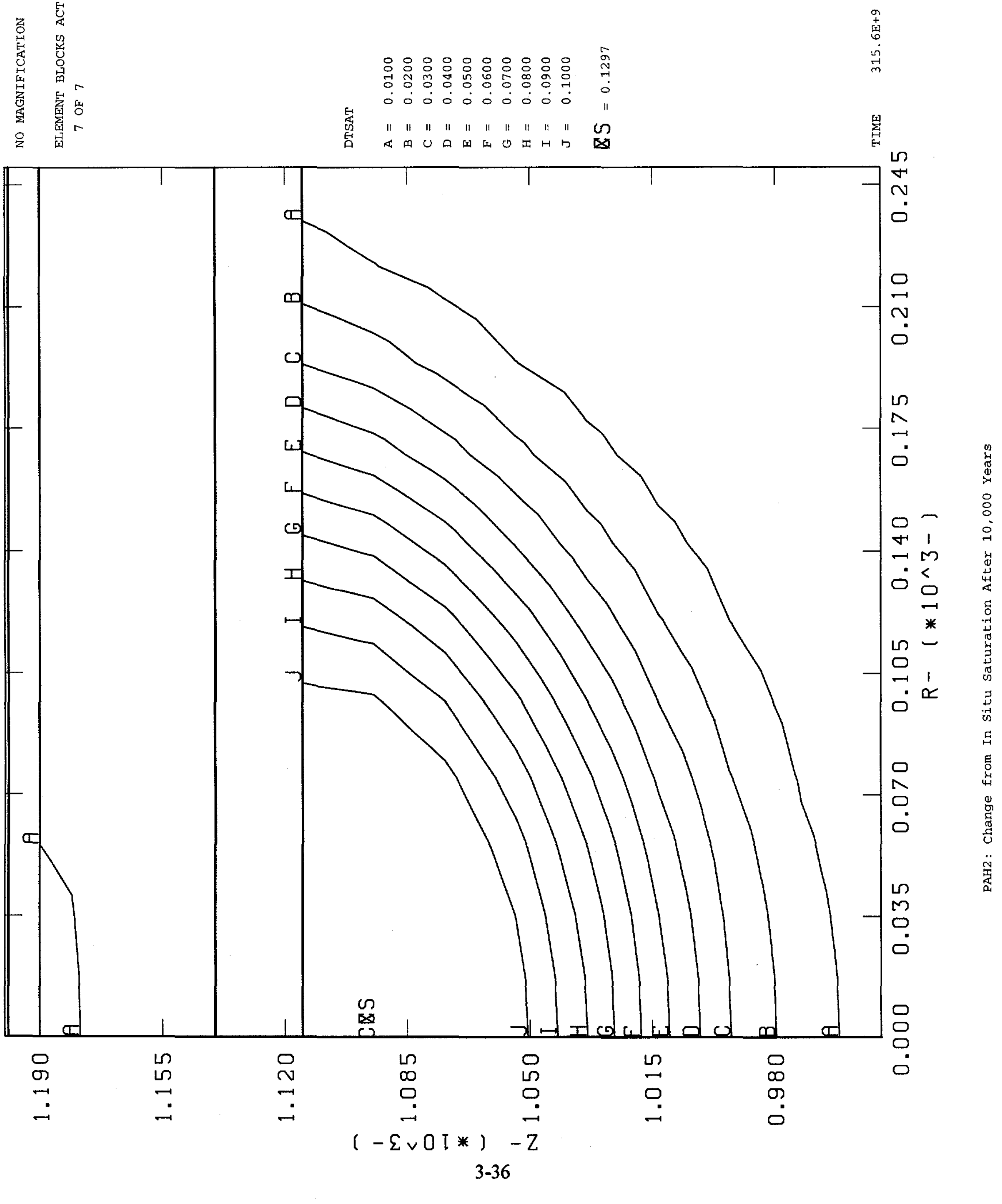

Figure 3.2-29: Change in Saturation After 10,000 Years, Pond Water Calculations PTn Modeled as Tpt-TM

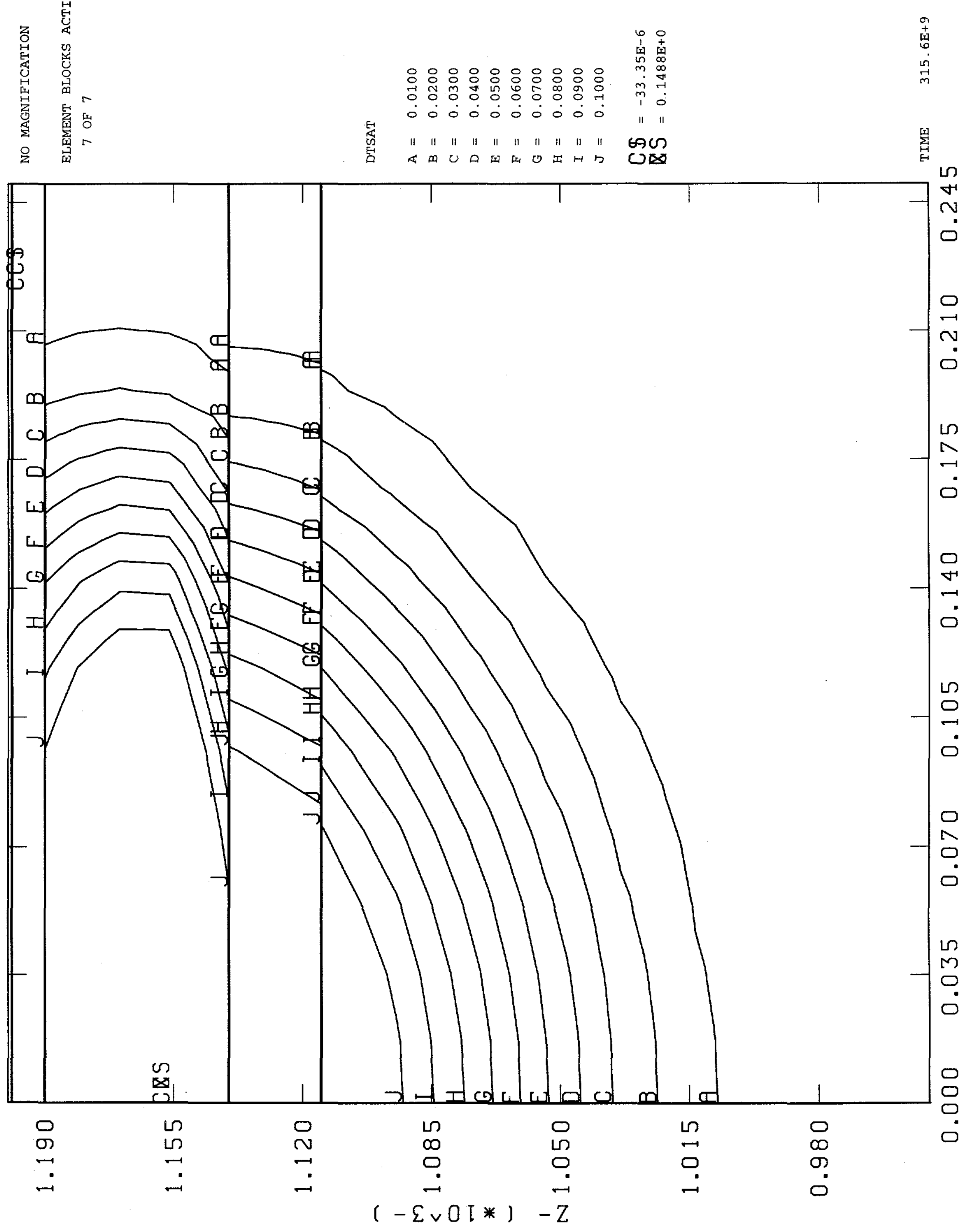

TM: Change from In Situ Saturation After 10,000 Years

Figure 3.2-30: Change in Saturation After 10,000 Years, Pond Water Calculations PTn Modeled as Tpc-TN

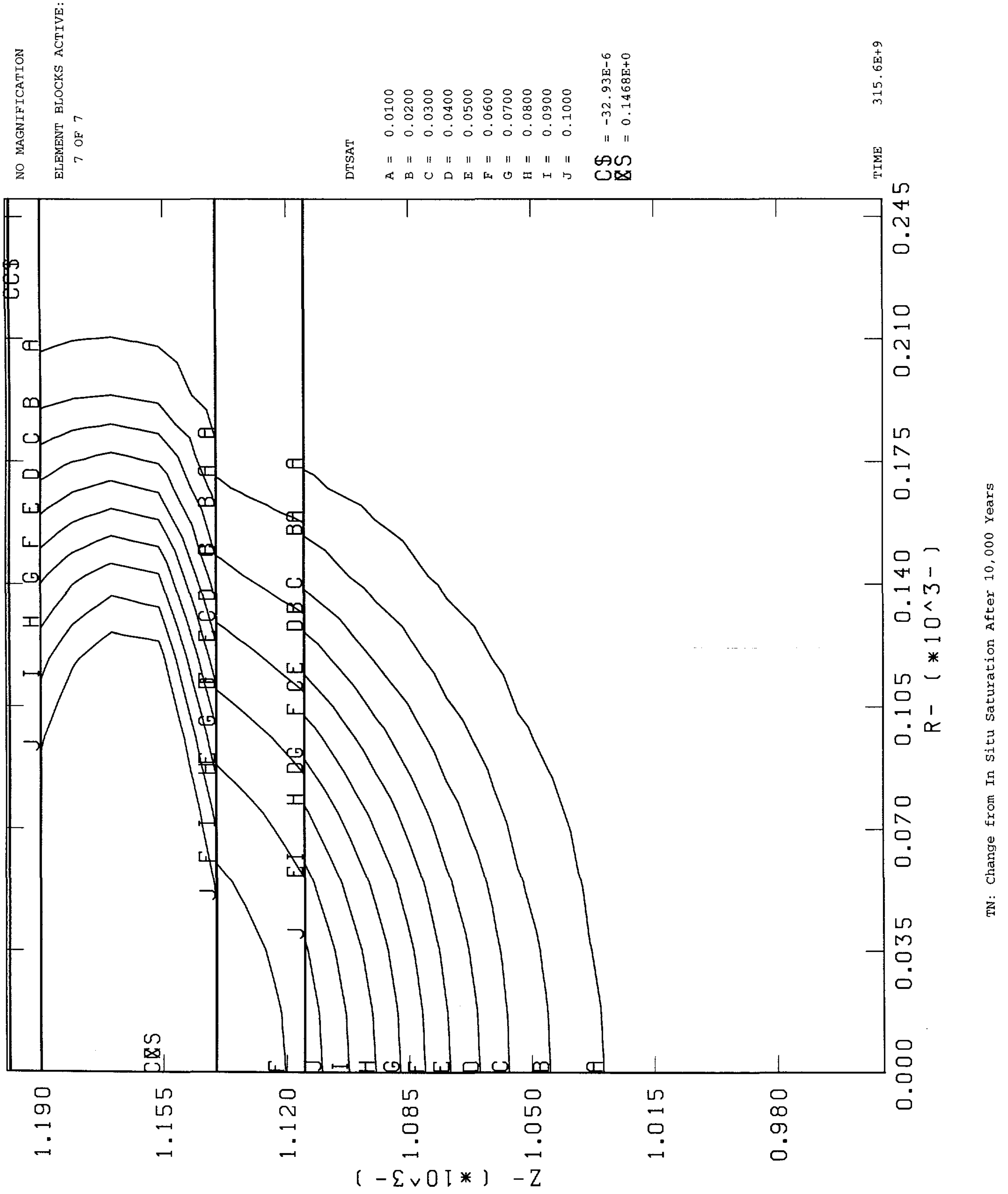

Figure 3.2-31: Change in Saturation After 10,000 Years, Pond Water Calculations PTn Modeled as Yucca Mountain Member

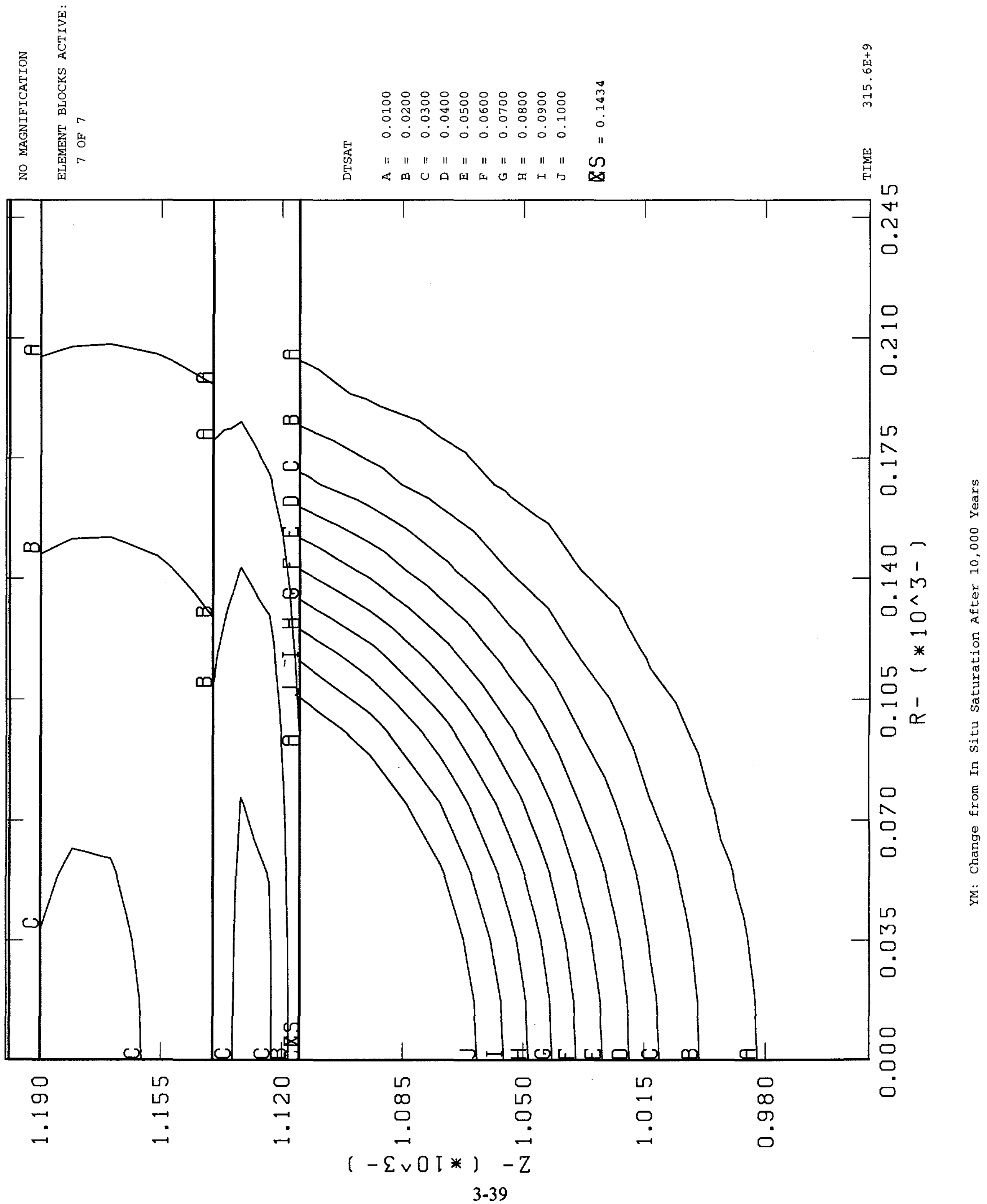

Figure 3.2-32: Change in Saturation After 10,000 Years, Pond Water Calculations PTn Modeled as Yucca Mountain Member (No Fractures)

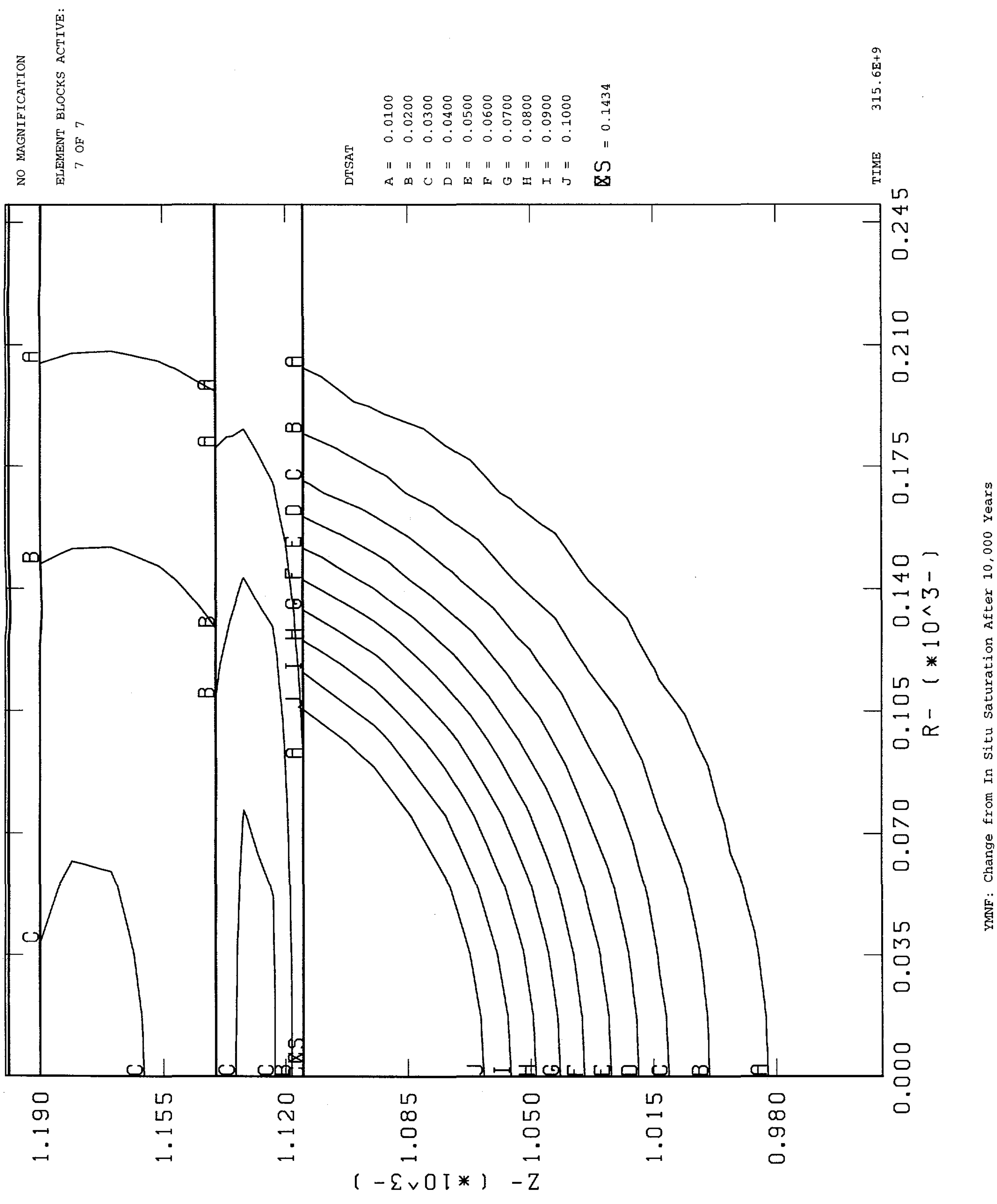

Figure 3.2-33: Change in Saturation After 10,000 Years, Pond Water Calculations PTn Modeled Per PACE-90

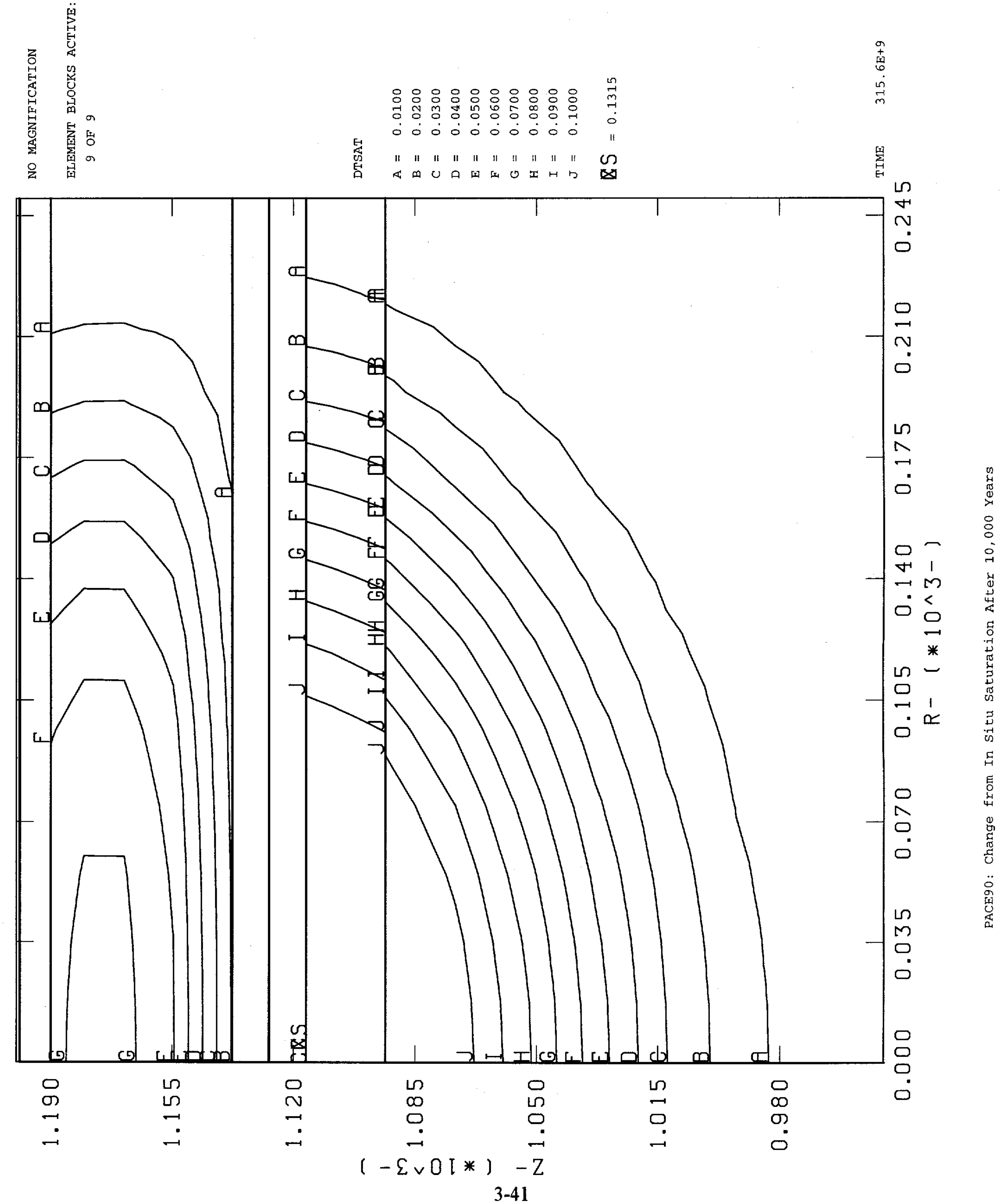

3.2.5 Discussion of Results

These calculations were performed in part to determine the potential sensitivity to the characterization of PTn of recommendations for ESF design suggested by performance assessment analyses. From the perspective of ESF and surface-based testing design activities, this analysis showed very little sensitivity of the conclusions to characterization of PTn. At 5 years, the amount of infiltrated water and the extent of its migration varied little between sets of calculations; recommendations regarding the location of surface ponds in proximity to surface-based experiments would be essentially the same for all cases. The multi-layered approach to modeling PTn, as expressed in the calculations with the PACE-90 stratigraphy, produced results which were not substantially different from the other cases with single homogeneous layers. Overall, the conclusion is that calculations of water movement due to large surficial ponds are not sensitive to the manner of characterization of PTn within the bounds performed for this analysis. In fact, the results of such calculations are probably much more dependent on the manner in which alluvium is modeled: alluvial depth, distribution of hydraulic properties, etc. This conclusion is additionally caveated by several other assumptions and limitations (equivalent continuum model vs. dual permeability model, no accounting for evapotranspiration, limited amount of hydraulic data for alluvium, etc.) which are discussed in Chapter 8.

3.3 Comparison with Surficial Water Calculations of ESF PA Analysis #12

The second set of calculations evaluates the sensitivity of the surficial, or road, watering analyses of ESF PA Analysis #12. These calculations specifically iterate on those done for Case #1. For this case, the variability in the lateral spread of water is of primary importance. The penetration of water toward the repository horizon at 5 and 10,000 years is also compared to the original calculations. The relationship between alluvial thickness, wetted area dimensions, and the resulting area affected by surficial watering is evaluated for its sensitivity to differing PTn parameters based on the results of the pond water and surficial water calculations performed for this study. A full description of the assumptions used to formulate the original surficial watering problem is in Sobolik and Fewell (1993); an abridged description is included for the new calculations.

3.3.1 Problem Definition

The problem is conceptualized as follows. Prior to the addition of water, the mountain is at the initial saturation conditions that correspond to a steady-state uniform infiltration of 0.01 mm/yr through the surface. At "time zero," a portion of the surface (wetted surface, or "road") is suddenly saturated and continuously maintained at saturation for five years, while water continues to infiltrate the remainder of the surface at 0.01 mm/yr. A saturated boundary condition is imposed at the water table. After five years, the boundary condition on the entire surface returns to uniform infiltration at 0.01 mm/yr. The movement of the surficial water is then followed for 10,000 years. This conceptual model assumes no surficial ponding of water.

Data for Well UE-25 a#1 (which is near the North Portal of the ESF) are used for locating the boundaries between stratigraphic layers. The hydrologic properties previously used in Sobolik and Fewell (1993) are used for these calculations, with of course the exception of the properties used for PTn. Seven different sets of values for PTn are used and compared with the original calculations (see Table 3.1-1): Tpc-BT, bedded tuff; Pah Canyon member; Tpt-TM, moderately welded, highly fractured tuff; Tpc-TN, nonwelded ashflow tuff; Yucca Mountain member; the Yucca Mountain member assuming no fractures (to test the sensitivity of the ECM model); and the parameters listed for USW G-4 in the current RIB (DOE-YMP, 1993a). An additional set of calculations use the PACE-90 stratigraphic model to define the PTn region (see Table 3.2-1). The thermomechanical properties in each layer are assumed to be homogeneous and isotropic throughout the layer. The effects of evapotranspiration are not included in the analysis.

The problem domain is two-dimensional and cartesian, extending from the water table to the surface. The stratigraphic units are modeled as horizontal and parallel. The width of a typical road (12 m) is used for the wetted surface area. Symmetry allows a no-flow boundary to be placed at the road centerline. The other vertical boundary is also defined as a no-flow boundary and placed 90 m from the road centerline.

The results of the original calculations for ESF Analysis #12 (Sobolik and Fewell, 1993), with alluvium as the top layer, indicated that there would be no effect on experiments in the ESF or on potential repository performance because surficially applied water does not result in changes in saturation at repository depth. The primary difference between the road watering problem here and the pond problem described in Section 3.2 is that the road width is much closer to the alluvial depth than the pond radius. The results of Case #1 from Sobolik and Fewell (1993) were used as the benchmark to which eight new sets of results are compared. The results of these calculations are compared at three points: after 5 years of water infiltration from the surface pond and after 25 and 10,000 years of movement of this water. The results of the calculations run with Yucca Mountain member properties both with and without fractures yielded identical results, so figures representing these calculations are shown only for the case with fractures.

Figures 3.3-1 and 3.3-2 show the computational grids in the location where the effects of the road water primarily occur for the calculations using the USW G-4 stratigraphy (all except PACE-90) and the PACE-90 stratigraphy, respectively. The in situ saturation profiles are essentially the same for this problem as they were for the pond problem because the same stratigraphies and material properties were used, with the exception of the use of the more appropriate set of material properties for the TSw3 unit (see Section 3.2). Figure 3.3-3 displays the in situ saturation profiles calculated for the case using USW G-4 values for matrix saturated conductivity in the PTn. This saturation profile is identical beneath the PTn-TSw1 interface (385 m above the water table) to the previous profiles, with the exception of a slight jog at the TSw3-CHn interface. For the G-4 case, the in situ saturation in the PTn ranged from 10% to 18%, and in the TCw from 78% to 82%. There was also some significant variation in the saturation levels in the TCw. The level of saturation in the alluvium in essentially the same for all cases. The in situ water content of the two-dimensional section of mountain modeled for these calculations is shown for each of the cases in Table 3.3-1; a similar relationship between the amount of in situ water and the level of saturation in TCw displayed for the pond problem in Table 3.2-2 can be seen in the road water calculations.

3.3.2 Results After 5 Years

Figure 3.3-4 is a contour plot of Δsat which shows the extent of water movement after 5 years for the original calculations from ESF Analysis #12. Figures 3.3-5 through 3.3-11 are similar contour plots showing the extent of water movement when the calculations used bedded tuff, USW G-4, the Pah Canyon member, Tpt-TM, Tpc-TN, and the Yucca Mountain member properties, and the PACE-90 stratigraphy, respectively, for PTn. The extent of lateral and vertical water movement is marked by the location of the outermost contours, which represent a Δsat of 2.5%. Qualitatively, in terms of the lateral and vertical extent of water movement, there is very little difference amongst the eight sets of results. Table 3.3-1 shows the lateral extent of values of Δsat of 2%; this value for Δsat was used in Sobolik and Fewell (1993) as the criterion for determining a potential effect of surficial water use on near-surface testing. All of the other sets of PTn properties produced approximately the same lateral extent of water movement along the alluvium-TCw interface as the original properties. Note that only with the Pah Canyon and Yucca Mountain (Figures 3.3-7 and 3.3-10, respectively) properties does the model predict fairly significant penetrations of road water into the PTn; these calculations also indicate the greatest lateral spread of water at the TCw-PTn interface. As in the pond problem, water penetration into PTn after 5 years seems to occur only where the TCw directly above the interface with PTn becomes nearly saturated; the high suction pressures predicted for less than ~90% saturation in TCw prevent water movement into PTn. Table 3.3-1 shows the volume of water imbibed through the road surface after 5 years for each of the eight sets of calculations. Again, there is no significant difference in the amount of imbibed water, with the minor exception of Pah Canyon and Yucca Mountain properties (their high initial saturation levels for TCw mean a lower capacity for water imbibition and storage). These minor differences indicate that in areas of thick alluvial deposits the predicted amount and migration of imbibed surficial water does not appear to be significantly sensitive to the characterization of PTn.

Table 3.3-1: Results of Road Water Calculations

PTn Modeled as	In Situ Water Content (m^2)	5-Year Change in Water Content (meters of head through road surface[5])	5-Year Change in Water Content (cubic meters per 1-m length of road)	Lateral Extent of Δsat=2% After 5 Yr (m)	K_{sat}, bulk (m/s)	Matrix K_{sat} (m/s)	Matrix Porosity	Fractures
Tpc-TN	6421.51	24.00	144.0	74.5	2.00×10^{-11}	2.00×10^{-11}	0.5	no
Yucca Mtn.	5932.18	22.88	137.3	74.7	1.91×10^{-7}	1.75×10^{-7}	0.436	yes
Pah Canyon	5792.48	23.23	139.4	74.7	7.30×10^{-7}	7.14×10^{-7}	0.47	yes
USW G-4	5466.69	24.05	144.3	74.7	1.70×10^{-8}	5.00×10^{-10}	0.4	yes
ESF 12	5405.49	23.80	142.8	74.7	4.06×10^{-7}	3.90×10^{-7}	0.4	yes
Bedded Tuff	4970.91	24.05	144.3	74.7	2.40×10^{-6}	2.40×10^{-6}	0.22	no
PACE90	4893.09	23.85	143.1	74.7				
Tpt-TM	4754.64	24.00	144.0	74.5	1.22×10^{-9}	2.00×10^{-11}	0.1	yes

3.3.3 Results After 25 Years

Figure 3.3-12 is a contour plot of Δsat which shows the extent of water movement after 25 years for the original calculations from ESF Analysis #12. Figures 3.3-13 through 3.3-19 are similar contour plots showing the extent of water movement when the calculations used bedded tuff, USW G-4, the Pah Canyon member, Tpt-TM, Tpc-TN, and the Yucca Mountain member properties, and the PACE-90 stratigraphy, respectively, for PTn. Only three cases show infiltration of water into the TSw1: the original ESF Analysis #12 calculations; Pah Canyon (Figure 3.3-15), which had a significant amount of water in PTn after 5 years; and the bedded tuff (Figure 3.3-13), which has the highest conductivity of all the unit representations used for PTn. In fact, these three cases have the three highest values for saturated conductivity in PTn. Note the slow downward penetration of water through the Tpt-TM (Figure 3.3-16), Tpc-TN (Figure 3.3-17), and the Tpt-TM section of the PACE-90 case (Figure 3.3-19), all indicative of the low hydraulic conductivity in PTn and the low initial saturation in TCw for the three cases. For all the cases, the lateral spread of the water has run into the right-hand vertical boundary, setting up a quasi-one-dimensional flow for the remainder of the problem. As this study attempts to test the sensitivity of previous calculations to the characterization of PTn, no attempt was made to extend the vertical boundary further away from the road centerline.

3.3.4 Results After 10,000 Years

Figure 3.3-20 is a contour plot of Δsat which shows the extent of water movement after 10,000 years for the original calculations from ESF Analysis #12. Figures 3.3-21 through 3.3-27 are similar contour plots showing the extent of water movement when the calculations used bedded tuff, USW G-4, the Pah Canyon member, Tpt-TM, Tpc-TN, and the Yucca Mountain member properties, and the PACE-90 stratigraphy, respectively, for PTn. The Pah Canyon (Figure 3.3-

---

[5] "Meters of head through road surface" = Volume of imbibed road water / Area of road.

23) and the bedded tuff (Figure 3.3-21) results predicted deeper penetration of water into the mountain than the ESF Analysis #12 calculations; the depth of penetration predicted by the Pah Canyon and bedded tuff cases are near enough to the planned elevation of the nearest section of the potential repository (960 m) that different recommendations for those previously made by ESF Analysis #12 might result. The Yucca Mountain member (Figure 3.3-26) and PACE-90 (Figure 3.3-27) predicted approximately the same as ESF Analysis #12, and the USW G-4 (Figure 3.3-22), Tpt-TM (Figure 3.3-24), and Tpc-TN (Figure 3.3-25) predicted significantly less penetration.

3.3.5 Discussion of Results

These calculations were performed in part to determine the potential sensitivity to the characterization of PTn of recommendations for ESF design suggested by performance assessment analyses. From the perspective of ESF and surface-based testing design activities, this analysis showed very little sensitivity of the conclusions to characterization of PTn. At 5 years, the amount of infiltrated water and the extent of its migration varied little between sets of calculations; recommendations regarding the location of surface-based experiments in proximity to roads maintained by surficial watering would be essentially the same for all cases. The PACE-90 representation of PTn is the most geologically realistic of the cases shown here, in that it represents PTn as a series of alternating welded and nonwelded tuffs. The high conductivity of the bedded tuff section is counterbalanced by the low conductivities of the Tpt-TM and Tpc-TN sections, resulting in a predicted penetration after 10,000 years nearly equal to what was originally predicted. An analysis of the pond and road watering calculations in the manner followed by Sobolik and Fewell, 1993 (p. 76, Equation 1) reveals very little sensitivity of lateral water dispersion to the choice of parameters used for PTn. Because of the PACE-90 results, the combined results of the pond and road watering calculations, and some of the assumptions used in producing these calculations (e.g., no accounting for evapotranspiration and for periodic as opposed to continuous watering, ECM versus. dual permeability model, etc.), no changes to any previous recommendations regarding surficial water usage are justified. As for the pond water calculations, the results of these surficial watering calculations are probably much more dependent on the manner in which alluvium is modeled: alluvial depth, distribution of hydraulic properties, etc.

Figure 3.3-1: Computational Grid for Road Water Calculations PTn Modeled as Single Homogeneous Unit

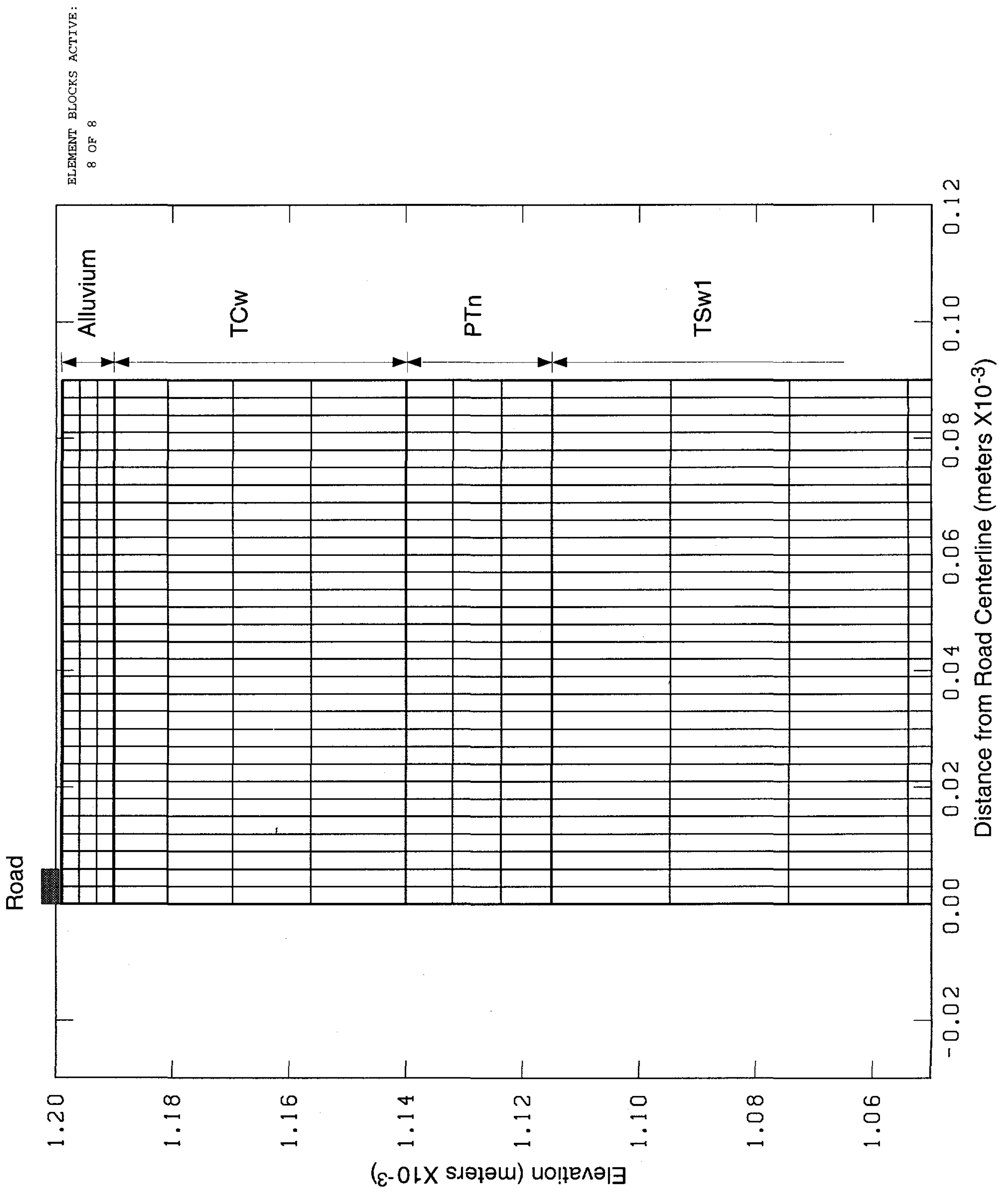

Computational Grid for Road Water Calculations
PTn Modeled as Single Homogeneous Unit

Figure 3.3-2: Computational Grid for Road Water Calculations PTn Modeled as Per PACE-90 Stratigraphy

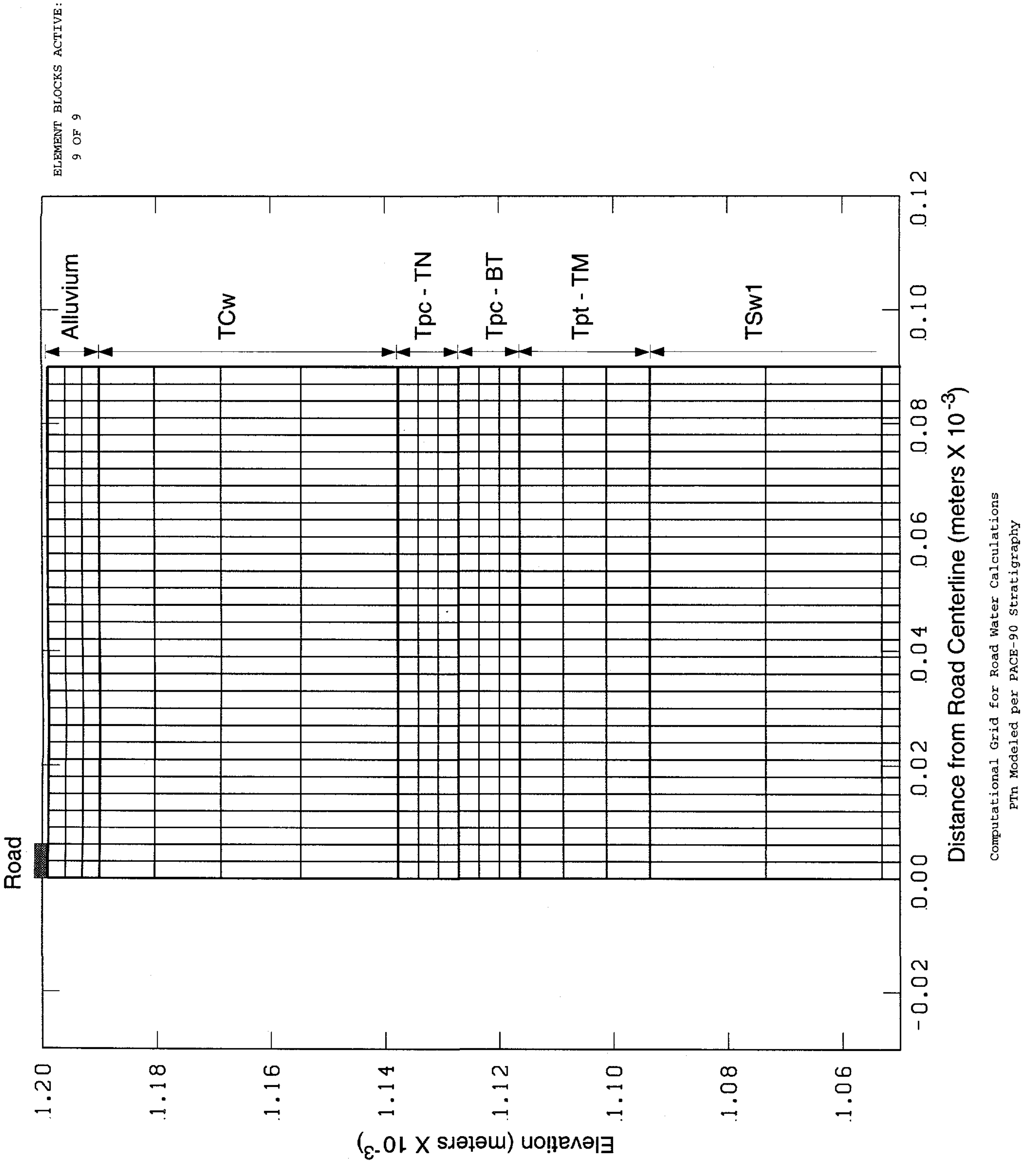

Figure 3.3-3: In Situ Saturation Profile, Road Water Calculations PTn Modeled as USW G-4

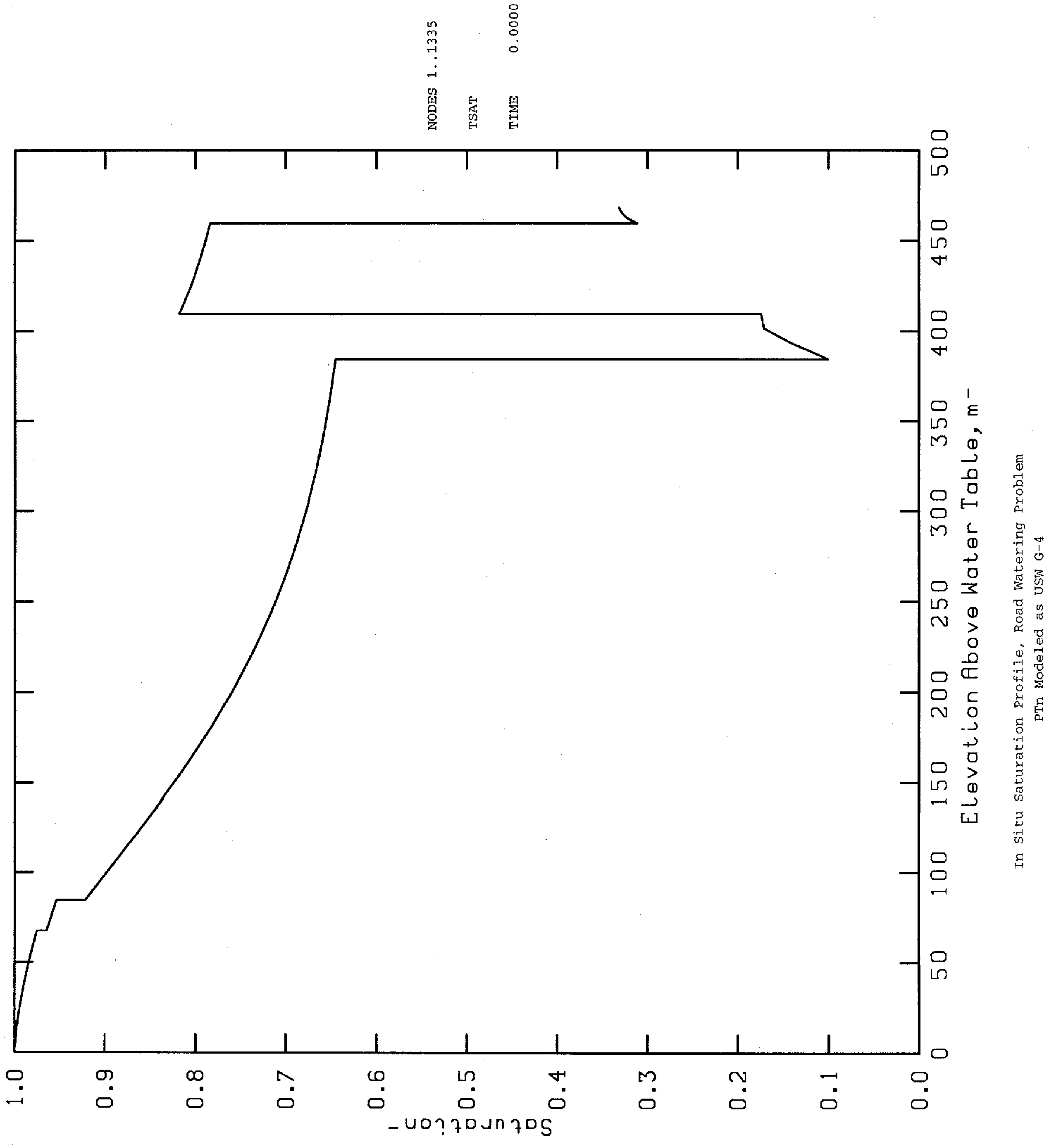

Figure 3.3-4: Change in Saturation After 5 Years, Road Water Calculations
PTn Modeled Per ESF12

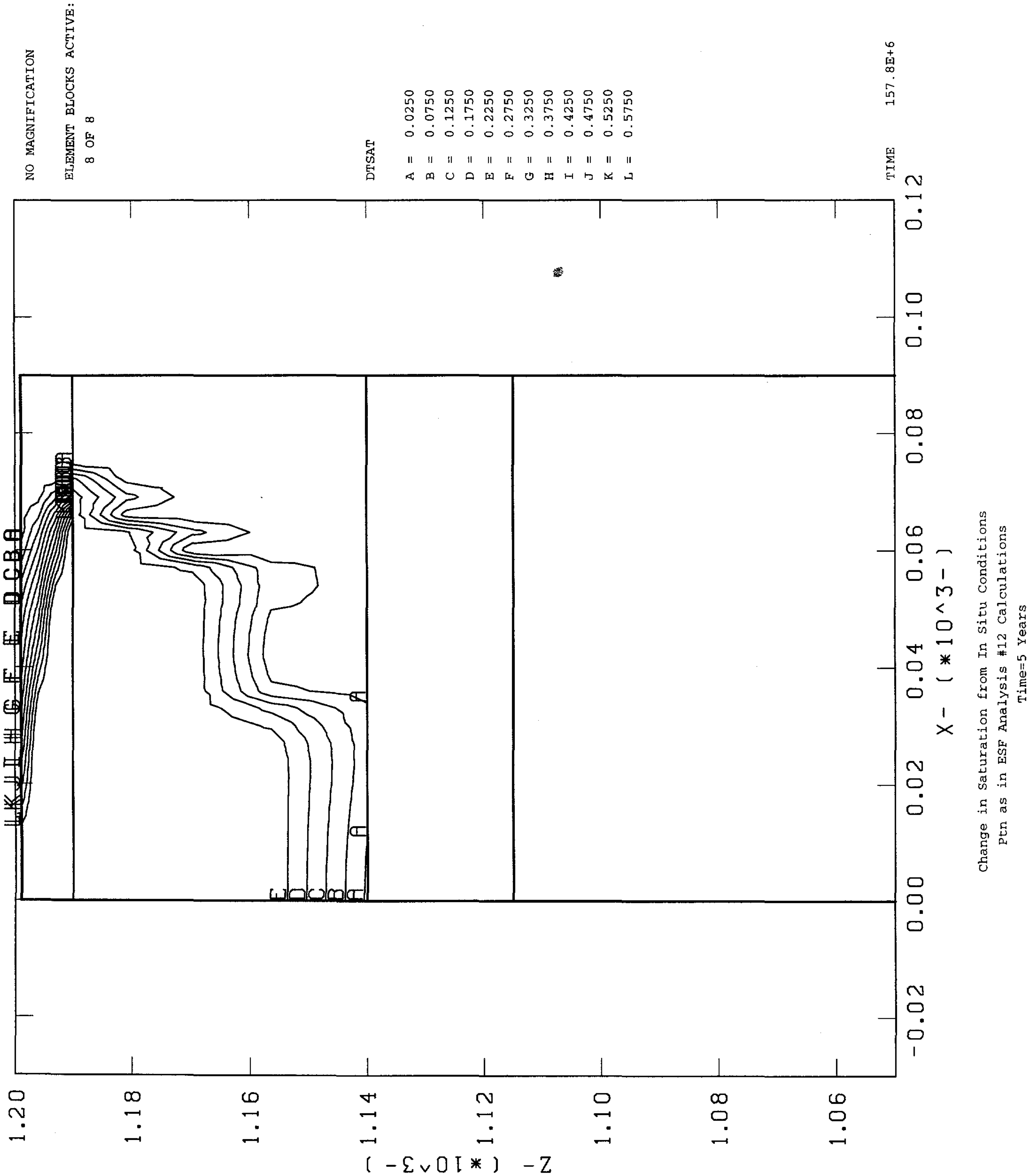

Figure 3.3-5: Change in Saturation After 5 Years, Road Water Calculations PTn Modeled as Bedded Tuff

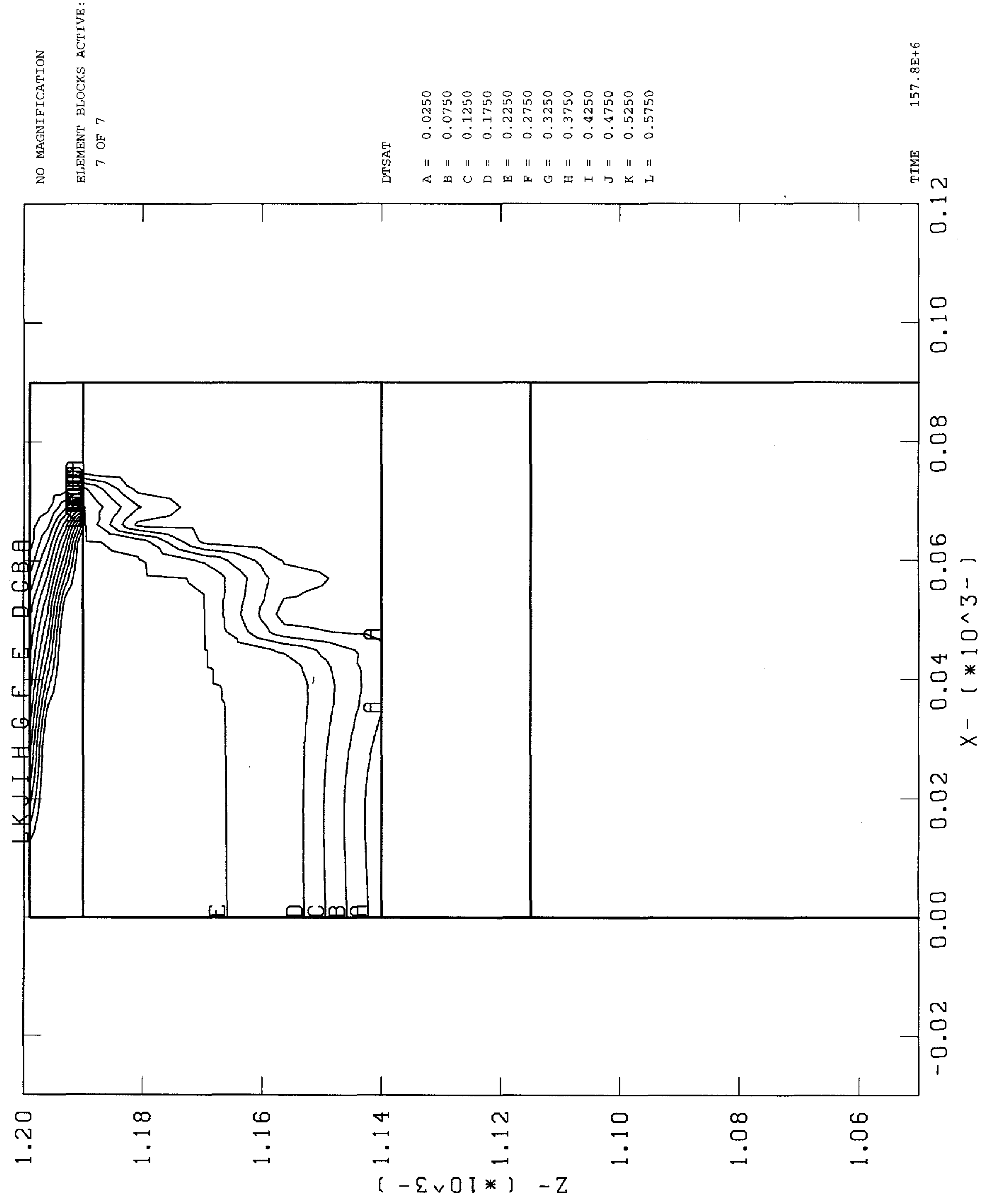

Change in Saturation from In Situ Conditions
Ptn Modeled as Bedded Tuff
Time=5 Years

Figure 3.3-6: Change in Saturation After 5 Years, Road Water Calculations PTn Modeled as USW G-4

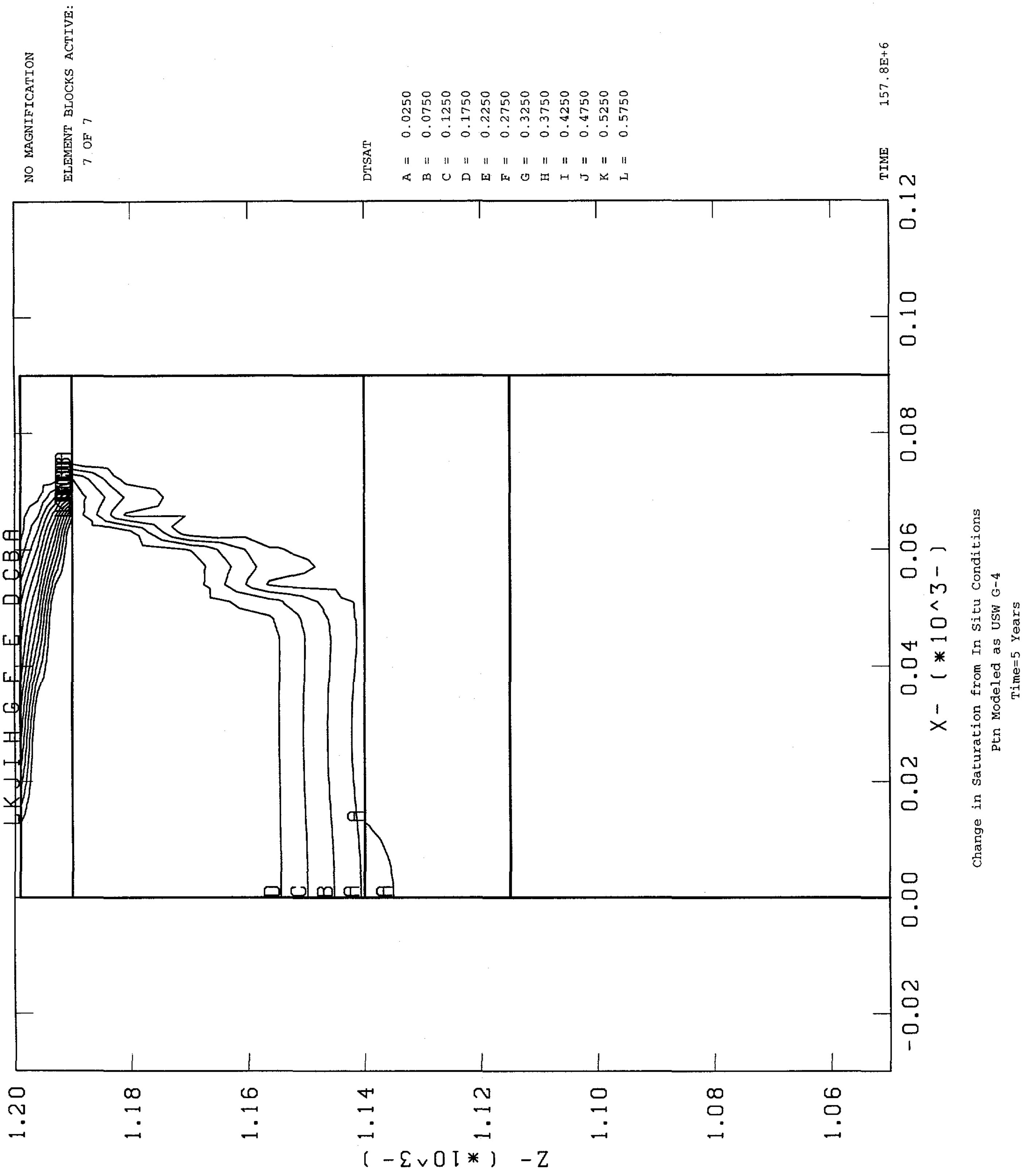

Figure 3.3-7: Change in Saturation After 5 Years, Road Water Calculations PTn Modeled as Pah Canyon Member

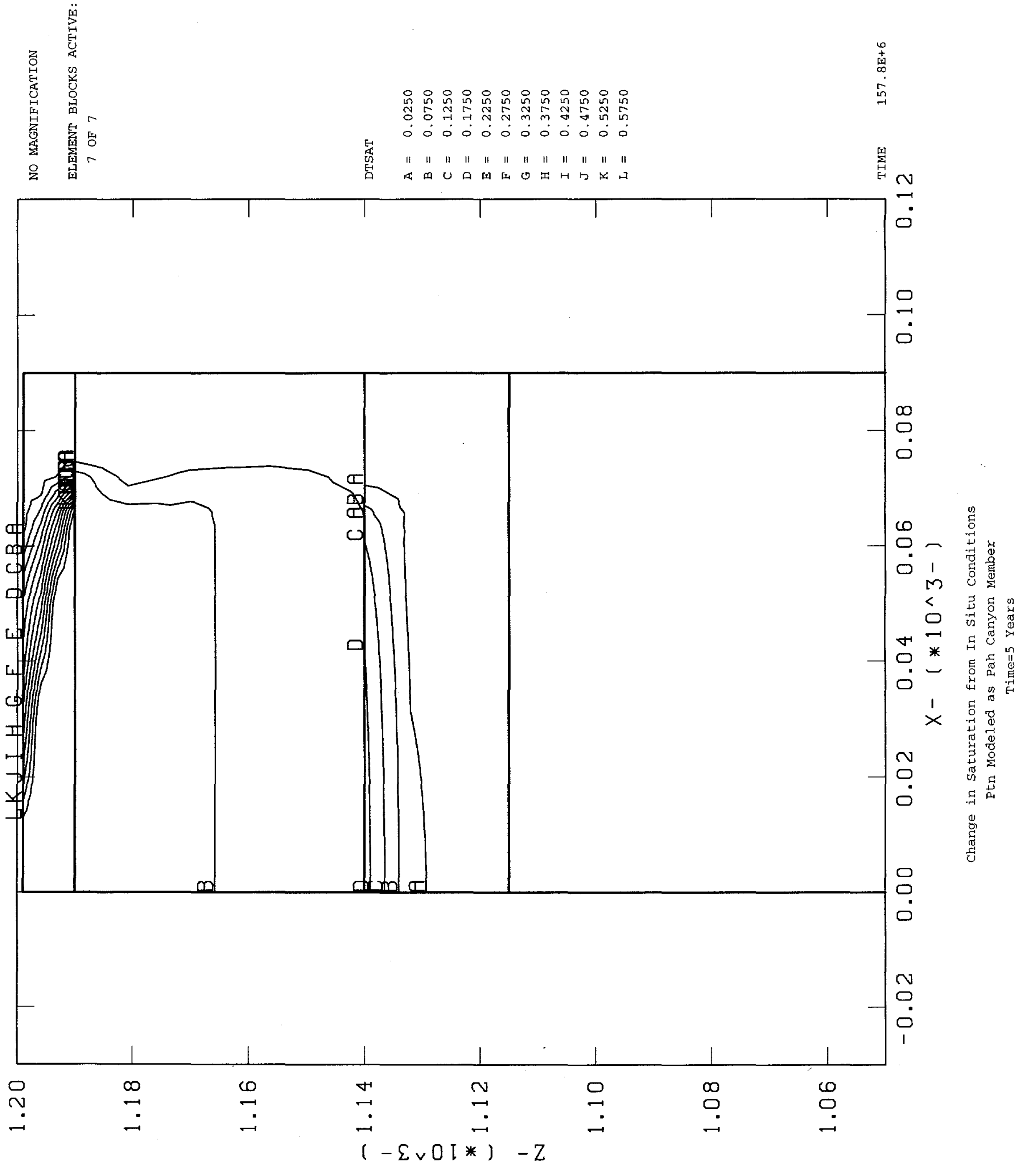

Figure 3.3-8: Change in Saturation After 5 Years, Road Water Calculations PTn Modeled as Tpt-TM

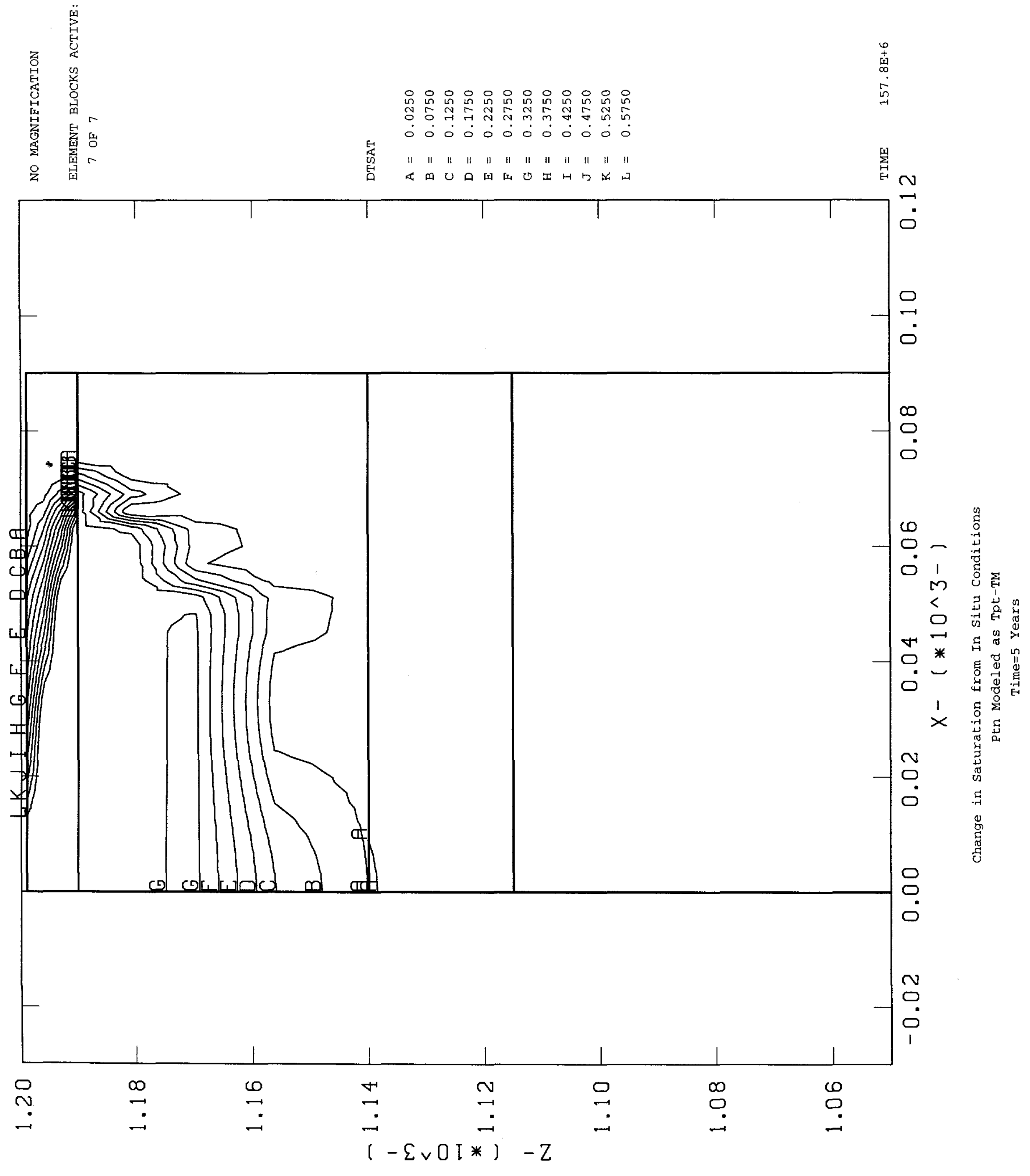

Figure 3.3-9: Change in Saturation After 5 Years, Road Water Calculations PTn Modeled as Tpc-TN

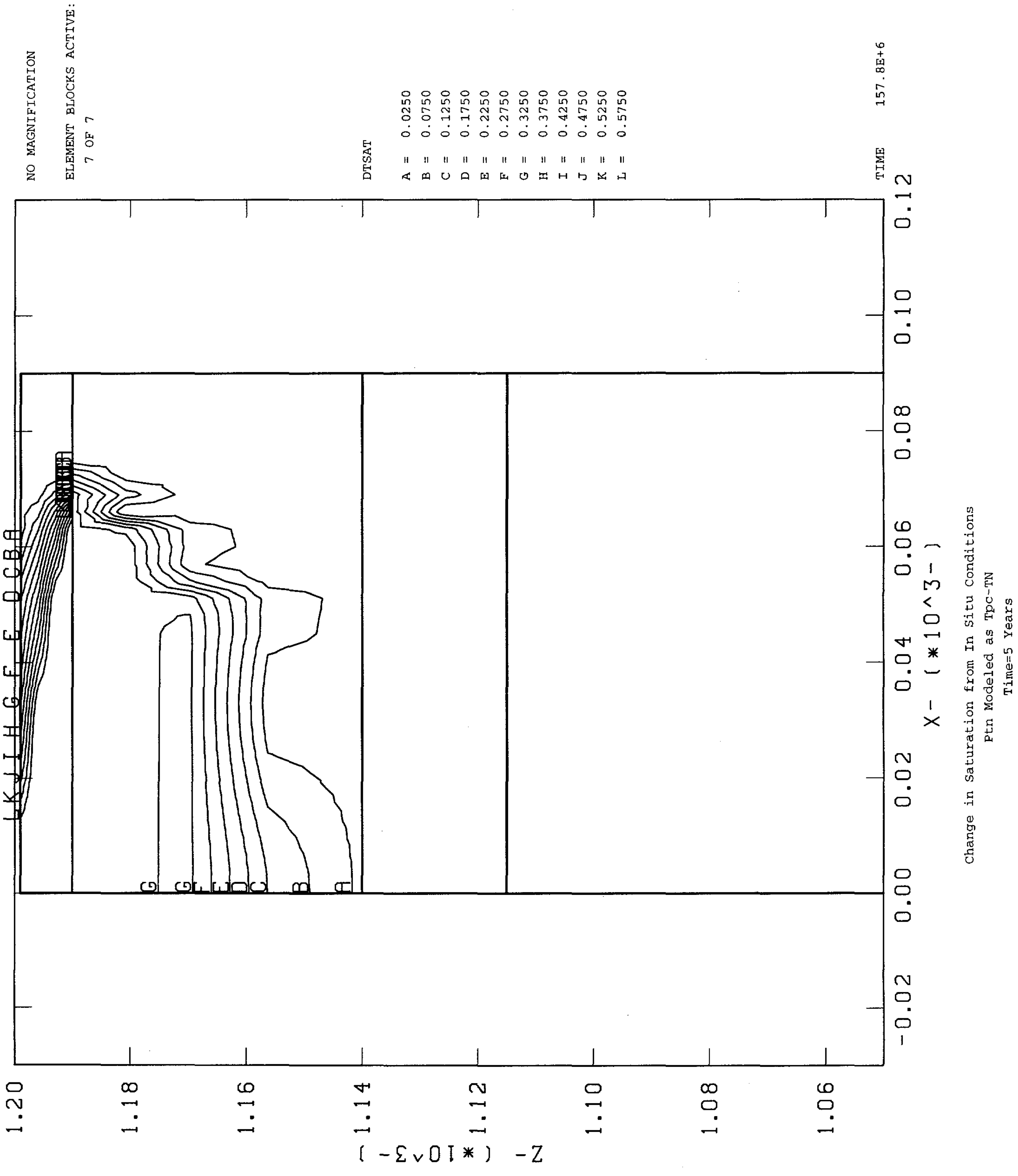

Figure 3.3-10: Change in Saturation After 5 Years, Road Water Calculations PTn Modeled as Yucca Mountain Member

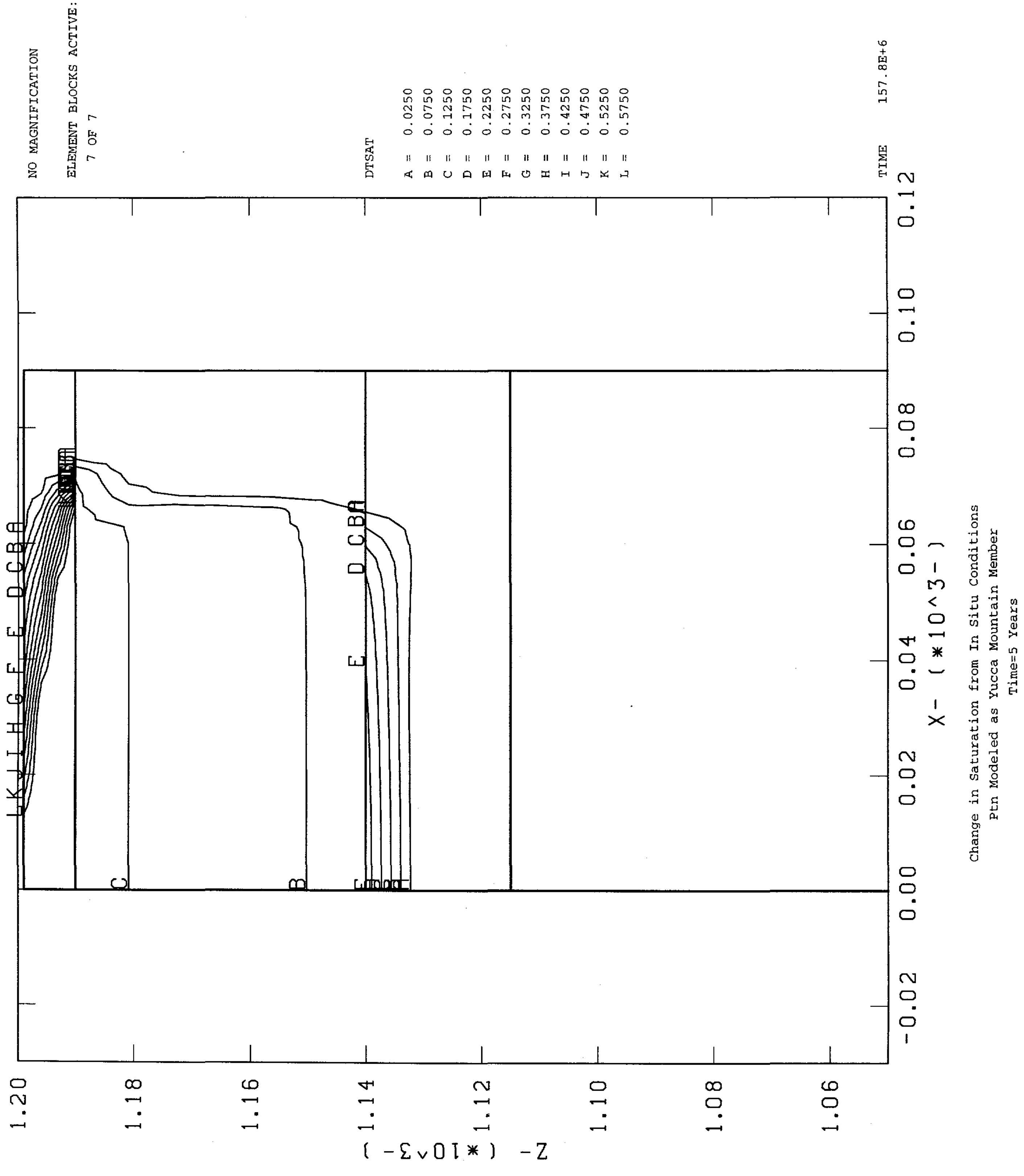

Figure 3.3-11: Change in Saturation After 5 Years, Road Water Calculations
PTn Modeled Per PACE-90

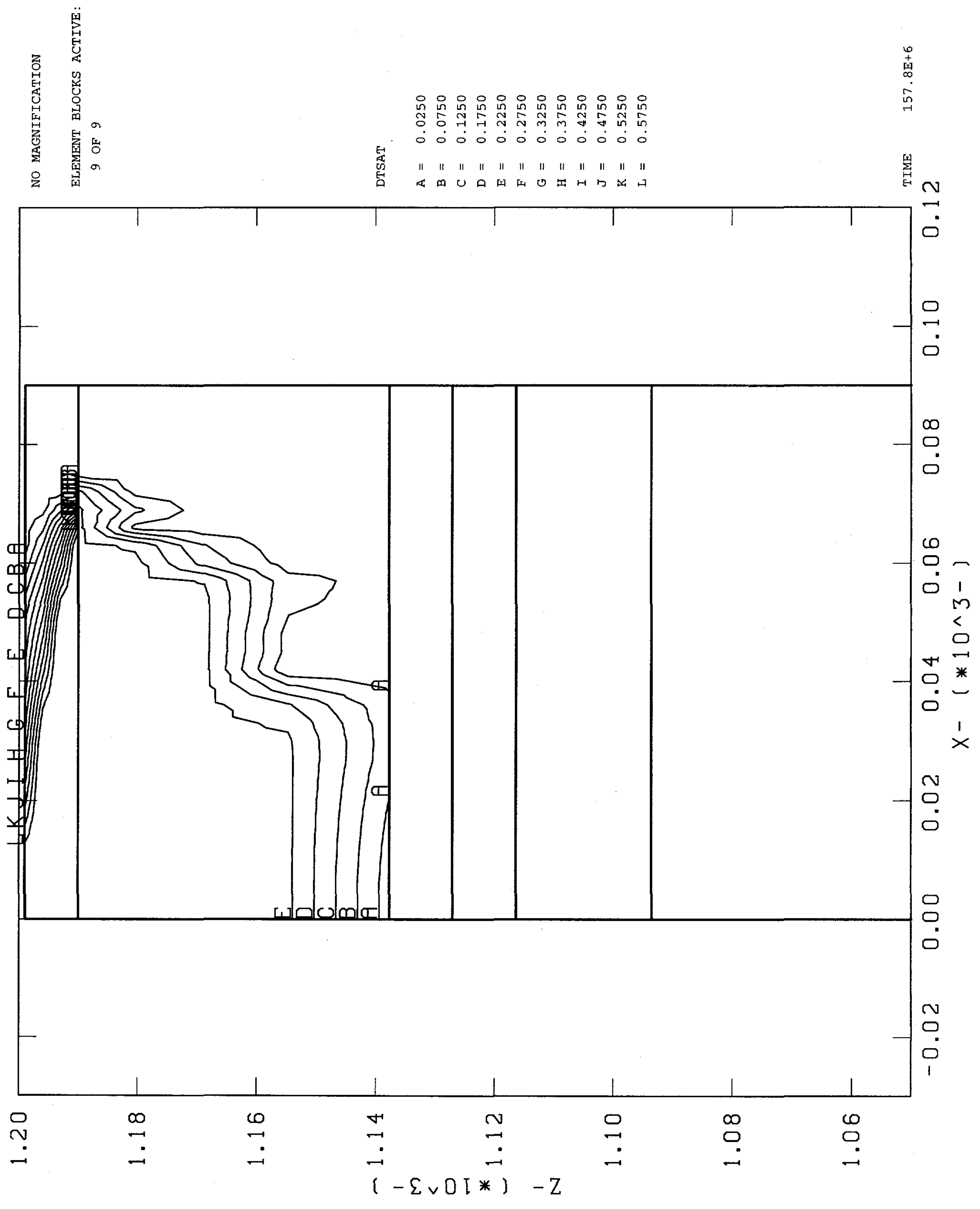

Change in Saturation from In Situ Conditions
Ptn Modeled as per PACE-90 Studies
Time=5 Years

Figure 3.3-12: Change in Saturation After 25 Years, Road Water Calculations PTn Modeled Per ESF12

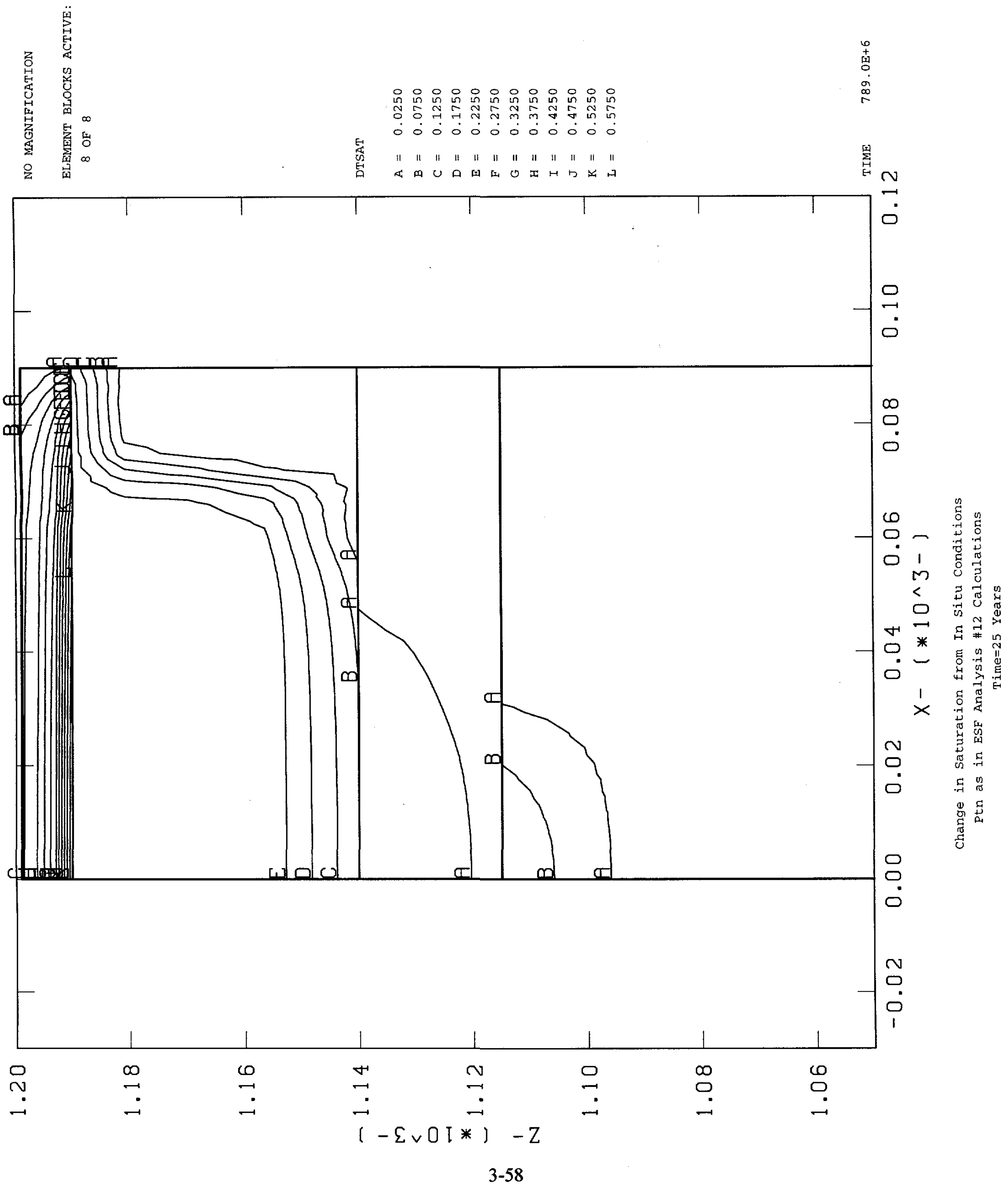

Figure 3.3-13: Change in Saturation After 25 Years, Road Water Calculations PTn Modeled as Bedded Tuff

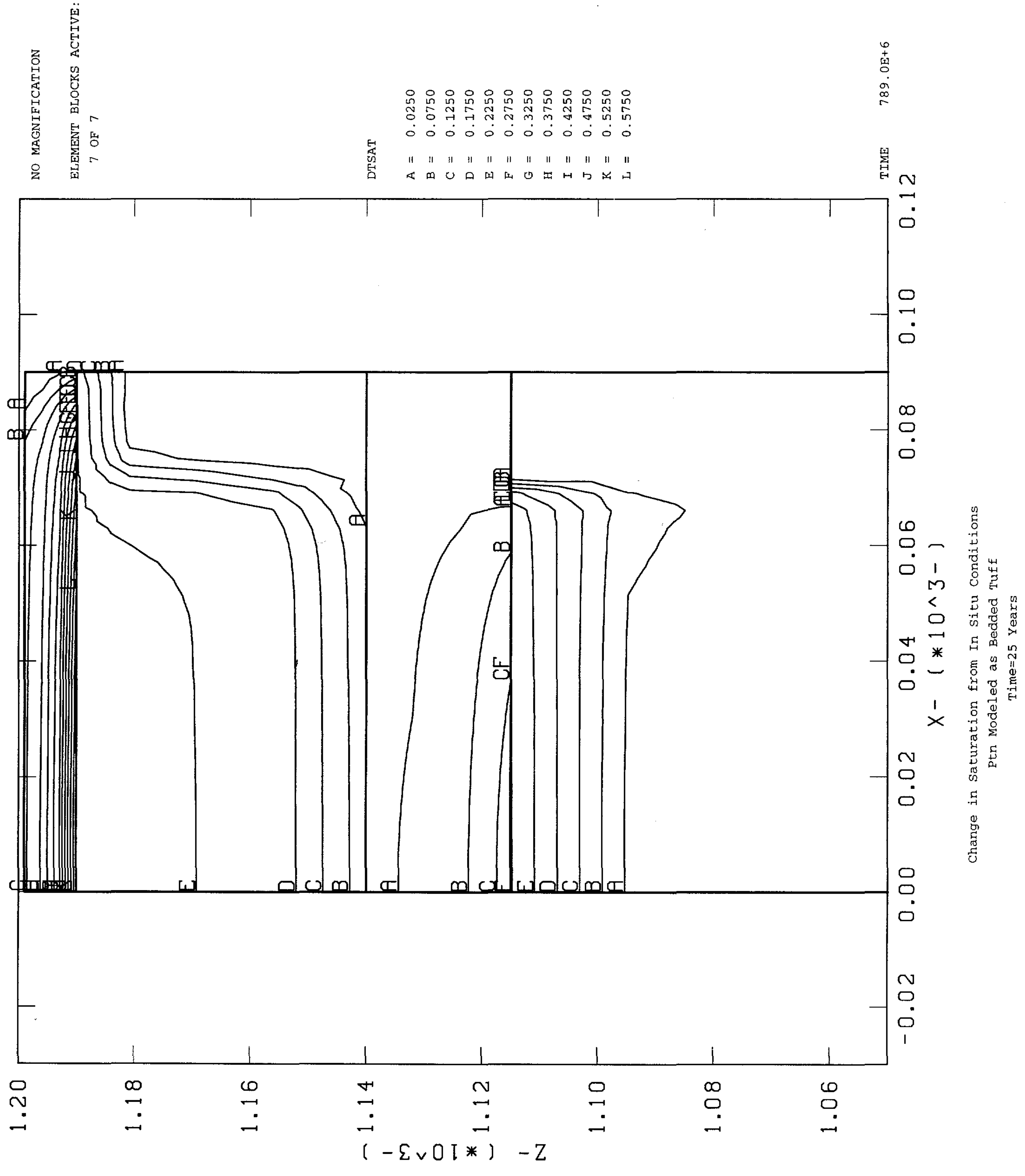

Figure 3.3-14: Change in Saturation After 25 Years, Road Water Calculations PTn Modeled as USW G-4

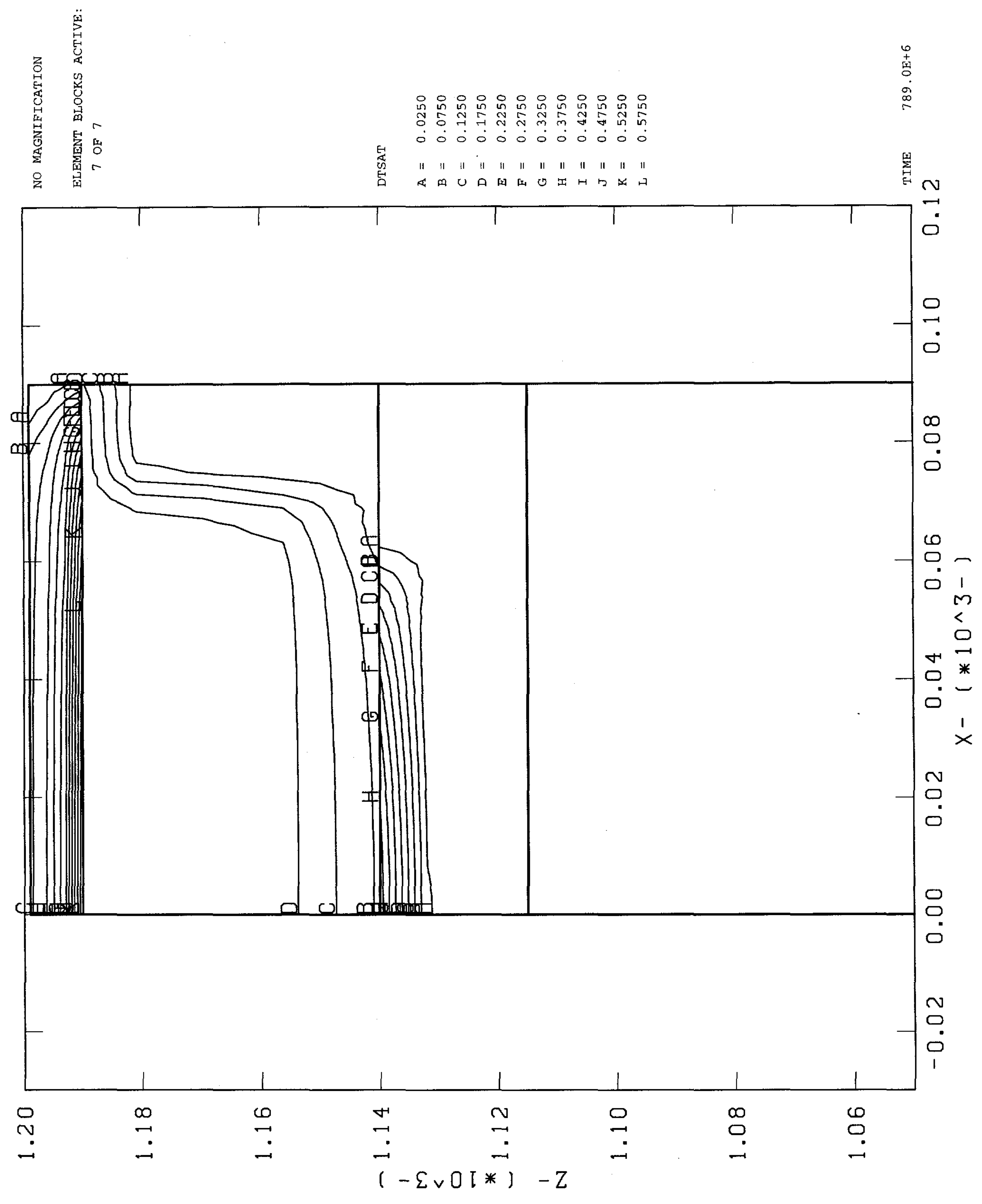

Change in Saturation from In Situ Conditions
Ptn Modeled as USW G-4
Time=25 Years

Figure 3.3-15: Change in Saturation After 25 Years, Road Water Calculations PTn Modeled as Pah Canyon Member

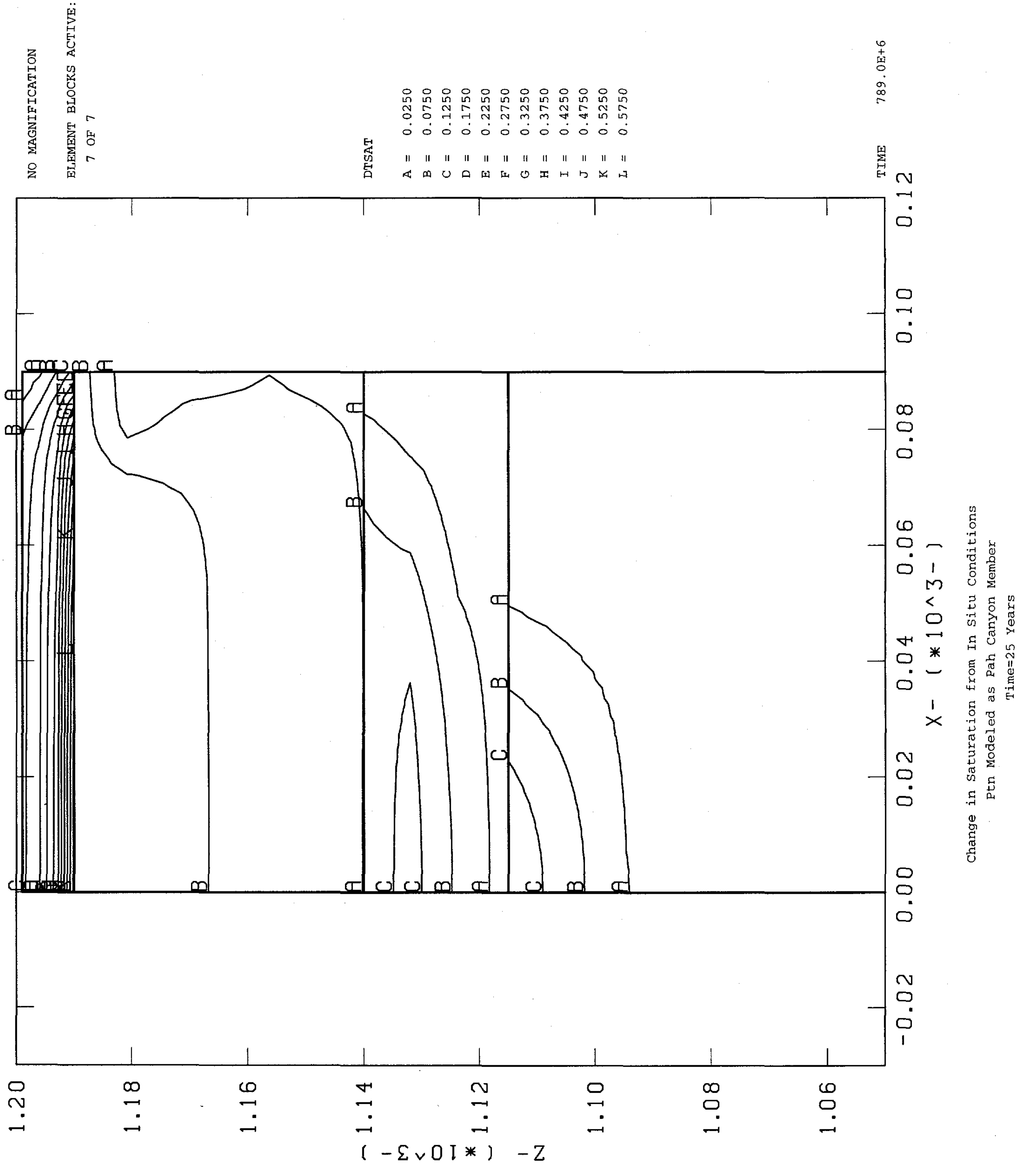

Figure 3.3-16: Change in Saturation After 25 Years, Road Water Calculations PTn Modeled as Tpt-TM

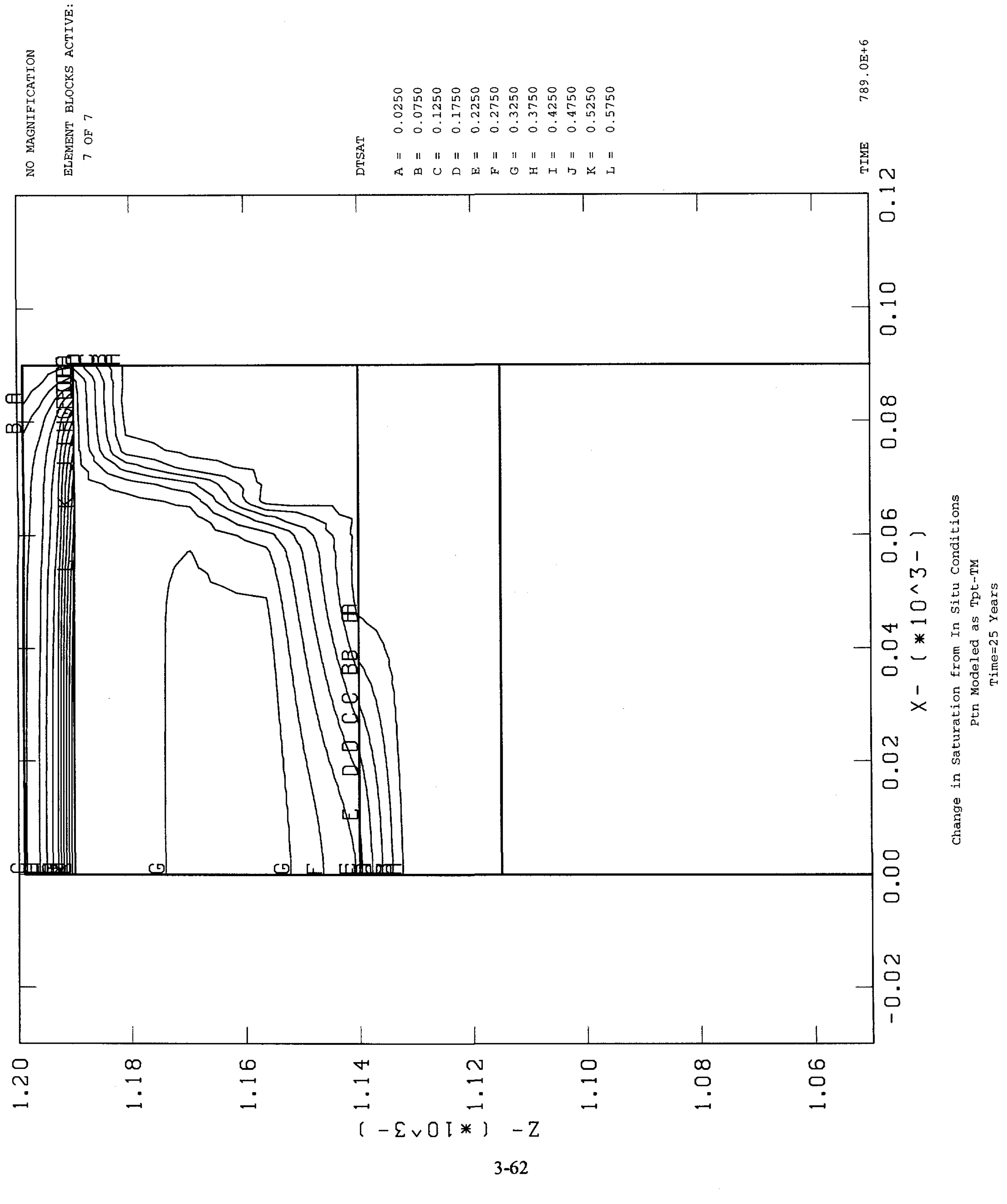

Change in Saturation from In Situ Conditions
Ptn Modeled as Tpt-TM
Time=25 Years

Figure 3.3-17: Change in Saturation After 25 Years, Road Water Calculations PTn Modeled as Tpc-TN

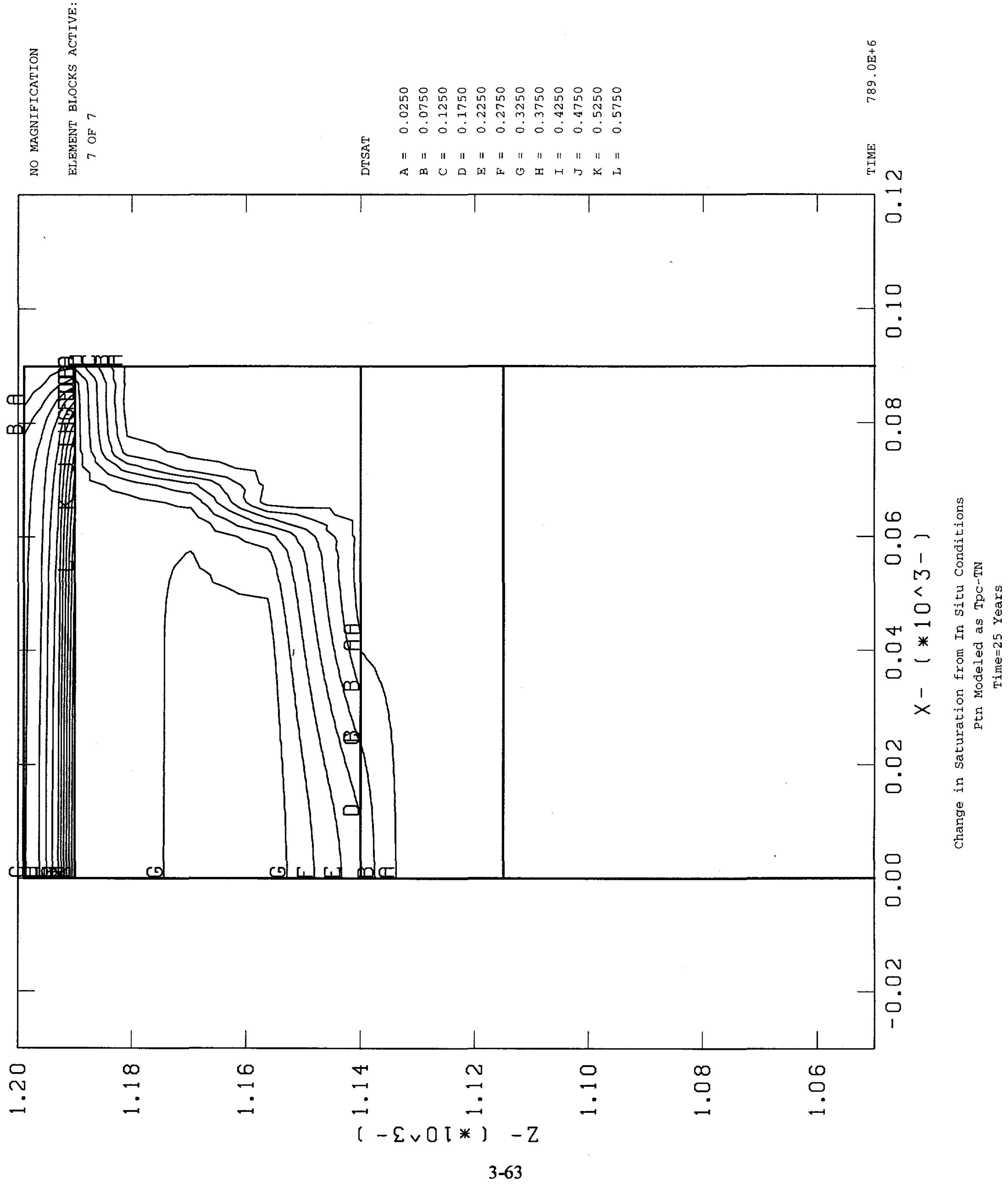

Figure 3.3-18: Change in Saturation After 25 Years, Road Water Calculations PTn Modeled as Yucca Mountain Member

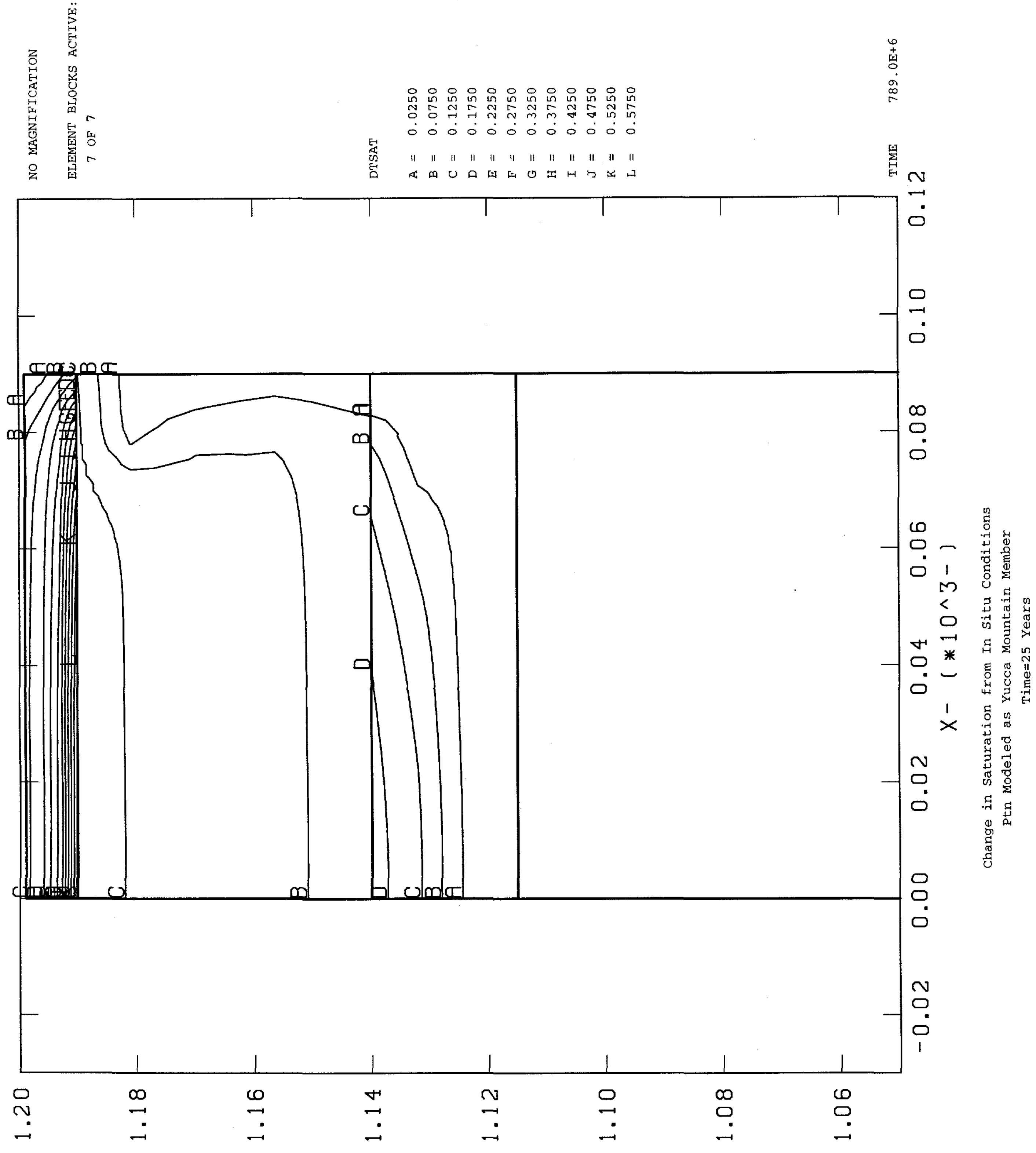

Change in Saturation from In Situ Conditions
Ptn Modeled as Yucca Mountain Member
Time=25 Years

Figure 3.3-19: Change in Saturation After 25 Years, Road Water Calculations PTn Modeled Per PACE-90

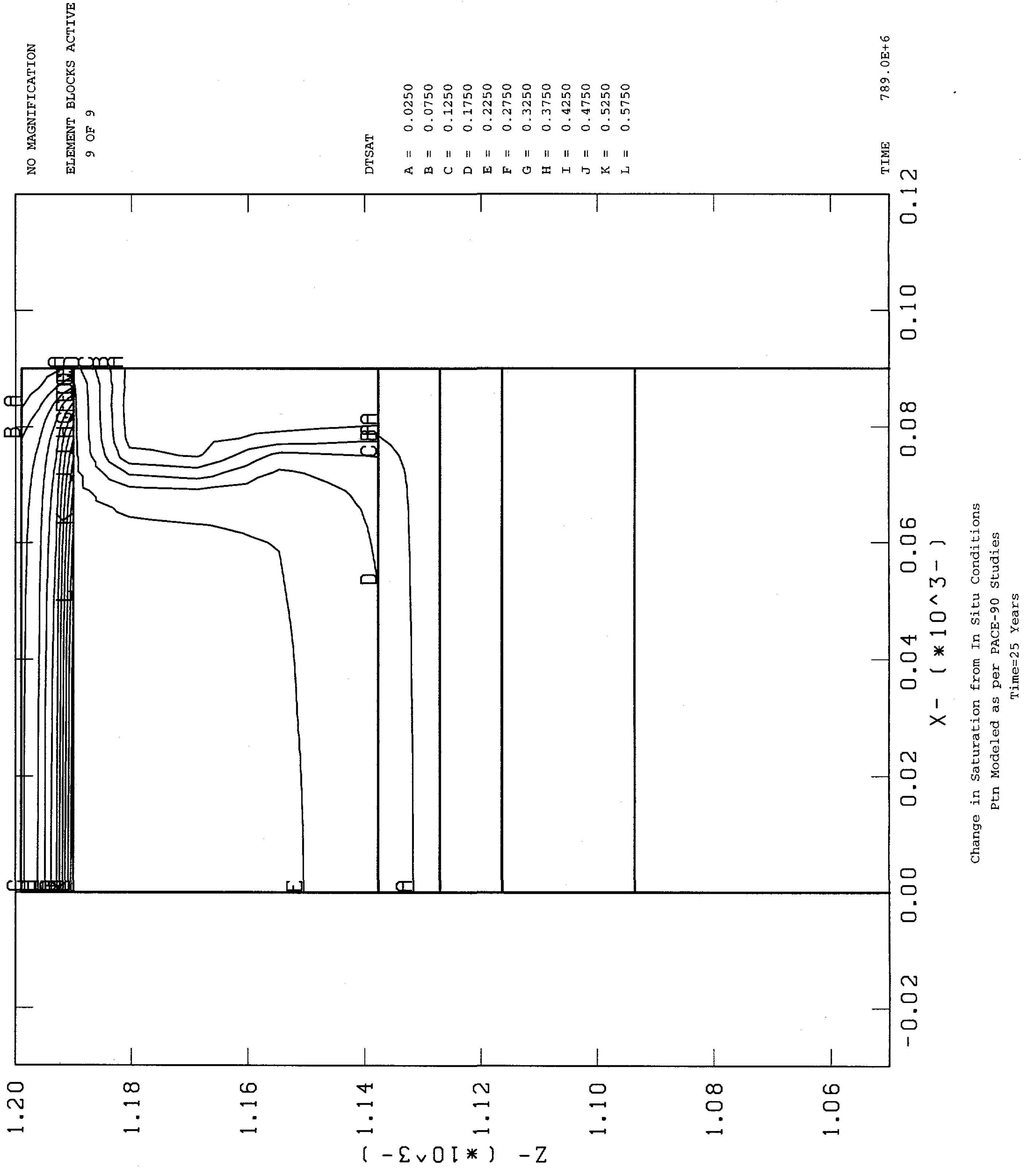

Figure 3.3-20: Change in Saturation After 10,000 Years, Road Water Calculations PTn Modeled Per ESF12

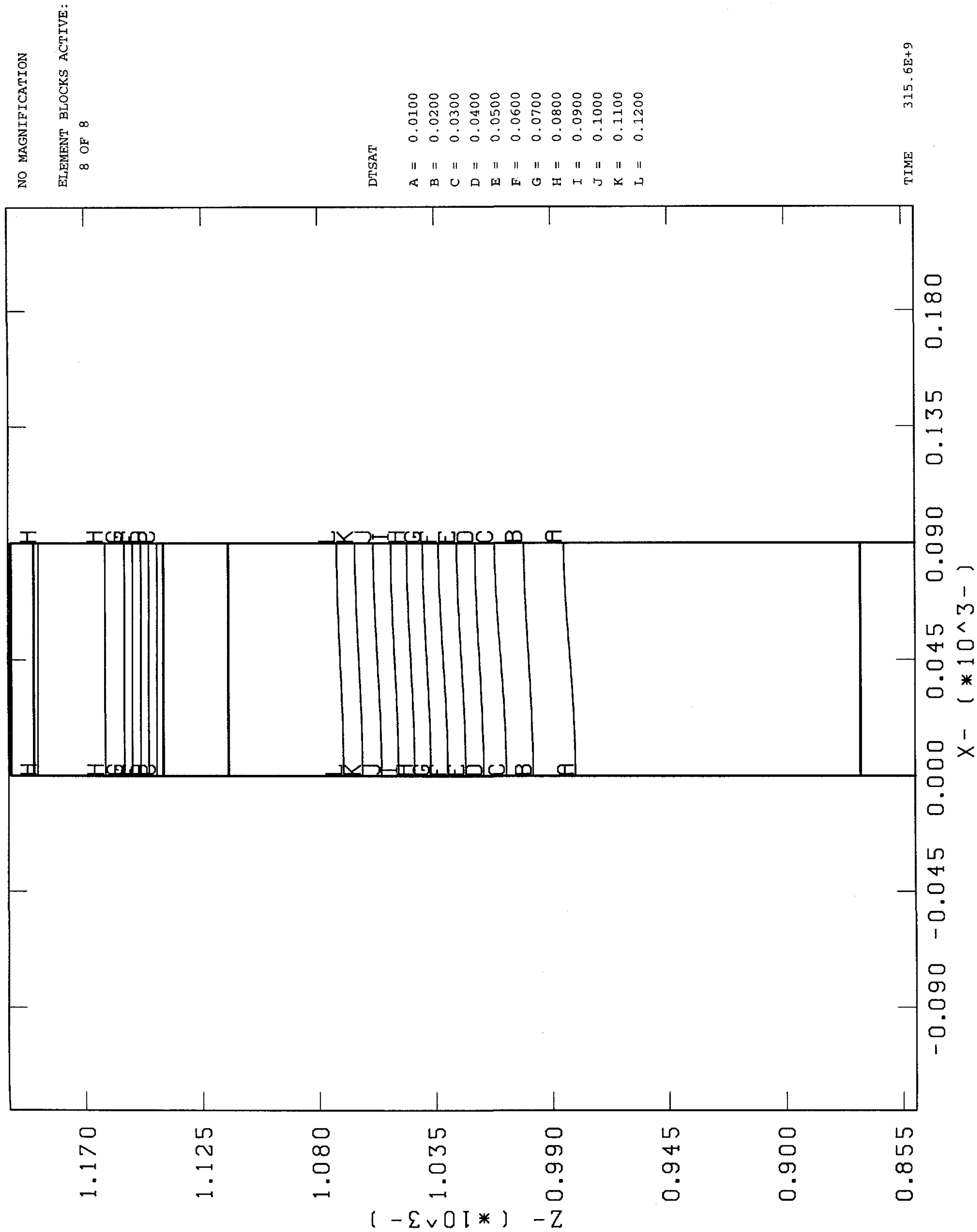

Change in Saturation from In Situ Conditions
Ptn as in ESF Analysis #12 Calculations
Time=10,000 Years

Figure 3.3-21: Change in Saturation After 10,000 Years, Road Water Calculations PTn Modeled as Bedded Tuff

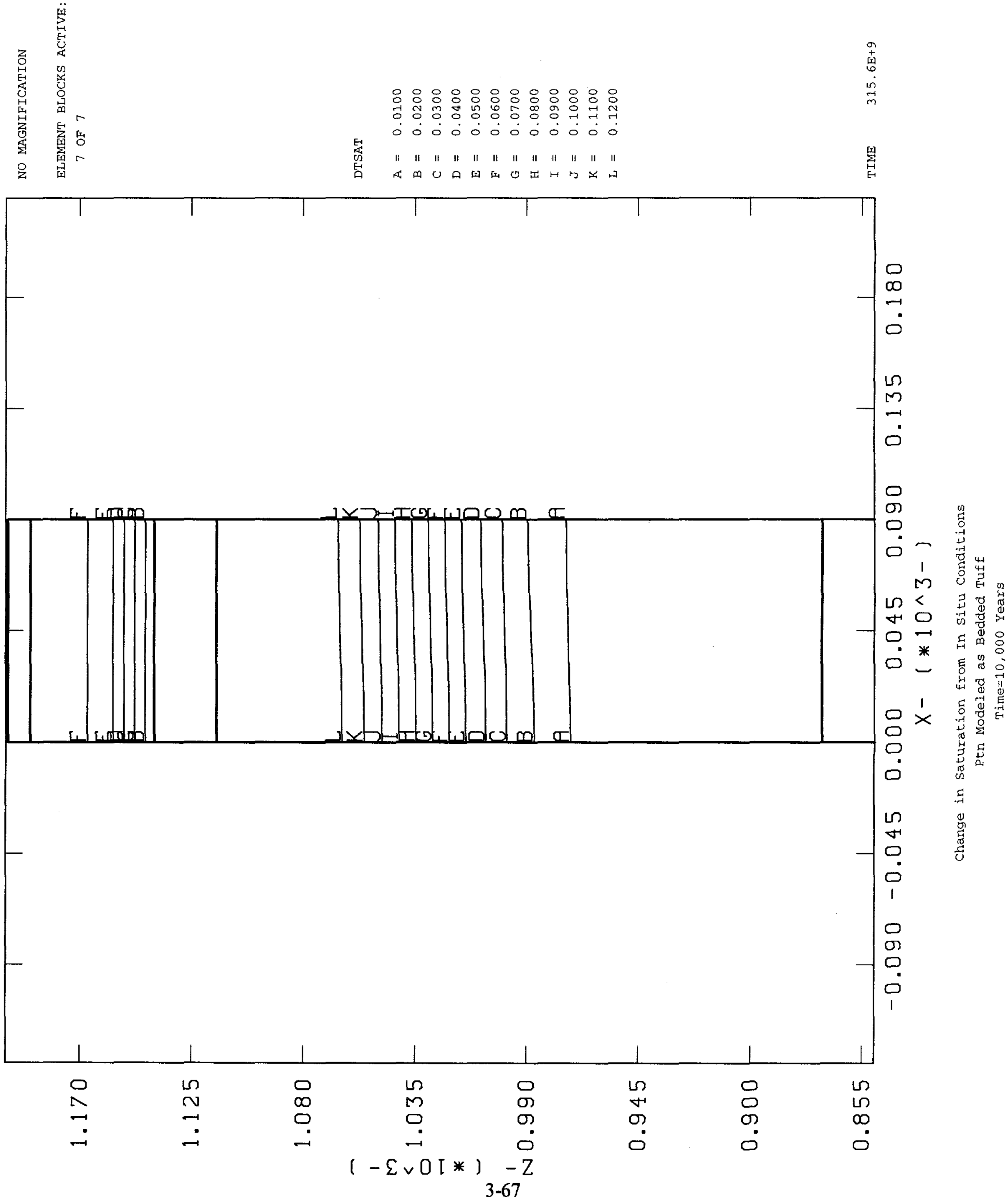

Figure 3.3-22: Change in Saturation After 10,000 Years, Road Water Calculations PTn Modeled as USW G-4

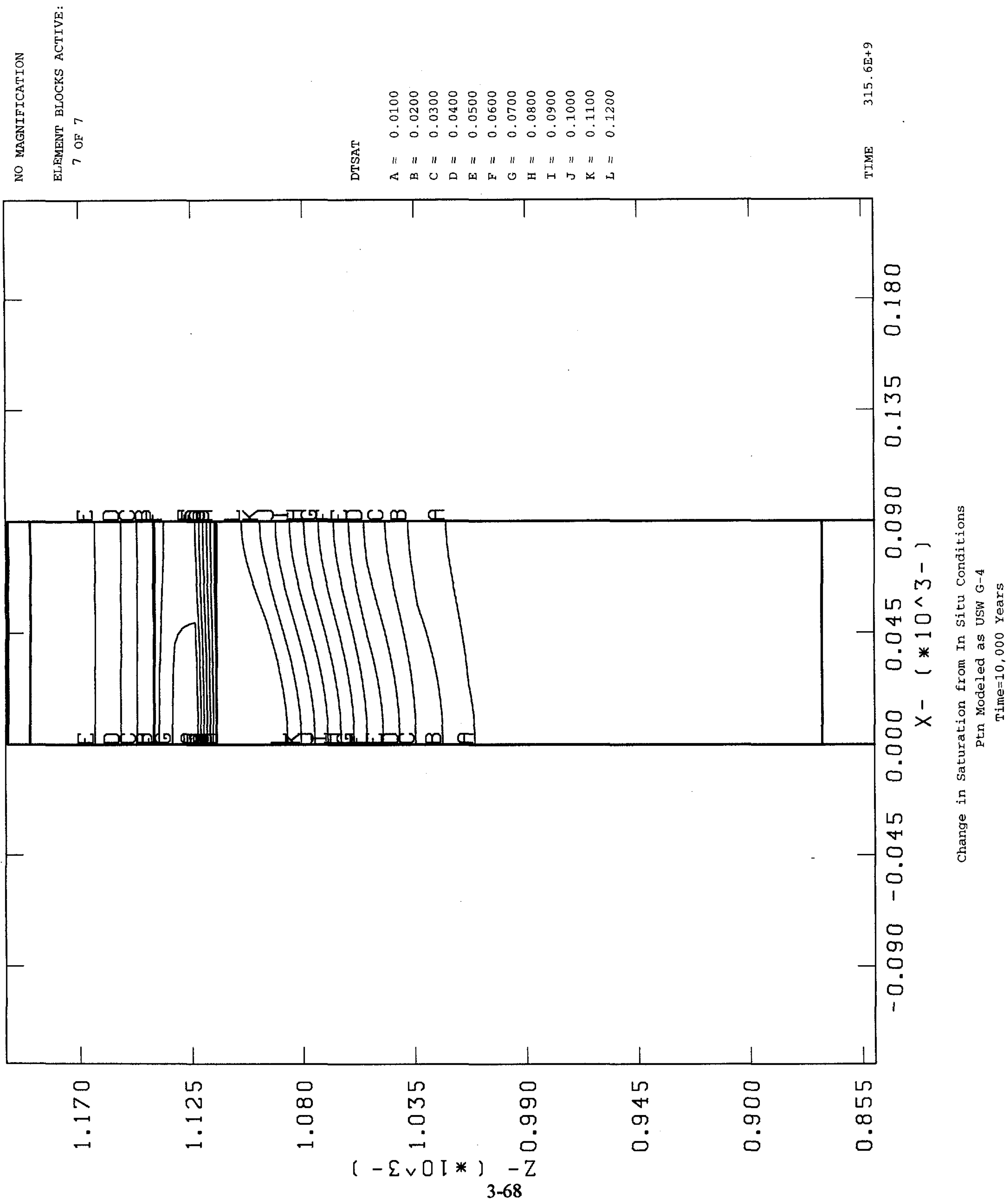

Figure 3.3-23: Change in Saturation After 10,000 Years, Road Water Calculations PTn Modeled as Pah Canyon Member

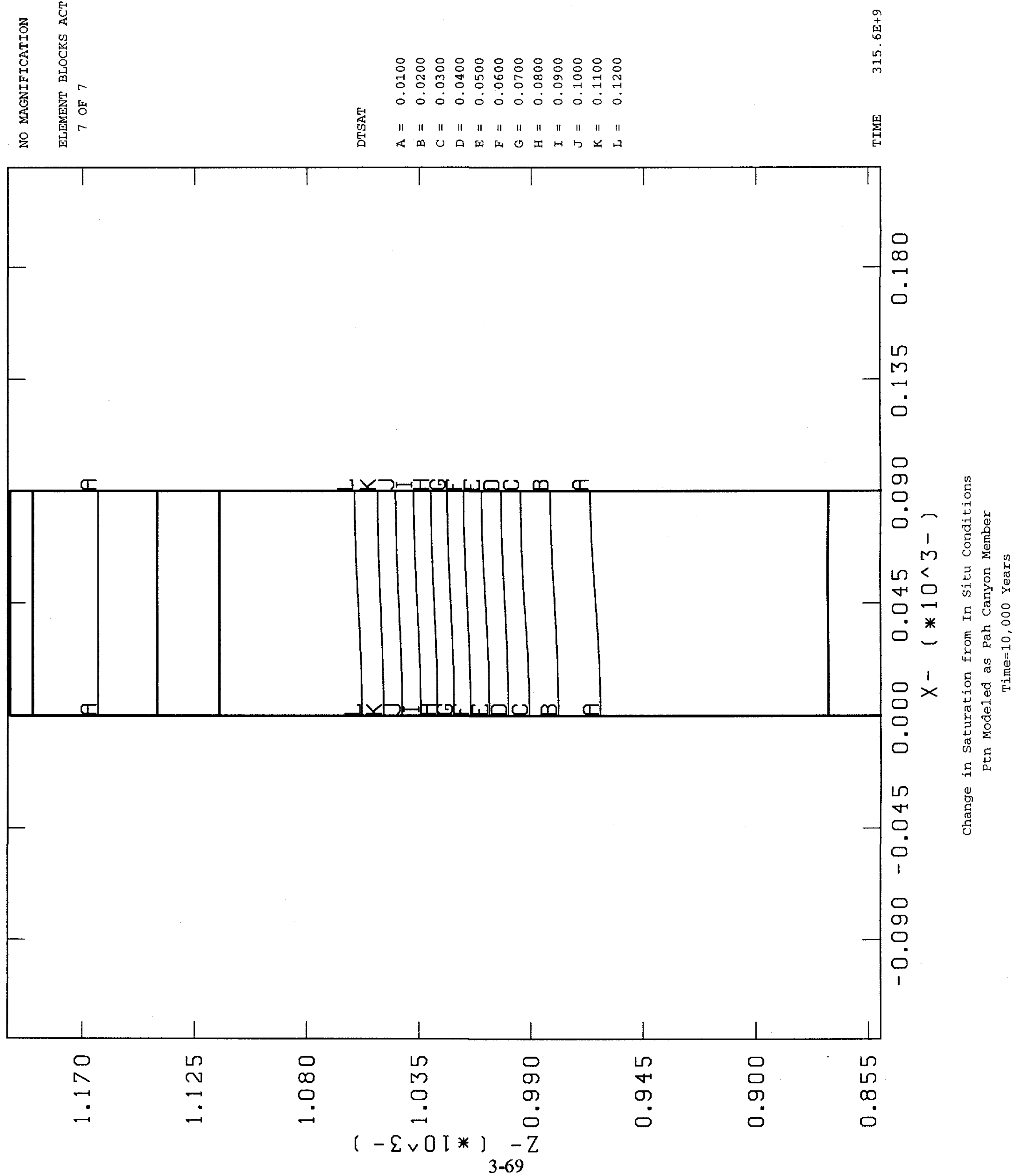

Figure 3.3-24: Change in Saturation After 10,000 Years, Road Water Calculations PTn Modeled as Tpt-TM

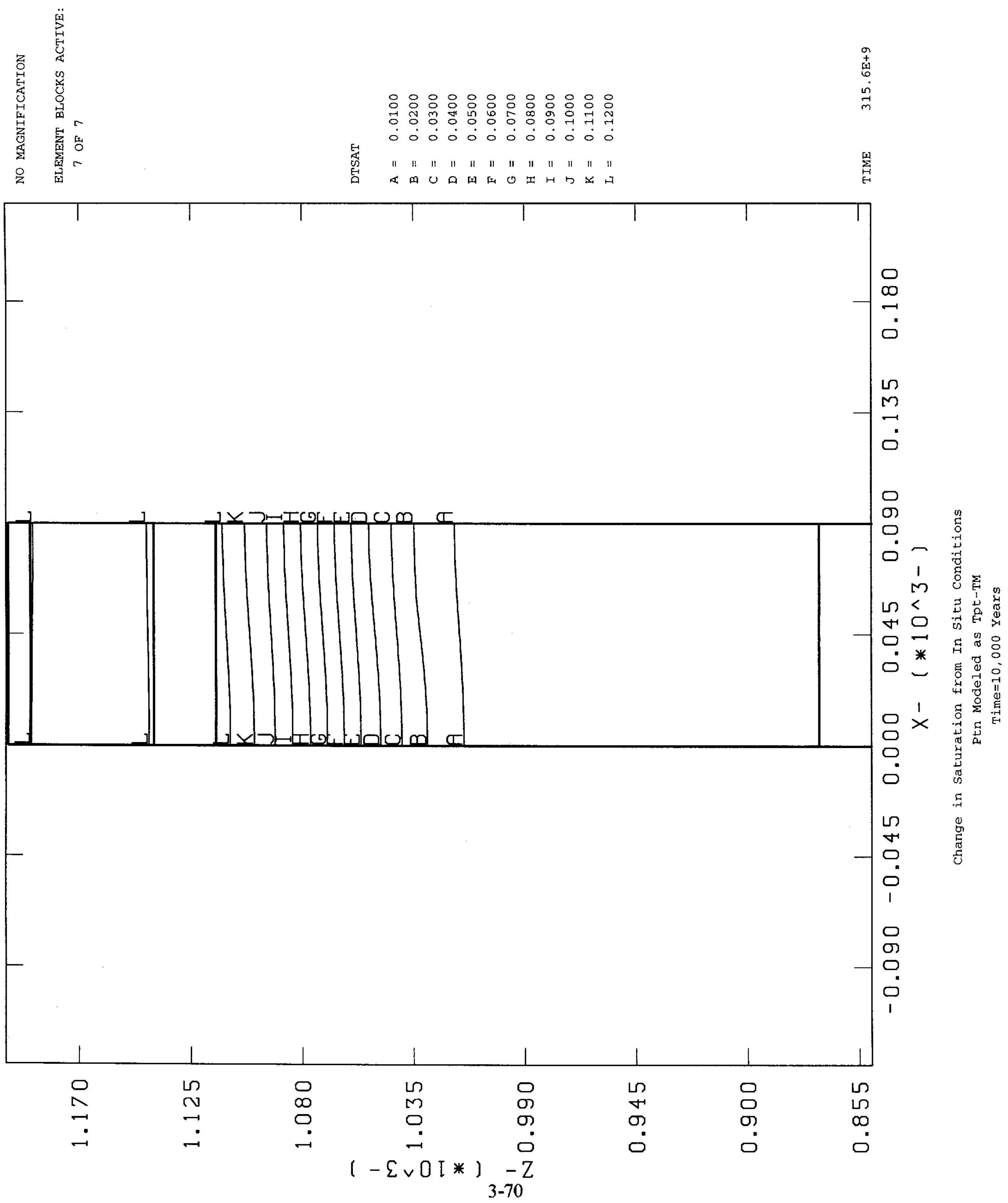

Figure 3.3-25: Change in Saturation After 10,000 Years, Road Water Calculations PTn Modeled as Tpc-TN

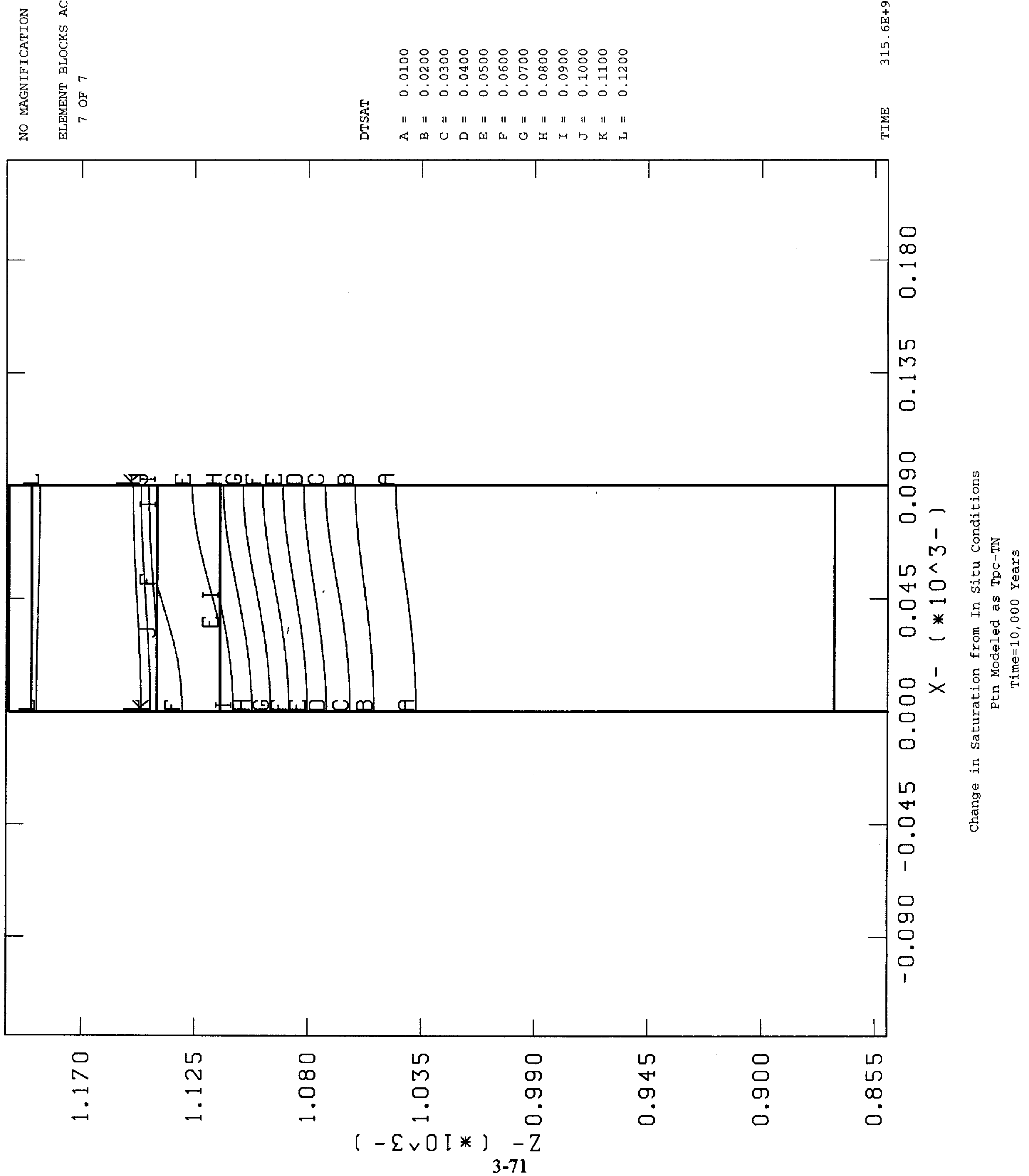

Figure 3.3-26: Change in Saturation After 10,000 Years, Road Water Calculations PTn Modeled as Yucca Mountain Member

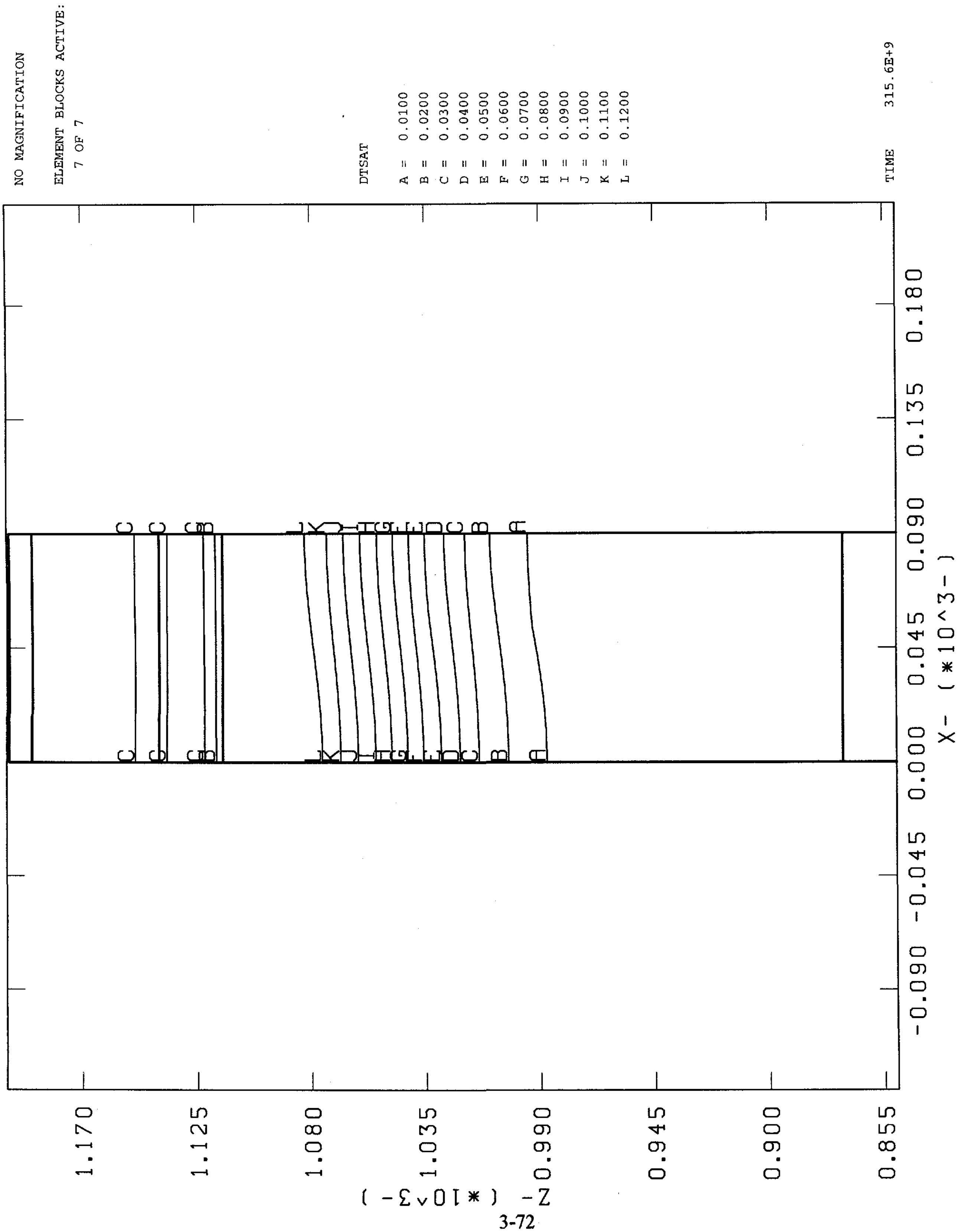

Change in Saturation from In Situ Conditions
Ptn Modeled as Yucca Mountain Member
Time=10,000 Years

Figure 3.3-27: Change in Saturation After 10,000 Years, Road Water Calculations PTn Modeled Per PACE-90

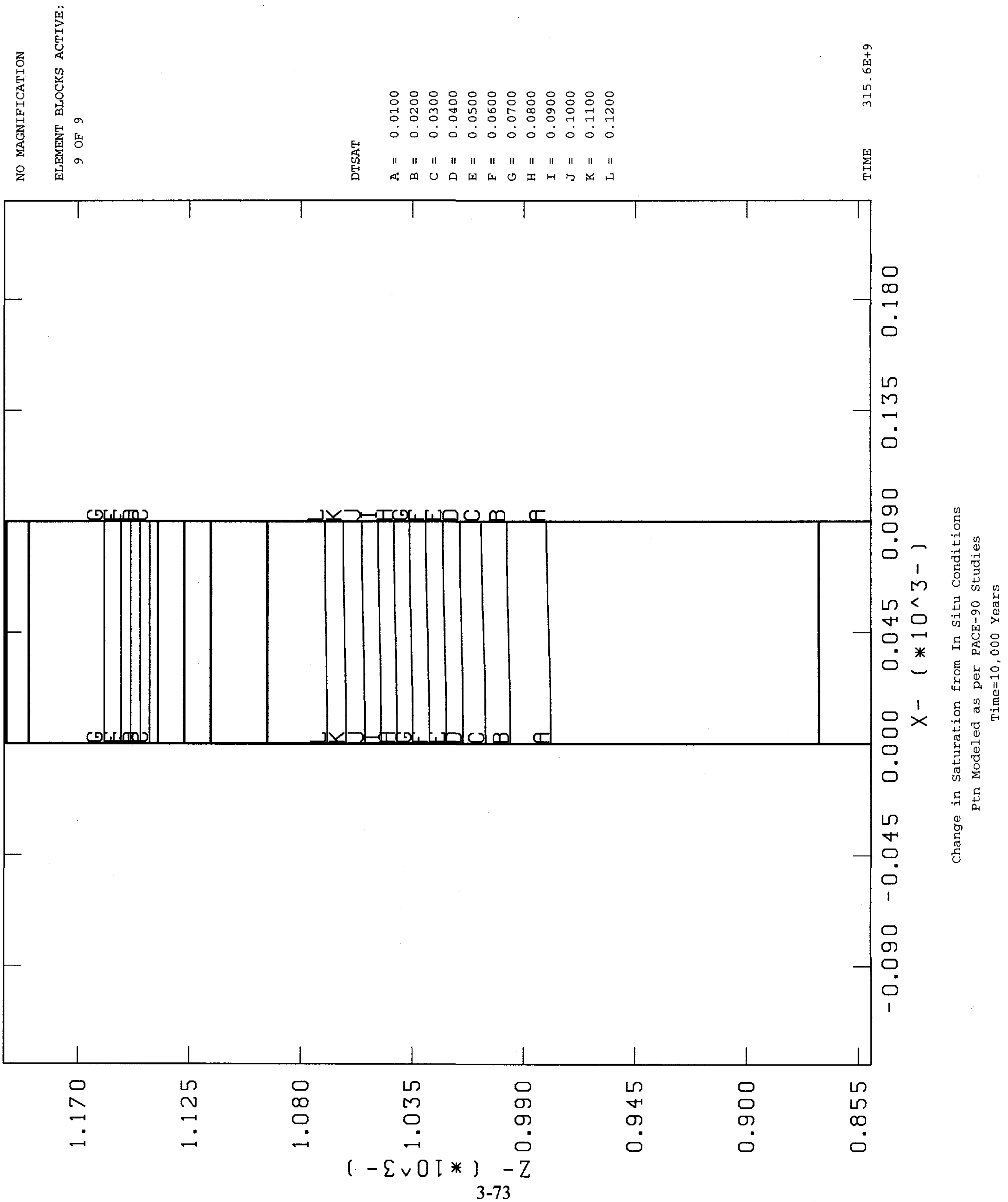

Change in Saturation from In Situ Conditions
Ptn Modeled as per PACE-90 Studies
Time=10,000 Years

3.4 Comparison with Underground Water Calculations of ESF PA Analysis #13

This set of calculations evaluates the sensitivity of the underground watering analyses of ESF PA Analysis #13 to the values chosen for material properties in PTn. Specifically, these calculations iterate on those done previously for the section of the ESF tunnel in the PTn. For this case, the variability in the amount of infiltrated water and its vertical and lateral spread is of primary importance. A full description of the assumptions used to formulate the original surficial watering problem is in Dunn and Sobolik (1993); an abridged description is included for the new calculations.

3.4.1 Problem Definition

Computational analyses were performed to simulate a scenario for water usage or spillage in the ESF tunnel excavated in the Paintbrush Tuff nonwelded unit (PTn). The scenario simulates the continuous saturation of the tunnel walls due to various water application activities. The surface of the tunnel walls are assumed to remain saturated for one month. For these calculations, the finite element code NORIA-SP (Hopkins et al., 1991), Version 0.10, was used to perform the calculations.

The problem is conceptualized as follows. Prior to the construction of the tunnel and the addition of water, a vertical cross-section of the mountain at the location of the simulation is at in situ saturation conditions. This in situ saturation profile through the tunnel was produced by calculations assuming steady-state flow with a uniform infiltration of water of 0.01 mm/yr through the ground surface. These steady-state solutions were used as the initial conditions for the transient calculations. At "time zero," a tunnel with a cross-section of 10 m × 10 m was excavated through the PTn unit. The tunnel walls were then wetted with water for a period of one month. The amount of water that infiltrated the rock and the extent of its movement were evaluated. These calculations were conducted for each of the sets of material properties considered for PTn.

The stratigraphy that was used for computing the in situ saturation profile through the tunnel in PTn was that for the borehole USW G-4. Although the PTn section of tunnel is to be located hundreds of meters from the USW G-4 location, this location was used for calculating the in situ saturation profile to be consistent with ESF Analysis #13. The problem domain for each case was two-dimensional and cartesian, extending from the water table to the surface for the steady-state calculations, and from the TSw2-TSw1 interface to the TCw-UO interface for the transient calculations. The stratigraphic units were modeled as horizontal and parallel. Symmetry allowed a no-flow boundary to be placed through the tunnel vertical centerline. The other vertical boundary was also defined as a no-flow boundary and placed 31 m from the tunnel centerline. The tunnel walls form additional boundaries at which the wetting boundary conditions were imposed. The wetting boundary condition for all the tunnel walls was implemented by setting the saturation at the wall surface nodes to 100%.

The material hydrogeologic properties that were used for all units except PTn were those used for ESF Analysis #13 (Dunn and Sobolik, 1993). Six different sets of values for PTn listed in Table 3.1-1 were used and compared with the original calculations: Tpc-BT, bedded tuff; Pah Canyon member; Tpt-TM, moderately welded, highly fractured tuff; Tpc-TN, nonwelded ashflow tuff;

Yucca Mountain member; and USW G-4. The thermomechanical properties in each layer were assumed to be homogeneous and isotropic throughout the layer. The effects of ventilation were not included in these calculations.

3.4.2 Results

The original calculations from Dunn and Sobolik (1993) simulated a flooding scenario, where an event such as the extinguishing of a large fire in the PTn section of the ESF main drift, would fill the tunnel from floor to ceiling with water for one month. Hydrogeologic properties for the Yucca Mountain member were used for PTn for those calculations. For the new sets of calculations performed for this study, a more likely scenario is simulated; the continuous wetting of the tunnel walls for dust control and mapping purposes for a period of one month. Results from calculations using six different sets of material properties for PTn are compared here.

Figure 3.4-1 shows the grid for the entire computational domain used for these calculations. A finer grid was used here than for the calculations in Dunn and Sobolik, and the domain was restricted to the TCw, PTn, and TSw1 layers. The in situ saturation conditions for these calculations were taken from the corresponding calculations done for the road water problem. Figures 3.4-2 through 3.4-7 are contour plots of Δsat which show the extent of water movement after one month of continuous wetting of the tunnel walls. The plots are shown in ascending order of the amount of water imbibed into the in situ rock: Tpc-TN (Figure 3.4-2), Tpt-TM (Figure 3.4-3), Yucca Mountain member (Figure 3.4-4), USW G-4 (Figure 3.4-5), Pah Canyon (Figure 3.4-6), and the bedded tuff (Figure 3.4-7). Table 3.4-1 also lists the amount of imbibed water for each case after one month. The results for the bedded tuff calculations are presented after 5 days in the simulation. Obviously, there is a substantial difference in the amount of imbibed water and the extent of its migration among the six cases. The amount of water imbibed into the in situ rock is highly dependent on the bulk hydraulic conductivity and also somewhat dependent upon the initial pore space available for water storage.

Table 3.4-1: Results of the PTn Tunnel Calculations

	Matrix		Fracture			
Unit Representation of PTn	K_{sat}	Porosity	K_{sat}	Porosity	$K_{sat,\ bulk}$	Infiltrated water after 1 month, m^3/m
Tpc-TN	2.00×10^{-11}	0.5	0	0	2.0×10^{-11}	0.188
Tpt-TM	2.00×10^{-11}	0.1	4.00×10^{-5}	3.00×10^{-5}	1.22×10^{-9}	2.14
Yucca Mtn.	1.75×10^{-7}	0.436	6.10×10^{-4}	2.70×10^{-5}	1.91×10^{-7}	17.7
USW G-4	5.00×10^{-10}	0.4	6.10×10^{-4}	2.70×10^{-5}	1.7×10^{-8}	21.7
Pah Canyon	7.14×10^{-7}	0.47	6.10×10^{-4}	2.70×10^{-5}	7.3×10^{-7}	70.8
Bedded Tuff * --- after 5 days	2.40×10^{-6}	0.22	0	0	2.4×10^{-6}	* 293.

From the scenario described above, it can be observed that the PTn unit can store a large amount of water. In the more porous sub-units of PTn, the movement of this water is gravity-driven, toward the TSw1 unit, and not laterally within the PTn. Because of the expected sub-layering within the PTn, a low permeability layer such as Tpc-TN directly below a layer of bedded tuff could force lateral flow to a substantially greater extent than indicated here; this lateral forcing might cause water flow to intersect with faults which typically run vertically. Because the section of the ESF North Ramp that is in PTn is 800 m from the proposed repository boundary, the lateral movement of water from the PTn through the matrix to the repository block is expected to be negligible. Potential impacts to the repository horizon may occur, however, if there is a sufficiently connected network of fractures and faults leading to the repository block. The existence or nonexistence of such a network is not currently known. Therefore, this analysis would indicate that water application in the PTn should be kept to the minimum required.

Figure 3.4-1: Computational Grid for Underground Water Calculations

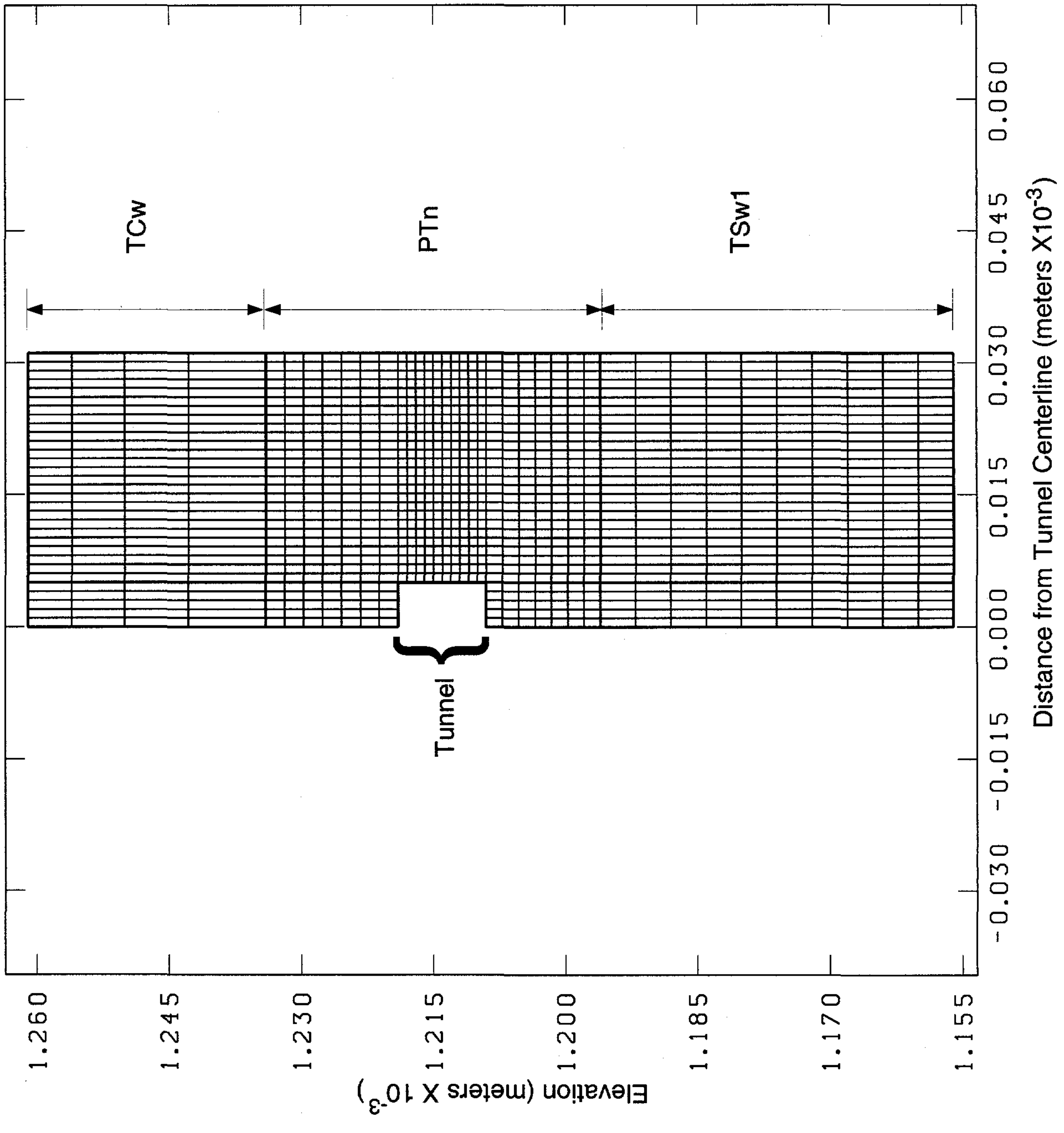

Study 14C.1 (UG Water): Mesh Used for the PTn Calculations

Figure 3.4-2: Change in Saturation After One Month, Underground Water Calculations PTn Modeled as Tpc-TN

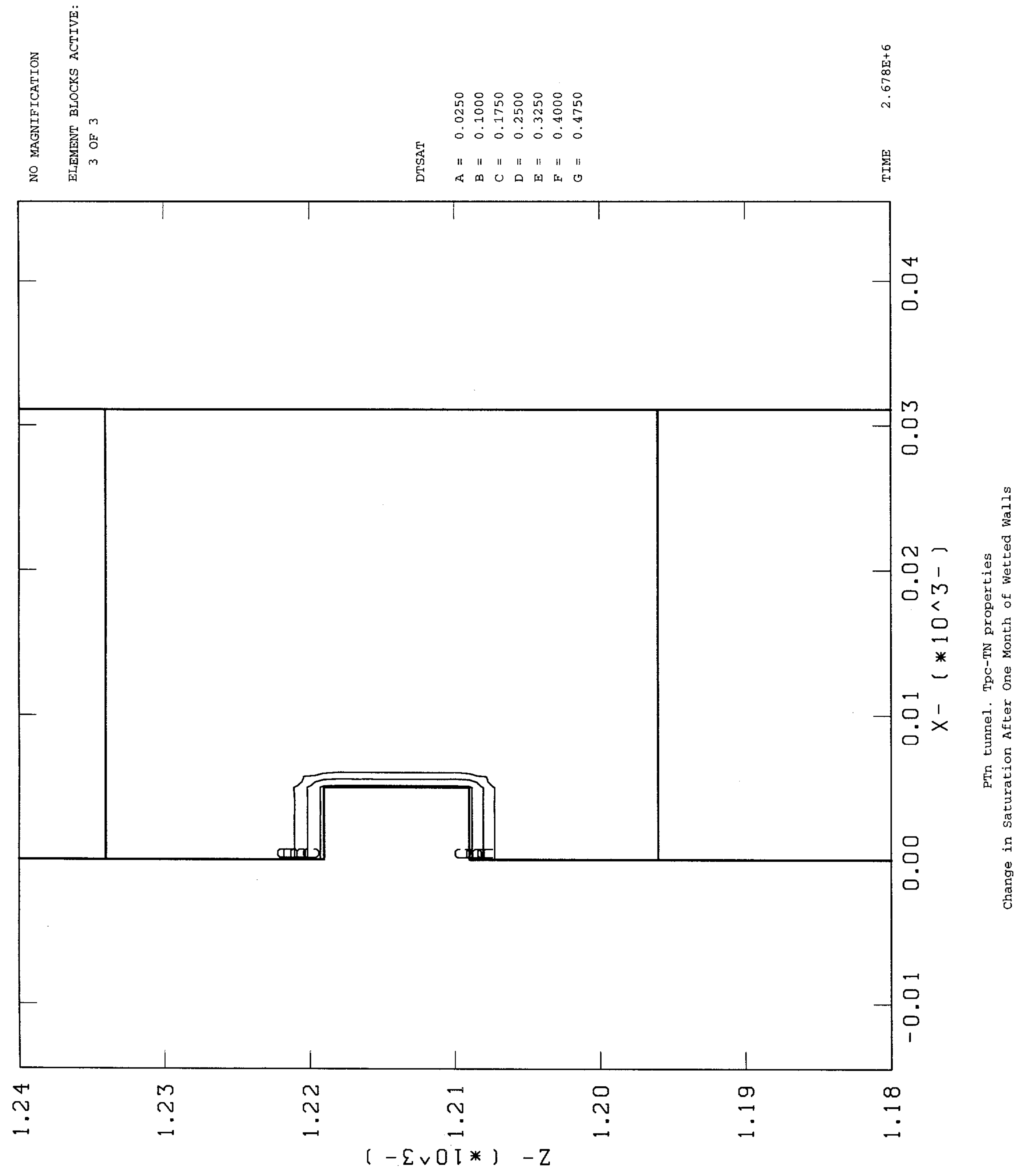

Figure 3.4-3: Change in Saturation After One Month, Underground Water Calculations PTn Modeled as Tpt-TM

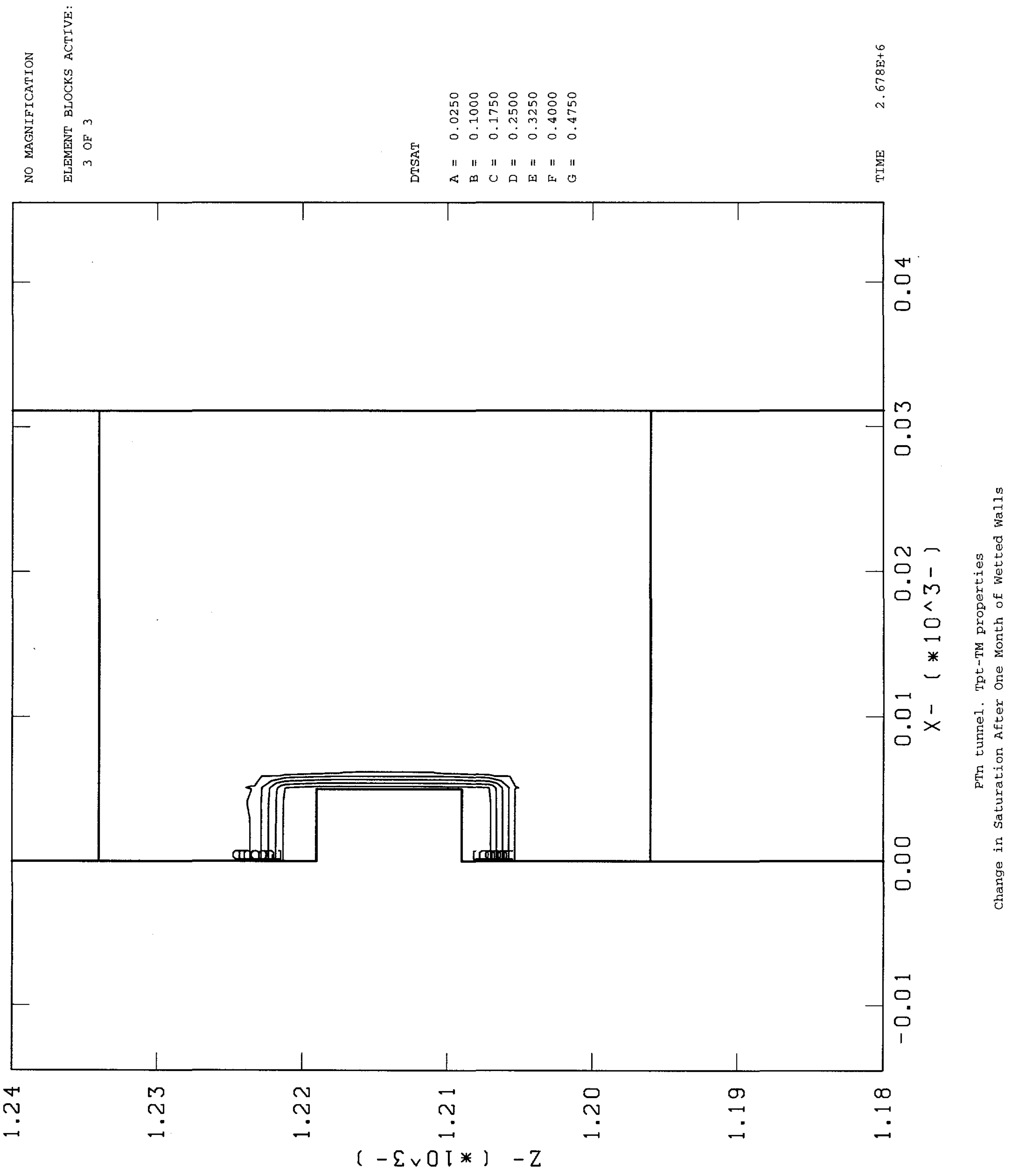

Figure 3.4-4: Change in Saturation After One Month, Underground Water Calculations PTn Modeled as Yucca Mountain Member

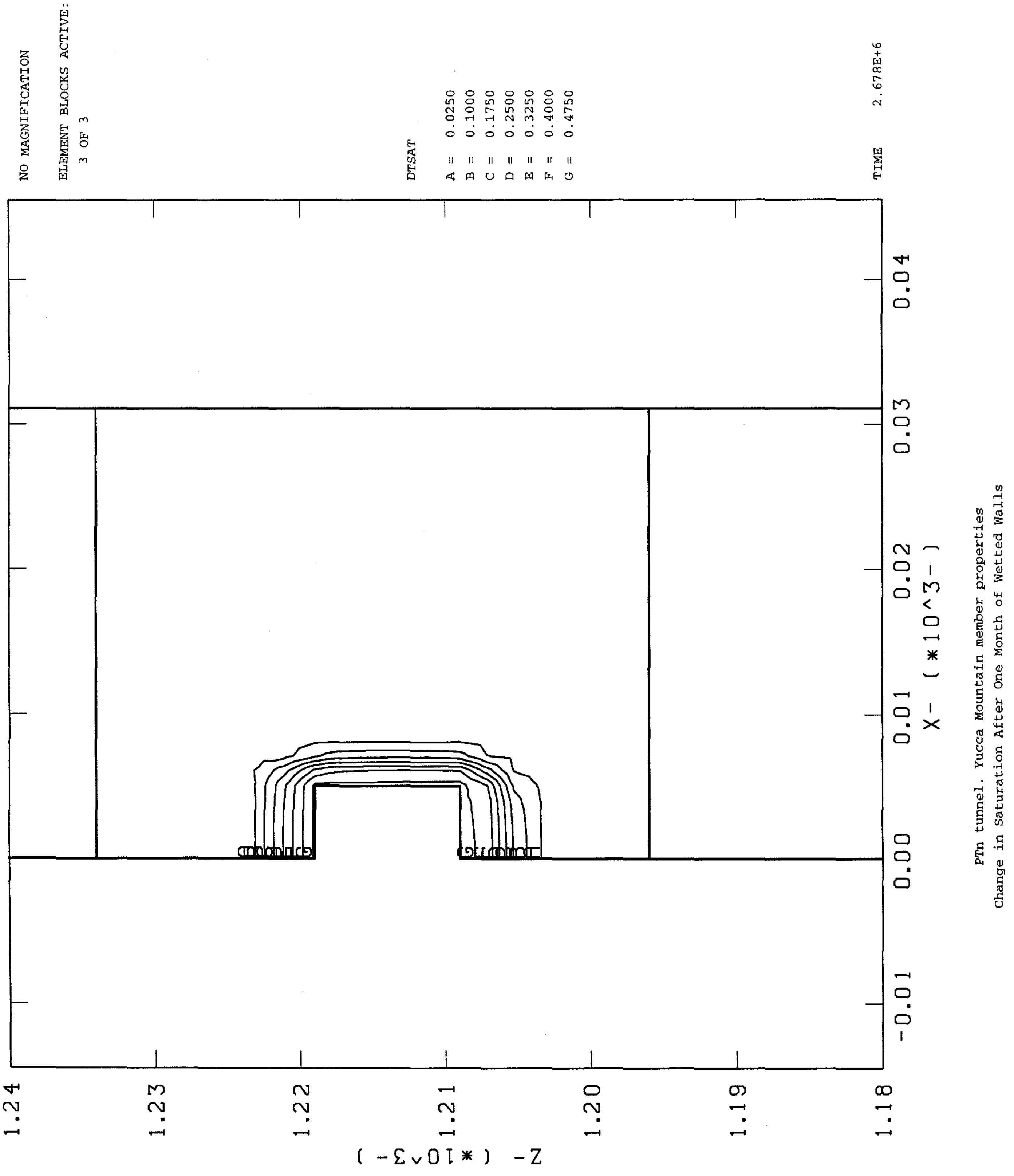

Figure 3.4-5: Change in Saturation After One Month, Underground Water Calculations PTn Modeled as USW G-4

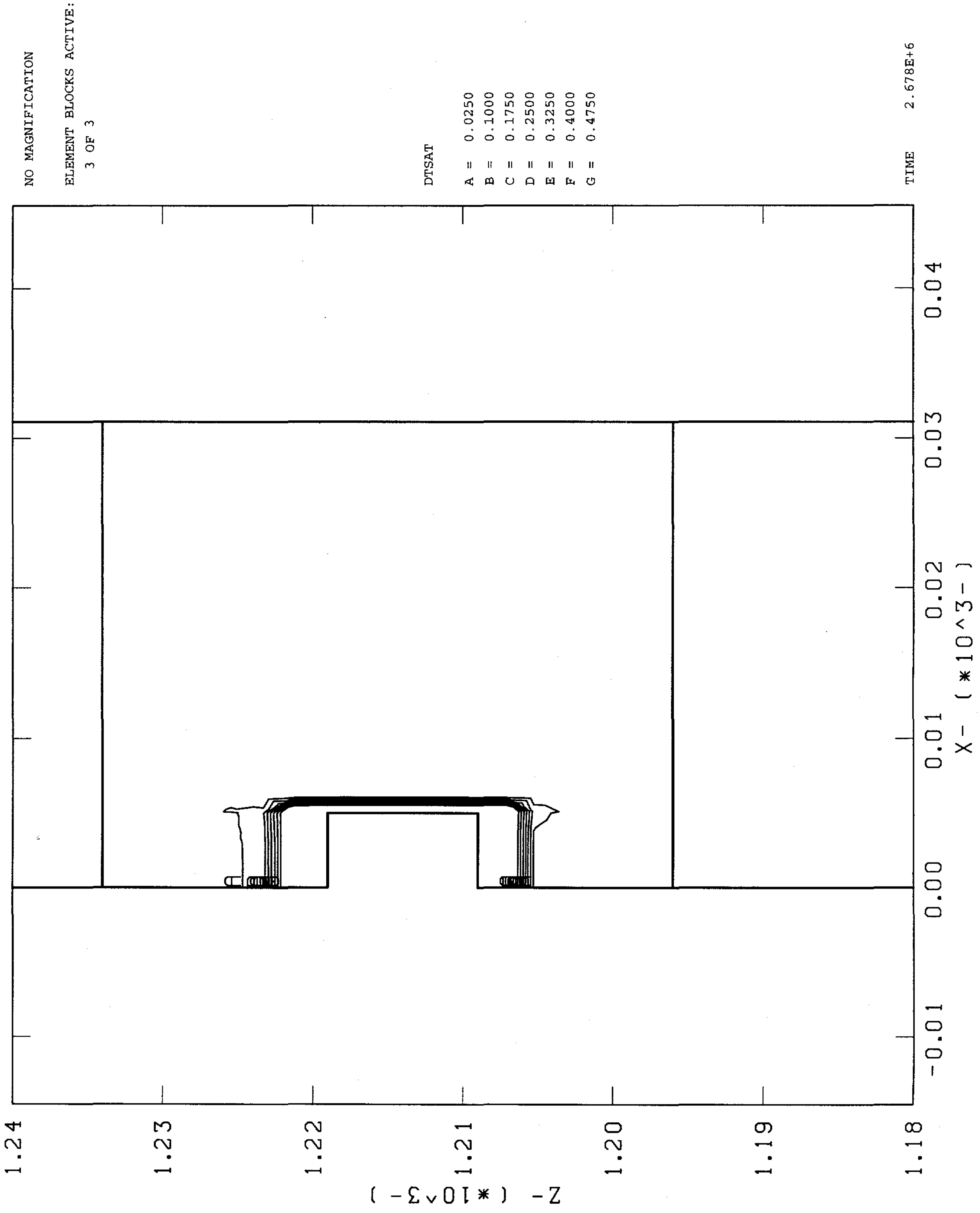

PTn tunnel. USW G-4 properties

Change in Saturation After One Month of Wetted Walls

Figure 3.4-6: Change in Saturation After One Month, Underground Water Calculations PTn Modeled as Pah Canyon Member

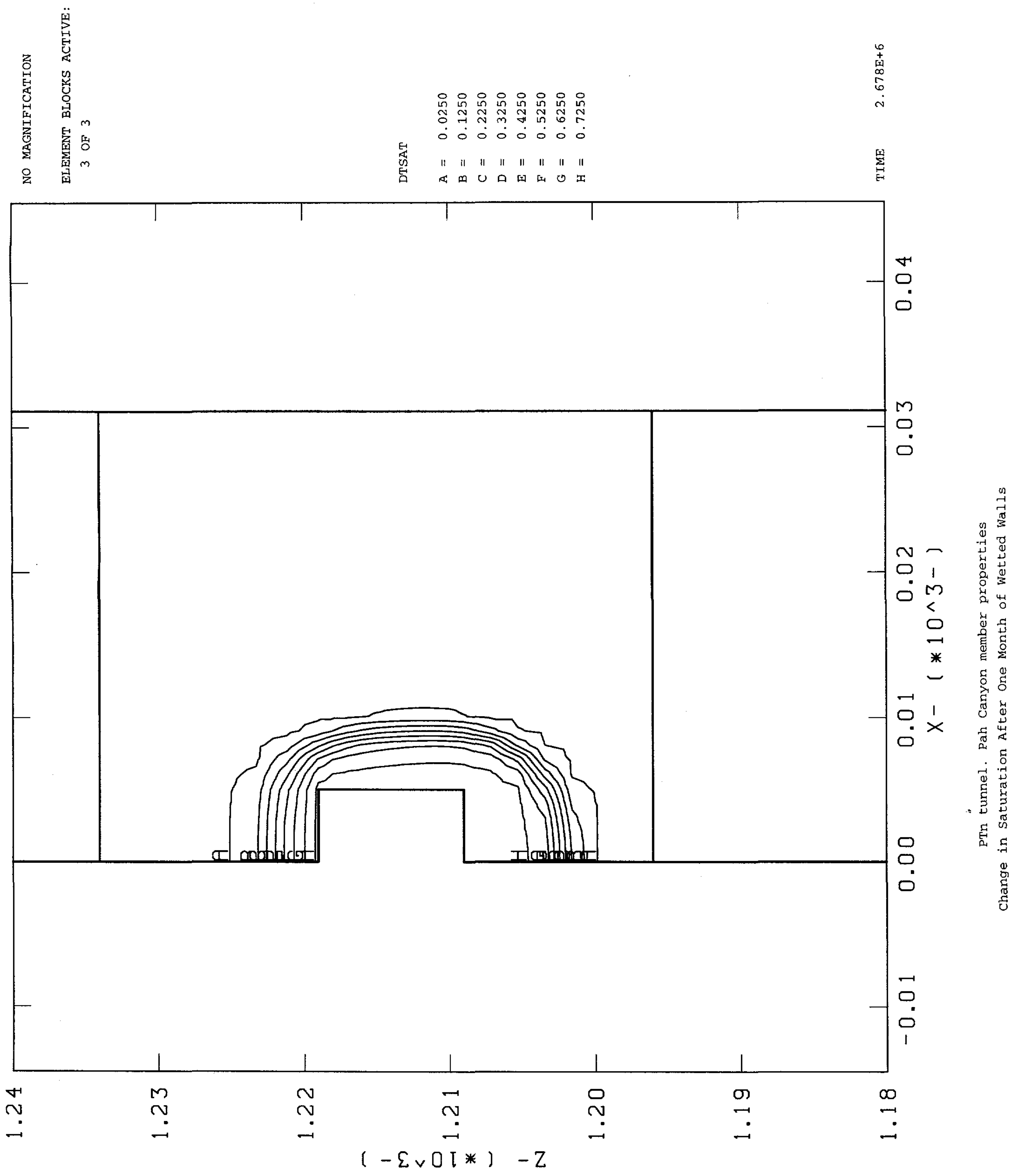

Figure 3.4-7: Change in Saturation After Five Days, Underground Water Calculations PTn Modeled as Bedded Tuff

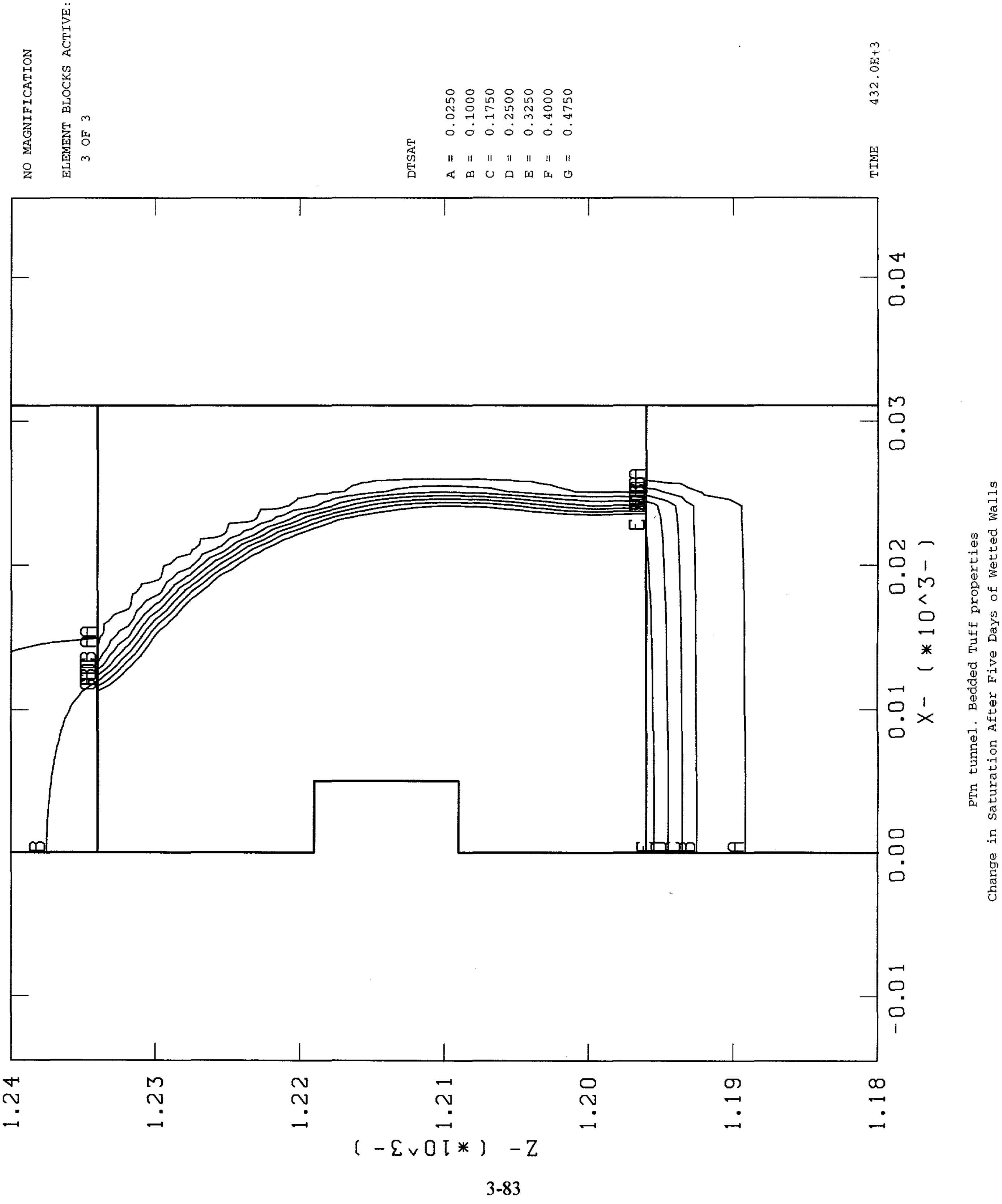

3.5 Conclusions

The calculations performed for ESF PA Analyses 3, 12, and 13 utilized a set of homogeneous material hydrological properties for the nonwelded Paintbrush Tuff unit (PTn) which has been used for many Yucca Mountain hydrological analyses. Due to the highly variable nature of the PTn described by recent sets of measured hydrological data, calculations from those analyses were repeated using several different sets of homogeneous properties for PTn.

Calculations performed to model the movement of surficially applied water (replicating ESF Analyses 3 and 12) showed little significant difference in the amounts of infiltrated water and the vertical and lateral spread of the wetting front, both at early (5 years) and late (10,000 years) times. These calculations simulated surficial water application in an area with a relatively deep alluvial overburden (9 m), and the large storage capacity and hydraulic conductivity of the alluvium is probably a more significant factor for water migration than the PTn. Future investigations, as required, into the sensitivity of analyses used to assess the effects of surficial water application on potential repository performance and on near-surface testing should evaluate other parameters such as the distribution of alluvial depths and material properties, the use of a different flow model such as the dual permeability model, and the effects of evapotranspiration at the surface.

On the other hand, calculations performed to model the movement of water applied underground in the PTn section of the North Ramp of the ESF (replicating ESF Analysis 13) displayed a strong sensitivity to bulk hydraulic conductivity for both the amount of infiltrated water and the vertical and lateral movement of the wetting front. Materials used to represent PTn similar to bedded tuff and highly fractured tuff were shown to be especially vulnerable to imbibing large amounts of water. Because of the large distance between the PTn section of tunnel and the potential repository horizon, and the expected system of vertical faults occurring between the two which should act as a barrier to lateral flow, there is no anticipated impact to waste isolation; however, the recommendation derived from ESF Analysis 13 cautioning about allowing the ponding of water in the PTn is reiterated.

4.0 Sensitivity of Evaluation of Water Movement to Heterogeneity of Material Properties

(Sobolik, Robey)

Previous ESF PA Analyses have assumed homogeneous hydraulic parameters (porosity, saturated hydraulic conductivity, van Genuchten parameters, etc.) within each stratigraphic unit (Sobolik and Fewell, 1992; Sobolik and Fewell, 1993; Dunn and Sobolik, 1993). The calculations performed for these analyses have used material property values first established by Klavetter and Peters (Peters et al., 1984; Klavetter and Peters, 1986). These PA analyses and additional analyses performed by other Yucca Mountain Project participants help to form a foundation of knowledge of the physical processes active at Yucca Mountain which may be tested by the use of new site material property data and new insight into the conceptual models used for the analyses.

New calculations have been performed to investigate the sensitivity of hydrologic PA analyses to heterogeneity of hydraulic parameters, and to assess the effect of this sensitivity on the recommendations provided by previous PA analyses. The heterogeneous material properties are based on measurements taken from core samples from several boreholes in and near Yucca Mountain. (See Appendix B for the borehole stratigraphy data used for this study.) Determination of stratigraphies and material hydrologic properties was based in part on the work done for TSPA-1993 (Schenker et al., 1995). The hydrology code NORIA-SP (Hopkins et al., 1991) was used, employing the equivalent continuum model, or ECM, for a two-dimensional, single-phase, isothermal flow. The discussion below describes how stratigraphies and material properties were obtained first by using geostatistical methods on a very fine mesh, then upscaling those values to a computational grid suitable for use with NORIA-SP. This chapter will conclude with a discussion of the numerical results obtained with NORIA-SP, the sensitivity of this type of PA calculation to the use of heterogeneous properties, and the implications of the results on previous recommendations made for the ESFDR.

4.1 Problem Definition

The problem which is used as the base problem for this study is the road watering problem Case #1 from ESF PA Analysis #12 (Sobolik and Fewell, 1993); this is the same problem evaluated by the calculations described in Section 3.3. This problem simulated surficially applied water on a road surface near the location of borehole UE25 a#1. The road surface was kept continuously saturated for five years in the calculations, with no allowance for evapotranspiration of the water from either the road surface or surrounding surface. The two-dimensional slice of mountain modeled in the original calculations was assumed to have several homogeneous, horizontal, parallel layers; these layers were defined as alluvium, TCw, PTn, TSw1, etc. as has been the usual practice for PA calculations for Yucca Mountain. The hydrologic properties used for the original calculations were those derived from measurements taken several years ago from boreholes USW G-4 and USW GU-3 (Klavetter and Peters, 1986; Peters et al., 1984). Of primary concern here are the values listed for PTn, as more recent studies indicate a great deal of variability in the hydrologic characteristics of this unit (e.g., Flint and Flint, 1990). For the new calculations performed for this study, three locations and orientations were chosen:

- UE25 a#1, N-S cross-section (nearly horizontal and parallel layers, much like the original calculations)
- UE25 a#1, E-W cross-section (exhibiting significant downdip)
- USW G-4, E-W cross-section (significant downdip, different location)

4.2 Development of the Geostatistical Grids

The procedure for producing geostatistical realizations based on borehole data is described in detail by Schenker et al. (1995) and was used for the recent TSPA-1993 effort (Wilson et al., 1994). Four codes were used which transform stratigraphic and porosity information from several boreholes into a series of two-dimensional realizations corresponding to each one of the three cases described above. The two geostatistical codes are based on those from the widely known geostatistical library GSLIB (Deutsch and Journel, 1992), while the other two codes are a pre-processor and post-processor.

The code STRAT transforms stratigraphical information from boreholes logs into three-dimensional coordinates assigning an indicator corresponding to a rock type to several points in vertical lines at the borehole locations. The thermal/mechanical units can be grouped into one of the three rock types: welded, nonwelded, or zeolitic. In addition, alluvium is also modeled. These numbers are used as input to the SISIMPDF program. Data from the following boreholes were used with the STRAT program to generate input to SISIMPDF (these data are included in Appendix B):

UE25 a#1 UE25 a#4 UE25 a#5 UE25 a#6 UE25 a#7
UE25 b#1 USW G-4 USW H-4 USW H-5 USW UZN-53
USW NRG-6 USW UZ-16 USW WT-2

The code SISIMPDF uses the information generated by STRAT and other user input information to generate a full two-dimensional grid with corresponding indicators in the plane provided by the user. For the three simulation cases described above, the following geostatistical grids are specified as input to these programs:

- For UE25 a#1, N-S cross-section, the geostatistical grid is 180 m wide with one vertical boundary located at the borehole, and ranges from 725.5 m to 1225.5 m elevation, with 1-m spacing both vertically and horizontally;
- For UE25 a#1, E-W cross-section, the geostatistical grid is 180 m wide centered at the borehole, and ranges from 725.5 m to 1225.5 m elevation, with 1-m spacing both vertically and horizontally;
- For USW G-4, E-W cross-section, the geostatistical grid is 180 m wide centered at the borehole, and ranges from 725.5 m to 1355.5 m elevation, with 1-m spacing both vertically and horizontally.

The code SGSIM creates a file of spatially correlated unconditional random numbers based on a normal distribution; these numbers correspond to the same user-generated two-dimensional grid as was specified by the user for SISIMPDF. Finally, the code CAT2POR uses output from SISIMPDF and converts the indicators to thermal/mechanical units. Then CAT2POR uses the output from SGSIM, and parameters for a probability distribution function (PDF) based on a beta distribution of porosity for each thermal/mechanical unit, to assign values of porosity to each point in the grid. The beta distribution parameters that were used for these calculations are described in Table 4.2-1. These beta distribution parameters have been derived from several sets of porosity measurements according to the techniques described in Schenker et al. (1995), and have been further developed in support of SNL's groundwater travel time (GWTT) studies. The statistical summary of the measured data used to derive the beta distribution parameters in Table 4.2-1 can be found in the SNL YMP Local Records Center in the records file kept for this analysis. Plots of the beta distributions along with their corresponding histograms are shown Figure C.1 in Appendix C.

Table 4.2-1: Beta Distribution Parameters for Porosity PDFs

(See Table A.1 for descriptions of the geologic unit designators)

unit	a	b	α	β
Alluvium	0.026	0.478	1.24503	3.14807
TCw	0.024	0.269	1.55742	6.67343
PTn	0.104	0.652	1.42557	1.05128
TSw	0.000	0.486	5.08268	15.2322
vitrophyre (TSbv)	0.014	0.148	-0.08034	0.34799
vitric (CHnv)	0.154	0.513	1.31958	0.79996
zeolitic (CHnz)	0.133	0.472	3.77375	3.04832

4.3 Upscaling of Geostatistical Properties to a Computational Grid

Geostatistical grids, adaptive grids, material property calculations, and (in most cases) NORIA-SP calculations were performed for the cases listed in Table 4.3-1; the cases differ by the seed used for the statistical calculations, the two-dimensional cross-section being modeled, and the set of material property distributions used for alluvium (previous ESF analyses versus 92% sand).

Table 4.3-1: Case Descriptors Used for Calculation Runs

Case descriptor	Cross-section	Seed value	Alluvium properties set	NORIA-SP run performed?
a1ews1	UE25 a#1, E-W	69069	ESF Analyses	Yes
a1ews2	UE25 a#1, E-W	70070	ESF Analyses	Yes
a1ews4	UE25 a#1, E-W	69069	92% Sand	Yes
a1nss1	UE25 a#1, N-S	69069	ESF Analyses	Yes
a1nss2	UE25 a#1, N-S	70070	ESF Analyses	Yes
a1nss3	UE25 a#1, N-S	71071	ESF Analyses	Yes
a1nss5	UE25 a#1, N-S	70070	92% Sand	Yes
g4ews1	USW G-4	69069	ESF Analyses	No

4.3.1 Generating Geostatistical Grids

Two computer programs were used which transform the geostatistical grids and their corresponding porosity fields into computational grids suitable to a hydrology code such as NORIA-SP and a corresponding set of matrix and fracture material properties for each finite element. The two codes described below are GAG, which generates adaptive grids, and UPSCALE, which converts geostatistically derived porosities and other matrix properties in the original fine grid to volumetrically-representative material properties for each of the adaptive grid elements.

The code GAG stands for "geostatistical adaptive grid," because it adapts the computational flow grid to minimize the heterogeneity of the geostatistical porosity field within each element of the flow grid. It uses input parameters chosen by the programmer to create a field of finite elements that model the geohydrological stratigraphy as estimated by the geostatistical grid generated by CAT2POR. The controlling input file contains calls to some other input files: data files defining the top, bottom, left, and right boundary locations; and the porosity output file from CAT2POR, which identifies a value for porosity and stratigraphic unit type for each geostatistical grid point. From this input, GAG creates a grid by defining elements containing primarily one stratigraphic unit as defined in the porosity output file as a result of minimizing heterogeneity. Three types of output files are generated by GAG: a debug file printing run parameters; a grid output file which prints out the x- and y-coordinates of the adaptive grid points and a connectivity matrix showing the points included in each individual grid element; and a file which includes for each geostatistical node the corresponding flow element.

4.3.2 Matrix Material Properties

Material properties were generated based on the unit and porosity data described below. In order to mimic Yucca Mountain as much as possible, the observed correlations in drill core data are used. Thus the proper scale on which to generate matrix material properties is on the fine-scaled geostatistics grid. The geostatistics grid is still a coarser scale than core scale, but the difference is much less than between the scale of the flow grid and core scale. Once the matrix material properties are generated for the geostatistics grid, then the matrix element properties are generated for the flow grid using the various scaling rules depending on the particular material property. Although the scaling rules are subject to considerable uncertainty, the potential for error is greatly reduced by minimizing heterogeneity through use of the adaptive grid generated by GAG. The methodology and borehole data used for obtaining material properties for these calculations is described in Schenker et al. (1995) and Robey (1994).

As described above, porosity fields corresponding to the geostatistical grids were calculated with the code CAT2POR based on beta distributions of borehole data. The PDF parameters for the beta distributions used to calculate porosity are listed in Table 4.2-1. The borehole data used to obtain the porosity PDFs are described in Appendix B.

The saturated hydraulic conductivities for each matrix element are assumed to be a function of matrix porosity. Core data are used to estimate a linear regression relationship between the two properties. From the core data (Schenker et al., 1995), saturated hydraulic connectivities have been split into the Calico Hills zeolitic unit and the rest of the hydrogeologic units (nonzeolitic).

Linear regression results for the saturated hydraulic conductivity (k_s) as a function of porosity (ϕ) are of the form

$$\ln k_s = c_0 + c_1 \phi. \tag{4-1}$$

The correlation coefficients are 81% and 31%, respectively. The data and linear regressions are shown in Figure C.2 in Appendix C. The errors in the predictions of ln k_s can then be calculated and fit with beta distributions of the form

$$p(x) = c\,(x-a)^{\alpha}(b-x)^{\beta}. \tag{4-2}$$

Equation 4-2 is the general form of the equation to assess prediction errors for all of the following linear regression fits used to characterize the several material properties. The values used for the linear regression and error correlations for saturated hydraulic conductivity are listed in Table 4.3-2. The values for the zeolitic Calico Hills (CHnz) and the nonzeolitic tuffs are obtained from core data. Practically no measured data correlating saturated hydraulic conductivity with porosity for alluvium at Yucca Mountain currently exist. Therefore, two sets of values were used for the linear regression curve for k_s for alluvium: those which produce a homogeneous value of 5×10^{-7} m/sec, the value that was used for the previous ESF analyses; and those which produce a homogeneous value of 2.65×10^{-4} m/sec, which corresponds to a soil with 92% sand (Campbell, 1985).

Table 4.3-2: Linear Regression Parameters for Saturated Hydraulic Conductivity

Unit	c_0	c_1	a	b	α	β	c
Alluvium, fit to previous ESF Analyses	-14.509 [$\ln(5\times10^{-7}$ m/s)]	0	0	0	1	1	
Alluvium, fit to sand	-8.2358 [$\ln(2.65\times10^{-4}$ m/s)]	0	0	0	1	1	
TCw	-26.999	25.272	-9.9849	8.8099	4.0328	3.4406	6.6688×10^{-9}
PTn	-26.999	25.272	-9.9849	8.8099	4.0328	3.4406	6.6688×10^{-9}
TSw	-26.999	25.272	-9.9849	8.8099	4.0328	3.4406	6.6688×10^{-9}
TSbv	-26.999	25.272	-9.9849	8.8099	4.0328	3.4406	6.6688×10^{-9}
CHnv	-26.999	25.272	-9.9849	8.8099	4.0328	3.4406	6.6688×10^{-9}
CHnz	-27.686	13.980	-3.7921	3.8129	0.61181	0.62062	0.033698

The incomplete gamma function is being used to describe the moisture retention curve (the manner in which the incomplete gamma function is used is described in Section 4.3.4). The underlying gamma function can then be interpreted as a pore size distribution. The incomplete gamma function is fitted to moisture retention data, where the fitting parameters are closely related to the average pore size and the standard deviation of the pore size. Figure C.3 shows the correlation of the average pore size with matrix porosity. The average pore size, ave(r), is correlated with matrix porosity (pore size is given in μm):

$$\ln \mathrm{ave}(r) = c_0 + c_1 \phi. \qquad (4\text{-}3)$$

The core data for obtaining the linear regression fits for the tuffs were split into three groups: welded, nonwelded, and zeolitic. Table 4.3-3 lists the linear regression parameters for calculating the average pore size. Similar linear regression parameters for calculating the average pore size for alluvium are described in the next section.

Table 4.3-3: Linear Regression Parameters for Average Pore Size

Unit	c_0	c_1	a	b	α	β	c
TCw	-3.7024	12.652	-3.1108	3.0848	2.6060	2.5759	9.5124×10^{-4}
PTn	-4.1786	8.1079	-3.3439	4.3601	0.63272	1.1289	0.16745
TSw	-3.7024	12.652	-3.1108	3.0848	2.6060	2.5759	9.5124×10^{-4}
TSbv	-3.7024	12.652	-3.1108	3.0848	2.6060	2.5759	9.5124×10^{-4}
CHnv	-4.1786	8.1079	-3.3439	4.3601	0.63272	1.1289	0.16745
CHnz	-7.7691	16.438	-1.1925	2.0297	0.15397	0.96408	0.20433

It is shown in Figure C.4 in Appendix C that the standard deviation of the pore size and the mean of the pore size distribution are strongly correlated. The linear regression equation takes the form of:

$$\ln \sigma(r) = c_0 + c_1 \ln \mathrm{ave}(r). \qquad (4\text{-}4)$$

Data for the tuffs is split into the three groups as above, although there is not a great deal of difference between the three. Table 4.3-4 lists the linear regression parameters for the standard deviation of pore size.

Table 4.3-4: Linear Regression Parameters for Standard Deviation of the Pore Size

Unit	c_0	c_1	a	b	α	β	c
TCw	0.41983	1.0537	-0.52586	0.39342	1.5141	0.88087	10.444
PTn	0.21855	1.1057	-3.3098	0.81609	3.6835	0.15479	0.0068402
TSw	0.41983	1.0537	-0.52586	0.39342	1.5141	0.88087	10.444
TSbv	0.41983	1.0537	-0.52586	0.39342	1.5141	0.88087	10.444
CHnv	0.21855	1.1057	-3.3098	0.81609	3.6835	0.15479	0.0068402
CHnz	0.80519	1.1041	-0.20075	0.19750	0.56834	0.54297	19.622

Little data has been collected on matrix unsaturated hydraulic conductivity to date. The familiar Brooks-Corey (1964) and van Genuchten (1980) models are commonly used for representing the moisture retention curve; these models relate both saturation and relative conductivity to capillary pressure. For the incomplete gamma function used as the moisture retention curve for this study, the Brooks-Corey formula is used to obtain the relative conductivity curves. Klavetter and Peters (1986) describe a method for obtaining the Brooks-Corey constant, ε, which is adopted here. The Brooks-Corey constant is estimated based on the pore size distribution index λ_r:

$$\varepsilon = (2+3\lambda_r)/\lambda_r. \qquad (4\text{-}5)$$

Note that ε varies between 3 and infinity. The Brooks-Corey constants were calculated using this procedure from the incomplete gamma functions fitted to the moisture retention data. Figures C.5 and C.6 plot ε versus ave(r) and $\sigma(r)$, respectively; Figures C.7 and C.8 show similar plots for λ_r. Linear regressions were fitted for ε versus $\sigma(r)$ for welded, nonwelded, and zeolitic categories of tuff in the following equation form:

$$\ln \varepsilon = c_0 + c_1 \ln \sigma(r). \tag{4-6}$$

Table 4.3-5 lists the linear regression parameters for the matrix Brooks-Corey constant.

Table 4.3-5: Linear Regression Parameters for Brooks-Corey Constant

Unit	c_0	c_1	a	b	α	β	c
TCw	2.1005	0.084913	-0.54445	0.45466	2.0503	1.5472	21.358
PTn	2.0224	0.13599	-0.58836	0.88376	0.31874	0.98083	1.2418
TSw	2.1005	0.084913	-0.54445	0.45466	2.0503	1.5472	21.358
TSbv	2.1005	0.084913	-0.54445	0.45466	2.0503	1.5472	21.358
CHnv	2.0224	0.13599	-0.58836	0.88376	0.31874	0.98083	1.2418
CHnz	2.4865	0.13208	-0.27487	0.25271	1.0457	0.88072	36.492

4.3.3 Alluvium Pore Size Distribution Properties

In the previous section, it was stated that the hydrologic properties of alluvium would be modeled with two sets of values: one set was based on those used for the previous ESF analyses; and the second set was based on those which correspond to a soil with 92% sand (Campbell, 1985). An incomplete gamma function was fit as closely as possible to the van Genuchten moisture retention curve used for previous ESF analyses (van Genuchten parameters α_{VG}=0.423 m^{-1}, β_{VG}=2.06). The assumption used here for alluvium is that the average pore size is constant with respect to porosity, which is certainly not a good assumption, but does make it easier to set the moisture retention curve to be roughly equivalent to the van Genuchten curve used for previous analyses.

Figures 4.3-1 and 4.3-2 show saturation versus suction pressure curves assuming different sets of values of ave(r) and σ for alluvium and 92% sand, respectively. The three Brooks-Corey curves shown for alluvium in Figure 4.3-1 are different by factors of ten in ave(r) and σ, so the three curves are identical except for being shifted left to right on the graph. The values for ave(r) and σ of 5 μm and 5.5 μm respectively (Alluvium Case 2) produce a curve similar to the van Genuchten curve used for alluvium in previous ESF analyses; the primary difference between the curves is the assumption of a residual saturation of 0.3 for the van Genuchten curve, with no such assumption for the Brooks-Corey curve. The values for ave(r) and σ of 700 μm and 4000 μm respectively correspond to a soil with 92% sand (Campbell, 1985); for the sake of comparison, values for ave(r) and σ of 0.7 μm and 4 μm were also considered. The curves in Figure 4.3-2 for 92% sand also show the similar left-to-right shifting based on factors of ten as was shown for the alluvium cases in Figure 4.3-1. Note the large range of suction pressure values over which a 20% change in saturation is predicted to occur in the 92% sand. The corresponding linear regression parameters for Figures 4.3-1 and 4.3-2 are listed in Tables 4.3-6 and 4.3-7, respectively.

Figure 4.3-1: Comparison of Saturation versus Suction Pressure for Different Moisture Retention Curves for Alluvium Using Incomplete Gamma Function

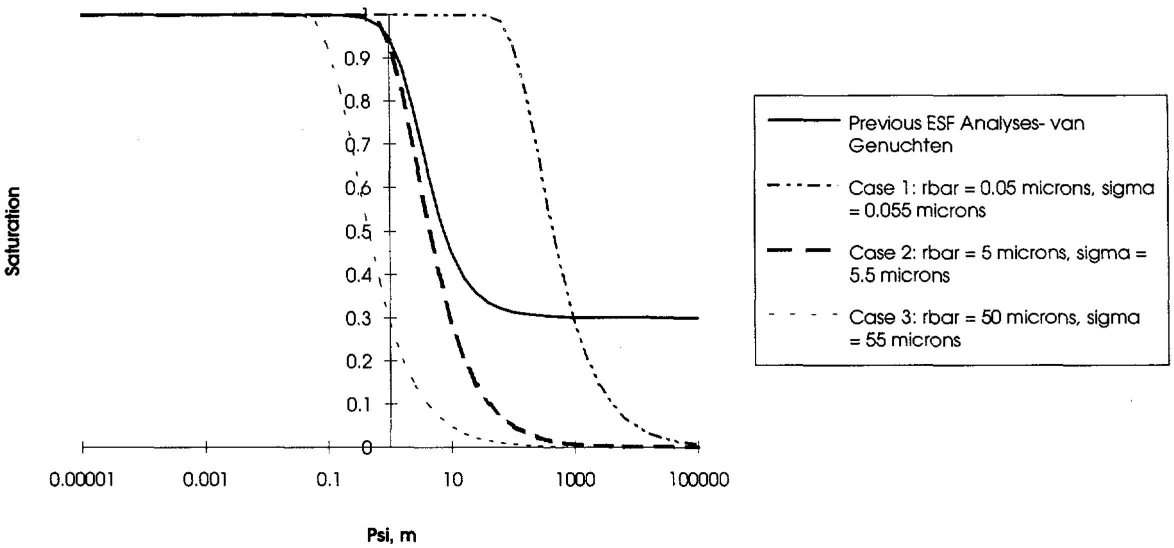

Figure 4.3-2: Comparison of Saturation versus Suction Pressure for Different Moisture Retention Curves for 92% Sand Using Incomplete Gamma Function

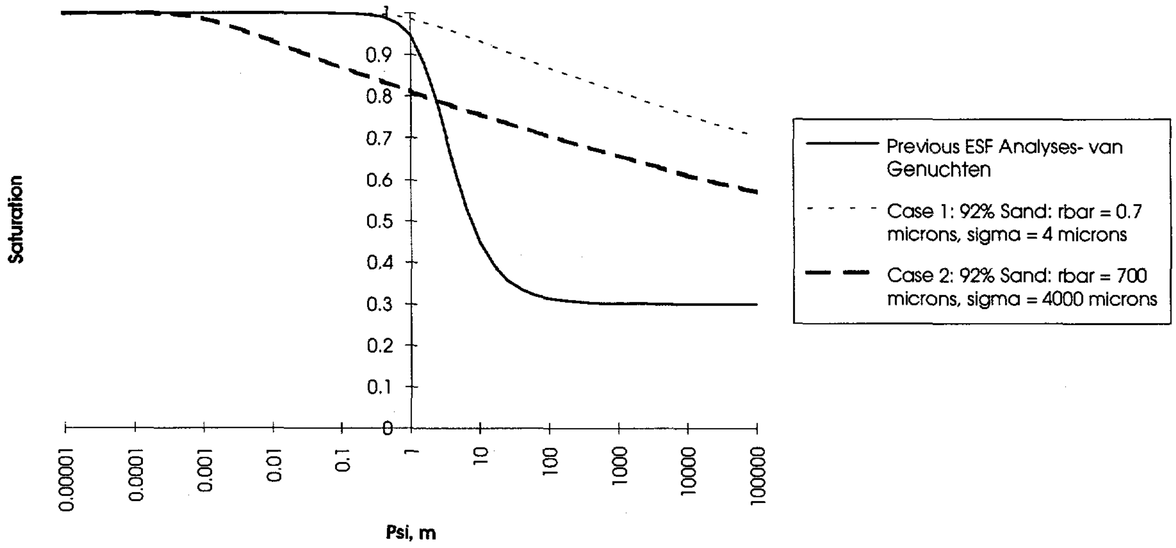

Table 4.3-6: Linear Regression Parameters for Average Pore Size for Alluvium

Unit	c_0	c_1	a	b	α	β	c
Alluvium, Case 1	-2.99573 [ln(0.05 μm)]	0	0	0	1	1	
Alluvium, Case 2	1.60944 [ln(5 μm)]	0	0	0	1	1	
Alluvium, Case 3	3.91202 [ln(50 μm)]	0	0	0	1	1	
Alluvium, 92% Sand, Case 1	-0.35668 [ln(0.7 μm)]	0	0	0	1	1	
Alluvium, 92% Sand, Case 2	6.55108 [ln(700 μm)]	0	0	0	1	1	

Table 4.3-7: Linear Regression Parameters for Standard Deviation of the Pore Size for Alluvium

Unit	c_0	c_1	a	b	α	β	c
Alluvium, Case 1	-2.90042 [ln(0.055 μm)]	0	0	0	1	1	
Alluvium, Case 2	1.70475 [ln(5.5 μm)]	0	0	0	1	1	
Alluvium, Case 3	4.00733 [ln(55 μm)]	0	0	0	1	1	
Alluvium, 92% Sand, Case 1	1.38629 [ln(4.0 μm)]	0	0	0	1	1	
Alluvium, 92% Sand, Case 2	8.29405 [ln(4000 μm)]	0	0	0	1	1	

Because the Brooks-Corey model assumes relative hydraulic conductivity to be a function only of the saturation and the Brooks-Corey constant ε, the relationship between relative hydraulic conductivity and saturation is independent of pore size parameters (as illustrated in Figure 4.3-3). The value of ε for alluvium used to replicate the previous ESF analyses was derived from the van Genuchten parameter $\beta_{VG}=2.06$. The pore size distribution $\lambda_r=\beta_{VG}-1$, or 1.06; this value results in an ε of 4.8868 ($\ln \varepsilon = 1.5865$). For simulating 92% sand (Campbell, 1985), $\lambda_r=1.996$, resulting in an $\varepsilon=4.002$. The corresponding linear regression parameters for ε are listed in Table 4.3-8.

Table 4.3-8: Linear Regression Parameters for Brooks-Corey Constant for Alluvium

Unit	c_0	c_1	a	b	α	β	c
Alluvium, Cases 1, 2, and 3	1.5865 [ln(4.8868)]	0	0	0	1	1	
Alluvium, 92% Sand Cases 1 and 2	1.3868 [ln(4.002)]	0	0	0	1	1	

Figure 4.3-3: Relative Conductivity Curves for Different Averages and Standard Deviation of Pore Sizes in Alluvium

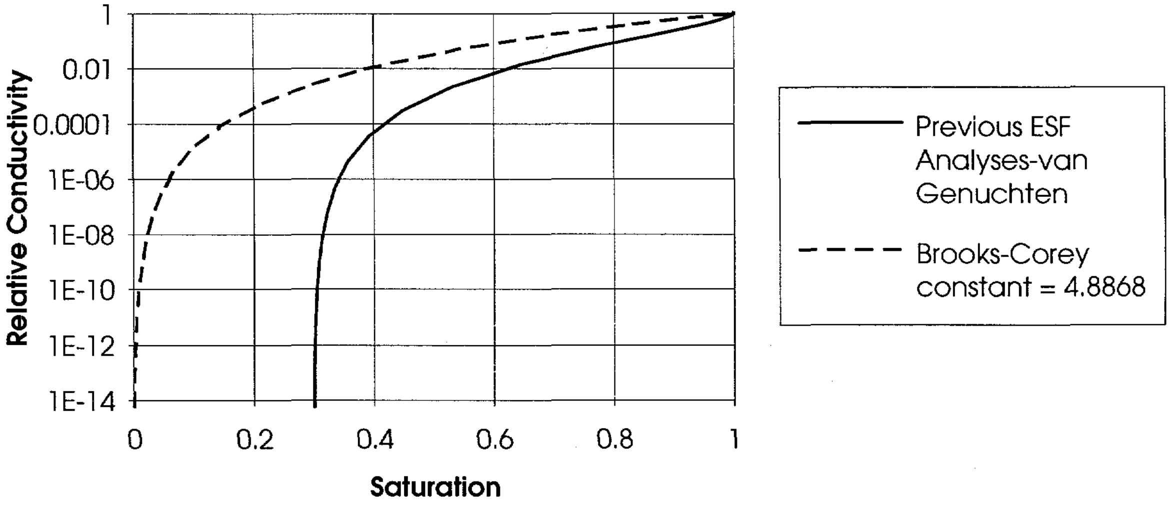

Steady-state calculations were performed with NORIA-SP to estimate the in situ saturation levels for the three alluvium and two 92%-sand-as-alluvium cases. These steady-state calculations provided a glimpse into the sensitivity of flow calculations to parameters chosen to model unsaturated flow. The steady-state calculations for the alluvium cases used the tuff properties corresponding to Seed 1 as described in Section 4.4.1; for the 92% sand cases, tuff properties corresponding to Seed 5 in the same section were used.

The steady-state calculations for Case 1 predicted the in situ saturation levels in the alluvium to be in the 50%-60% range. However, the corresponding values for ave(r) and σ, 0.05 and 0.055 μm, are much smaller than would be expected for alluvial soils. Steady-state calculations using the parameters for Alluvium Case 2 (which, according to Figure 4.3-1, seem to most accurately match the original van Genuchten parameters) predicted in situ saturations in alluvium from a maximum of about 5% near the surface to under 1% at the alluvium-TCw interface (One computational cell identified as an alluvium cell and located next to TCw had an in situ saturation of 24% at one node; this was due to the ave(r) and σ calculated for this cell from the volumetrically-averaged porosity produced from the GAG program). The saturations below the alluvium-TCw interface were nearly identical for Alluvium Cases 1 and 2. When attempts were made to calculate the flow induced by the road watering problem using the Case 2 in situ conditions as initial conditions, NORIA-SP produced nearly real-time calculations (i.e., it took about two-thirds of a day of CPU time to proceed to a simulation time of about three days). Computational instability due to a large pressure gradient seemed to be the cause of the slow run time; an unrealistically large capillary pressure was calculated for one of the side nodes in an alluvium element located next to TCw (the cell described above parenthetically). For the Alluvium Case 3, a maximum in situ saturation in alluvium of 2% was predicted, and the road water problem did not complete one day of simulation time after approximately twenty-four hours of CPU time. Similar results were encountered with the 92% sand calculations, with the results for Seed 1 encountering less computational problems and expected ranges of values for in situ saturation. For reasons to be discussed in greater detail in Section 4.5, it was decided to perform flow calculations using the pore size parameters of Alluvium Case 1 and 92% Sand Case 1 only. The calculations for Alluvium Case 1 are identified as those for Seed 1 in Section 4.4.1, and those for 92% Sand Case 1 are identified as Seed 5 in the same section.

4.3.4 Moisture Retention and Relative Conductivity Curves

The incomplete gamma function is

$$F(r)=\int_0^r f(x)dx=\frac{\Gamma(a,\lambda r)}{\Gamma(a)}=\frac{\int_0^{\lambda r} e^{-u}u^{a-1}du}{\Gamma(a)}, \tag{4-7}$$

where a and λ are the two gamma parameters, and r is the pore size diameter. It is assumed that all pores of diameter greater than r are desaturated (assuming no trapping of moisture); therefore, the incomplete gamma function is the moisture retention curve corresponding to a particular gamma function. One of the advantages of the gamma function is the ease with which it is possible to switch back and forth between the pore size distribution and moisture retention curve. Another advantage is that because the two gamma parameters are functions of the mean, ave(r), and the standard deviation, σ(r), given by

$$a=\left[\frac{\mathrm{ave(r)}}{\sigma(r)}\right]^2, \tag{4-8}$$

$$\lambda=\frac{\mathrm{ave(r)}}{\sigma(r)^2}, \tag{4-9}$$

fitting the incomplete gamma function to sparse data is much better posed than fitting the van Genuchten function.

The incomplete gamma function can also be expressed in terms of pressure, ψ, using

$$\psi=\frac{c}{r}. \tag{4-10}$$

The constant c is given by

$$c=\frac{2\gamma\cos\theta}{\rho g}=1.4185\times10^{-5}\,\mathrm{m}^2 \tag{4-11}$$

where γ=0.072 N/m is the surface tension of water, $\theta = 15°$ is the contact angle of water (Klavetter and Peters, 1986), ρ=1000 kg/m^3 is the density of water, and g=9.806 N/kg is the gravitational constant. Equation (4-10) is substituted into the incomplete gamma function, Equation 4-7, to transform the solution for saturation s (i.e., the solution of Equation 4-7) into a function of capillary pressure. The corresponding relative conductivity function uses the computed saturation and the Brooks-Corey constant:

$$k_r = \frac{k(s)}{k_s} = s^{\varepsilon} = (F(r))^{\varepsilon}. \qquad (4\text{-}12)$$

Due to the inverse relationship between ψ and r, the incomplete gamma function is equal to 1 at a capillary pressure of 0 and approaches 0 as the magnitude of the capillary pressure increases.

4.3.5 Fracture Properties

Measured data for fracture properties is based on fracture aperture and spacing assumptions used for fracture conductivity estimations for calculations of GWTT at Yucca Mountain; these calculations were performed as a test case for the INTRAVAL project (Robey, 1994). Table 4.3-9 lists beta distribution parameters for fracture porosity; these values are taken from Table 7-19 of the report on TSPA-1993 (Wilson et al., 1994). Table 4.3-10 lists the beta distribution parameters for fracture saturated conductivity (Robey, 1994). The beta distribution curves for alluvium are set so that near-zero values are calculated for fracture porosity and conductivity. The average pore size, standard deviation of pore size, and Brooks-Corey constant for all fractures were 178., 178., and 5.08, respectively (Robey, 1994).

Table 4.3-9: Beta Distribution Parameters for Fracture Porosity

Unit	min	max	α	β
Alluvium	-12.01	-12.	1.	1.
TCw	-4.179	-1.966	1.815	1.805
PTn	-4.825	-2.354	1.982	2.189
TSw	-4.301	-1.371	1.457	2.072
TSbv	-4.367	-1.427	1.483	2.072
CHnv	-4.834	-1.860	1.594	1.932
CHnz	-5.073	-2.174	1.608	2.001

Table 4.3-10: Beta Distribution Parameters for Fracture Hydraulic Conductivity

Unit	min	max	α	β
Alluvium	-12.01	-12.	1.	1.
TCw	-6.6364	-3.9355	8.6953	3.1302
PTn	-6.7506	-3.6273	1.0015	1.2136
TSw	-5.3193	-3.9355	0.4656	1.0499
TSbv	-5.3193	-3.9355	0.1389	0.5930
CHnv	-6.7506	-3.6273	0.5717	0.7382
CHnz	-7.3599	-4.8697	0.8862	0.4127

The code UPSCALE uses the output files from CAT2POR and GAG to assign material properties to each individual element. The material properties (saturated hydraulic conductivity, moisture retention curves, Brooks-Corey constants, etc. for matrix and fractures) are all defined as explicit or implicit functions of porosity as described above. The parameters used to define the distribution curves for the various material properties are input to UPSCALE through a user input file. Two output files are produced: one which includes the material properties for each element; and one which contains the grid point and element specifications in a format to be used for the NORIA-SP input file. GAG and UPSCALE were run for each of the cases listed in Table 4.3-1.

4.4 Results

Geostatistical grids, corresponding porosity fields, and upscaled computational grids were calculated for the eight cases described in Table 4.3-1. Of these cases, seven sets of numerical experiments using NORIA-SP were performed. The computational grid calculated for the USW G-4 case had some consistency problems due to a lack of complete information on nearby alluvial depths, and thus was not used for NORIA-SP runs.

4.4.1 UE25 a#1, North-South Orientation Cases

This first section contains a discussion of the results obtained for the four cases simulating a north-south transect through the borehole UE25 a#1 (most similar to the problem in Sobolik and Fewell, 1993). These cases are referred to as Seed 1, Seed 2, and Seed 3, which used three different seed numbers for calculating the geostatistical grids and the alluvial properties for hydraulic conductivity fit to those in Sobolik and Fewell (1993), and Seed 5, which actually uses the same geostatistical and computational grids as Seed 2 but uses properties for hydraulic conductivity in the alluvium approximating a soil made of 92% sand.

The computational grids used for Seeds 1, 2, 3, and 5, are displayed in Figures 4.4-1 through 4.4-4. For these north-south cases, the computational grids that were used are 90 m wide. The stratigraphic units are, in descending order, alluvium, welded Tiva Canyon (TCw), nonwelded Paintbrush Tuff (PTn), the welded Topopah Spring (TSw), the Topopah Spring vitrophyre (TSbv), the vitric Calico Hills (CHnv), and the zeolitic Calico Hills (CHnz). Note that the grids in Figures 4.4-2 and 4.4-4 are identical. All four grids have 25 columns and 60 rows of elements. The layers are primarily horizontal and of constant thickness except for the alluvium and TCw. The thickness of alluvium ranges from 5 to 40 meters. The left-to-right dip of the alluvium-TCw interface is due to the geostatistical representation of the borehole data used as input, but the surface of the alluvium is set to be horizontal in the boundary definition data files used with GAG, and thus might not represent the true surface boundary. The four grids model the boundaries between stratigraphic units very similarly.

Steady-state calculations were performed with NORIA-SP to estimate the in situ saturation levels for the four cases. An infiltration rate of 0.01 mm/yr was assumed. Figures 4.4-5 through 4.4-8 show the in situ saturation conditions for Seeds 1, 2, 3, and 5, respectively. (The white areas in these plots are saturation levels less than 50%.) For Seeds 1, 2, and 3, the saturation levels in the alluvium are in the 50%-60% range, and in TCw they are primarily in the 60%-70% range. While the conditions throughout the grids for Seeds 1 and 2 are quite similar, Seed 3 exhibits a much larger region of 50%-60% saturation in the TSw and a large region in CHnz of less than 90% saturation. The saturation level for Seed 5 in the alluvium layer is in the 80%-90% range; however, a comparison with Seed 2 shows that the computed saturation fields below the alluvium-TCw interface are nearly identical. One point needs to be stressed about these steady-state calculations. For previous calculations using homogeneous properties, NORIA-SP was run to a simulation time of 10^{19} seconds, by which time the time steps were the same order of magnitude as the accumulated time and changes in pressure from one time step to the next were very small. As a matter of standard procedure, steady-state calculations were performed for this study in the same manner. Closer examination of the results of the steady-state calculations some time after all the calculations for this study were completed indicated that some might not have

Figure 4.4-1: Computational Grid, N-S Orientation, Seed 1

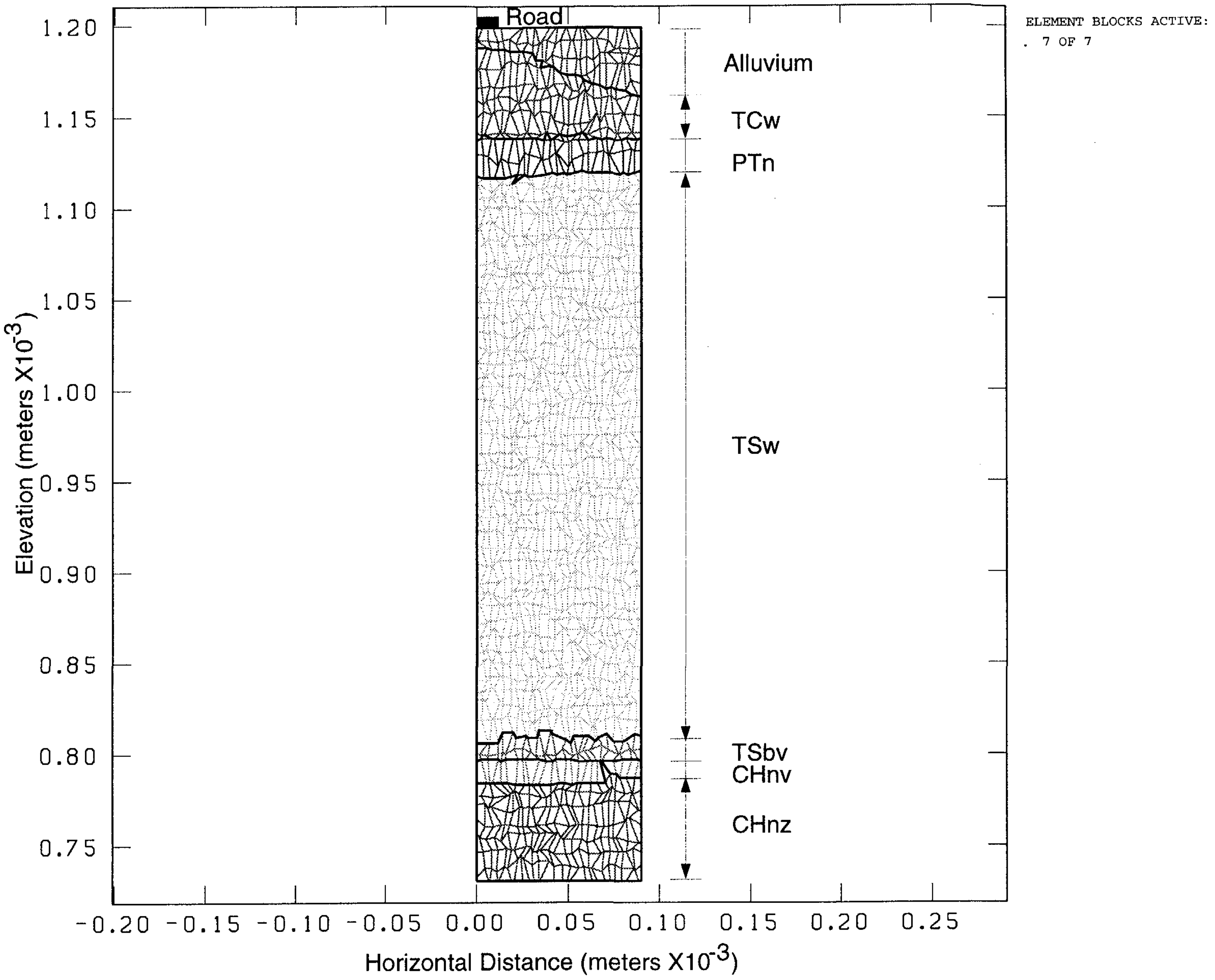

Saturation Near UE25 a#1 Resulting from Road Watering
N-S Transect, Seed #1, Alluvium Conductivity per ESF Analyses
Computational Grid

Figure 4.4-2: Computational Grid, N-S Orientation, Seed 2

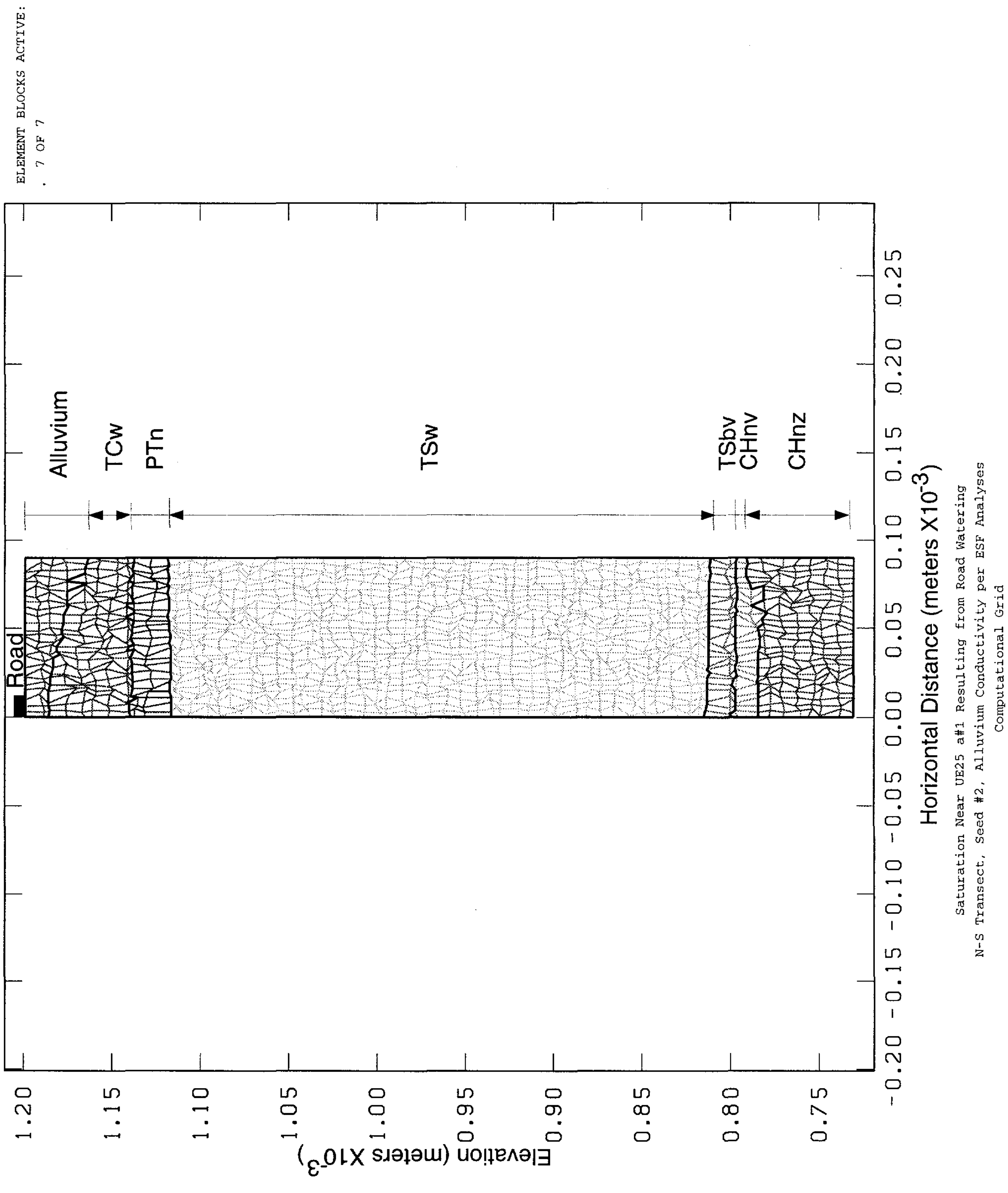

Figure 4.4-3: Computational Grid, N-S Orientation, Seed 3

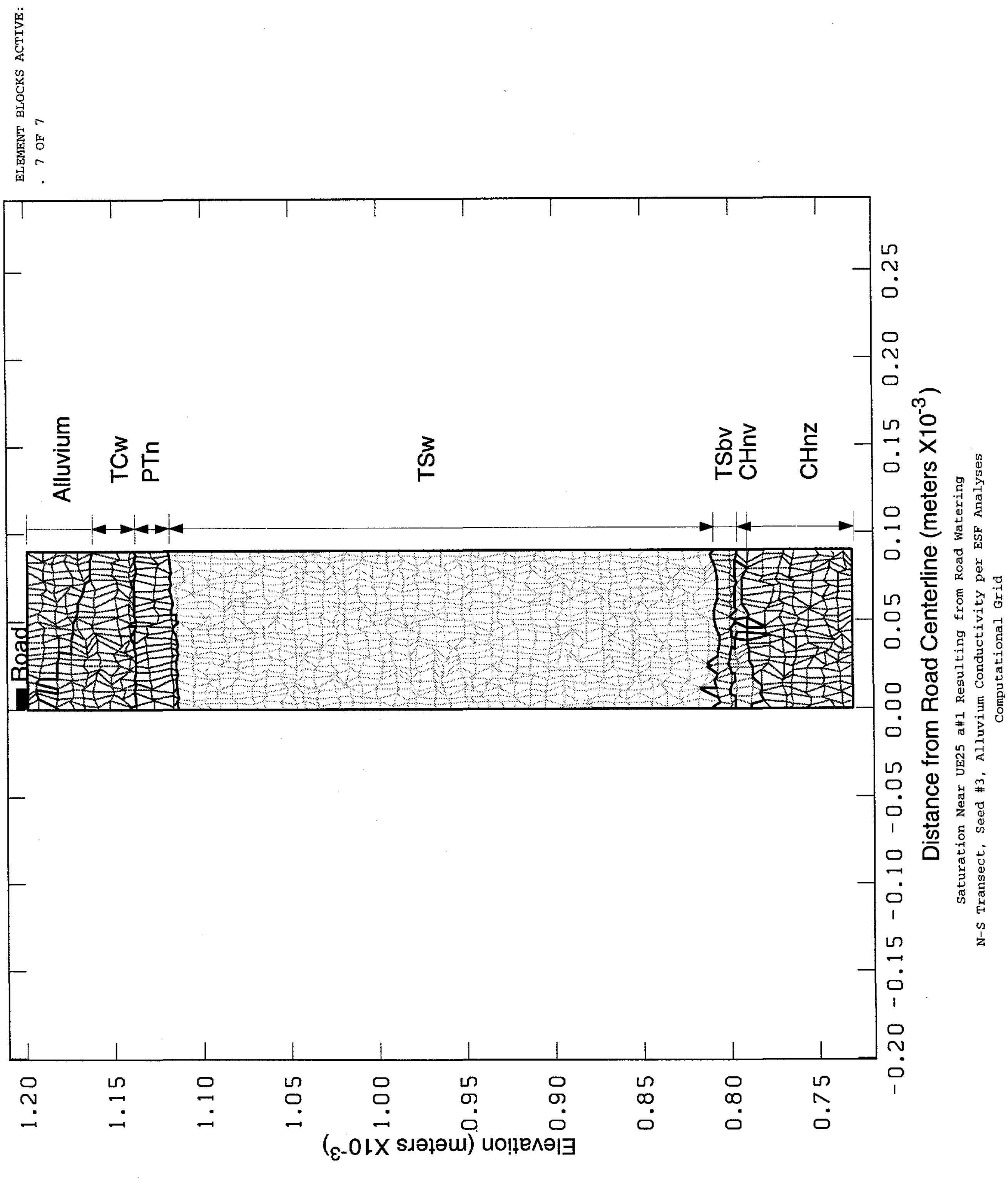

Figure 4.4-4: Computational Grid, N-S Orientation, Seed 5

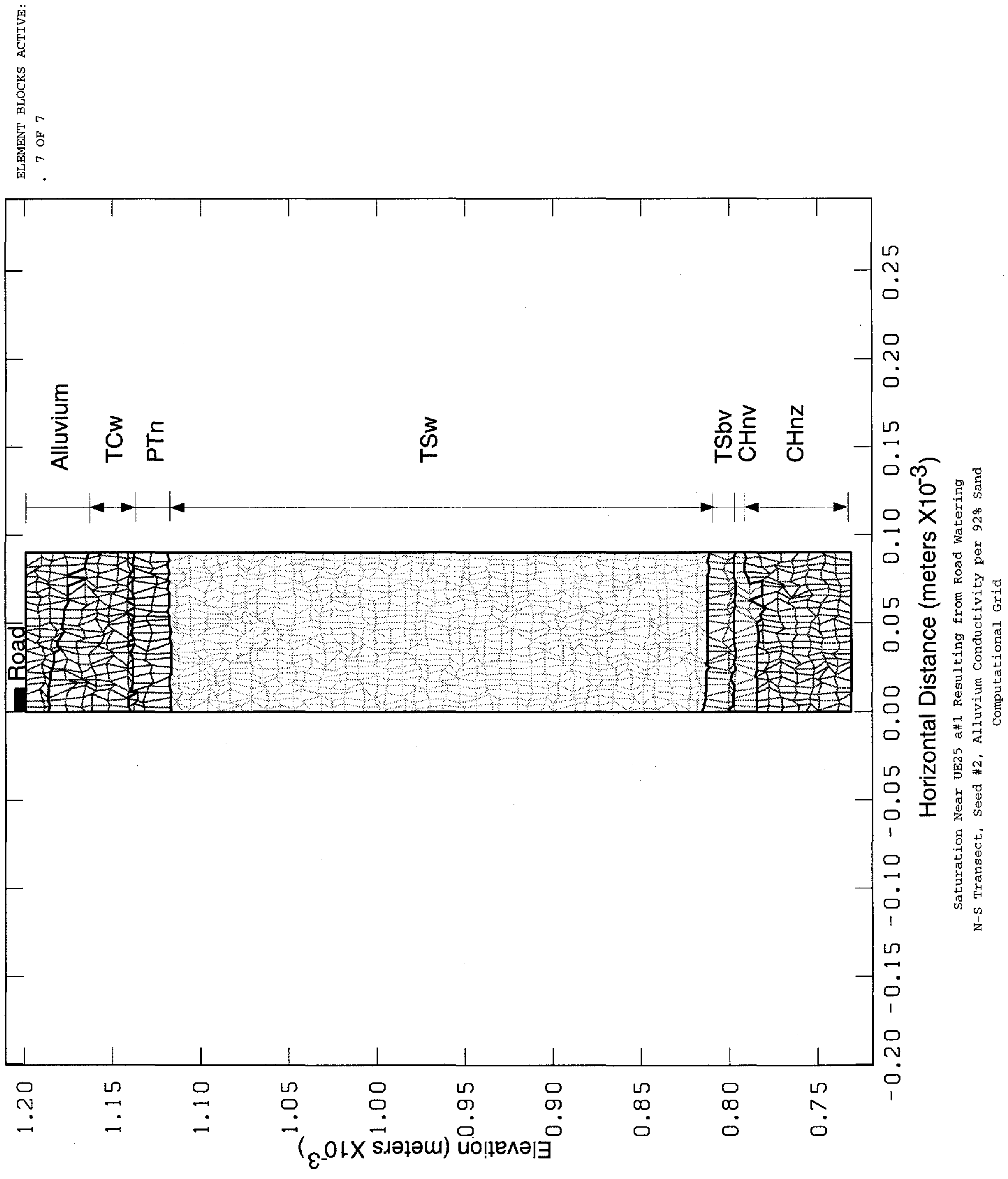

Saturation Near UE25 a#1 Resulting from Road Watering
N-S Transect, Seed #2, Alluvium Conductivity per 92% Sand
Computational Grid

Figure 4.4-5: In Situ Saturation, N-S Orientation, Seed 1

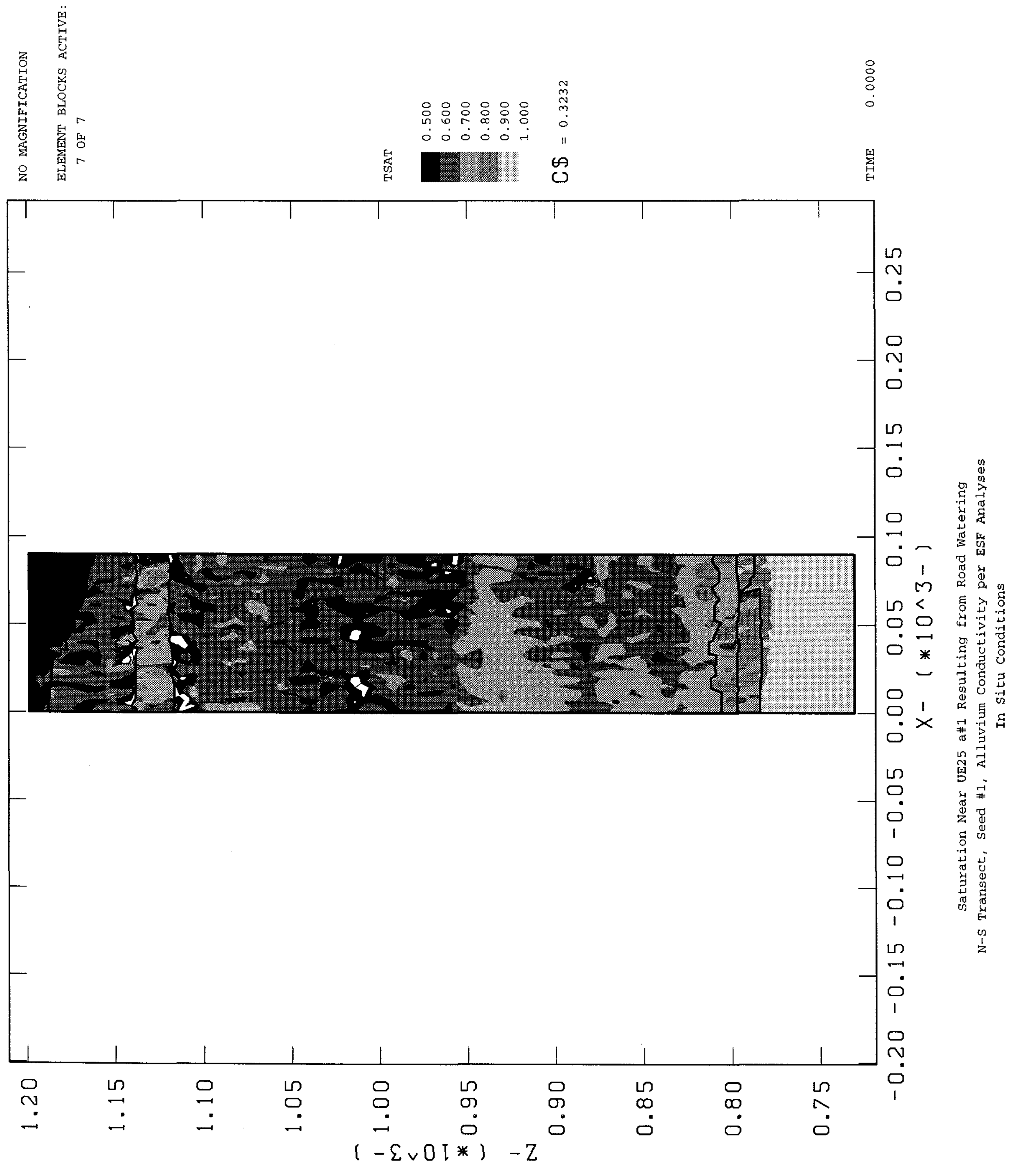

Figure 4.4-6: In Situ Saturation, N-S Orientation, Seed 2

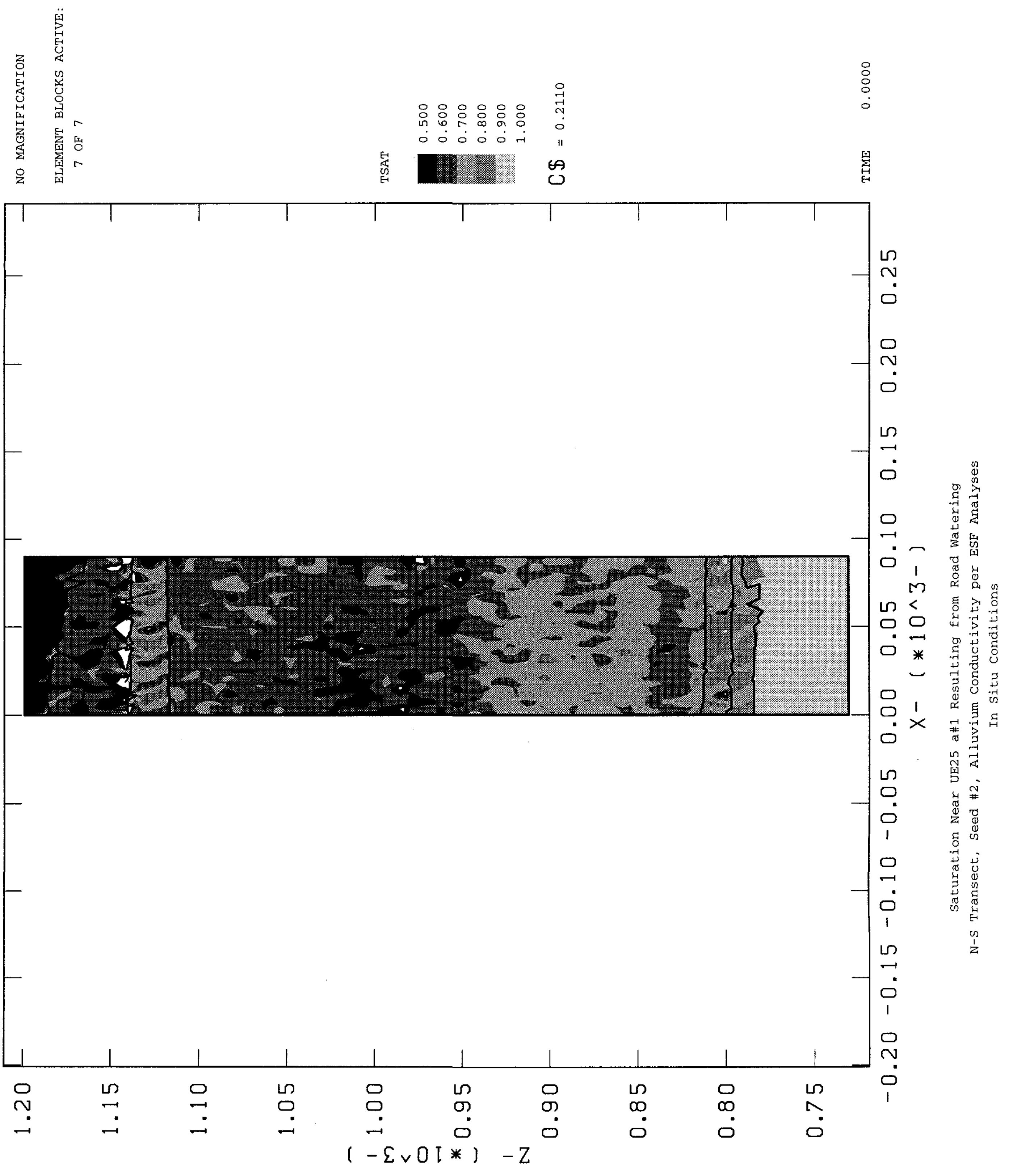

Figure 4.4-7: In Situ Saturation, N-S Orientation, Seed 3

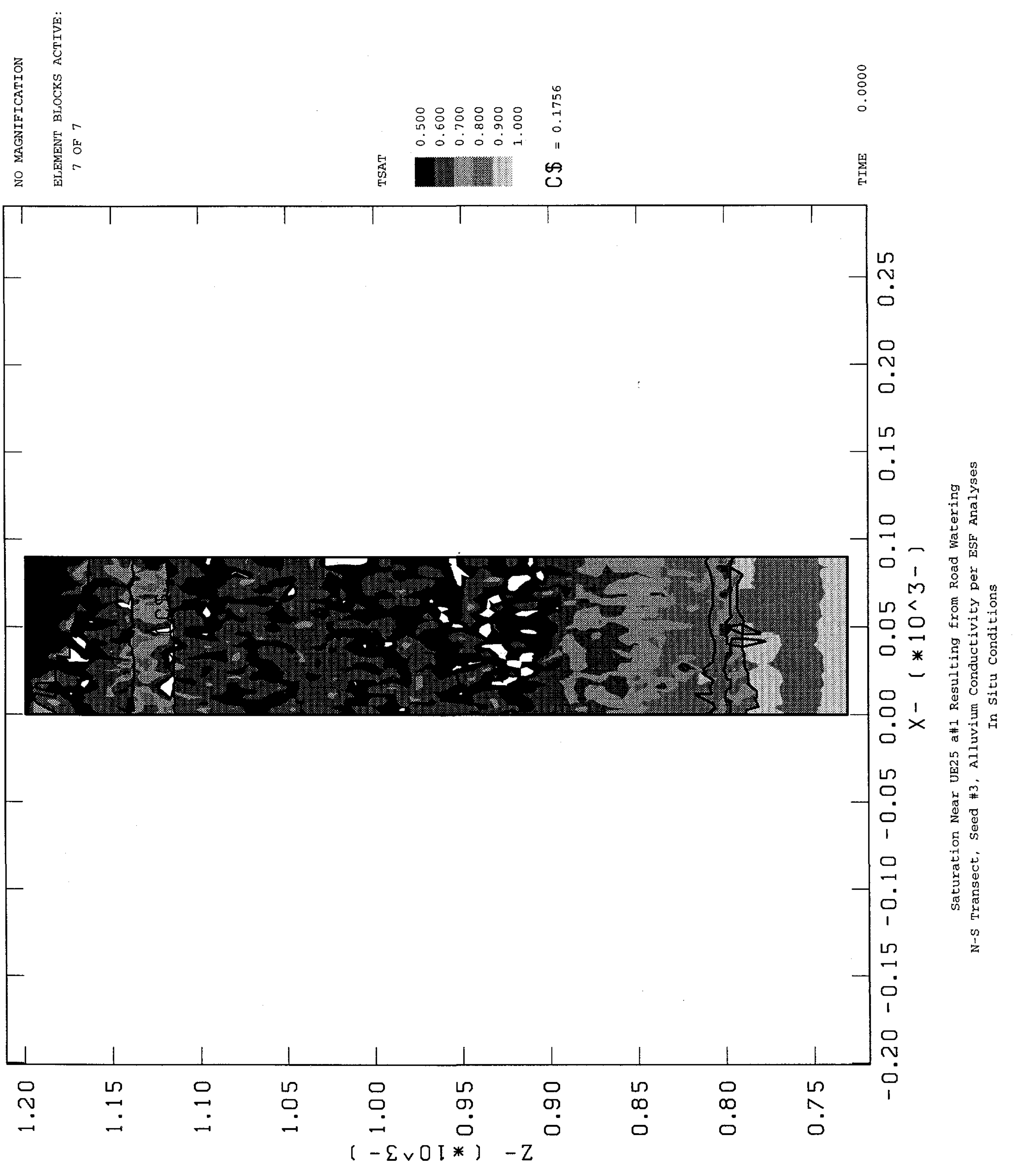

Saturation Near UE25 a#1 Resulting from Road Watering
N-S Transect, Seed #3, Alluvium Conductivity per ESF Analyses
In Situ Conditions

Figure 4.4-8: In Situ Saturation, N-S Orientation, Seed 5

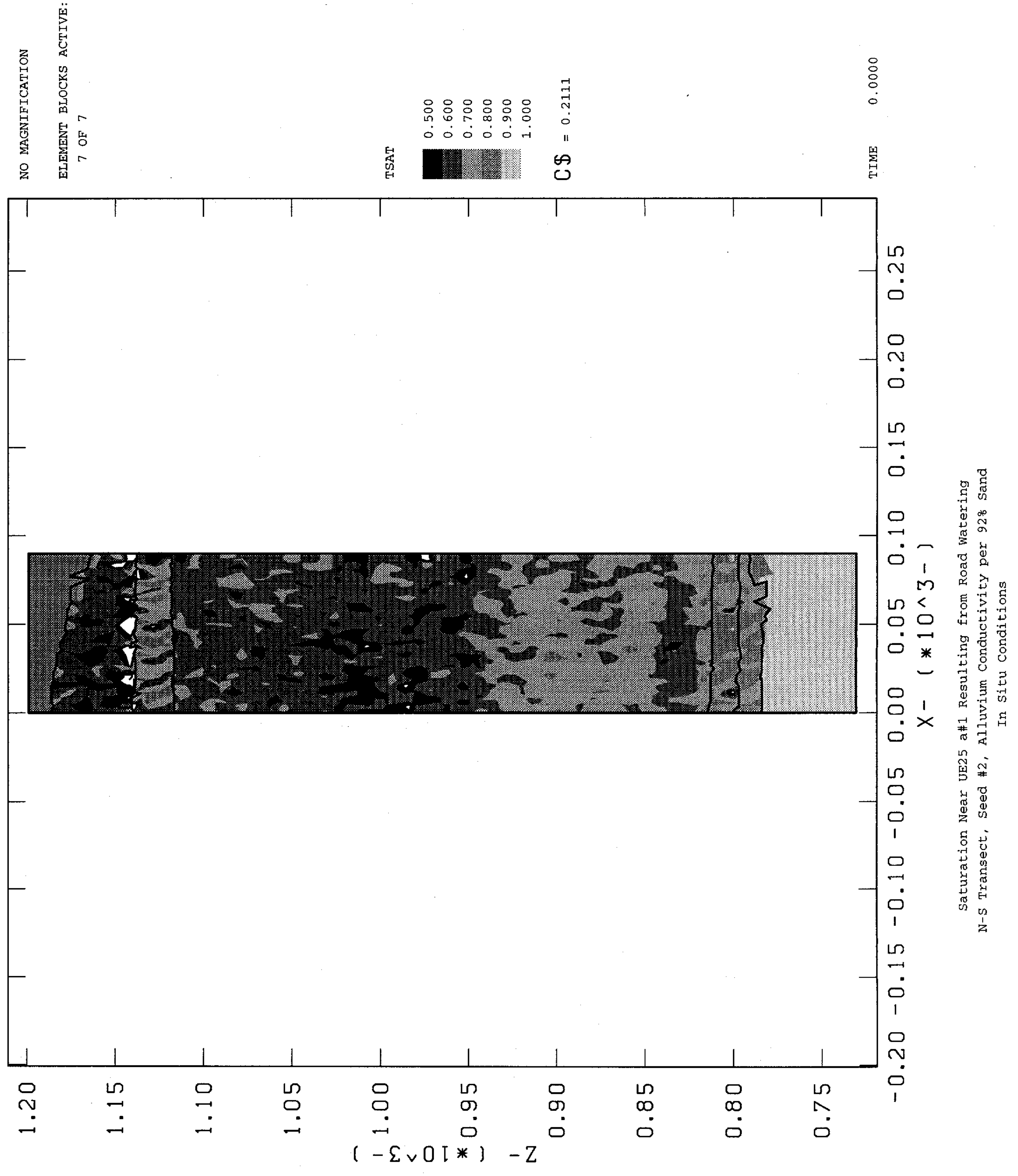

reached a steady-state condition by the allotted time, although they seemed to be close. It is unclear at this point how an incomplete steady-state solution affected the results described below.

Figure 4.4-9(a) shows the in situ saturation conditions calculated for Seed 1 in the alluvium, TCw, PTn, and upper TSw layers. Figures 4.4-9 (b), (c), and (d) show the saturation after road watering has been in effect for 6 months, 1 year, and 5 years. The change between (a) and (b) is dramatic, as the entire alluvium changes from 50%-60% saturation to 80%-90% saturation. Figure 4.4-9 (c) shows the lower part of the alluvium filling up with water to over 90% saturation. Interestingly, there is very little difference between (c) and (d), even though the times they represent are four years apart. In fact, nearly all the water that gets added to the simulated mountain due to road watering infiltrates during the first six months; Table 4.4-1 shows the time progression of water addition. The value of 157.2 m^3 after five years of surficial watering can be compared to the corresponding value obtained for Case #1 of ESF Analysis #12 (Sobolik and Fewell, 1993), 142.8 m^3. Additional comparisons can be made to the values obtained for the PTn sensitivity calculations in Table 3.3-1. Note that the values calculated using the Seed 1 scenario predict more infiltrated water than any of the cases described in Section 3.3 of this report.

Table 4.4-1: Amount of Infiltrated Water for Seed 1 Calculations

Time, years	Amount of infiltrated water, m^3
0	0
0.5	141.3
1	154.0
5	157.2

Many of the results of the calculations are best presented in terms of the change of saturation from in situ conditions due to the movement of water through the rock. This change in saturation, or **Δsat**, indicates the extent of movement of the infiltrated water. Figures 4.4-10 (a) through (c) show Δsat for 6 months, 1 year, and 5 years, respectively, for Seed 1. The difference between Figures 4.4-10 (b) and (c) of the progression of the contour showing Δsat=2% indicates little movement of the water during this time. After five years, the road watering is stopped and an infiltration rate of 0.01 mm/yr is established over the entire surface. Figures 4.4-11 (a) through (d) plot Δsat to represent water movement at 5, 10, 100, and 1,000 years, and Figure 4.4-12 plots the same at 10,000 years. One observation is that water tends to drain quickly from TCw to TSw through the PTn, but only at certain locations; some locations in PTn remain unwetted, while others absorb a small amount of water and act as a path for water flow to TSw. A comparison of Figure 4.4-11 (d) to Figure 4.4-9 indicates that the locations within PTn that tend to hold additional water are those where the in situ saturation was predicted to be less than 70%.

Figure 4.4-9: Saturation, 5-Year Road Watering Period, N-S Orientation, Seed 1

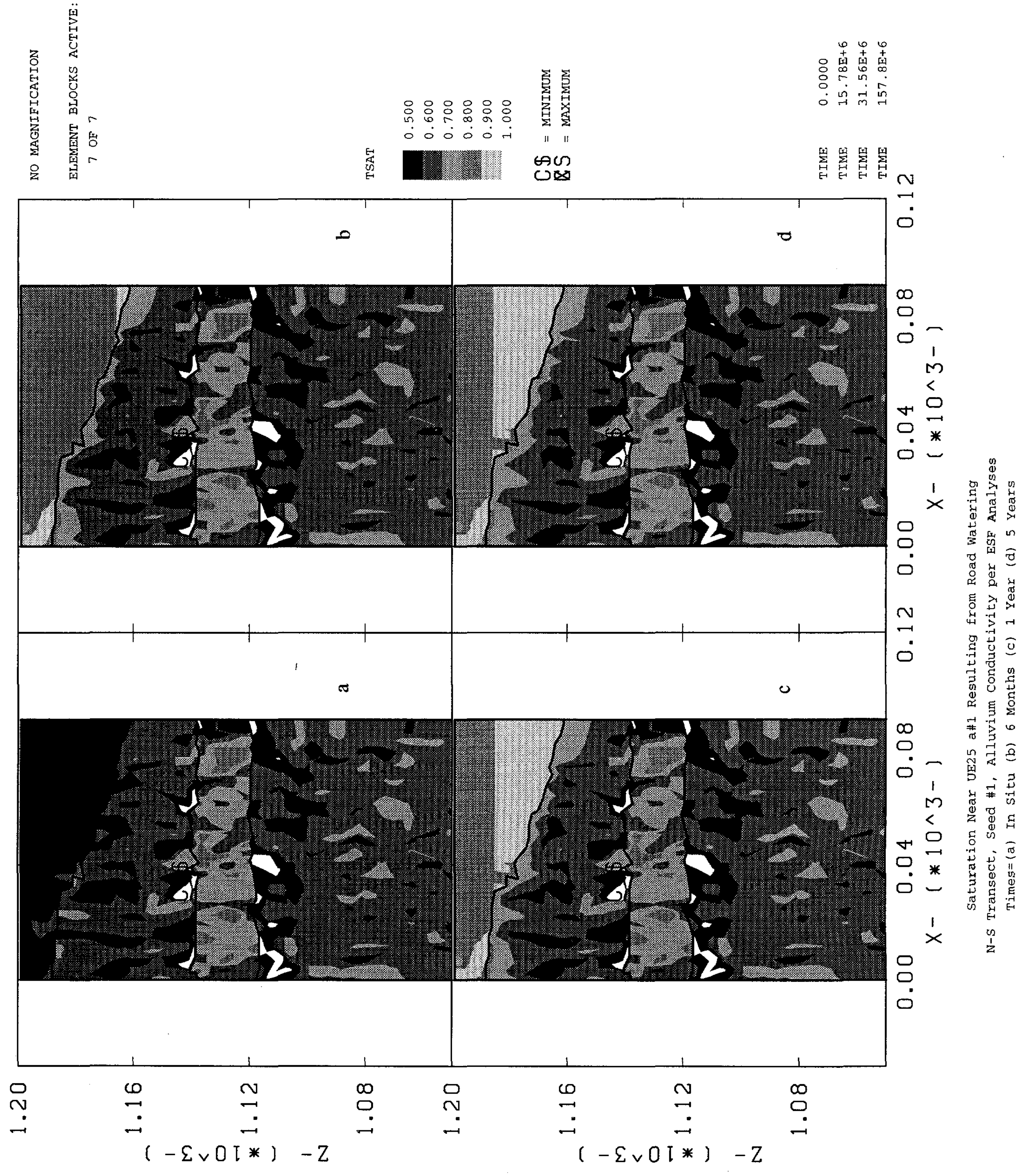

Figure 4.4-10: ΔSat, 5-Year Road Watering Period, N-S Orientation, Seed 1

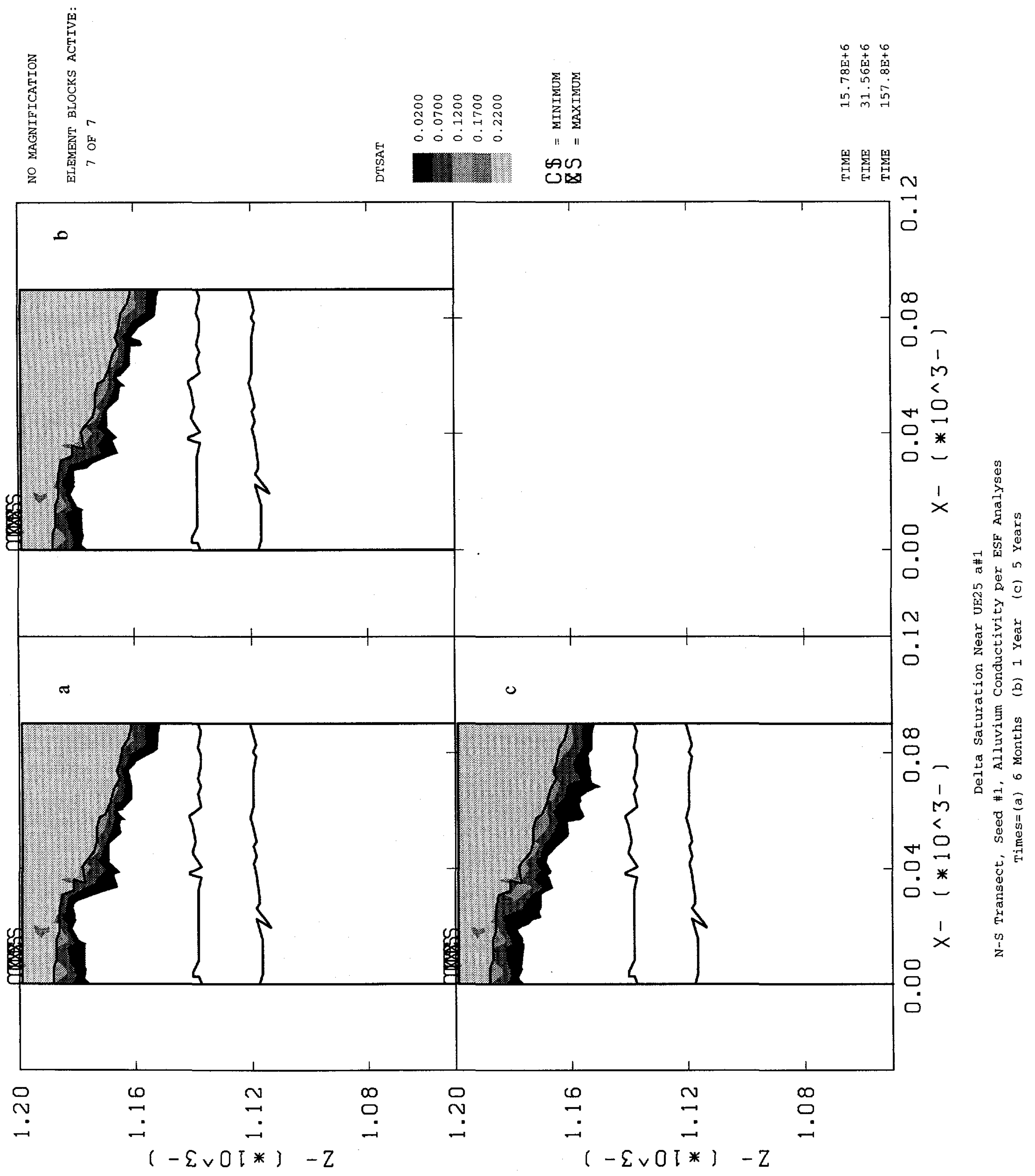

Figure 4.4-11: ΔSat Through 1000 Years
N-S Orientation, Seed 1

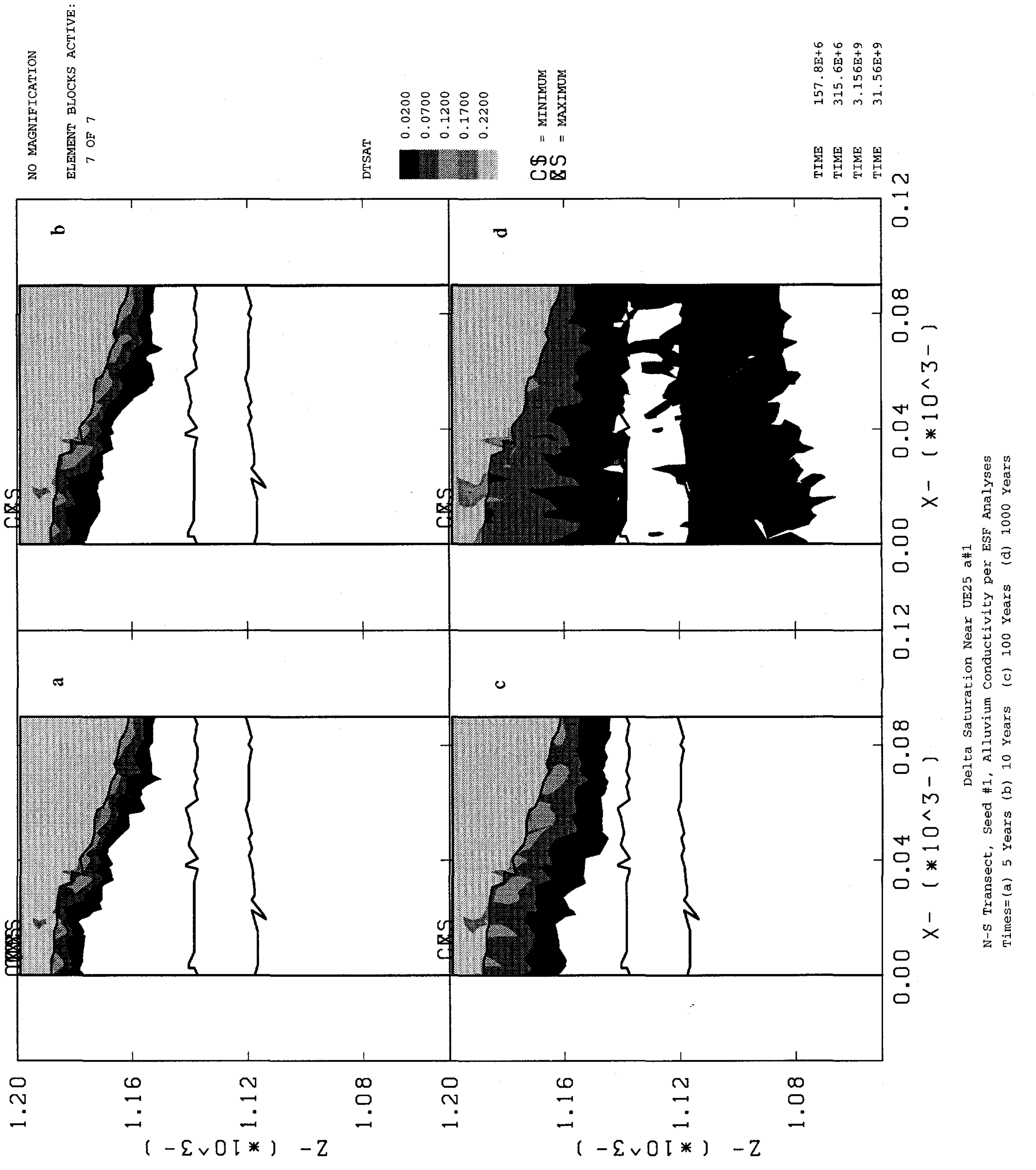

Figure 4.4-12: ΔSat at 10,000 Years
N-S Orientation, Seed 1

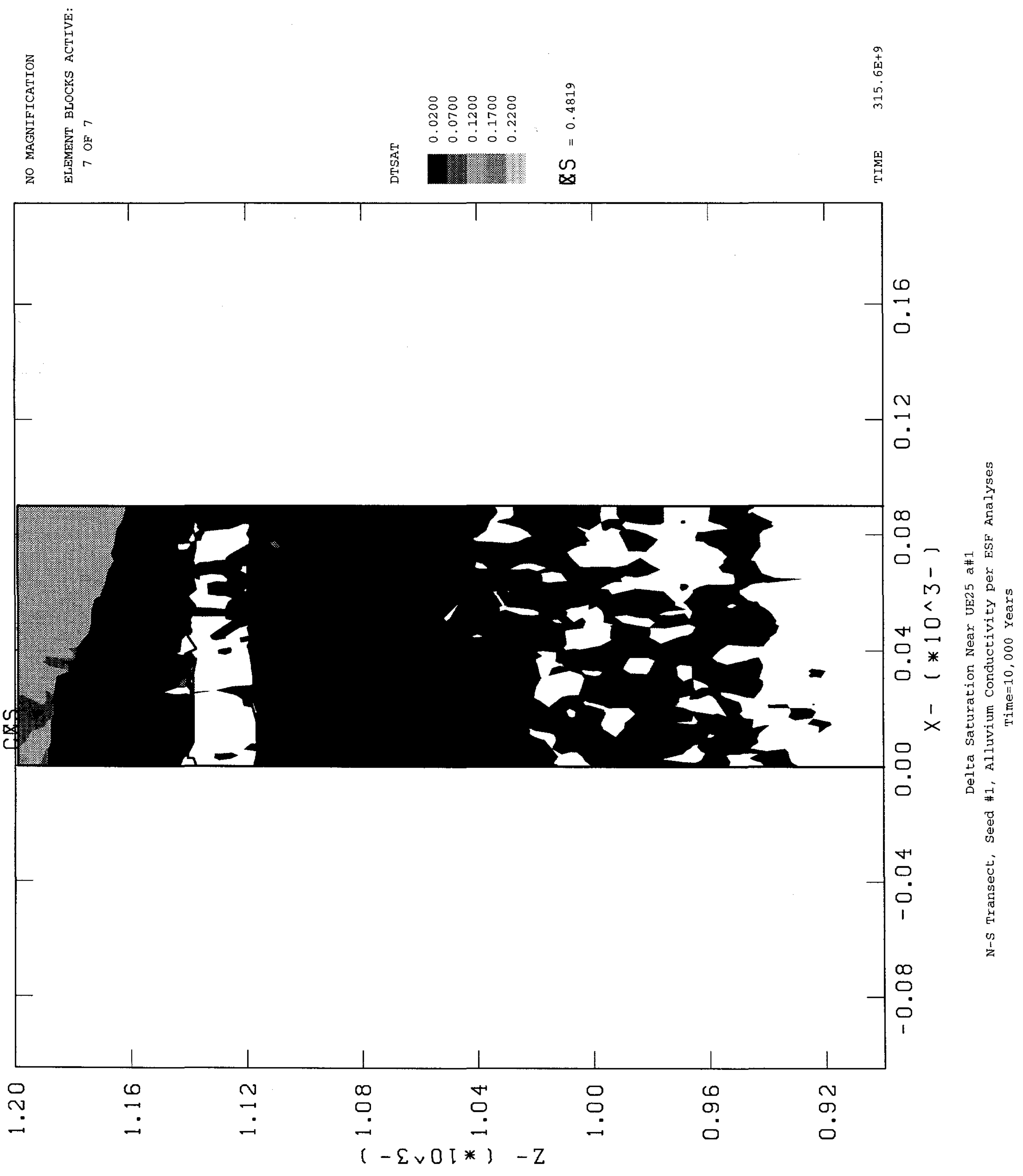

Figure 4.4-13 (a) shows the in situ saturation conditions calculated for Seed 2 in the alluvium, TCw, PTn, and upper TSw layers. Figures 4.4-13 (b) through (d) show the saturation after road watering has been in effect for 6 months, 1 year, and 5 years. The resulting saturation levels are similar to those obtained for Seed 1. A total of 110.4 m^3 of water infiltrated the simulated mountain for Seed 2. Figures 4.4-14 through 4.4-16 plot Δsat to represent water movement at 6 months, and 1, 5, 10, 100, 1,000, and 10,000 years. Again the results are similar to those obtained for Seed 1. The most striking difference may be observed at 10,000 years (Figures 4.4-12 and 4.4-16), at which the water in the Seed 1 simulation has achieved a greater penetration beneath the 1020-m elevation than the water in the Seed 2 simulation; this is probably due to the greater amount of infiltrated water predicted for the Seed 1 case.

Figure 4.4-17 (a) shows the in situ saturation conditions calculated for Seed 3 in the alluvium, TCw, PTn, and upper TSw layers. Figures 4.4-17 (b) through (d) show the saturation after road watering has been in effect for 6 months, 1 year, and 5 years. The resulting saturation levels are less similar to those obtained for Seed 1 than were those obtained for Seed 2. Particularly interesting is that the alluvium remains primarily below 90% saturation during the five years of surficial watering. A total of 88.1 m^3 of water infiltrated the simulated mountain for Seed 3 during the five-year surficial watering period. Figures 4.4-18 through 4.4-20 plot Δsat to represent water movement at 6 months, and 1, 5, 10, 100, 1,000, and 10,000 years. The results are similar to those obtained for Seed 1. However, the extent of vertical migration of water into the TSw after 10,000 years is significantly less for Seed 3 than for either Seeds 1 or 2.

Table 4.4-2: Amount of Infiltrated Water at 5 Years for UE25 a#1, North-South Calculations

Case	Amount of infiltrated water, m^3
Case #1, ESF Analysis #12 (Sobolik and Fewell, 1993)	142.8
Seed 1	157.2
Seed 2	110.4
Seed 3	88.1
Seed 5	11.4

The results for Seed 5 were obtained using the same geostatistical and computational grids and porosity fields as were used for Seed 2, but using different material properties for alluvium: a higher saturated hydraulic conductivity by nearly three orders of magnitude; and pore size parameters and a Brooks-Corey constant resulting in a moisture retention curve much less steep than for the original alluvium properties. An earlier comparison between Figures 4.4-2 and 4.4-4 showed a significant difference in the resulting predictions of in situ saturation in the alluvium (50% for original properties versus 80% for sand properties), but almost identical results below the alluvium-TCw interface. Figure 4.4-21 (a) shows the in situ saturation conditions calculated for Seed 3 in the alluvium, TCw, PTn, and upper TSw layers. Figures 4.4-21 (b) through (d) show the saturation after road watering has been in effect for 6 months, 1 year, and 5 years. These plots show very little change in the saturation in alluvium during the surficial watering period. A total of 11.4 m^3 of water infiltrated the simulated mountain for Seed 5; Table 4.4-2 lists the added volume of water for all the north-south transect calculations, including the base case from Sobolik and Fewell (1993). Figures 4.4-22 through 4.4-24 plot Δsat to represent water movement at 6 months, and 1, 5, 10, 100, 1,000, and 10,000 years. Again, very little change is seen during the first five years. At 1,000 and 10,000 years, nearly all the additional water is in the TCw, with a little bit having penetrated to TSw.

A significant anomaly can be observed in the plots described above. In all the calculations performed for this study, the grid points representing the road surface are given a saturated condition during the first five years; afterwards, original infiltration rate of 0.01 mm/yr is imposed as the boundary condition on the road. For some as yet unidentified reason, after the first five years the value of pressure at the grid point at the surface node representing the right-hand edge of the road remains very high, and in fact increases to unrealistically large values. The primary result of this anomaly seems to be a slowing of the program execution; the erroneous value does not seem to propagate itself to more than one cell away. This anomaly shows itself in the Δsat plots at 1,000 and 10,000 years in particular. All the calculations performed for this study experienced this anomaly, but the cause has not yet been determined. It is believed that the anomaly does not affect the results during the simulations of the first five years, so the results can be used to make general conclusions regarding the sensitivity of these PA calculations to the use of heterogeneous properties.

Two phenomena observed in these calculations shall be discussed in detail at the end of this chapter: one, the apparent manner that TCw seems to act as a barrier to flow when the alluvium layer reaches a nearly saturated state; two, the relatively immediate infiltration of water into alluvium during the first six months, followed by almost no infiltration afterwards.

Figure 4.4-13: Saturation, 5-Year Road Watering Period, N-S Orientation, Seed 2

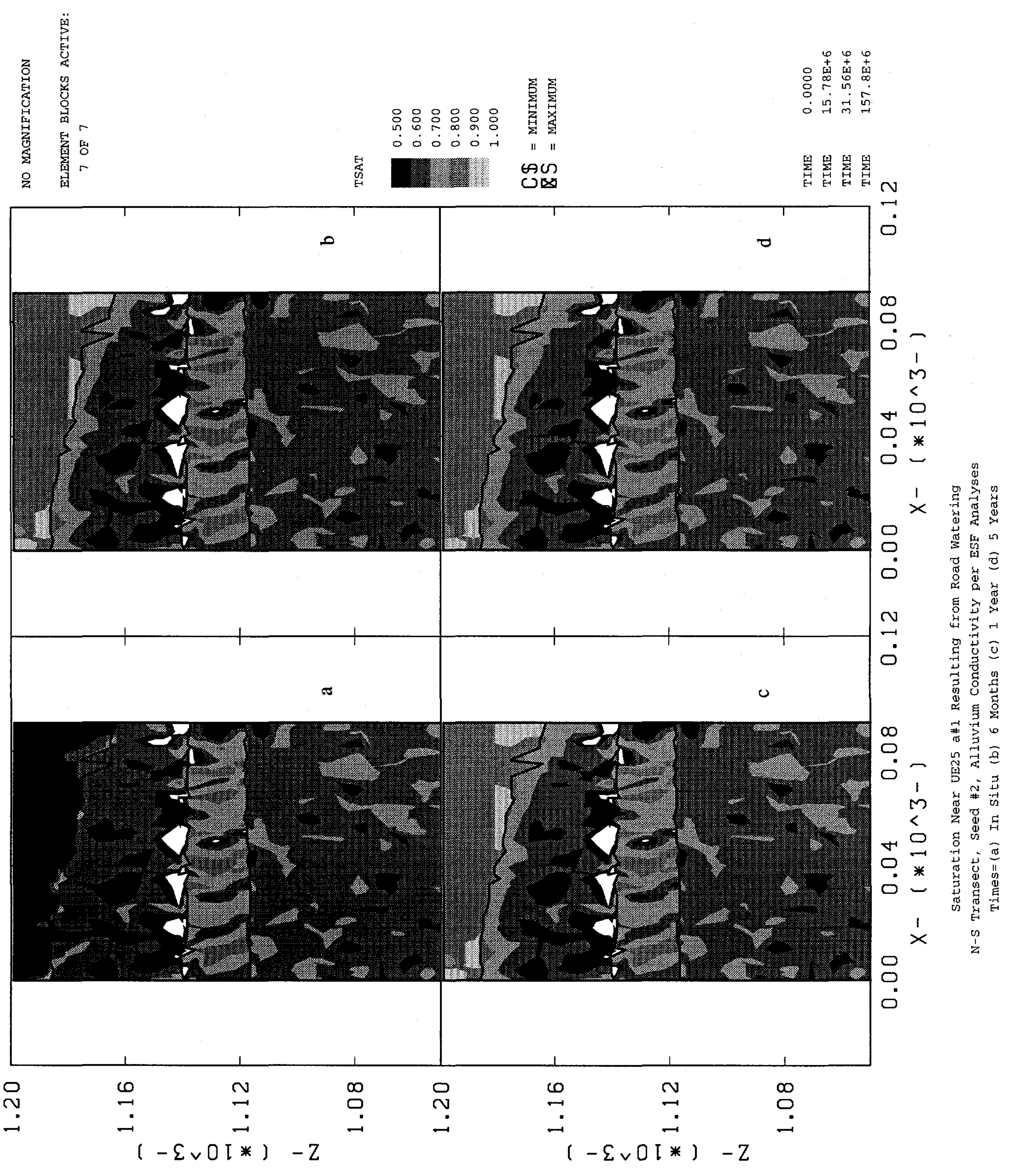

Figure 4.4-14: ΔSat, 5-Year Road Watering Period, N-S Orientation, Seed 2

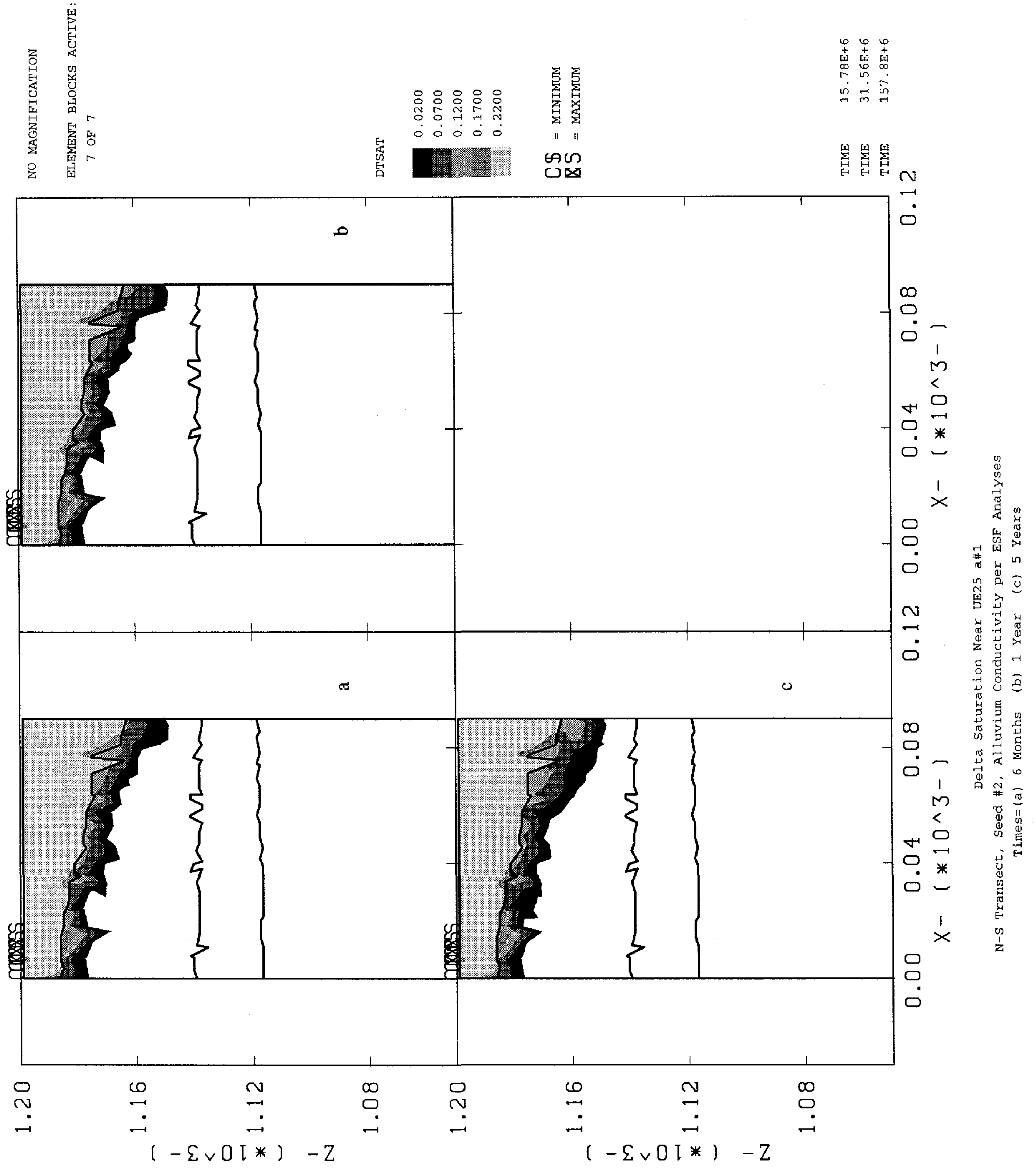

Figure 4.4-15: ΔSat Through 1000 Years
N-S Orientation, Seed 2

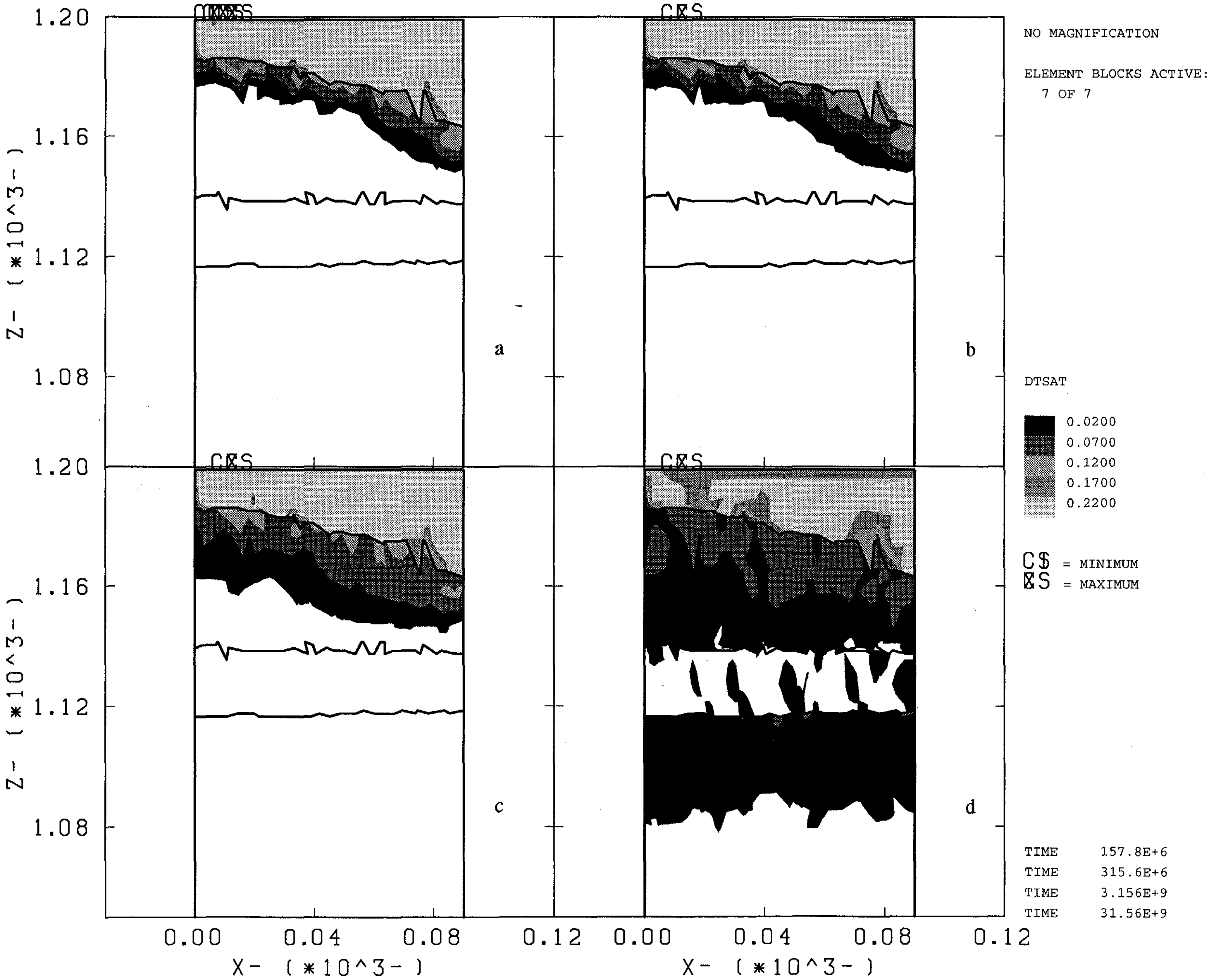

Delta Saturation Near UE25 a#1
N-S Transect, Seed #2, Alluvium Conductivity per ESF Analyses
Times=(a) 5 Years (b) 10 Years (c) 100 Years (d) 1000 Years

Figure 4.4-16: ΔSat at 10,000 Years
N-S Orientation, Seed 2

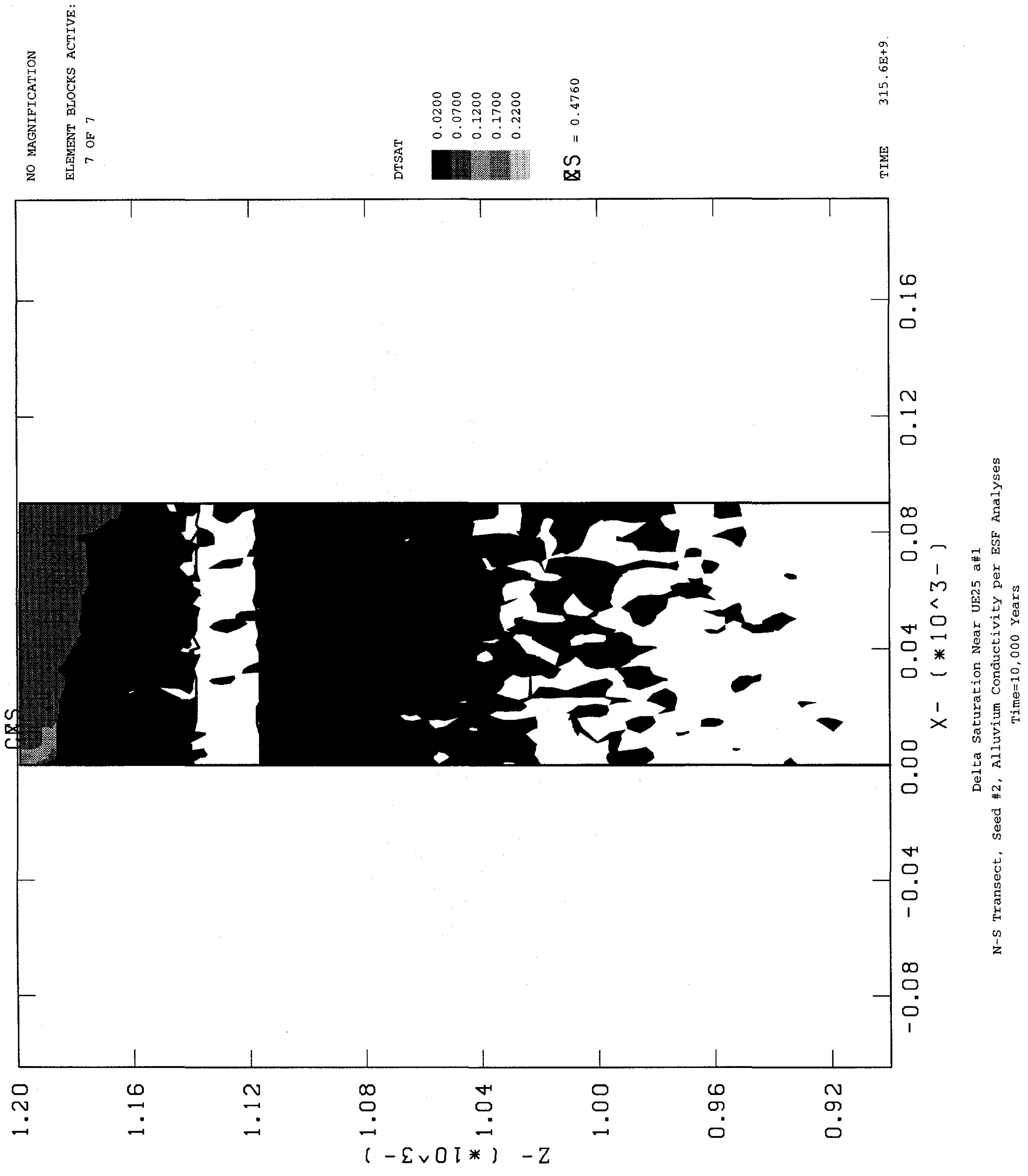

Figure 4.4-17: Saturation, 5-Year Road Watering Period, N-S Orientation, Seed 3

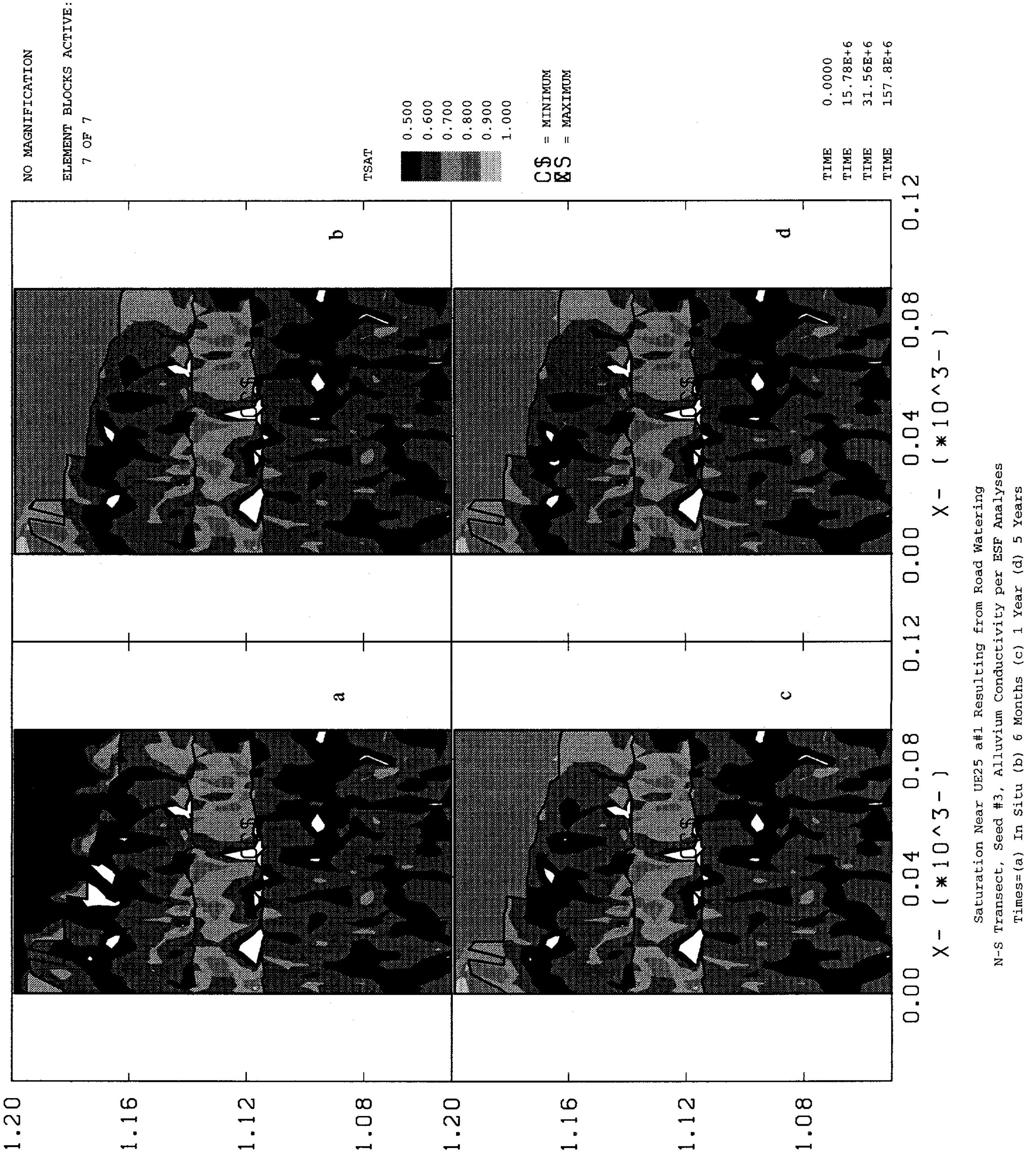

Figure 4.4-18: ΔSat, 5-Year Road Watering Period, N-S Orientation, Seed 3

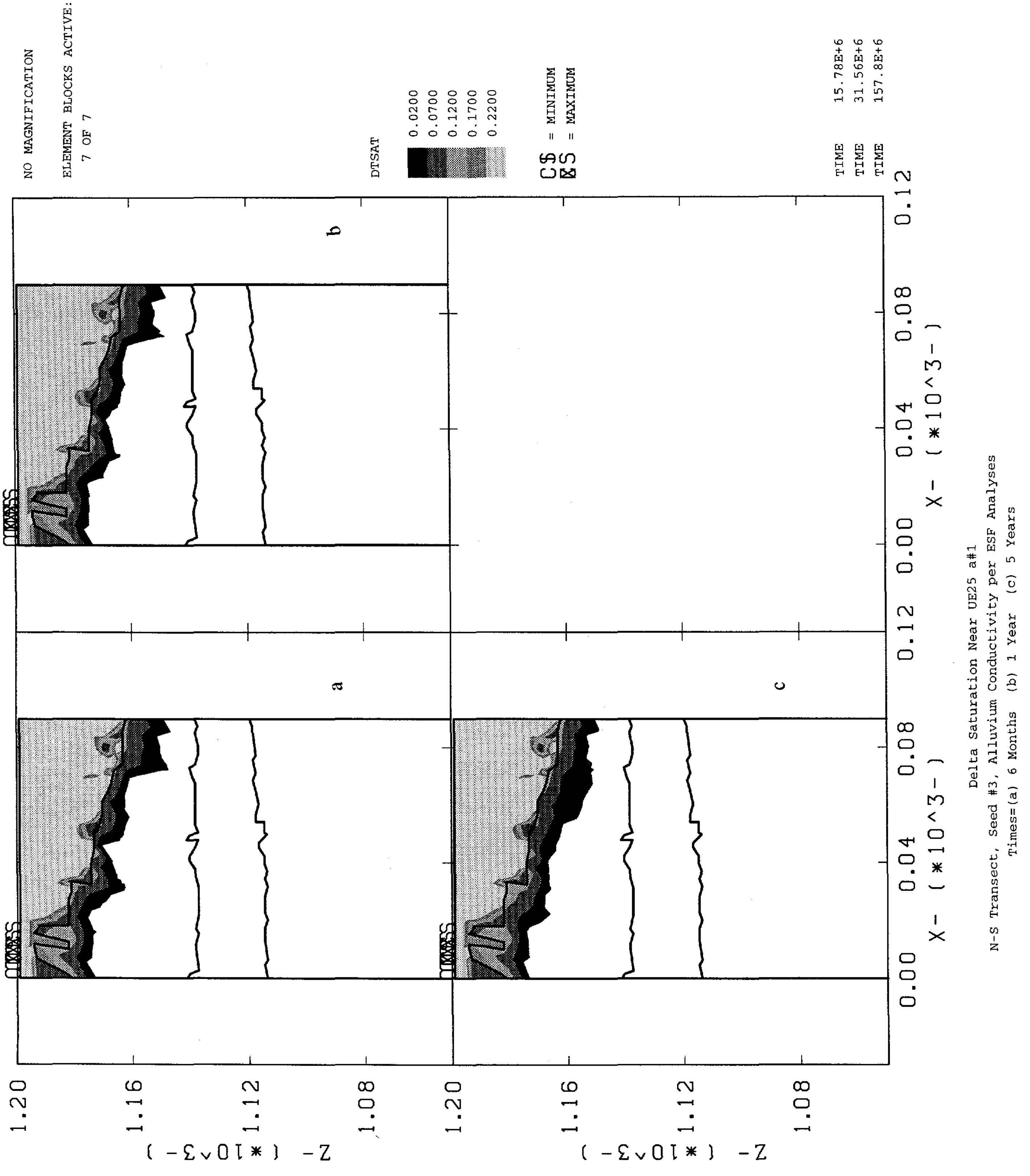

Delta Saturation Near UE25 a#1
N-S Transect, Seed #3, Alluvium Conductivity per ESF Analyses
Times=(a) 6 Months (b) 1 Year (c) 5 Years

Figure 4.4-19: ΔSat Through 1000 Years
N-S Orientation, Seed 3

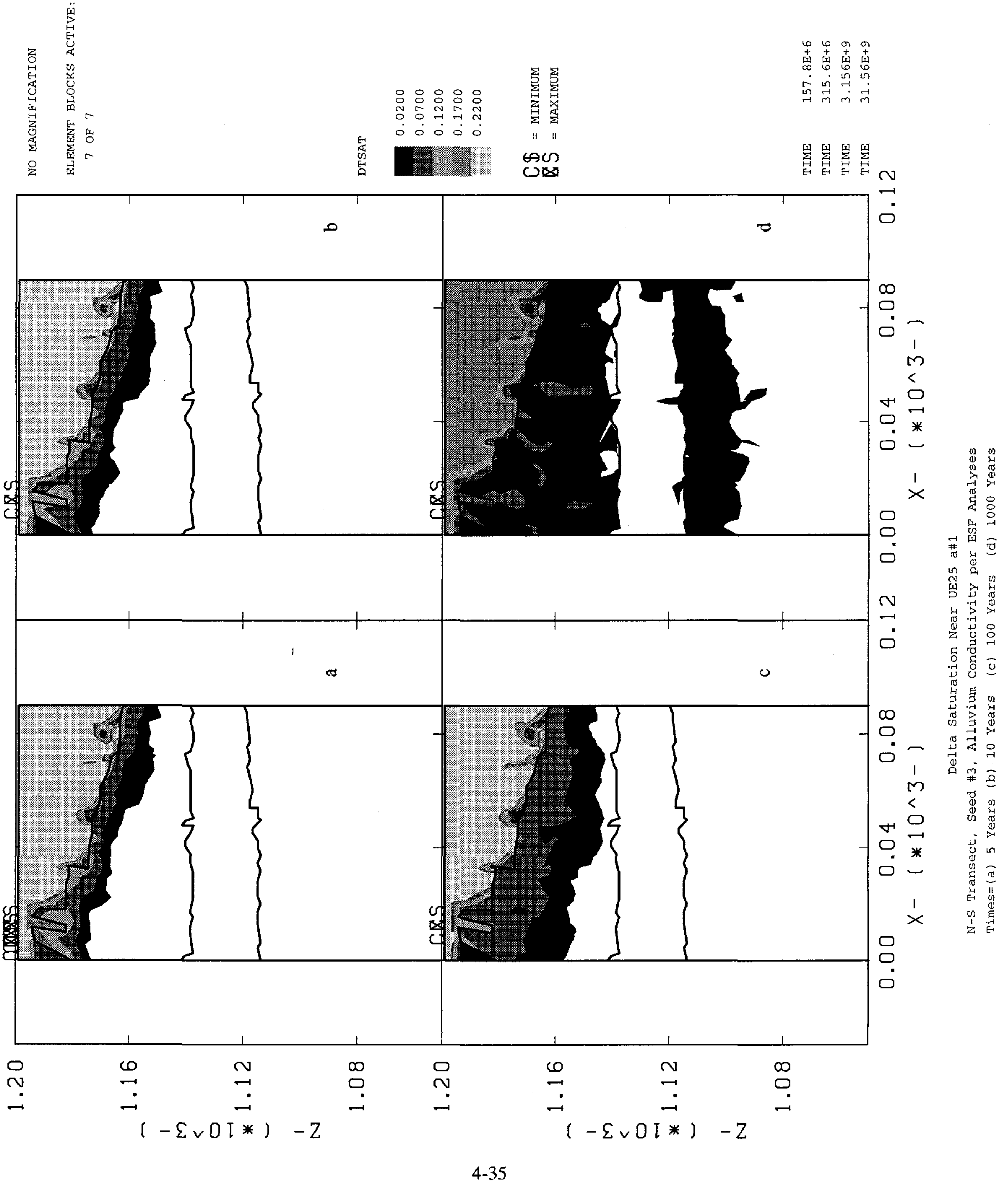

Figure 4.4-20: ΔSat at 10,000 Years
N-S Orientation, Seed 3

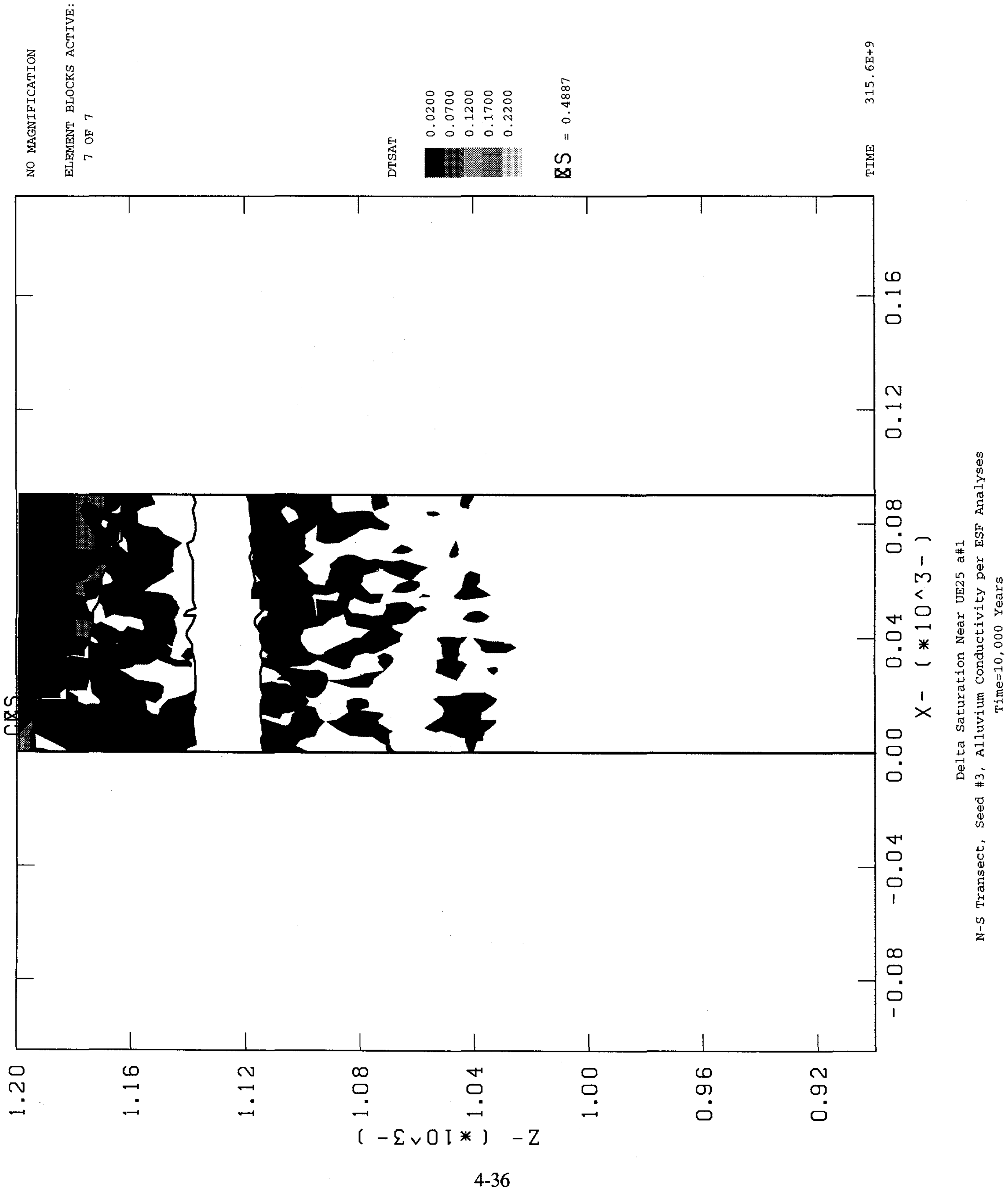

Figure 4.4-21: Saturation, 5-Year Road Watering Period, N-S Orientation, Seed 5

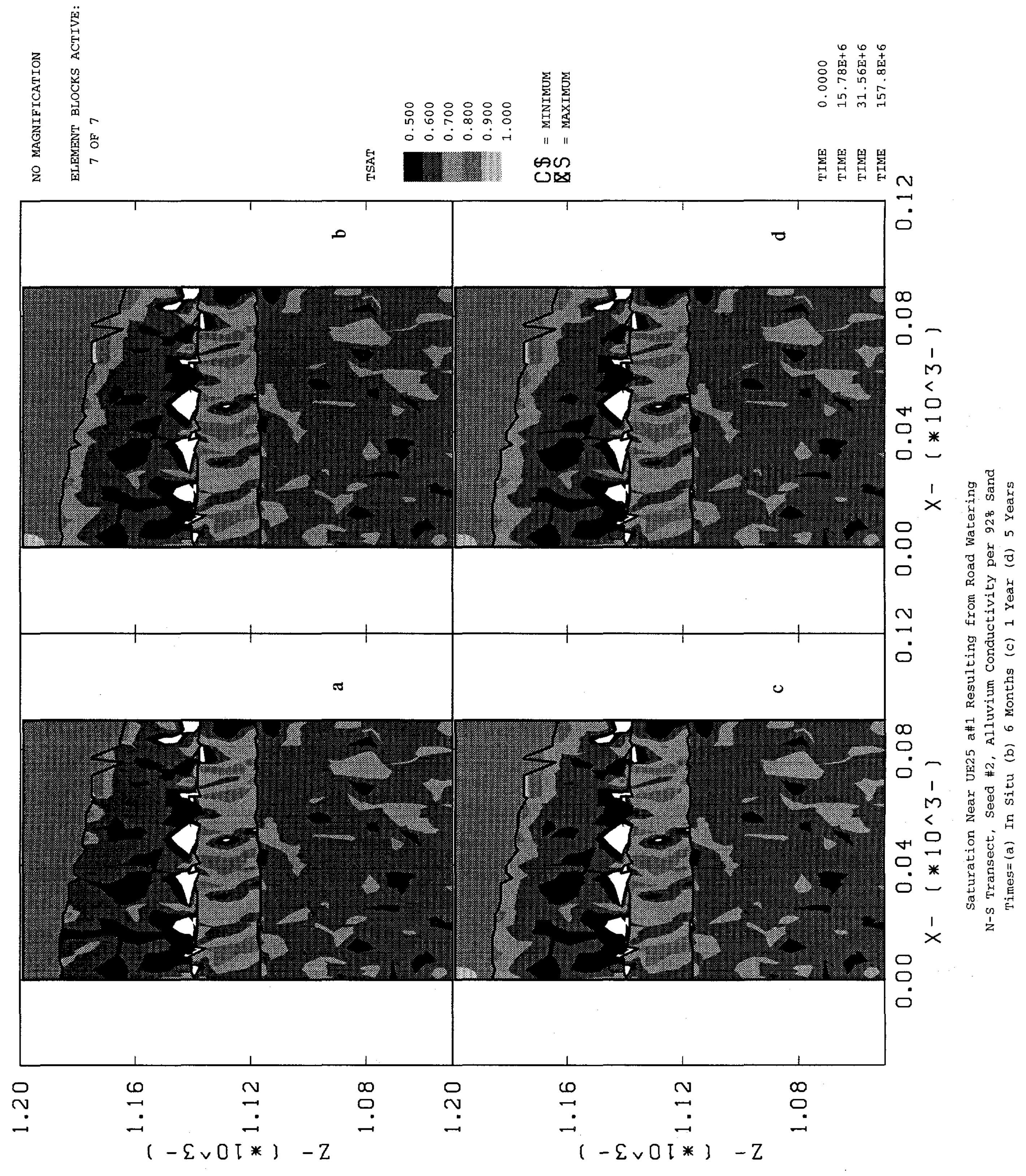

Figure 4.4-22: ΔSat, 5-Year Road Watering Period, N-S Orientation, Seed 5

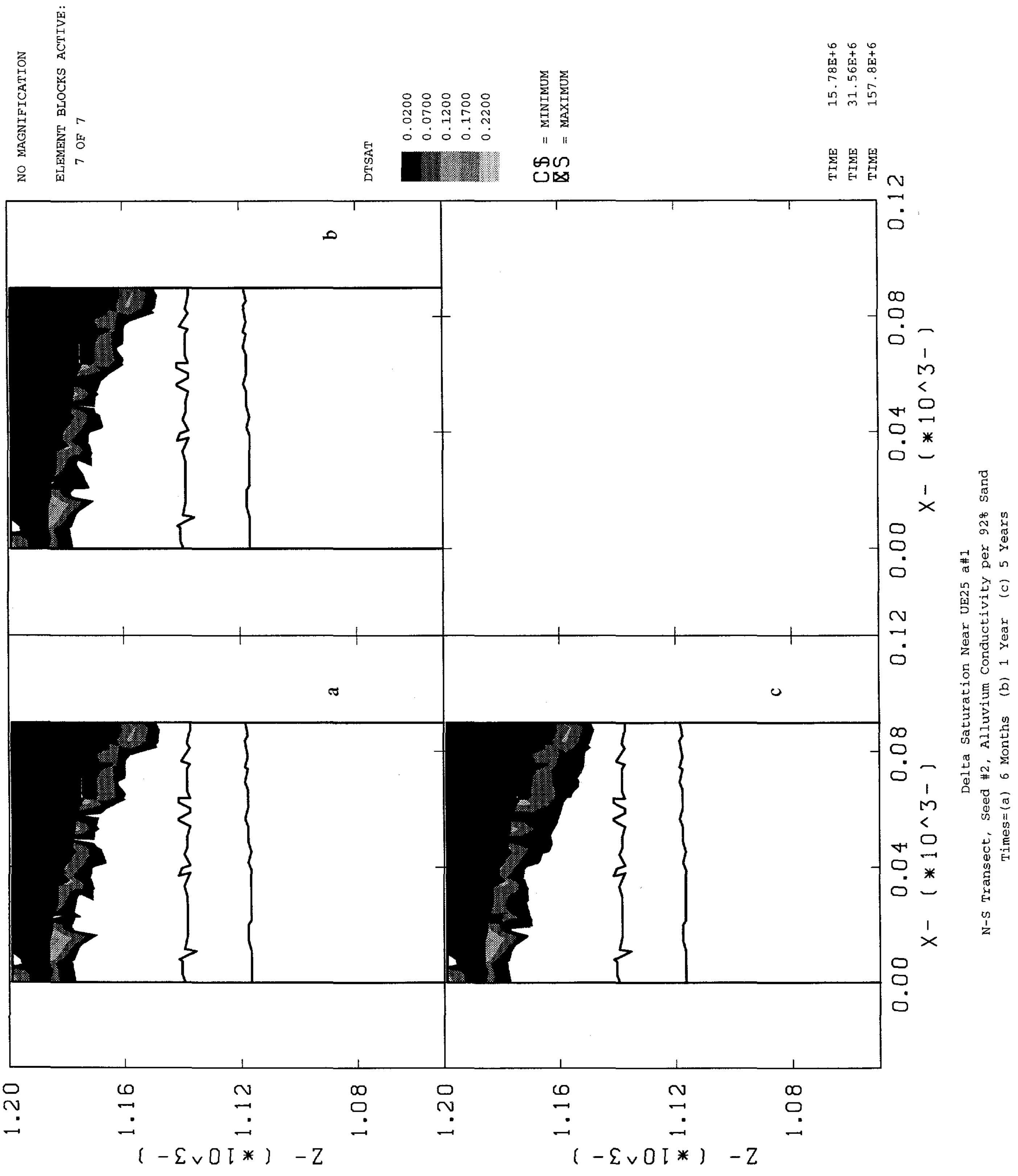

Figure 4.4-23: ΔSat Through 1000 Years
N-S Orientation, Seed 5

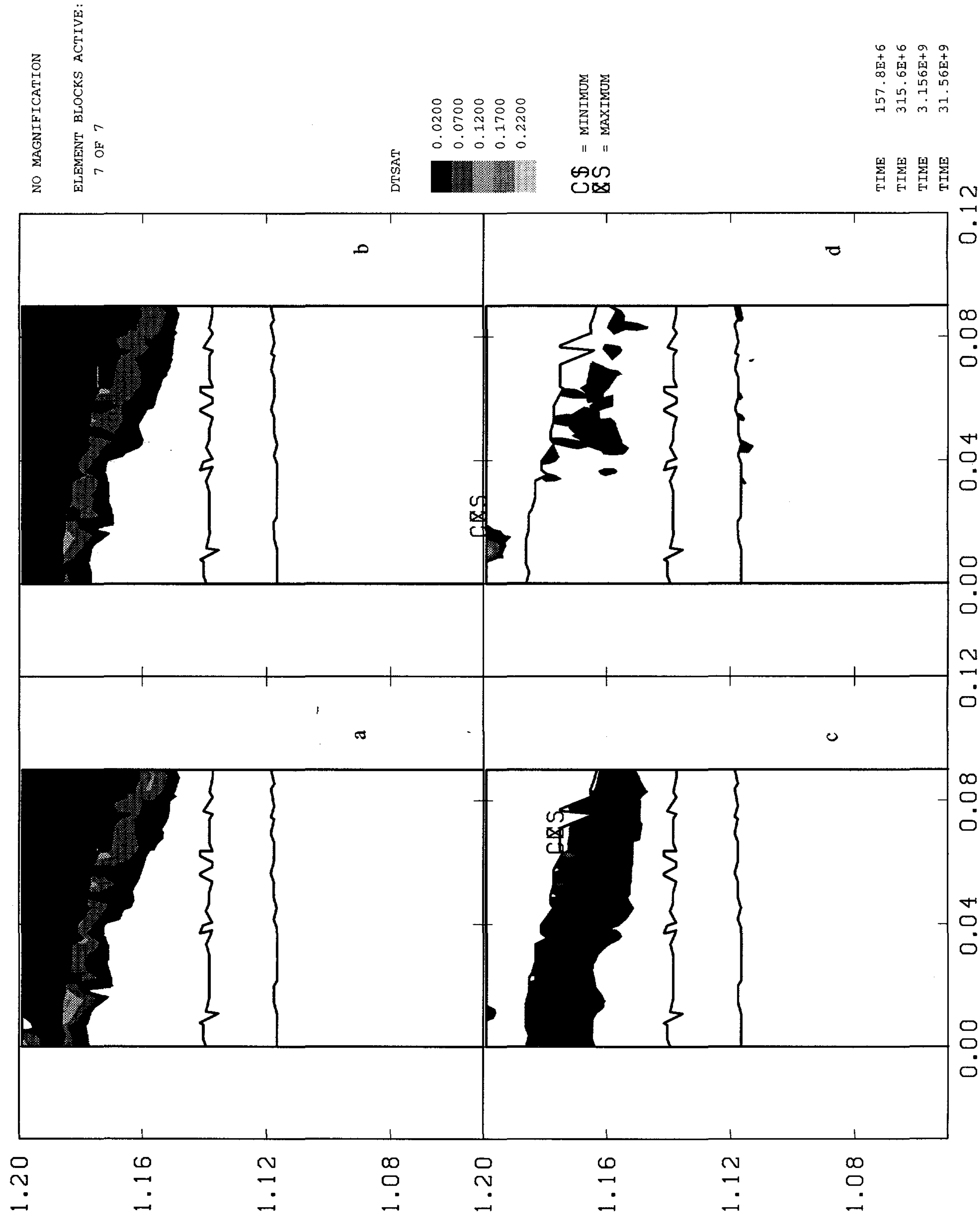

Figure 4.4-24: ΔSat at 10,000 Years
N-S Orientation, Seed 5

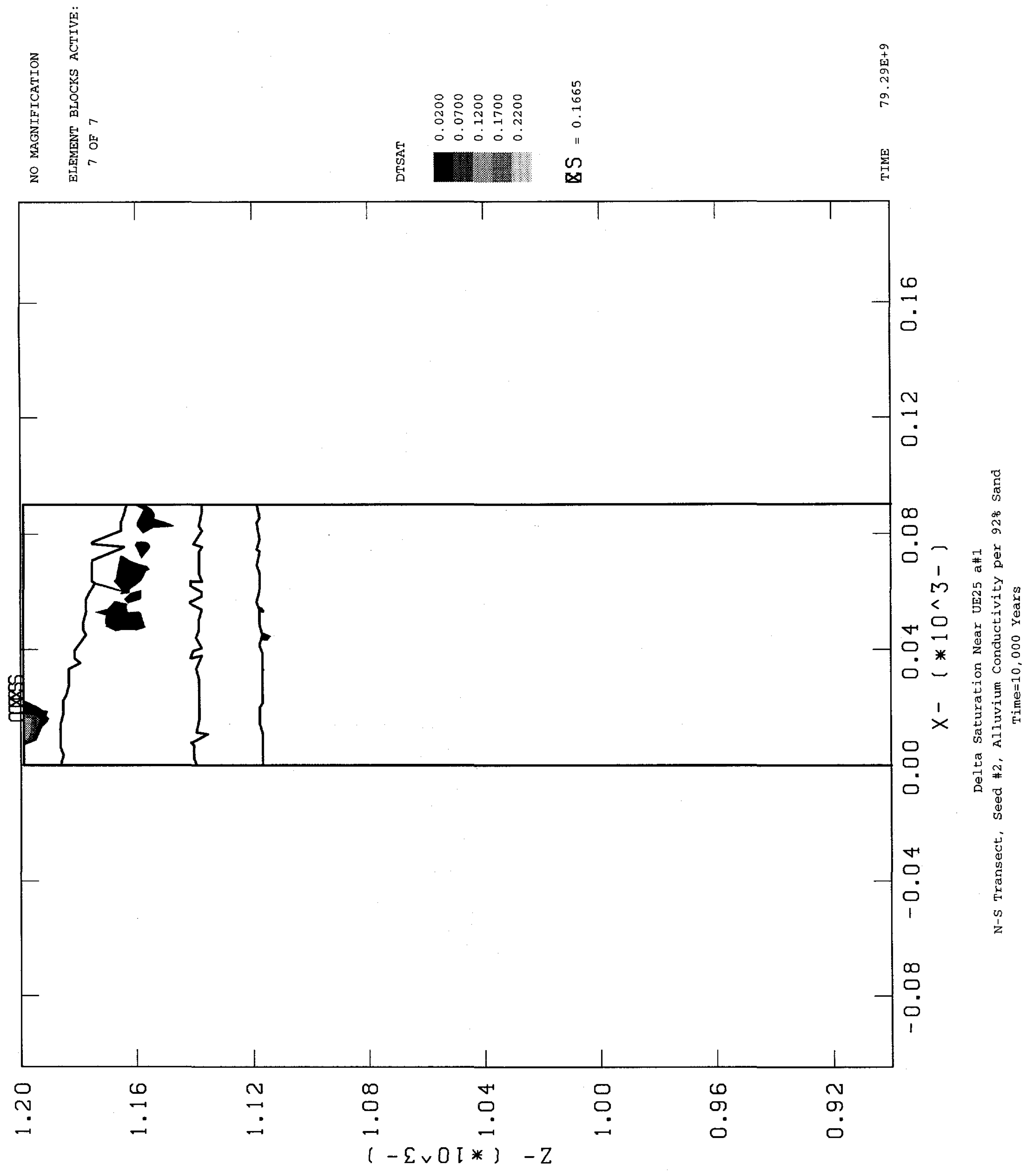

4.4.2 UE25 a#1, East-West Orientation Cases

This section contains a discussion of the results obtained for the three cases simulating an east-west transect through the borehole UE25 a#1, a problem that includes the natural slope of the region. These cases are referred to as Seeds 1 and 2, which used two different seed numbers for calculating the geostatistical grids and the alluvial properties for hydraulic conductivity fit to those in Sobolik and Fewell (1993), and Seed 4, which actually uses the same geostatistical and computational grids as Seed 1 but uses properties for hydraulic conductivity in the alluvium approximating a soil made of 92% sand.

The computational grids used for Seeds 1 and 2 are displayed in Figures 4.4-25 and 4.4-26; the grid used for Seed 4 was the same as that shown for Seed 1. These grids each have 24 columns and 60 rows of elements. The 12-m wide road is located at the center of the surface of the grid (x-coordinates 84 m to 96 m). The most striking difference is that the grid for Seed 2 has a continuous alluvium layer across the top, whereas the grids for Seeds 1 and 4 have some places where TCw is at the surface. In fact, the two cells representing the road in Figure 4.4-25 are one alluvium and one TCw. This discrepancy in the formulation of the alluvium layer illustrates the need for additional data regarding alluvial depths at various locations on and around Yucca Mountain. The TCw layer seems to be thicker for Seed 2 than for Seeds 1 and 4. The two grids model the boundaries between stratigraphic units below PTn very similarly.

Steady-state calculations were performed with NORIA-SP to estimate the in situ saturation levels for the three cases. An infiltration rate of 0.01 mm/yr was assumed. Figures 4.4-27 through 4.4-29 show the in situ saturation conditions for Seeds 1, 2, and 4, respectively. (The white areas in these plots represent saturation levels less than 50%.) For Seeds 1 and 2, the saturation levels in the alluvium are in the 50%-60% range, and in TCw they are primarily in the 60%-70% range. The saturation level for Seed 4 in the alluvium layer is in the 80%-90% range; however, a comparison with Seed 1 shows that the computed saturation fields below the alluvium-TCw interface are nearly identical. One point of interest may be found in Figures 4.4-27 and 4.4-29. The plotting package BLOT plots the location of the minimum and maximum values of the variable being displayed (with the symbol "C$"). In Figures 4.4-27 and 4.4-29, the minimum value of saturation is in the TCw; that value is 4.5%. This would seem to be an extremely low value for saturation level anywhere in Yucca Mountain, and this anomaly might be the cause of some of the computing problems discussed below.

Figure 4.4-30 (a) shows the in situ saturation conditions calculated for Seed 1 in the alluvium, TCw, PTn, and upper TSw layers. Figure 4.4-30 (b) shows the saturation after road watering has been occurring for 5 years. The change between (a) and (b) is seen only in the TCw region near the road and in the alluvium downdip from the road. The alluvium changes from 50%-60% saturation to 80%-90% saturation. As for the north-south cases, nearly all the water that gets added to the simulated mountain due to road watering infiltrates during the first six months; Table 4.4-3 shows the time progression of water addition. The value of 11.4 m^3 of infiltrated water after five years of surficial watering may be compared to the same value obtained for a 12-m wide road based on Case #1 of ESF Analysis #12 (Sobolik and Fewell, 1993), 285.6 m^3. Figure 4.4-31 plots Δsat at 5 years; again, changes are visible only near the road and in the downdip section of alluvium. Calculations were attempted beyond five years, but were unable to progress (timesteps on the order of thousandths of microseconds). NORIA-SP has a history of execution problems under conditions where high pressure gradients exist; it is possible that one of the aforementioned anomalies caused this problem.

Table 4.4-3: Amount of Infiltrated Water at 5 Years for UE25 a#1, East-West Calculations

Case	Amount of infiltrated water, m^3
Compare with full 12-m road, Case #1, ESF Analysis #12 (Sobolik and Fewell, 1993)	$142.8 \times 2 =$ 285.6
UE25 a#1, E-W, Seed 1	11.4
UE25 a#1, E-W, Seed 2	105.3

Figure 4.4-32 (a) shows the in situ saturation conditions calculated for Seed 2 in the alluvium, TCw, PTn, and upper TSw layers. Figures 4.4-32 (b) through (d) show the saturation after road watering has been in effect for 6 months, 1 year, and 5 years. The resulting saturation levels are similar to those obtained for the north-south cases. A total of 105.3 m^3 of water infiltrated the simulated mountain for Seed 2. Figures 4.4-33 through 4.4-35 plot Δsat to represent water movement at 6 months, and 1, 5, 10, 100, 1,000, and 10,000 years. Again the results are similar to those obtained for the north-south cases. The small amount of infiltrated water resulted in very little penetration into TSw after 10,000 years.

Figure 4.4-36 shows partial results of the steady-state calculations for Seed 4 (Seed 1 grid geometry and sand properties for alluvium). The steady-state calculations for this case did not extend to the allotted simulation time of 10^{19} seconds after at least 24 hours of run time (most of the previous steady-state runs were completed in 4 to 10 hours). The results reached by 10^{17} seconds were very similar to those produced for Seed 1, other than the saturation in the alluvium layer was approximately 80%-90%.

Figure 4.4-25: Computational Grid, E-W Orientation, Seed 1

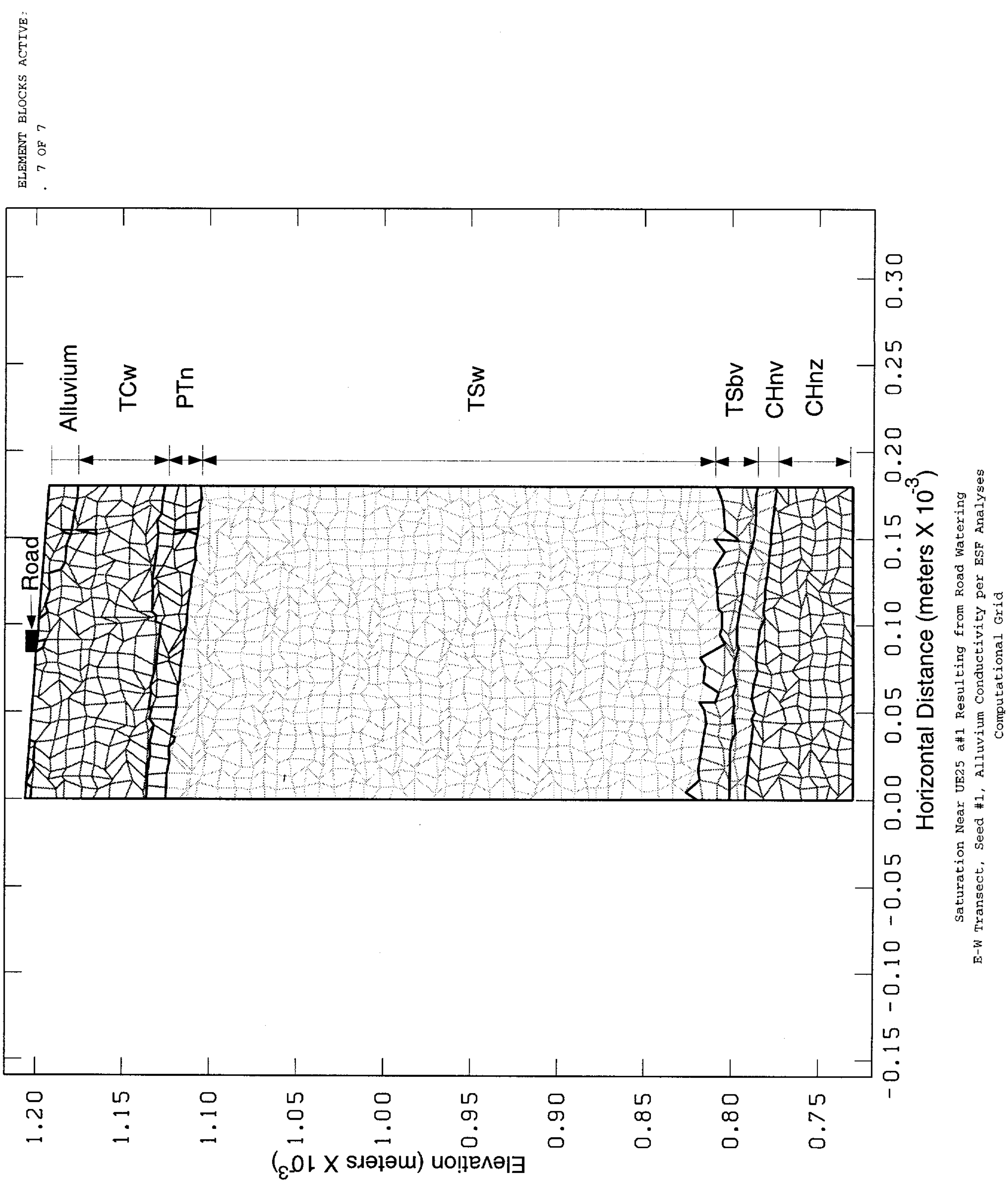

Saturation Near UE25 a#1 Resulting from Road Watering
E-W Transect, Seed #1, Alluvium Conductivity per ESF Analyses
Computational Grid

Figure 4.4-26: Computational Grid, E-W Orientation, Seed 2

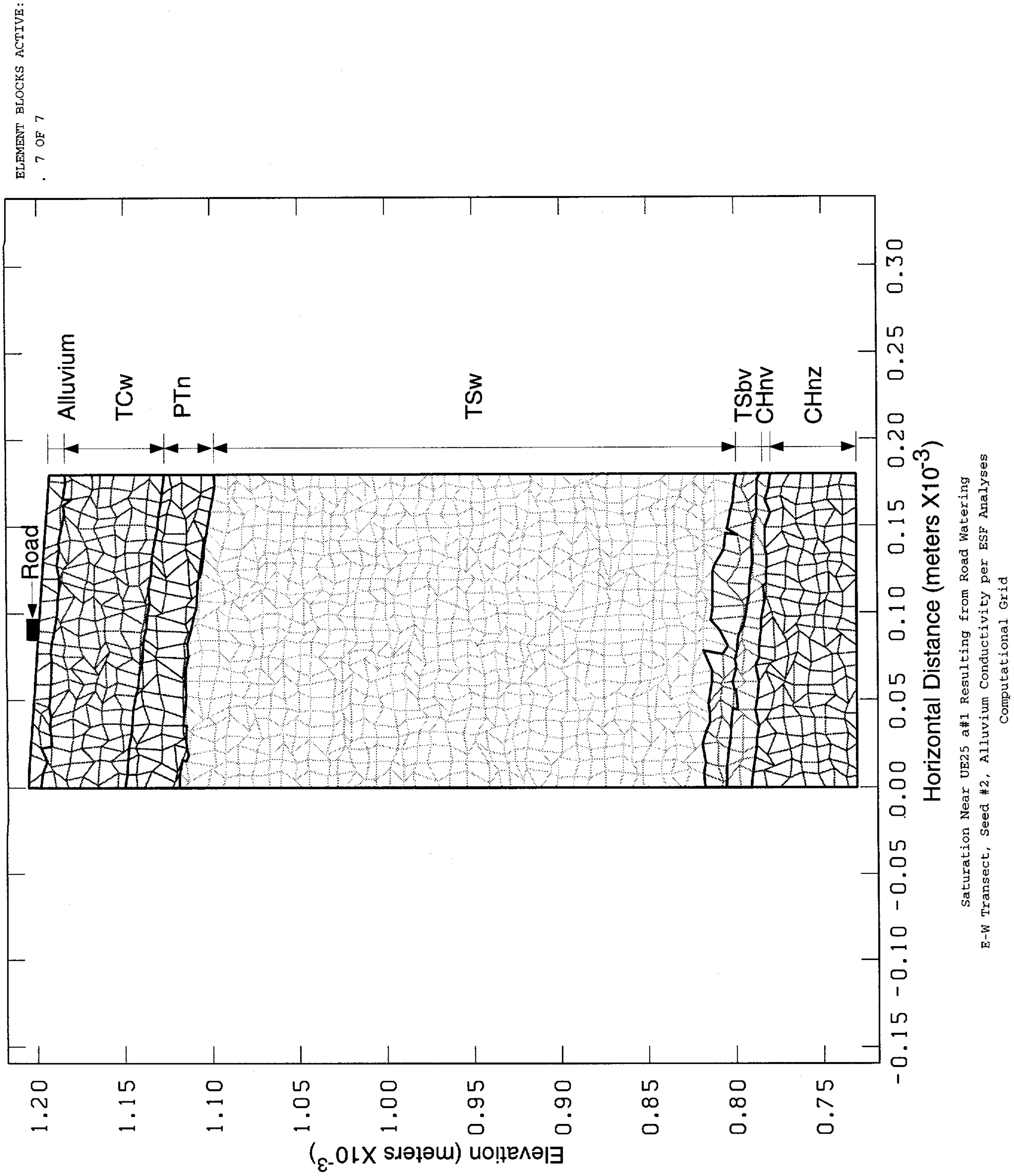

Saturation Near UE25 a#1 Resulting from Road Watering
E-W Transect, Seed #2, Alluvium Conductivity per ESF Analyses
Computational Grid

Figure 4.4-27: In Situ Saturation, E-W Orientation, Seed 1

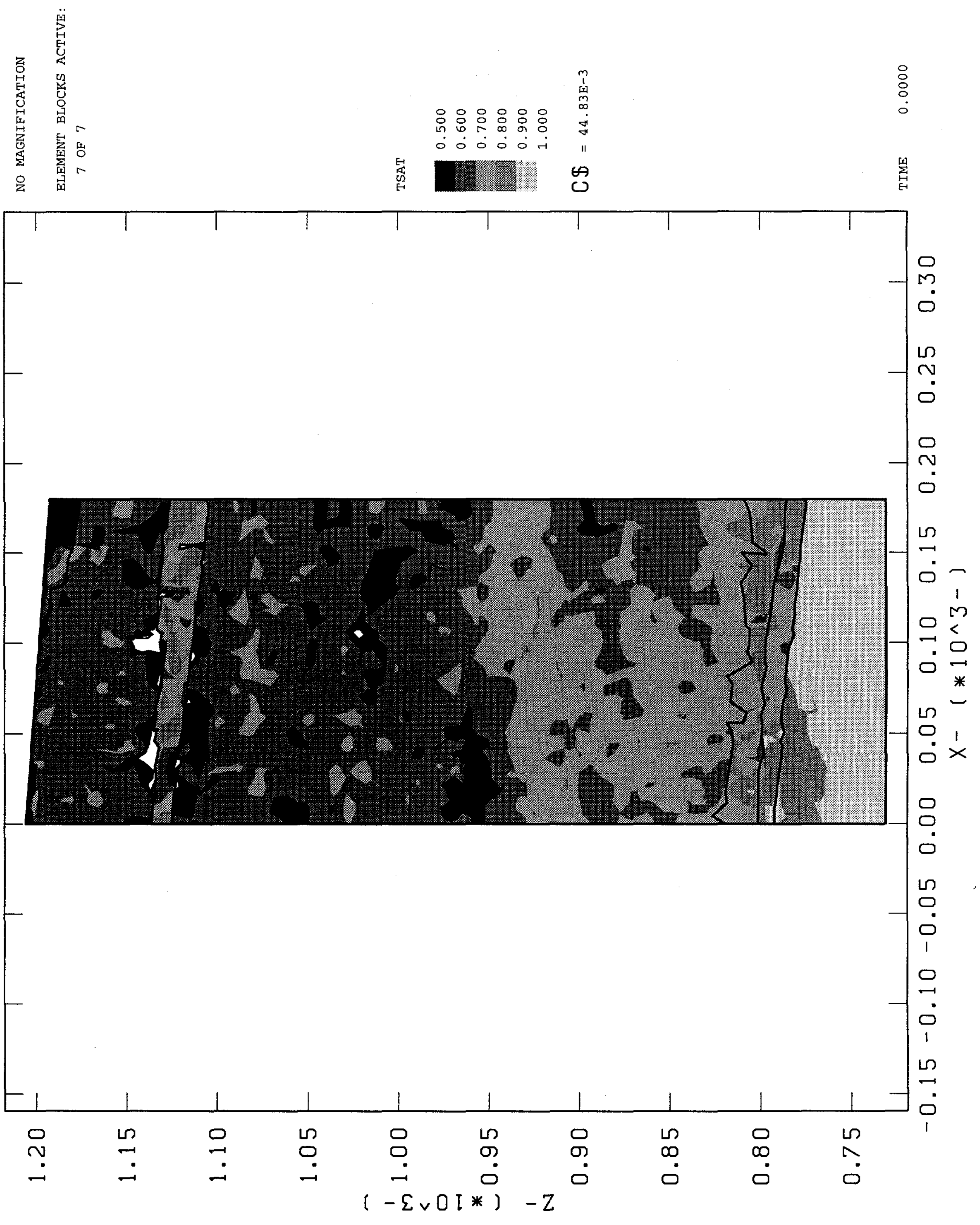

Saturation Near UE25 a#1 Resulting from Road Watering
E-W Transect, Seed #1, Alluvium Conductivity per ESF Analyses
In Situ Conditions

Figure 4.4-28: In Situ Saturation, E-W Orientation, Seed 2

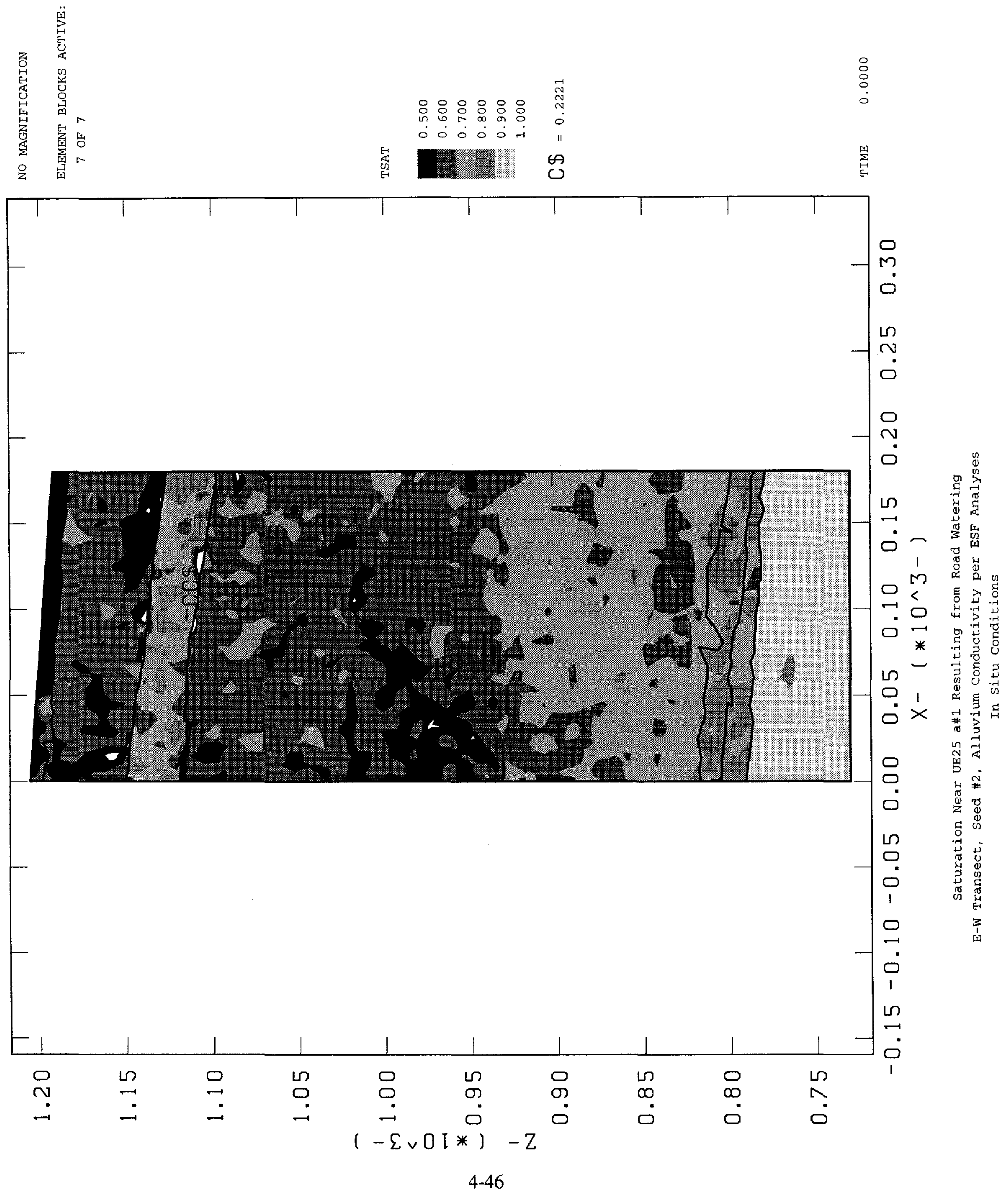

Figure 4.4-29: In Situ Saturation, E-W Orientation, Seed 4

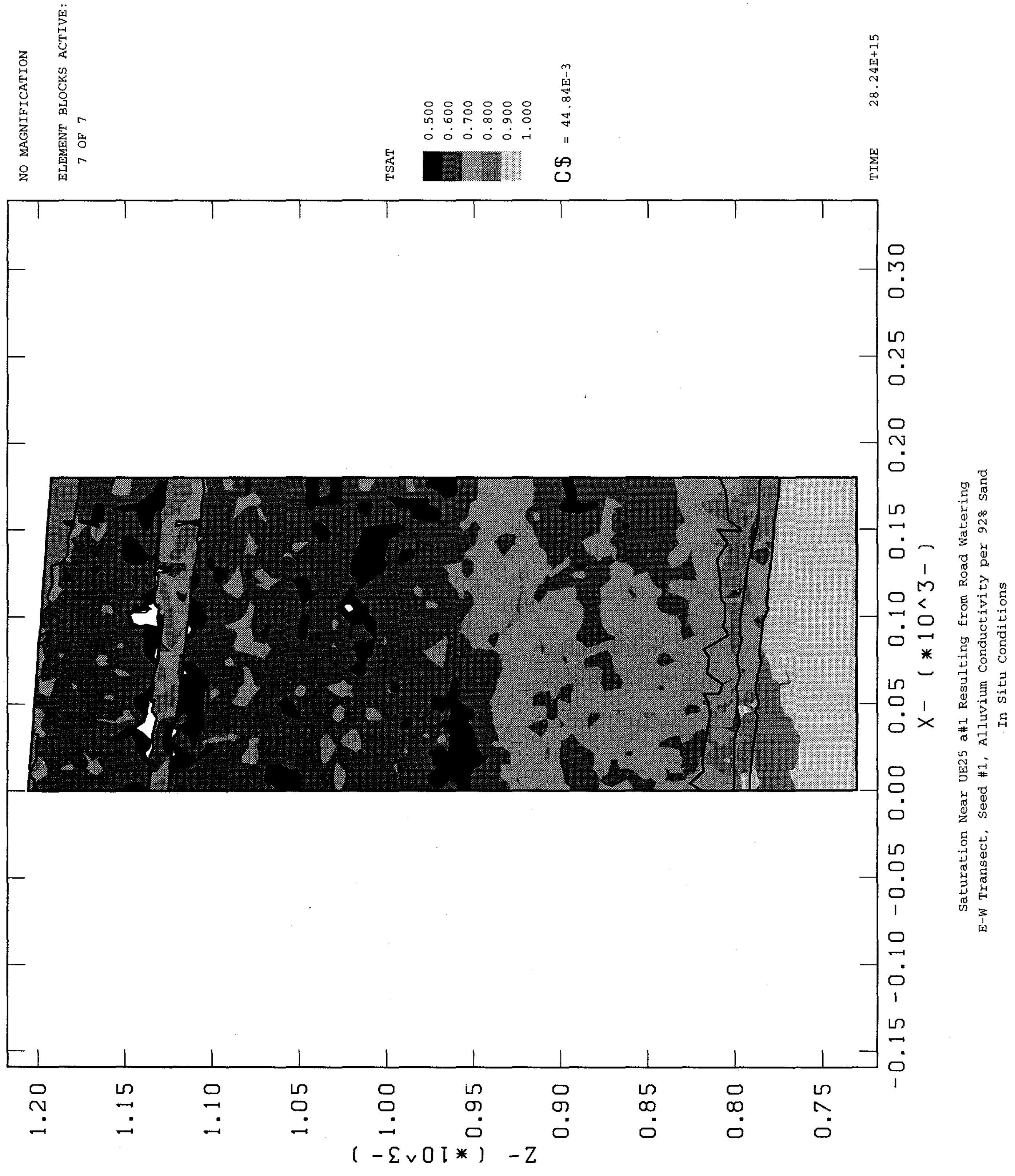

Figure 4.4-30: Saturation, 5-Year Road Watering Period, E-W Orientation, Seed 1

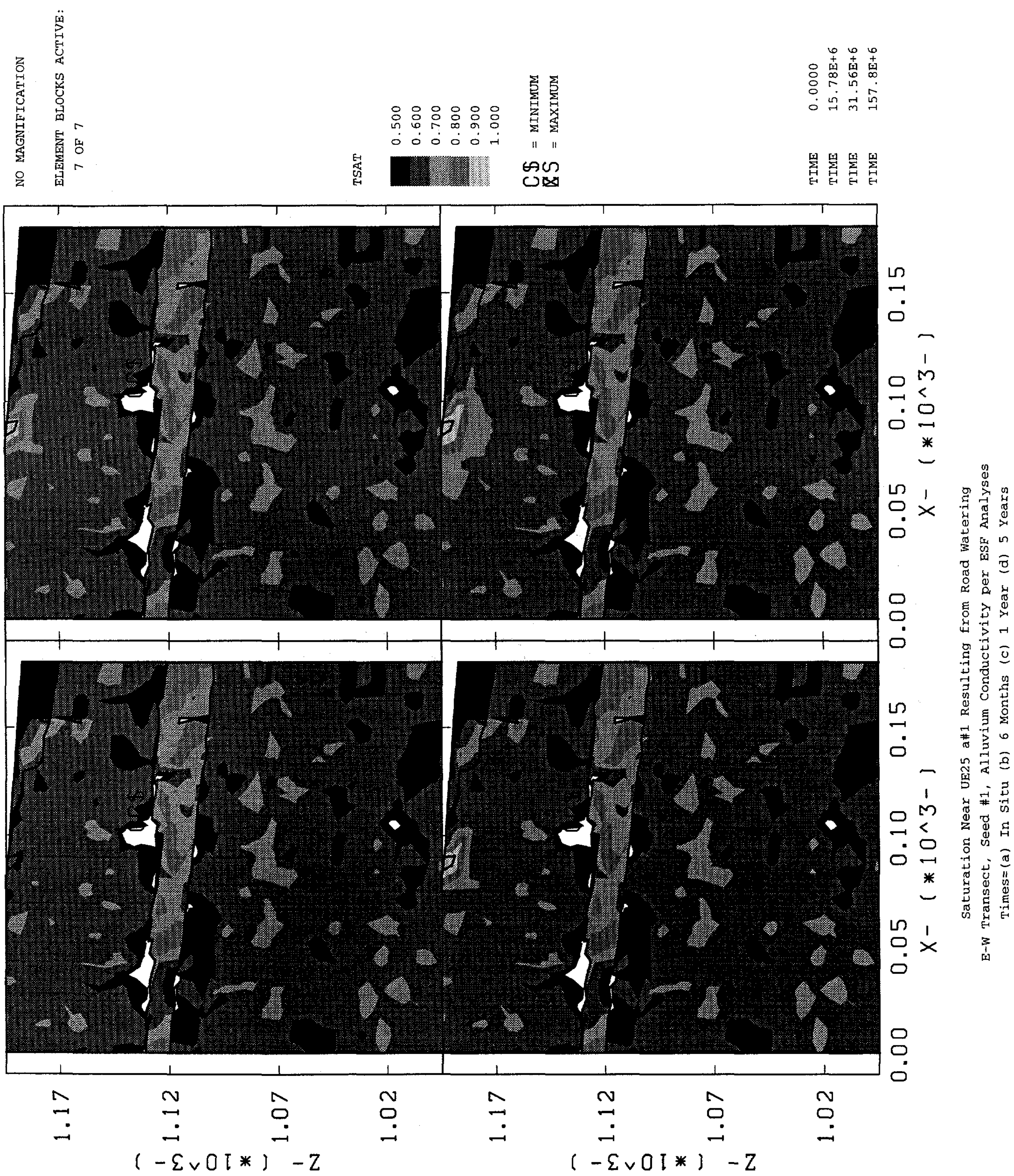

Figure 4.4-31: ΔSat, 5-Year Road Watering Period, E-W Orientation, Seed 1

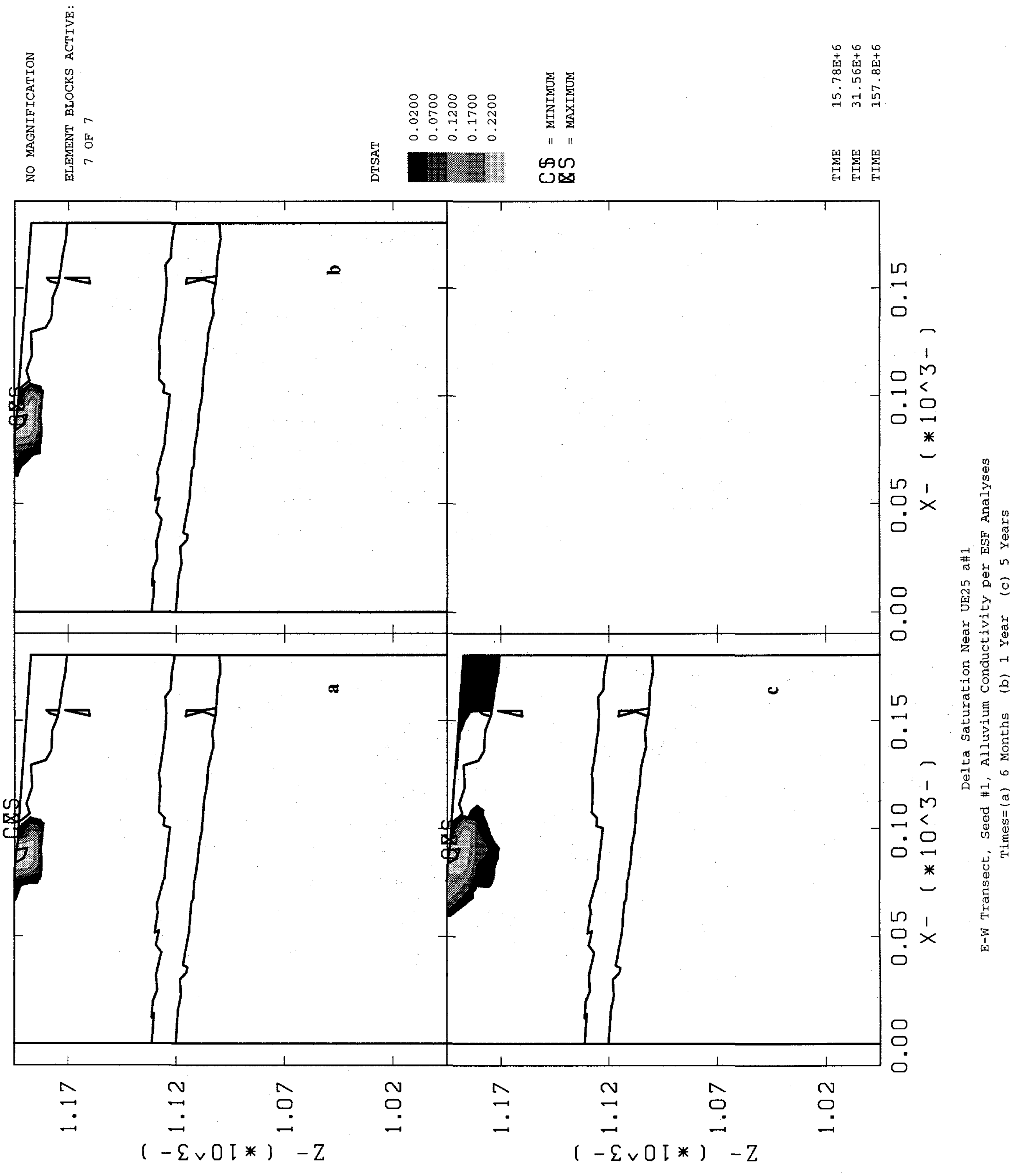

Figure 4.4-32: Saturation, 5-Year Road Watering Period, E-W Orientation, Seed 2

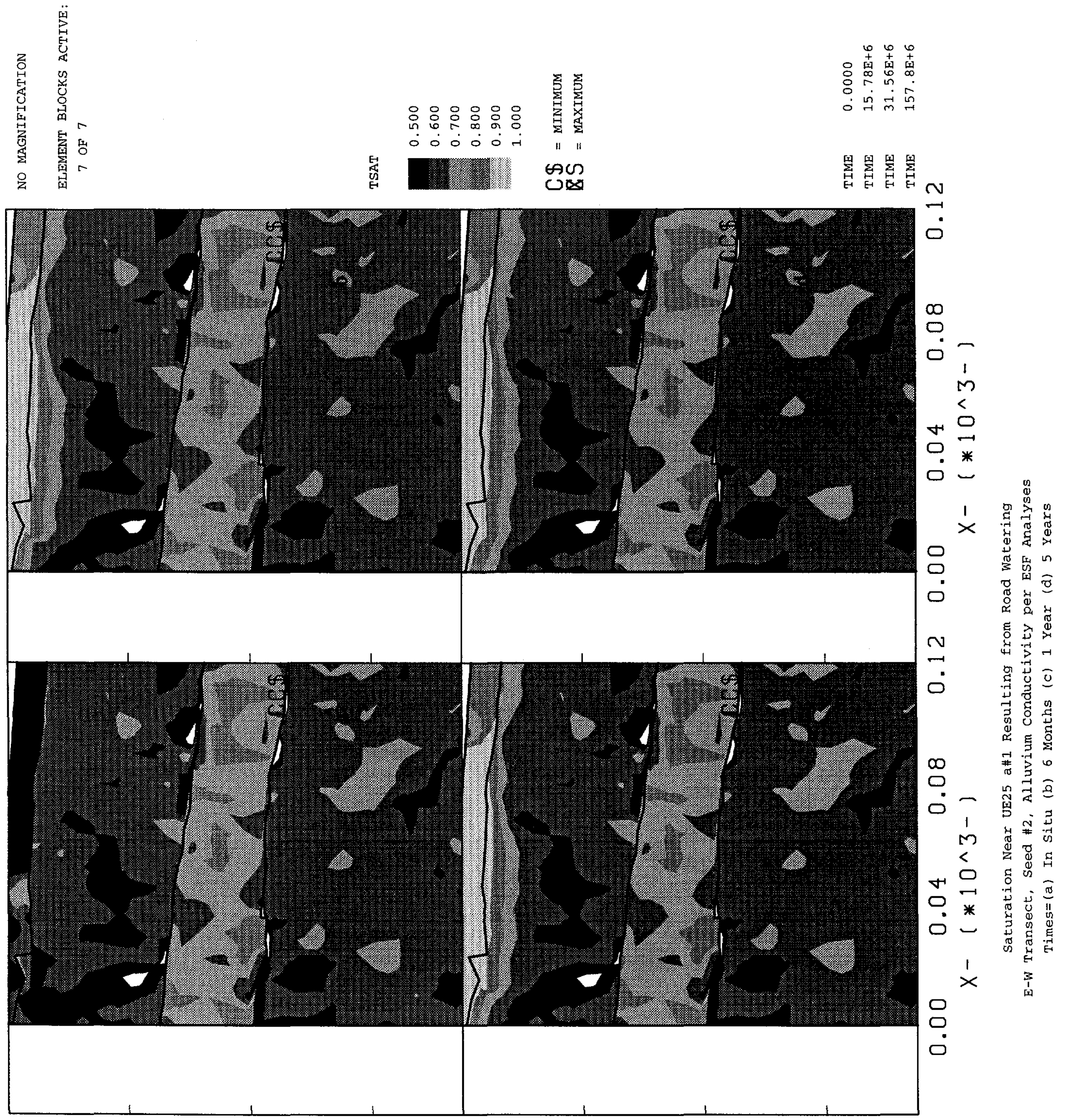

Figure 4.4-33: ΔSat, 5-Year Road Watering Period, E-W Orientation, Seed 2

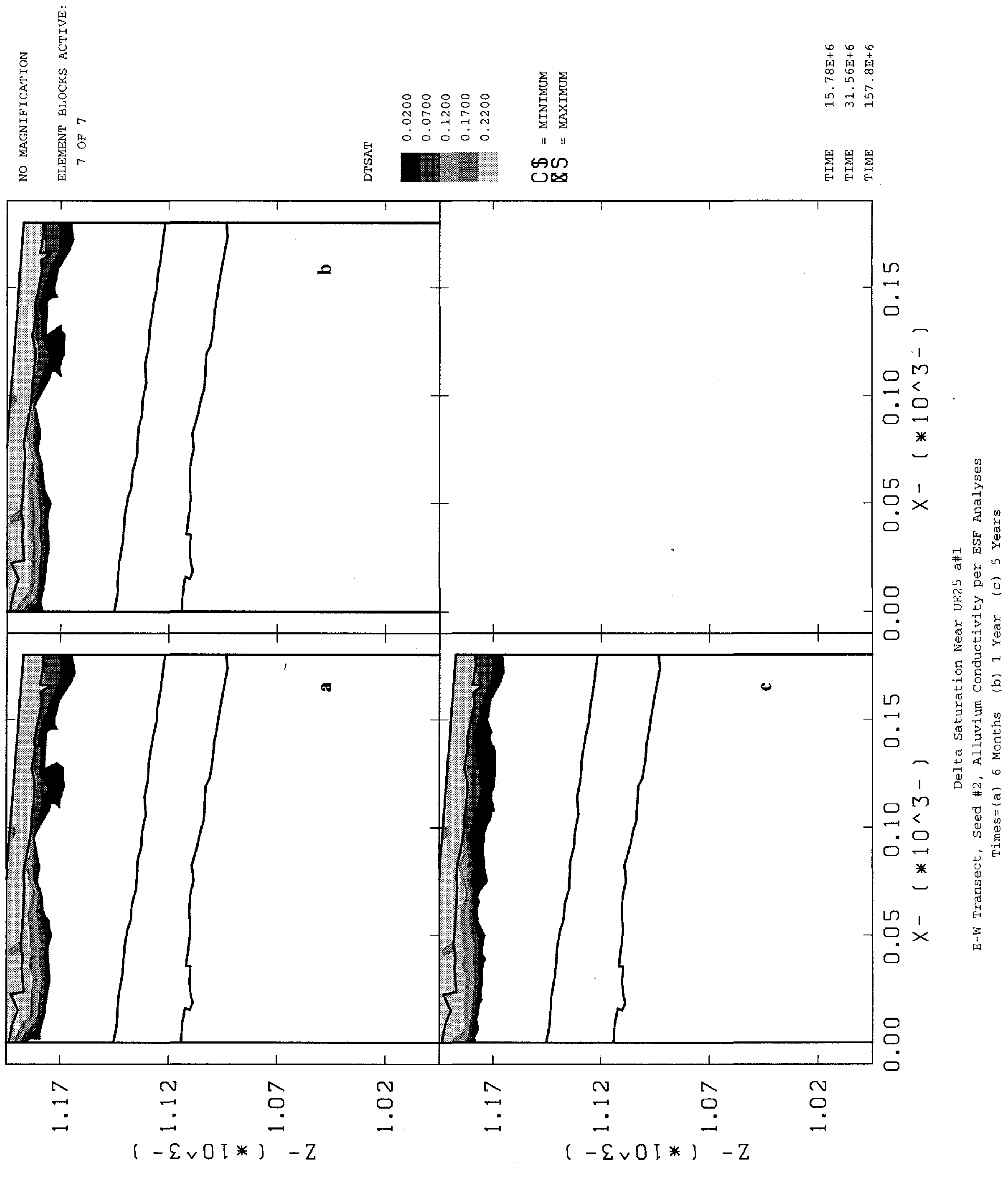

Figure 4.4-34: ΔSat Through 1000 Years
E-W Orientation, Seed 2

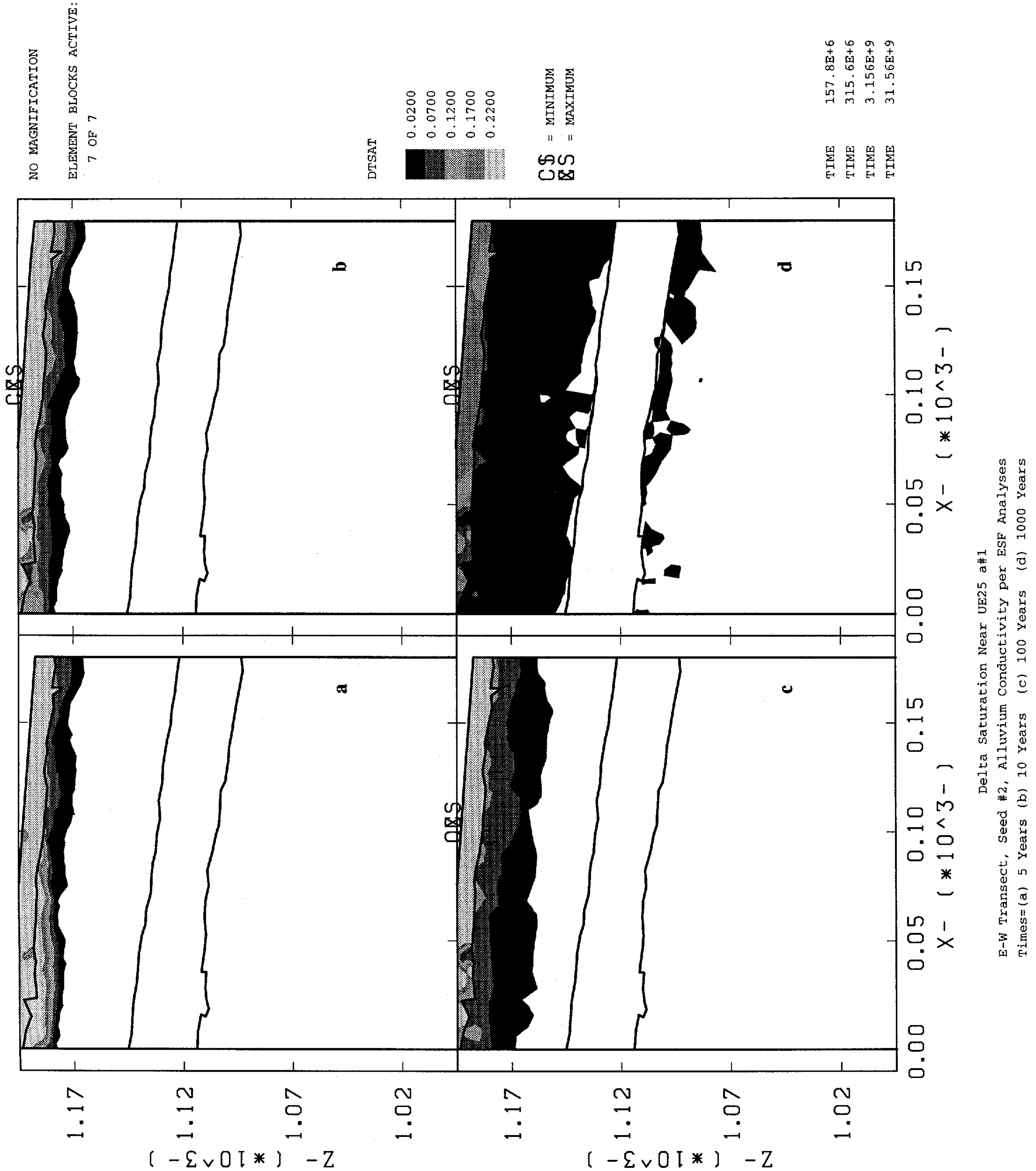

Figure 4.4-35: ΔSat at 10,000 Years
E-W Orientation, Seed 2

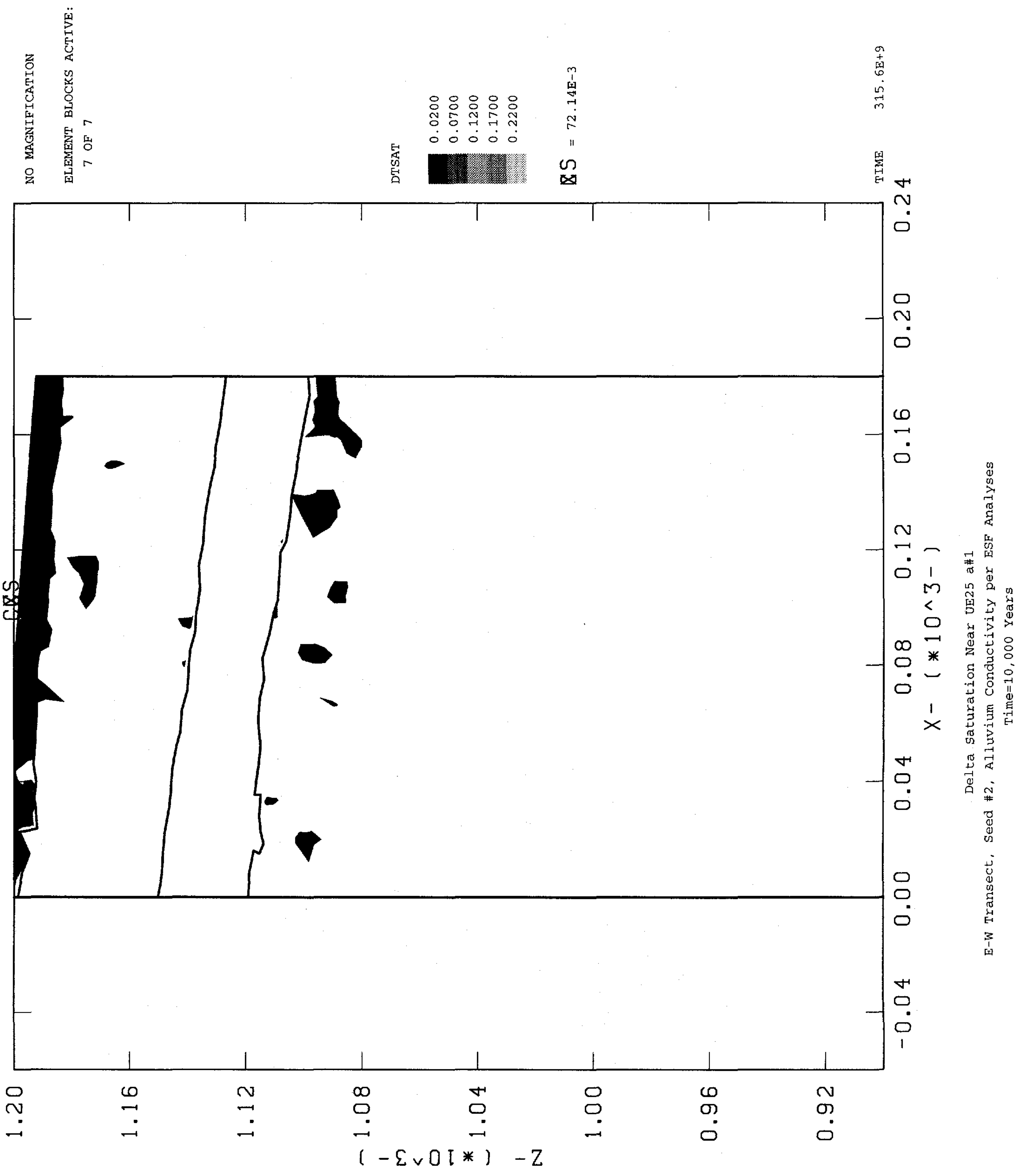

Figure 4.4-36: In Situ Saturation, E-W Orientation, Seed 4

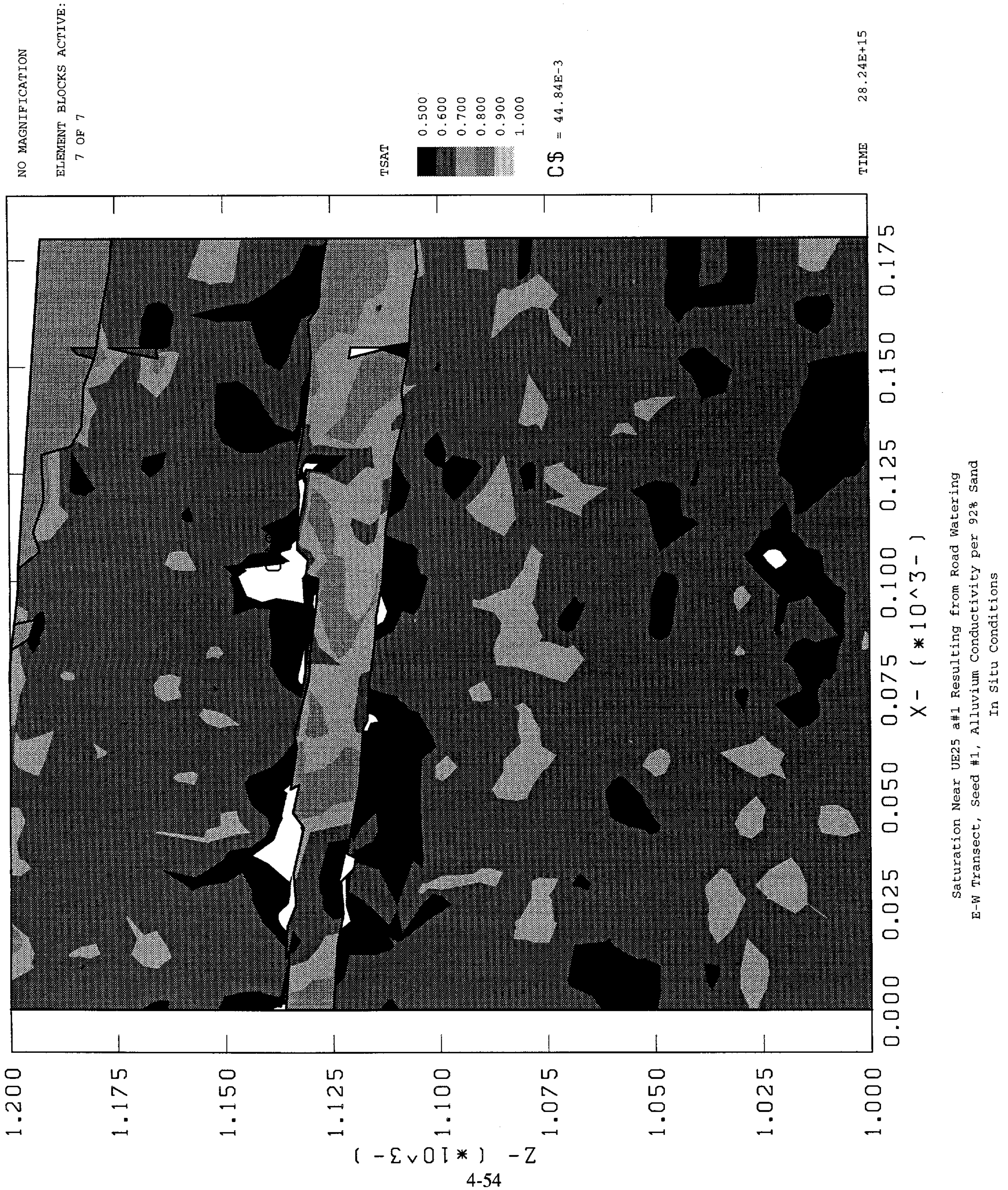

4.5 Conclusions

This was the first attempt by SNL to perform postclosure performance assessment analyses to model the movement of surficial water using a two-dimensional, isothermal, single-phase flow code (NORIA-SP) and heterogeneous material hydrological properties. These properties were derived from geostatistical calculations using measured data from several boreholes in and around Yucca Mountain as conditional data. The hydrological calculations showed a very high sensitivity of the degree of infiltration and migration of the water to the distribution of properties at the near surface (alluvium and welded Tiva Canyon units). Several problems were encountered in running these calculations: the inconsistent modeling of the thickness of the alluvium layer; the inability to achieve steady state flow to predict in situ conditions; and the creation of instability in the execution of the numerical codes due to pressures (thus, saturations) at certain nodes attaining unrealistic values. These problems indicate the sensitivity of the computational code to pressure and conductivity gradients and grid generation. The accumulation of additional site data will address the first two problems; it might also indirectly diminish the other two problems, although they could be caused by either the nature or the implementation of the flow code used. Regardless of these problems, some important observations about how PA analyses are sensitive to the characterization of the geohydrological properties of Yucca Mountain may be made. The primary results of these calculations are the identification of several site characterization and analytical methodology issues described below.

4.5.1 Recommendations

No specific recommendations for the ESF Design Requirements Document (ESFDR) have been identified from this study. A general recommendation for site characterization is the need for additional site data on the spatial distribution of alluvium, including thicknesses, porosities, pore size or grain size distribution (including correlation of that distribution to location and depth), and hydraulic conductivity. Site test data regarding water infiltration and evaporation from alluvial soils would also provide much needed support to the performance of postclosure PA analyses. Much of the current work being performed by USGS and SNL will meet these needs, although there is still some effort required to establish how much information is sufficient.

4.5.2 Observations from the Calculations

One of the most interesting observations to be made from these calculations is the way in which TCw seems to act as a barrier to downward flow of water. There are several potential explanations for this behavior, which is much more pronounced here than it was for Sobolik and Fewell (1993). TCw is a highly fractured, low porosity, welded tuff, and it is to be expected that it would have little capacity for storing surficial water. The value of saturated hydraulic conductivity for TCw used in previous PA analyses is 9.7×10^{-12} m/s (Peters et al., 1984); the corresponding value derived from the mean value of porosity from the borehole data was 1.31×10^{-11} m/s, and nearly all the values for saturated conductivity calculated for each of the TCw cells was within one order of magnitude of this value. Figure 4.5-1 compares the van Genuchten-based relative conductivity curve of Klavetter and Peters (Peters et al., 1984; Klavetter and Peters, 1986) with Brooks-Corey, geostatistically-based curves (calculated from two typical cells described in Table 4.5-1 that were modeled in the NORIA-SP calculations; the curves from most cells look similar). As a function of saturation, the two relative conductivity curves are very similar. However, as Figure 4.5-2 demonstrates, the relationships between matrix saturation and suction pressure can be significantly different, and this difference may explain the behavior observed in the numerical calculations. Robey (1994) observed that moisture retention curves derived for individual geostatistical grid points tend to be steep much like the van Genuchten curves, but the steepness is usually lost when the relevant material properties are volumetrically averaged during the upscaling to a computational grid. Note that currently there is little information to guide the upscaling of moisture retention curves. Steady-state calculations using either set of properties and moisture retention curve models yield similar values for the in situ saturation in TCw (65%-80%), but the corresponding suction pressures predicted for by the current calculations are much less than for previous calculations (e.g., Sobolik and Fewell, 1993). The resulting pressure gradient is smaller, which would tend to predict the barrier-type behavior observed here. Information and capabilities which would greatly enhance the understanding of flow through TCw include the further development of flow models such as dual permeability, more definitive fracture information (conductivity, moisture retention properties), and particularly a greater understanding of how to properly scale data measured from core-size samples to the size of computational grid cells (especially relating to moisture retention curves).

Table 4.5-1: Incomplete Gamma Function Parameters for Two Typical TCw Cells

	Cell 1	Cell 2
B.C. Parameter=	6.22641	7.02406
ave(r) (μm)=	0.111982	0.148206
σ(r) (μm)=	0.360711	0.283584

Figure 4.5-1: Tiva Canyon Moisture Retention Curve: Klavetter and Peters versus Geostatistical

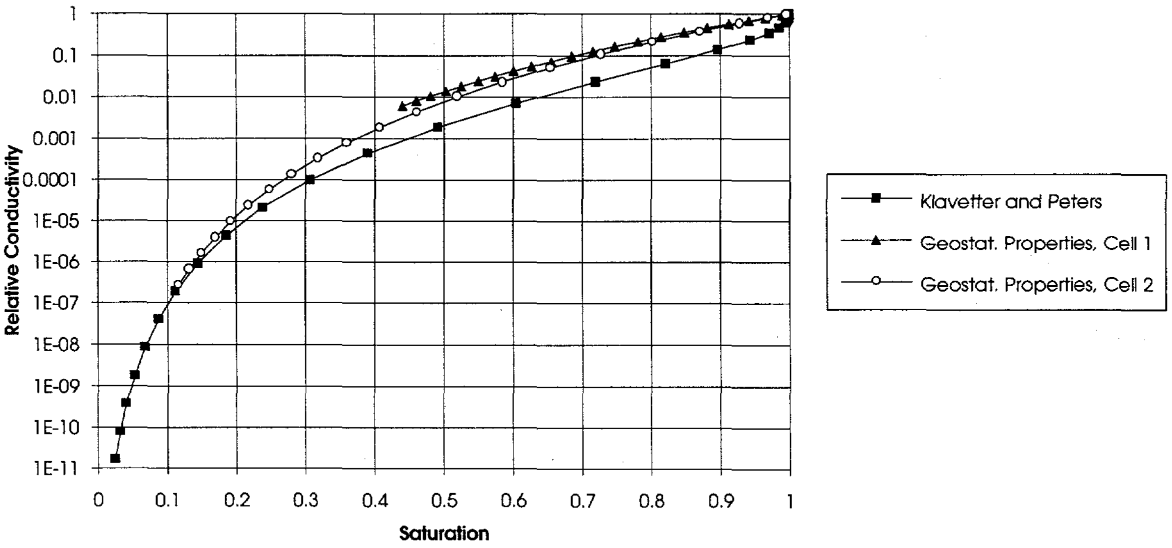

Figure 4-5.2: Comparison of Saturation versus Suction Pressure for Different Moisture Retention Curves

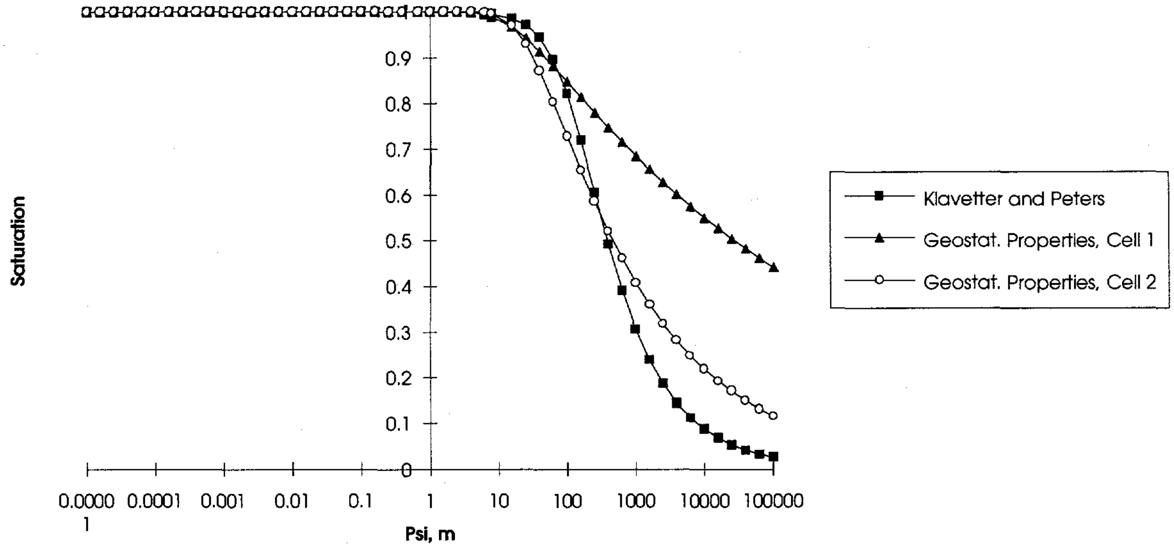

The phenomena regarding the alluvium properties discussed in Section 4.3.3 deserve further investigation here. Because the problems experienced in the calculations for Alluvium Case 3 were similar to the problems experienced for Alluvium Case 2, this discussion will continue by comparing the results of Alluvium Cases 1 and 2 only. Two observations can be made which might explain the cause of the computational problems and illustrate the sensitivity of flow calculations such as these to the modeling of unsaturated flow. The first observation concerns the surface infiltration rate used for the steady-state calculations, 0.01 mm/yr (or, in SI units, 3×10^{-13} m/s). For steady-state flow calculations, it would not be unexpected for the resulting capillary pressure field (particurly in the TCw unit) to correspond to a field of hydraulic conductivity values equal to the surface infiltration rate. Such a result was predicted for Alluvium Case 1; the predicted values for capillary pressure in TCw were approximately 400 m, with a fairly uniform vertical gradient and little horizontal variability. Because the values for saturated hydraulic conductivity for TCw tend to be in the 10^{-11} to 10^{-12} m/s range, values of relative conductivity of between 0.1 and 0.01 would correspond to a steady-state flow of 3×10^{-13} m/s. Figure 4.5-1 confirms that the relative conductivity for TCw indeed fell within the range of 0.01-0.1 for the predicted in situ saturation range of primarily 50%-70%. The capillary pressure in alluvium for Case 1 was predicted to be in the range of 380-420 m; this corresponds to saturations in the 50%-60% range. As the saturated hydraulic conductivity used for alluvium in all cases was 5×10^{-7} m/s, a value of relative conductivity of approximately 10^{-6} is required for the conductivity to be equal to the infiltration rate. As can be seen from Figures 4.3-1 and 4.3-2, such a low relative conductivity would require a saturation in alluvium near 5%, which for Case 1 represents a capillary pressure of at least 10,000 m!

The capillary pressures predicted for Alluvium Case 2 below TCw were essentially the same as for Case 1. There was a significantly different pressure gradient predicted in TCw and alluvium.

While the capillary pressure in TCw is still approximately 400 m, the pressure in alluvium ranges from 400 m near TCw to less than 150 m at the surface. The corresponding values for saturation in alluvium were approximately 1% near TCw to 5% at the surface. These values of saturation correspond directly to values of relative conductivity of approximately 10^{-6}, or in other words a steady-state flowfield where the hydraulic conductivity is approximately equal to the infiltration rate. The pressure differential between the alluvium and TCw in these steady-state calculations (~250 m) is much greater that those for the original calculations for the road watering problem (~120 m) (Sobolik and Fewell, 1993), and for Alluvium Case 1 described earlier. This relatively large pressure differential might explain some of the computational problems encountered when the road watering problem was attempted using the steady-state conditions of Alluvium Case 2 as the initial conditions.

The results obtained by the two sets of calculations for the 92% sand models showed a similar disposition to predict capillary pressures which would cause hydraulic conductivities in the sand and TCw to approximately equal the infiltration rate. The resulting pressure differential predicted for Case 2 was larger than that for Case 1. The sub-micron-scale values for ave(r) and σ for Case 1 are much smaller than what is thought to be typical for alluvial soils around Yucca Mountain, but its steady-state results indicated it would be the more likely of the two cases to run to a completed solution.

The second observation which might explain the computational problems is the unusual computational cell identified as an alluvium cell and located next to TCw. The Case 2 calculations predicted that an in situ saturation of 24% at one node. This saturation was exceedingly large compared to those of surrounding alluvial nodes, and was due to the ave(r) and σ calculated for this cell from the volumetrically-averaged porosity produced from the GAG program. The algorithms used to construct computational cells of minimal heterogeneity rely on vastly different values of porosity to perform this function. Because the PDF used for porosity in alluvium models an average porosity close to that for TCw, a few of the computational cells constructed as input to the NORIA-SP had some questionable values for porosity, average pore size, and standard deviation of pore size. This problem illustrates that more experience is required in determining scaled parameters from core-sample data, and that much more porosity and hydrological data for alluvium is required.

As has been discussed in previous analyses (see Sobolik and Fewell, 1993), there are several general limitations and assumptions associated with the flow model as implemented in NORIA-SP: the use of the equivalent continuum model as opposed to a dual permeability or discrete fracture model; the lack of an evapotranspiration model in the code; the choice of the Brooks-Corey model for the moisture retention curve, as opposed to a van Genuchten or hysteretic approach; and the fact that NORIA-SP models the flow as single-phase, with no air or vapor-phase components. These limitations and assumptions are discussed in greater detail in Chapter 8.

5.0 Sensitivity of the Evaluation of Water Movement to Fracture/Matrix Characterization

(Ho, Dunn)

5.1 Introduction

Previous analyses have considered water movement in the Topopah Spring welded unit (TSw2) resulting from flooding of the ESF tunnel (Dunn and Sobolik, 1993). In those studies, the equivalent continuum model (ECM) was used to represent fracture flow in the TSw2. In this study, alternative conceptual models of fracture flow are introduced and used to examine the sensitivity of the water movement to different models of fracture flow. Both the dual porosity (fracture flow only) and dual permeability (fracture and matrix flow) models are considered in this study. In addition, sensitivity analyses are performed on the equivalent continuum model to investigate the effects of aperture size and fracture permeability on water movement in the unsaturated fractured rock.

5.2 Alternative Conceptual Models of Fracture Flow

Three alternative conceptual models of fracture flow are considered in this study: the equivalent continuum model, the dual porosity model, and the dual permeability model. The following sections will describe each model in detail.

5.2.1 Equivalent Continuum Model

The equivalent continuum model represents flow in a partially saturated fracture-matrix system by assuming that the pressures in the matrix and fractures are equal. The governing equations for flow in this system are identical in form to the governing equations for flow in partially saturated porous media (Klavetter and Peters, 1986; Dudley et al. 1988). Therefore, the fracture-matrix system is effectively modeled as a single, composite medium whose properties are derived from volume averaged fracture and matrix properties. The following equations give the bulk porosity, ϕ_b, saturation, S_b, and permeability, k_b, of the composite material as a function of the porosity, saturation, and permeability of the matrix (subscript *m*) and fractures (subscript *f*):

$$\phi_b = \phi_f + (1-\phi_f)\,\phi_m \tag{5-1}$$

$$S_b = \frac{S_f\,\phi_f + S_m\,(1-\phi_f)\,\phi_m}{\phi_f + (1-\phi_f)\,\phi_m} \tag{5-2}$$

$$k_b = k_m\,(1-\phi_f) + k_f\,\phi_f \tag{5-3}$$

If unsaturated flows are being investigated, these relations must be used in conjunction with expressions relating liquid saturations and relative permeabilities to capillary pressure. In the multiphase, multidimensional code TOUGH2 (1991), the van Genuchten two-phase characteristic functions defined below for the fractures and matrix have been implemented:

$$S^* = [1+(\alpha_j P_c)^{\beta j}]^{-\lambda} \tag{5-4}$$

$$k_{r,j} = \frac{\left[1-(\alpha_j P_c)^{\beta_j - 1}\left[1+(\alpha_j P_c)^{\beta_j}\right]^{-\lambda_j}\right]^2}{\left[1+(\alpha_j P_c)^{\beta_j}\right]^{\lambda_j/2}} \tag{5-5}$$

where $\lambda = 1 - 1/\beta_j$, $S^* = (S_j - S_r)/(1 - S_{r,j})$, j = matrix or fracture

S is the liquid saturation, S_r is the residual liquid saturation, P_c is the capillary pressure, k_r is the liquid relative permeability, and α and β are curve-fitting parameters. Since TOUGH2 requires capillary pressures and relative permeabilities as a function of liquid saturation, the following method is used in TOUGH2 to obtain a table of capillary pressures and effective (composite) relative permeabilities as a function of effective (composite) saturations:

1) Use Equation (5-4) to obtain S_m and S_f for a given P_c
2) Use Equation (5-2) to obtain the effective saturation, S_b, for that P_c
3) Use Equation (5-5) to obtain $k_{r,m}$ and $k_{r,f}$ for the given P_c
4) Use $k_{r,m}$, $k_{r,f}$, and Equation (5-3) in the following equation to obtain the effective liquid relative permeability for the given P_c:

$$k_{b,r} = \frac{k_{r,m}k_m(1-\phi_f) + k_{r,f}k_f\,\phi_f}{k_b} \tag{5-6}$$

5) Tabulate the effective saturation, S_b, and the effective liquid relative permeability, $k_{b,r}$ for the given P_c (the gas-phase relative permeability is taken to be 1-$k_{b,r}$)
6) Repeat steps 1–5 using a different P_c

Figure 5.2-1(a) shows the capillary pressures as a function of liquid saturation, and Figure 5.2-1(b) shows the liquid relative permeabilities as a function of capillary pressures for the fracture, matrix, and composite materials. The properties that were assumed for the matrix and fractures are given in Table 5.2-1. Figure 5.2-1(a) shows that the capillary pressures of the composite material used in the ECM are nearly identical to the capillary pressures of the matrix for the set of van Genuchten parameters used in this study. Figure 5.2-1(b) shows that the relative permeability of the composite material matches the fracture relative permeability at low capillary pressures ($\leq 10^4$ Pa), but at higher capillary pressures the composite relative permeability follows more closely with that of the matrix.

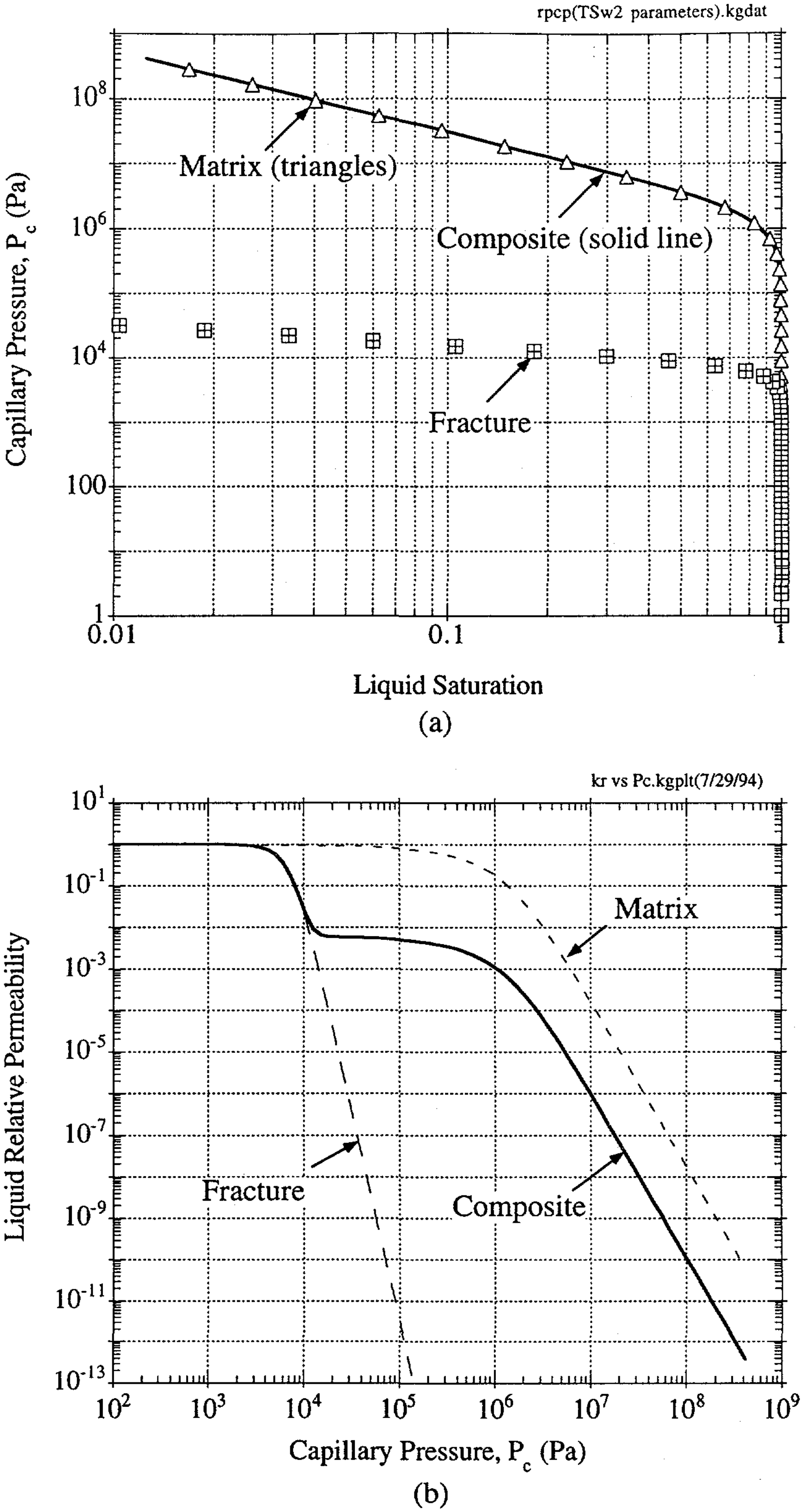

Figure 5.2-1. Two-phase characteristic curves of the fracture, matrix, and composite material: a) capillary pressure as a function of liquid saturation b) liquid relative permeability as a function of capillary pressure.

Table 5.2-1. Summary of fracture and matrix parameters used to calculate effective (composite) parameters for the equivalent continuum model†.

	matrix	fracture
permeability (m^2)	1.9×10^{-18}	1.7×10^{-12}
alpha parameter (Pa^{-1})	5.8×10^{-7}	1.3×10^{-4}
beta parameter	1.798	4.23
porosity	0.11	1.80×10^{-4}
residual liquid saturation	0.00	0.00

†The properties listed in Table 5.2-1 were taken from Dunn and Sobolik (1993) and represent the TSw2 unit of Yucca Mountain. Note, however, that the residual liquid saturation was set to zero in both materials in order to avoid numerical problems at low liquid saturations. The fracture aperture and density were assumed to be 4.55 mm and 40 fractures/m^3, respectively.

5.2.2 Dual Porosity and Dual Permeability Models

The equivalent continuum model is only valid for conditions when the pressures in the matrix and fractures are in equilibrium. In the studies presented here, rapid infiltration through the fractures from the flooded ESF tunnel may result in non-equilibrium pressure distributions in the matrix and fractures. As a result, the dual porosity and dual permeability models were considered to address this issue.

The dual porosity model has been formulated by previous investigators (Barenblatt et al., 1960; Warren and Root, 1963; Odeh, 1965) and implemented into numerical models (Pruess and Narasimhan, 1985). The basic principle in this model is that the fractures and matrix blocks are treated as separate, discrete entities. The fractures are lumped into one continuum, while the matrix blocks are lumped into another. The fractures and matrix blocks are then allowed to communicate through a mass transfer function. However, global flow is restricted to the fractures only. Therefore, the matrix blocks only act as a capacitance to the fractures at any local point.

The dual permeability model is similar to the dual porosity model, but in this approach the matrix blocks are connected to one another within the continuum. Therefore, flow can occur within both the fractures and matrix continua, as well as between fractures and matrix blocks. While this approach is more rigorous, application of the dual permeability model to unsaturated flow problems appears to be limited due to the increased computational requirements associated with this method.

The multiphase, multidimensional code TOUGH2 (Pruess, 1991) that was used in this study is capable of generating both the dual porosity and dual permeability models. When the dual porosity or dual permeability model is invoked, an existing primary mesh is duplicated and connections are established between the elements of the two meshes. The two meshes represent the fracture and matrix continua, and the connection area between fracture and matrix elements depends on parameters such as fracture porosity, fracture spacing, and grid block size (see Pruess, 1983, for complete details). As shown in Figure 5.2-2, a computational grid block can contain multiple matrix blocks depending on the specified fracture spacing. As a result, the interfacial area between fractures and matrix blocks will depend on the grid block size. In addition, the fractures are connected over an entire matrix block length as shown on the left side of Figure 5.2-2 (fracture

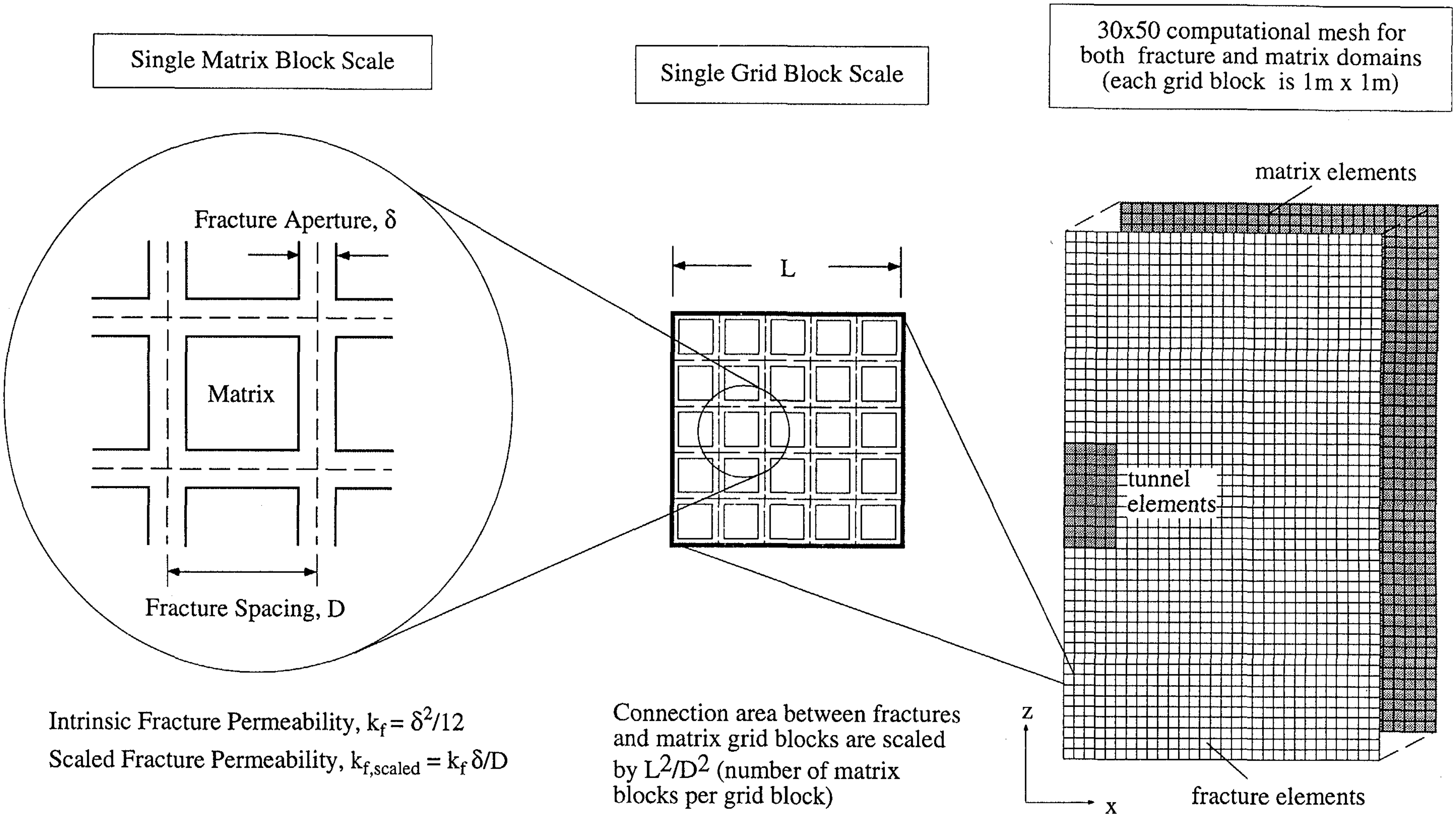

Figure 5.2-2. Conceptualization of the scaling behavior used in two-dimensional, dual-continuum TOUGH2 models. The TOUGH2 model uses a global computational mesh (far right) that consists of individual grid blocks (middle). The permeabilities of the grid blocks are scaled according to specified fracture spacings and apertures at the matrix block scale (far left). Interfacial areas between fracture and matrix grid blocks are also scaled.

Fig 1 dual-continua mesh.cnvs

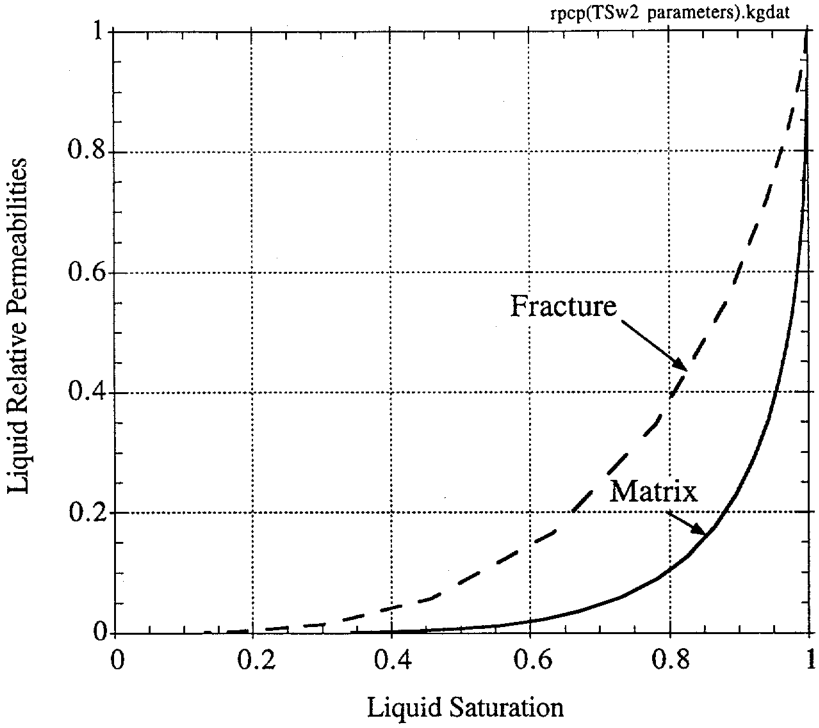

Figure 5.2-3. Liquid relative permeabilities of the fractures and matrix blocks as a function of liquid saturation used by the dual porosity and dual permeability models in TOUGH2.

5.3 The Equivalent Continuum Model of the Flooding Scenario

The equivalent continuum model of TOUGH2 was used to simulate movement of water through fractured TSw2 in response to 30 days (fewer in the case of large fractures) of flooding in the ESF tunnel. Seven different fracture apertures ranging from 4.55 to 100 μm were used in a series of calculations. The purpose was to assess the effect of fracture aperture on the rate of movement of saturation fronts in TSw2 subject to the given boundary and initial conditions of this problem.

For each fracture aperture, porosity and permeability parameters were approximated as if the fracture were a vacancy bounded on two sides by smooth flat plates:

Fracture porosity (ϕ_f) = fracture aperture × number of fractures per unit volume (40 fractures per cubic meter was assumed for each case)

Fracture permeability = aperture^2/12 (Freeze & Cherry, 1979).

Matrix permeability and porosity were those in Table 5.2-1, and the effective bulk porosity and permeability were derived using equations 5-1, and 5-4. Table 5.3-1 summarizes the porosity and permeability parameters used in the equivalent continuum model aperture variation calculations.

Table 5.3-1. Summary of fracture, matrix and effective (composite) porosity and permeability used in the aperture variation calculations.

aperture (μm)	ϕ_f	ϕ_m	k_f	k_m	ϕ_b	k_b
4.55	1.82×10^{-4}	.11	1.725×10^{-12}	1.9×10^{-18}	.1102	3.158×10^{-16}
12.5	5.0×10^{-4}	.11	1.302×10^{-11}	1.9×10^{-18}	.11045	6.51×10^{-15}
18	7.2×10^{-4}	.11	2.7×10^{-11}	1.9×10^{-18}	.1106	1.94×10^{-14}
25	1.0×10^{-3}	.11	5.2×10^{-11}	1.9×10^{-18}	.1109	5.2×10^{-14}
30	1.2×10^{-3}	.11	7.5×10^{-11}	1.9×10^{-18}	.111	9.0×10^{-14}
50	2.0×10^{-3}	.11	2.08×10^{-10}	1.86×10^{-18} *	.1118	1.67×10^{-12}
100	4.0×10^{-3}	.11	8.33×10^{-10}	1.86×10^{-18}	.11356	3.333×10^{-12}

*For 50 and 100 microns simulations, k_m was, by oversight, not rounded to 1.9×10^{-18} as for the 4.55 to 30 micron cases.

The computational mesh used in these simulations consists of a 30 × 50 grid of elements of one meter cubes as shown in two dimensions in Figure 5.3-1. The tunnel elements are shown as a 5 element × 10 element rectangular shaded region. Symmetry of the problem and a no flow vertical boundary along the center line of the tunnel allows the simulation in the right half space. Initial and boundary conditions include horizontal and vertical no flow boundaries and an initial saturation of the rock of 0.7. The tunnel elements are assigned a constant saturation of 1 for the duration of the simulation.

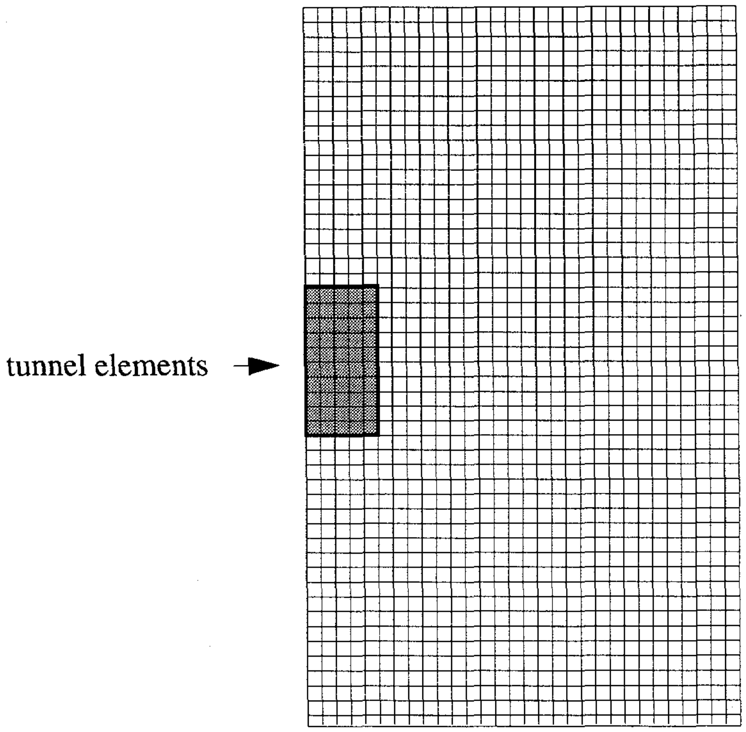

Figure 5.3-1 The computational mesh used for the aperture variation calculations consists of 30 × 50 one meter cube elements. Tunnel elements are shaded.

5.3.1 The 4.55 to 30 micron Simulations

The tunnel elements were saturated for 30 days and water was allowed to imbibe into the surrounding equivalent continuum matrix. Figures 5.3-2 through 5.3-6 show the expansion of the wetting front for each of the 5 apertures in this set of simulations. The 0.8 and 0.99 saturation contours are shown for these cases at simulation times from 0.5 to 30 days. Figure 5.3-7 summarizes the quantity of water imbibed into the half tunnel as a function of time for each of the five apertures examined.

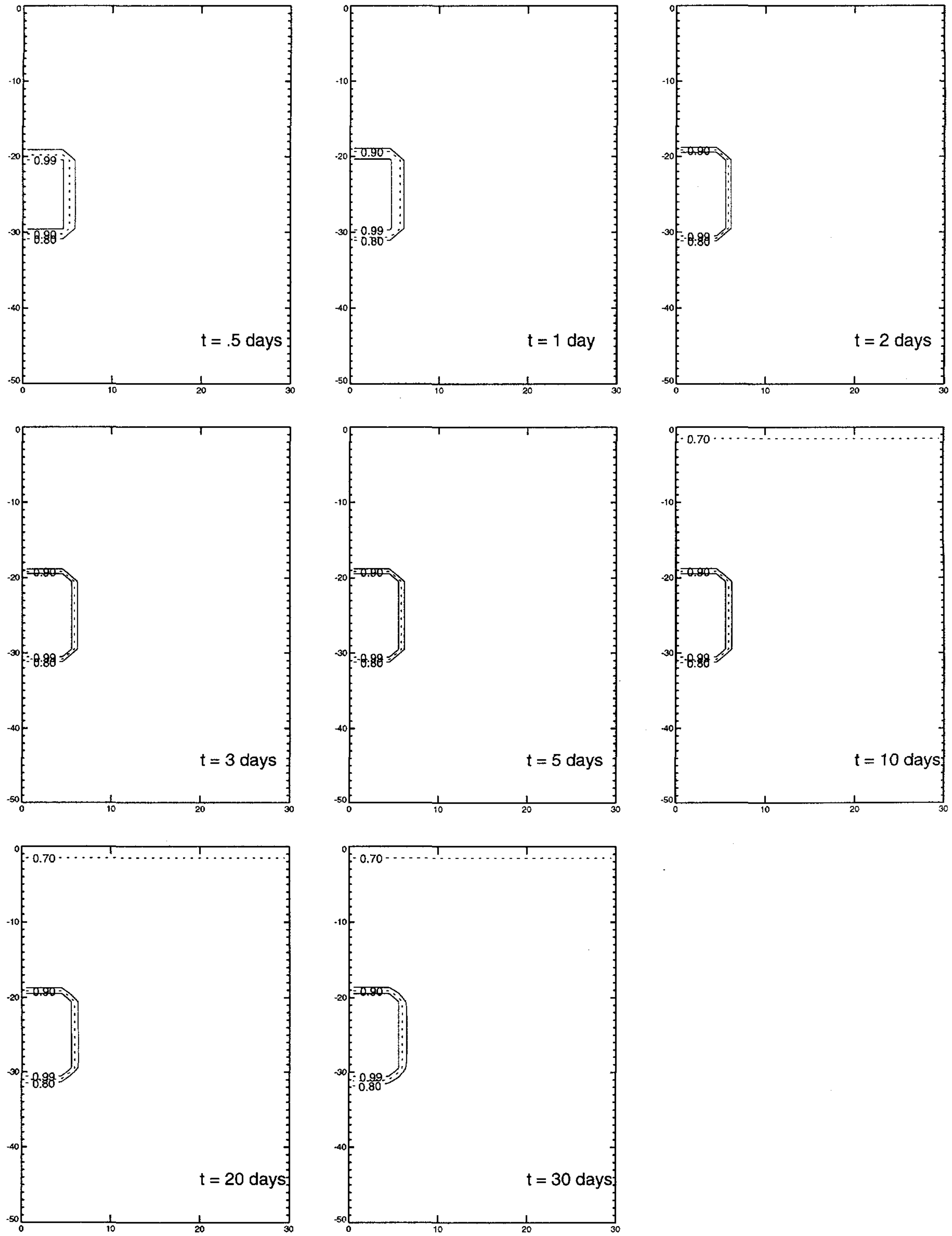

Figure 5.3-2 Equivalent continuum model prediction of saturation front movement over 30 days for 4.55 μm aperture fractures in TSw2 tuff.

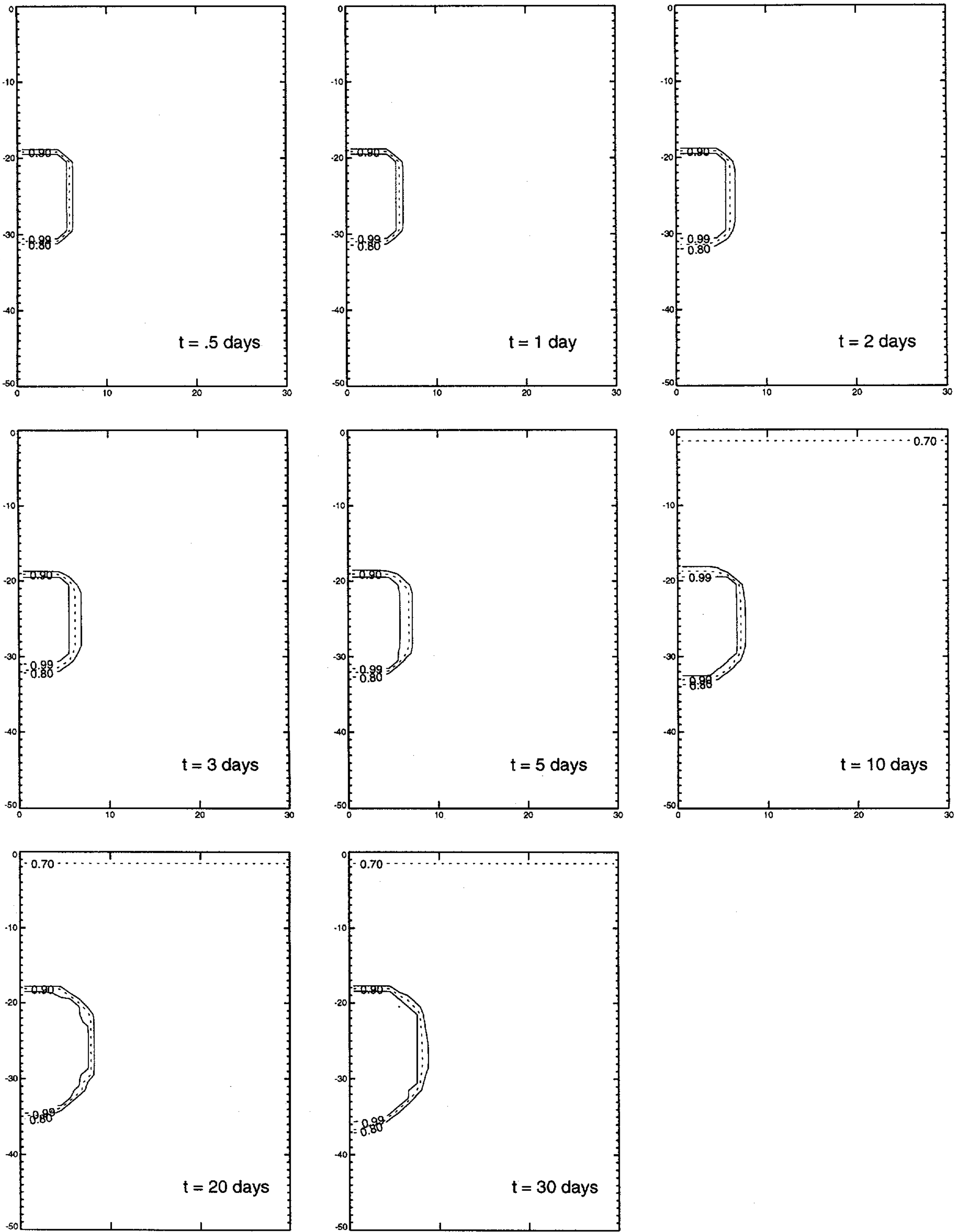

Figure 5.3-3 Equivalent continuum model prediction of saturation front movement over 30 days for 12.5 μm aperture fractures in TSw2 tuff.

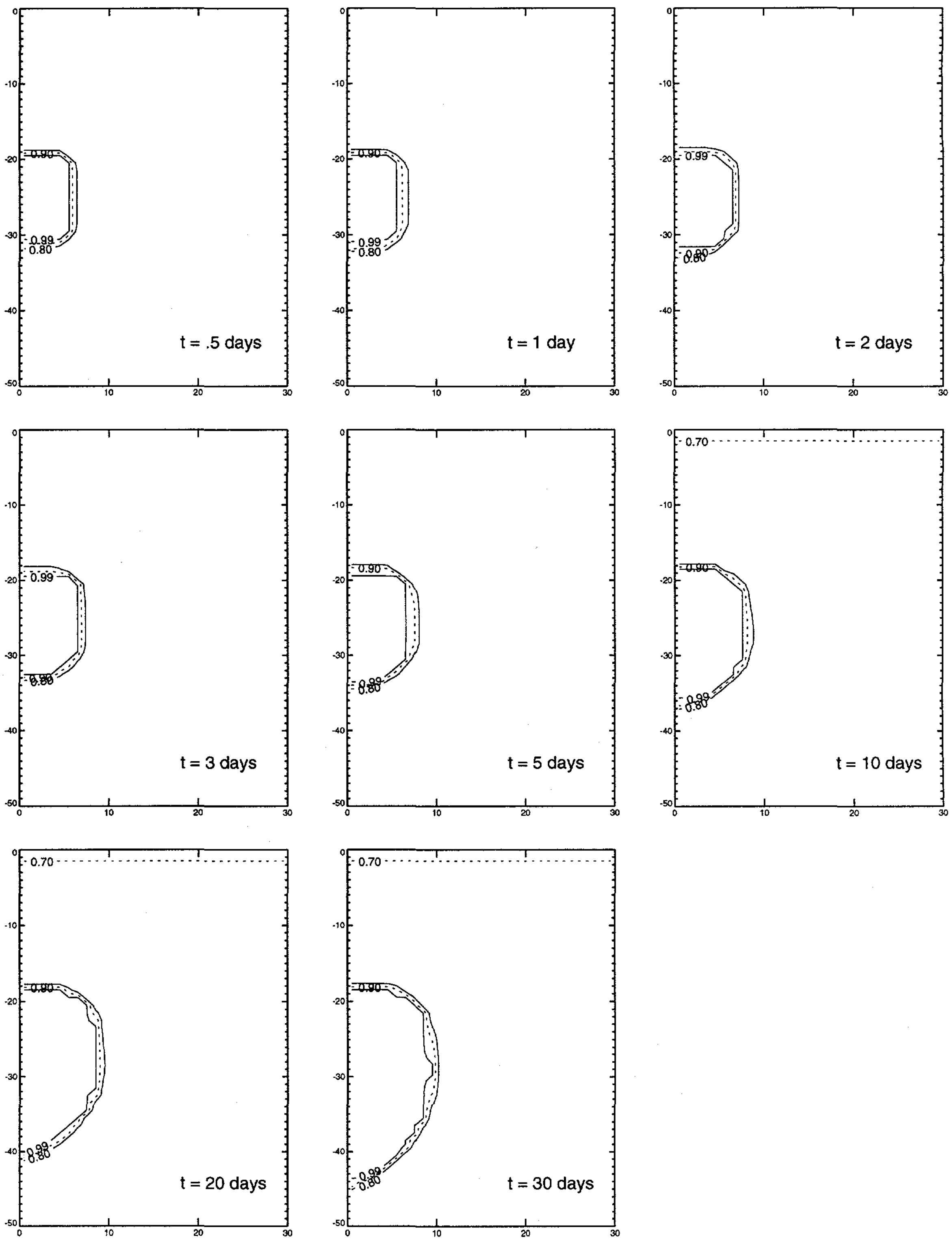

Figure 5.3-4 Equivalent continuum model prediction of saturation front movement over 30 days for 18 μm aperture fractures in TSw2 tuff.

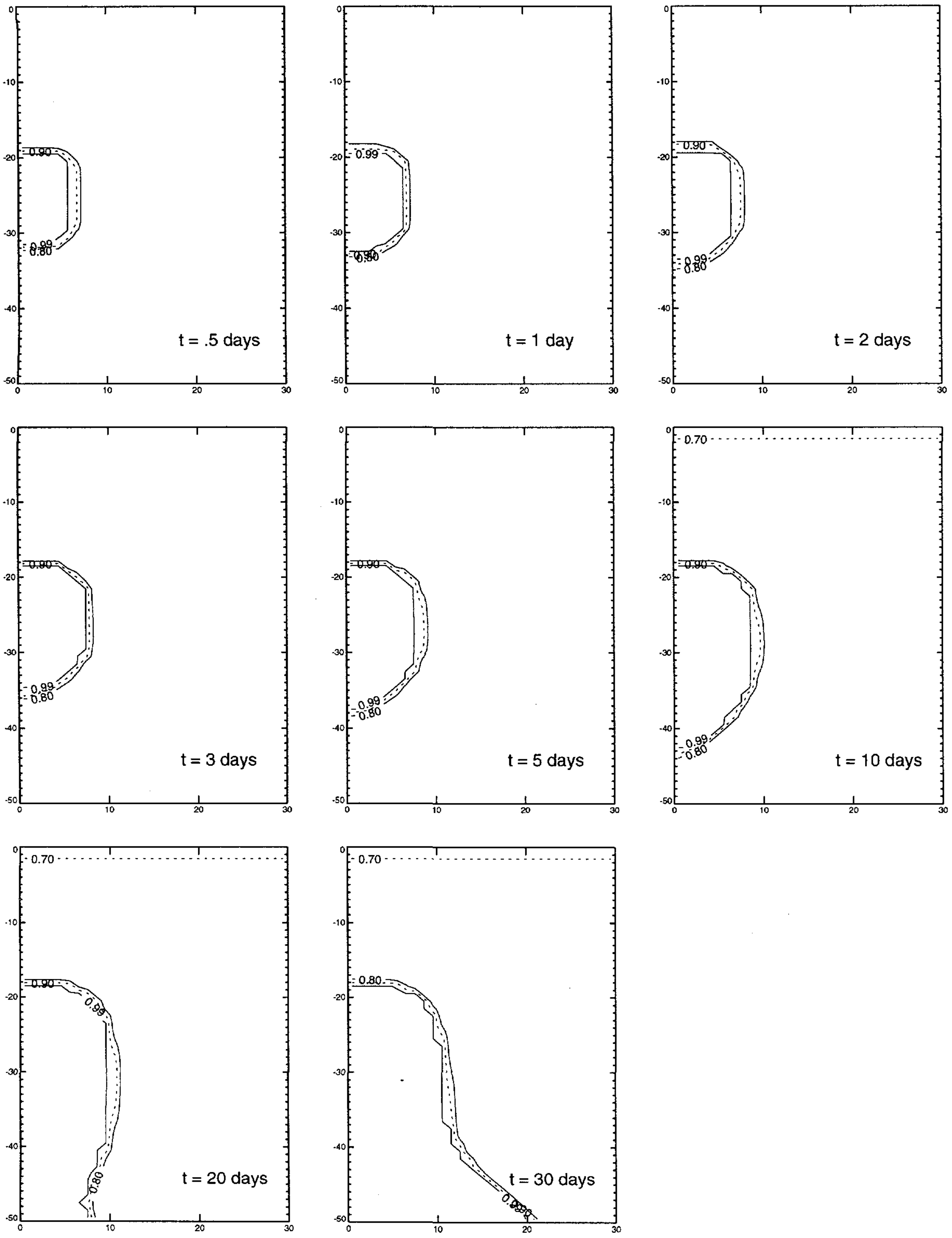

Figure 5.3-5 Equivalent continuum model prediction of saturation front movement over 30 days for 25 μm aperture fractures in TSw2 tuff. Ponding at 30 days is a result of the imposed no flow lower boundary condition.

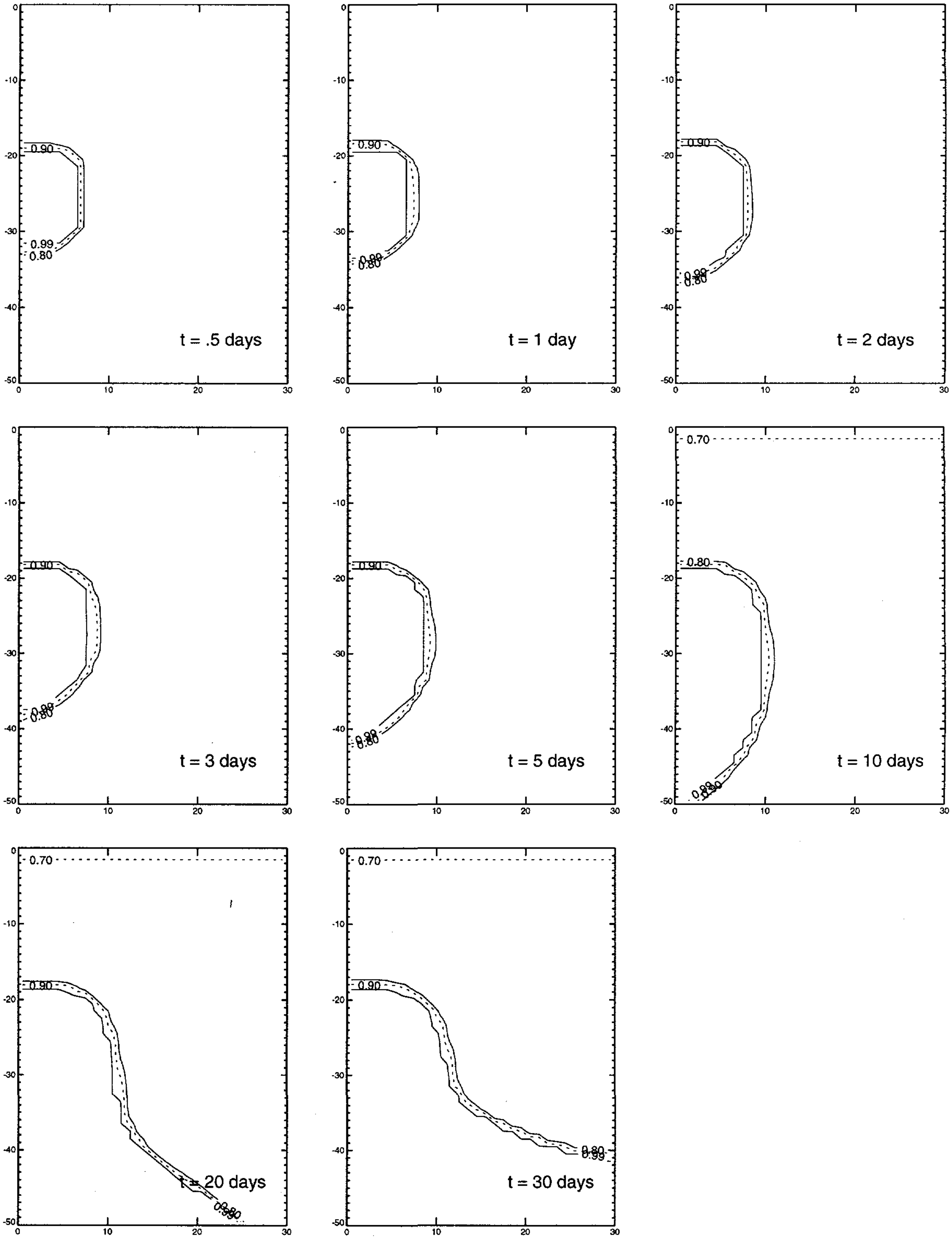

Figure 5.3-6 Equivalent continuum model prediction of saturation front movement over 30 days for 30 μm aperture fractures in TSw2 tuff.

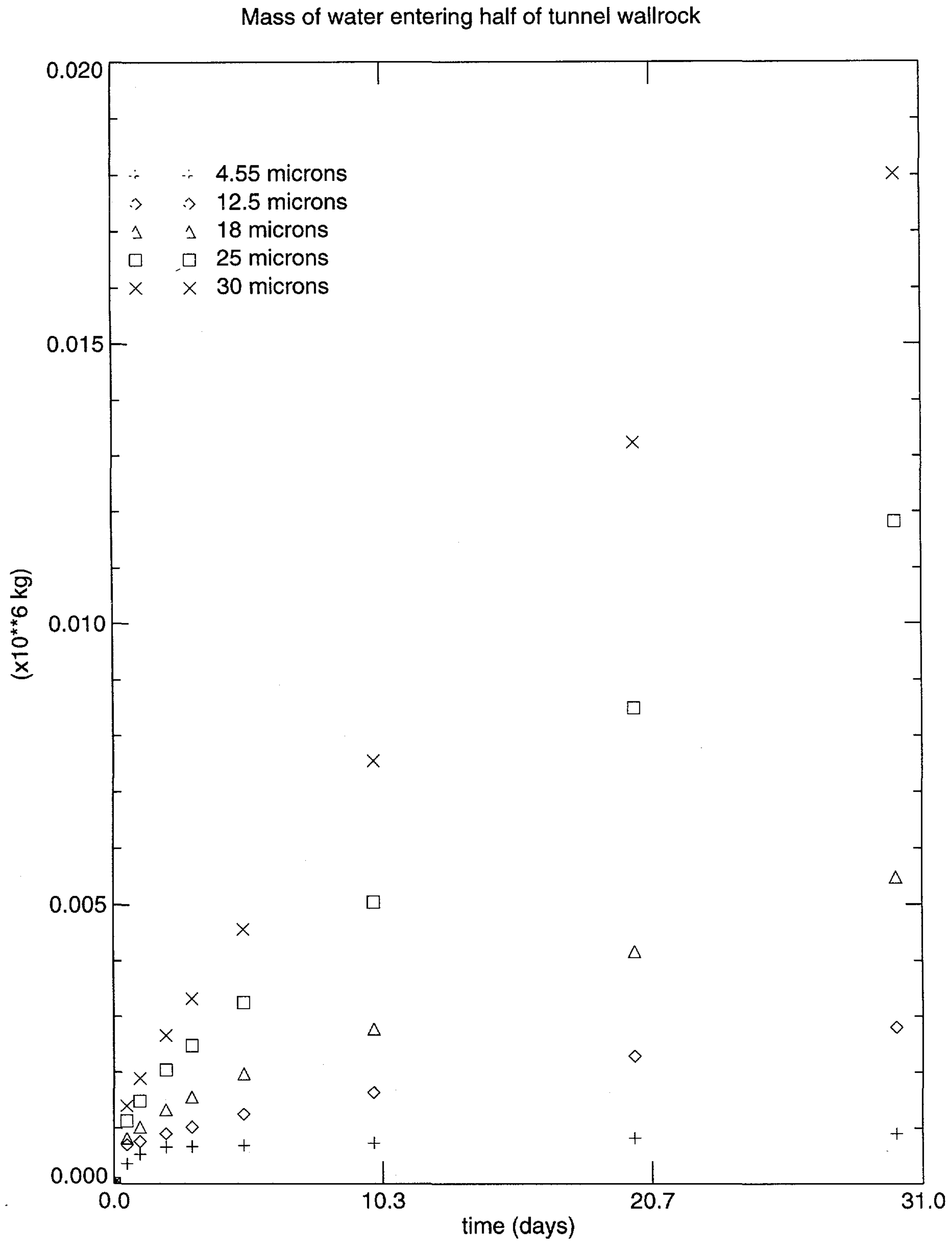

Figure 5.3-7 Equivalent continuum model prediction of the mass of water entering half of the tunnel wall rock for each of five fracture aperture calculations using TOUGH2.

Table 5.3-2 Quantity of water imbibed into TSw2 wall rock predicted by the ECM with various fracture apertures and resulting porosities and permeabilities.

aperture (μm)	ϕ_f	k_f	ϕ_b	k_b	kg	time	m^3
4.55	1.82×10^{-4}	1.725×10^{-12}	.1102	$3.158X10^{-16}$	890	30 days	.9
12.5	5.0×10^{-4}	1.302×10^{-11}	.11045	$6.51X10^{-15}$	2,810	30 days	2.81
18	7.2×10^{-4}	2.7×10^{-11}	.1106	1.94×10^{-14}	5,480	30 days	5.49
25	1.0×10^{-3}	5.2×10^{-11}	.1109	5.2×10^{-14}	11,820	30 days	11.84
30	1.2×10^{-3}	7.5×10^{-11}	.111	9.0×10^{-14}	18,010	30 days	18.05
50	2.0×10^{-3}	2.08×10^{-10}	.1118	1.67×10^{-12}	25,000	4 days	25.03
100	4.0×10^{-3}	8.33×10^{-10}	.11356	3.33×10^{-12}	25,910	4 days	25.95

Table 5.3-2 lists the total water increase in the rock at the end of 30 days. As would be expected, as the aperture size increases more water is able to penetrate the rock and water travels farther into the rock. For the 4.55 micron fracture case the gravitational influence is not discernible for the time scale examined; water is pulled uniformly away from the saturated surface in all directions. After 30 days a total of 0.9 m^3 per meter of tunnel was taken into the half region matrix. For the 12.5 micron case the gravitational effect is apparent after a few days. At the end of 30 days the 0.8 saturation contour has penetrated 2 meters above the tunnel boundary, 4 meters into the side wall, and 7 meters in the downward direction. The quantity of water imbibed has increased to 2.81 cubic meters. This trend of greater penetration and greater downward flow continues with aperture increase. At 25 microns the flow reaches the model imposed lower horizontal boundary and starts to pond. This ponding indicates that future simulations should be performed over a larger domain, or the lower boundary condition should be changed. The quantities of water imbibed for fracture aperture 25 microns and above listed in Table 5.3-2 are too low because of the ponding influence, but qualitatively the model predicts that water will flow downward from the saturated tunnel boundary at a rapidly increasing rate for aperture increases above 25 μm.

5.3.2 50 and 100 micron Simulations

When the fracture aperture was assumed as 50 μm and the associated parameters were submitted to TOUGH2 the resulting flow was so rapid that the time steps reduced and run time increased beyond an acceptable limit for the simulation. The duration for both 50 μm and 100 μm calculations was 4 days rather than 30 for the smaller fractures. Figures 5.3-8 and 5.3-9 show the 0.8 and 0.99 saturation contours at intervals over the 4 day period. In both cases the lower and vertical boundary conditions cause the region to fill with water. This filling reduces the hydraulic gradient and thus the flow so that the resulting volumes of water imbibed in Table 5.3-2 for these cases is unrealistically low (as well as being unrealistically high as a source for such quantities of water is improbable). The ECM predicts that fractures of one-twentieth to one-tenth of a millimeter will drain water ponded on TSw2 rapidly.

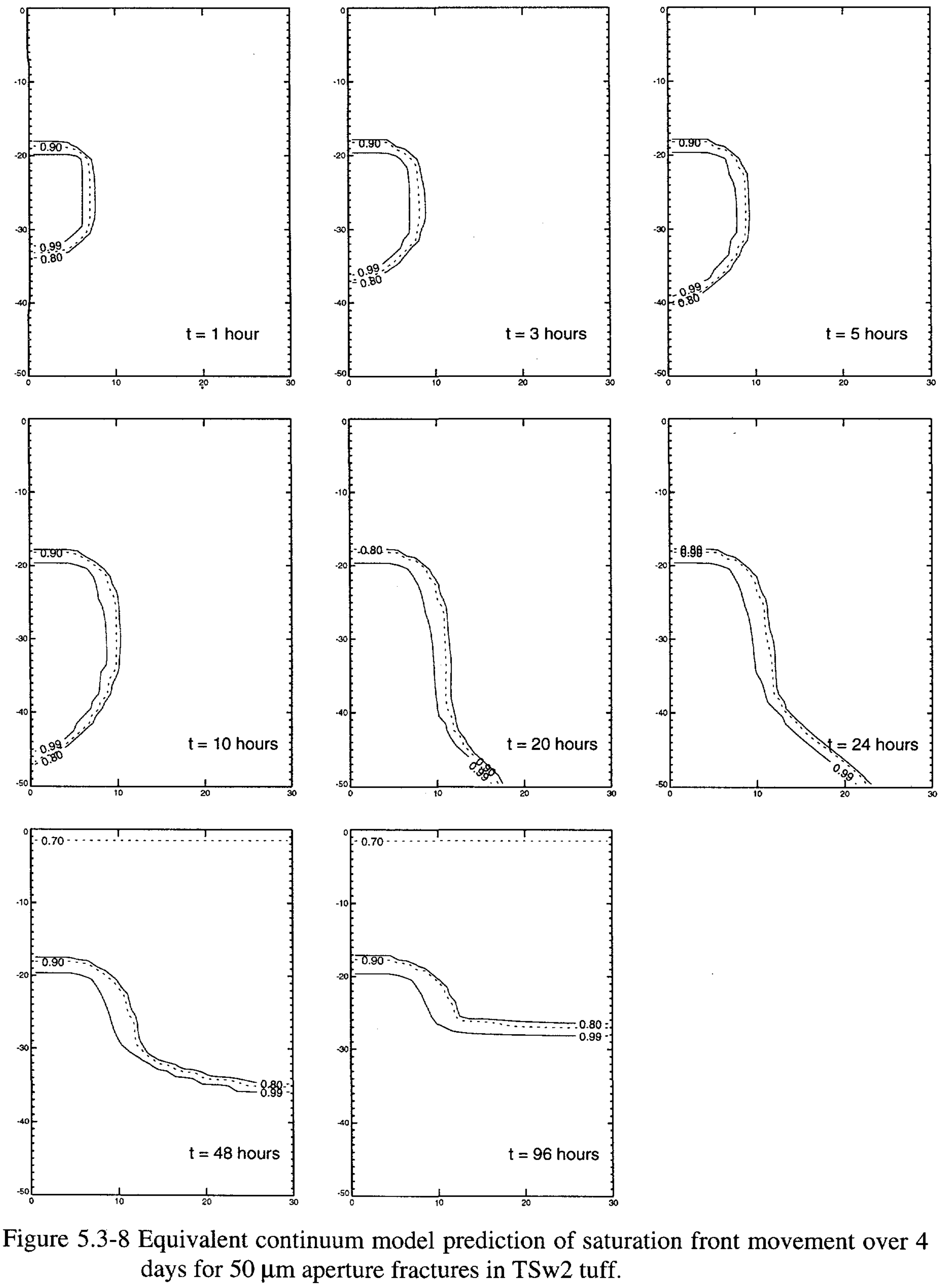

Figure 5.3-8 Equivalent continuum model prediction of saturation front movement over 4 days for 50 μm aperture fractures in TSw2 tuff.

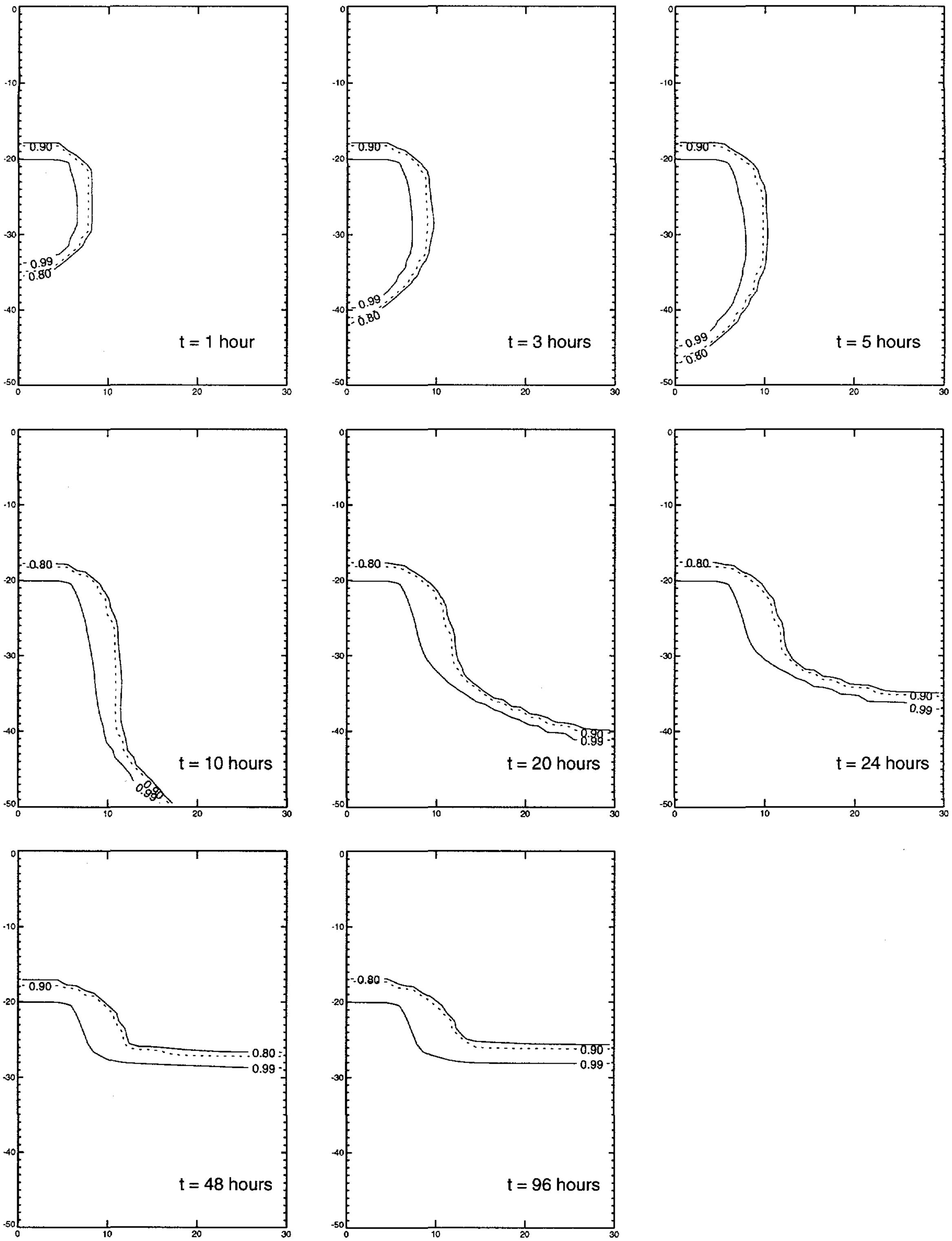

Figure 5.3-9 Equivalent continuum model prediction of saturation front movement over 4 days for 100 μm aperture fractures in TSw2 tuff.

5.3.3 Permeability Variation on the 25 μm Fracture Case

The previous simulations used a parallel plate model for the relationship between fracture aperture and permeability. The fracture is modeled as two smooth parallel plates bounding a vacancy. This model provides an upper bound for permeability for a given aperture. Rock fractures are more realistically rough and irregular. A simulation using the 25 micron fracture flooding scenario was implemented using a permeability function for the fractures defined by

$$\text{Fracture permeability} = 0.5\frac{(\delta)^2}{12}$$

This value is one half of the value used in the previous calculations. Table 5.3-3 compares the resulting parameters used for the 25 micron simulation reported above and the 25 micron simulation using the reduced permeability function value and the resulting bulk porosity and permeability found using equations 5-1 and 5-4.

Table 5.3-3 Porosity and permeability parameters used in the 25 μm ECM simulation and the 25 μm reduced permeability simulation.

aperture (μm)	ϕ_f	ϕ_m	k_f	k_m	ϕ_b	k_b
25	1.0×10^{-3}	.11	5.208×10^{-11}	1.9×10^{-18}	.1109	5.2×10^{-14}
25	1.0×10^{-3}	.11	2.604×10^{-11}	1.9×10^{-18}	.1109	2.6×10^{-14}

Figure 5.3-10 shows the ECM prediction of the saturation front movement as a function of time for the reduced permeability 25 micron aperture case. This figure should be compared with 5.3-5 to see the effect of the reduced permeability function. Table 5.3-4 compares the volume of water imbibed for the two cases; but, as cautioned before, the cases that reach ponding underpredict the quantity of water imbibed using the ECM.

Table 5.3-4 Comparison of the water imbibed for two models of permeability for the 25 μm aperture flooding of TSw2 scenario

aperture (μm)	ϕ_f	k_f	ϕ_b	k_b	kg	time	m^3
25	1.0×10^{-3}	5.208×10^{-11}	.1109	5.2×10^{-14}	11,820	30 days	11.84
25	1.0×10^{-3}	2.604×10^{-11}	.1109	2.6×10^{-14}	6,790	30 days	6.8

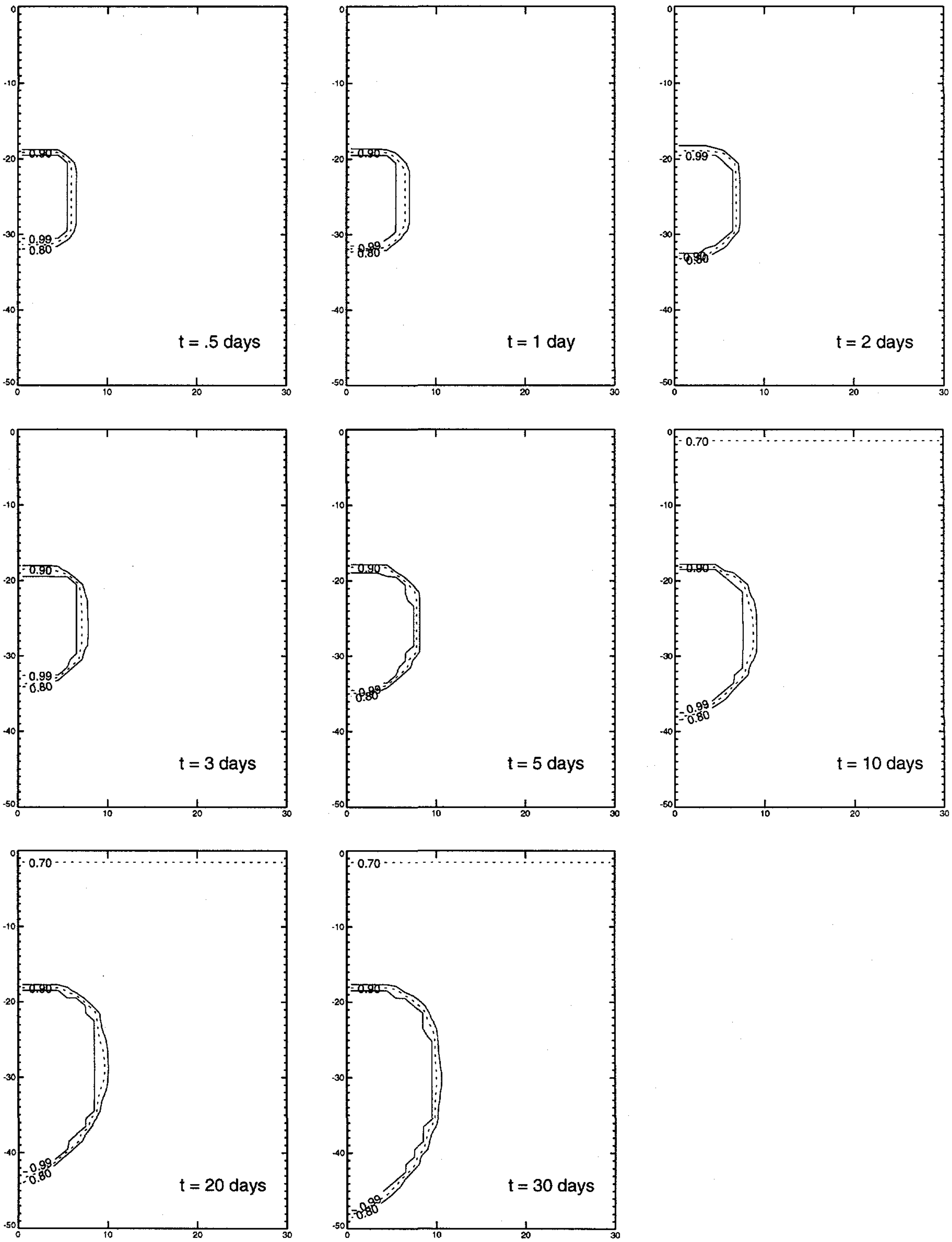

Figure 5.3-10 Equivalent continuum model prediction, using a reduced permeability function, of saturation front movement over 30 days for 25 μm aperture fractures in TSw2 tuff.

5.4 Dual Porosity and Dual Permeability Models of the ESF Flooding Scenario

The dual porosity and dual permeability models were used in TOUGH2 to simulate 30 days of flooding in the ESF tunnel. Two different fracture aperture sizes (4.55 and 25 µm) were used in the calculations. Comparisons were then made to corresponding simulations using equivalent continuum models presented in the previous section. The purpose was to assess the sensitivity of water flow through TSw2 to the different fracture flow models that can be used to represent flow through a fractured rock system subject to the given boundary and initial conditions of this problem.

The principles and concepts of the dual porosity and dual permeability models used in TOUGH2 have been presented in section 5.2.2. In this section results of four TOUGH2 simulations are presented for two fracture aperture sizes. Table 5.4-1 gives the properties and parameters that were used in the dual porosity and dual permeability runs. Parameters for the equivalent continuum model are also listed for comparison. Note that the bulk permeabilities used in the equivalent continuum model (ECM) are greater than the scaled fracture permeabilities used in the dual porosity and dual permeability models for the same fracture aperture size.

The computational mesh shown in Figure 5.2-2 was used for both the dual porosity and dual permeability models—the only difference was that the dual permeability model included matrix to matrix connections as well as fracture to matrix connections (the dual-porosity model does not include matrix to matrix connections). In all four simulations the van Genuchten parameters for the fractures and matrix given in Table 5.2-1 were maintained constant even though the fracture apertures were varied.

5.4.1 4.55 µm Simulations

The tunnel elements (shown in Figure 5.2-2) were saturated for 30 days, and water was allowed to imbibe into the surrounding matrix and fracture elements, which had initial water saturations of 0.7 and 0.0001, respectively. Figure 5.4-1 shows the water saturation contour plot at 15 days for the dual-porosity model using a fracture aperture of 4.55 µm. The imbibition from the saturated tunnel was restricted to the fractures in the dual porosity model, but subsequent imbibition from the fractures into the matrix could also occur. The uniform wetting front shown in Figure 5.4-1 is qualitatively similar to the wetting front resulting from the corresponding equivalent continuum model presented in the previous section. Careful examination of the saturations in the fractures and matrix reveals that the water in the fractures did not propagate significantly before being imbibed into the matrix elements. The influx rate through the fractures at this fracture aperture size was apparently small enough to allow equilibration between the fractures and matrix. However, since direct imbibition from the saturated tunnel elements into the surrounding elements was limited to the fractures, the amount of water entering this dual porosity system was less than the amount of water entering the equivalent continuum system (see Table 5.4-2 and Figure 5.4-2). On the other hand, the dual permeability model should allow more water into the system than the dual porosity model since the matrix elements are also connected to the tunnel elements. Unfortunately, no data exists for the dual permeability model using a fracture aperture of 4.55 µm since the time steps were automatically reduced in TOUGH2, causing run times to become excessive. Further studies need to be conducted with different meshes or with different parameters to assess this problem.

Table 5.4-1. Formation parameters used in TOUGH2 models.

	δ = 4.55 μm			δ = 25 μm		
	Dual Porosity	Dual Permeability	Equivalent Continuum[†]	Dual Porosity	Dual Permeability	Equivalent Continuum
Matrix block length, D (m)	.075	.075	.075	.075	.075	.075
α_m (Pa^{-1})	5.8 x 10^{-7}	5.8 x 10^{-7}	5.8 x 10^{-7}	5.8 x 10^{-7}	5.8 x 10^{-7}	5.8 x 10^{-7}
λ_m (1-1/β)	0.444	0.444	0.444	0.444	0.444	0.444
α_f (Pa^{-1})	1.3 x 10^{-4}	1.3 x 10^{-4}	1.3 x 10^{-4}	1.3 x 10^{-4}	1.3 x 10^{-4}	1.3 x 10^{-4}
λ_f (1-1/β)	0.764	0.764	0.764	0.764	0.764	0.764
$S_{r,m}$	0	0	0	0	0	0
$S_{r,f}$	0	0	0	0	0	0
ϕ_m	0.11	0.11	0.11	0.11	0.11	0.11
ϕ_f	1.8 x 10^{-4}	1.8 x 10^{-4}	1.8 x 10^{-4}	1 x 10^{-3}	1 x 10^{-3}	1 x 10^{-3}
ϕ_{bulk}	N/A	N/A	0.1102	N/A	N/A	5.2 x 10^{-4}
k_m (m^2)	1.9 x 10^{-18}	1.9 x 10^{-18}	1.9 x 10^{-18}	1.9 x 10^{-18}	1.9 x 10^{-18}	1.9 x 10^{-18}
k_f (m^2)	1.7 x 10^{-12}	1.7 x 10^{-12}	1.7 x 10^{-12}	1.7 x 10^{-12}	1.7 x 10^{-12}	1.7 x 10^{-12}
$k_{f,scaled}$[††] (m^2)	1.05 x 10^{-16}	1.05 x 10^{-16}	N/A	1.74 x 10^{-14}	1.74 x 10^{-14}	N/A
k_{bulk} (m^2)	N/A	N/A	3.2 x 10^{-16}	N/A	N/A	5.2 x 10^{-14}

[†] The equivalent continuum model uses the 'bulk' properties

[††] The scaled fracture permeability is used in the dual-continuum models ($k_{f,scaled} = k_f \delta/D$)

Table 5.4-2. Mass of water added to half the tunnel wall-rock per meter of tunnel during 30 days of flooding.

	δ = 4.55 μm			**δ = 25 μm**		
	Dual Porosity	Dual Permeability	Equivalent Continuum	Dual Porosity	Dual Permeability	Equivalent Continuum
Initial mass (kg)	1.1144×10^5	1.1144×10^5	1.1166×10^5	1.1135×10^5	1.1135×10^5	1.1237×10^5
Mass added in 0.5 days (kg)	—	—	360	—	—	1130
Mass added in 1.0 day (kg)	—	—	530	—	—	1490
Mass added in 5.0 days (kg)	40	—	690	1680	1820	3250
Mass added in 10 days (kg)	80	—	730	2480	2620	5040
Mass added in 15 days (kg)	130	—	—	3210	3360	—
Mass added in 20 days (kg)	—	—	820	—	—	8490
Mass added in 30 days (kg)	—	—	900	5260	5450	11820

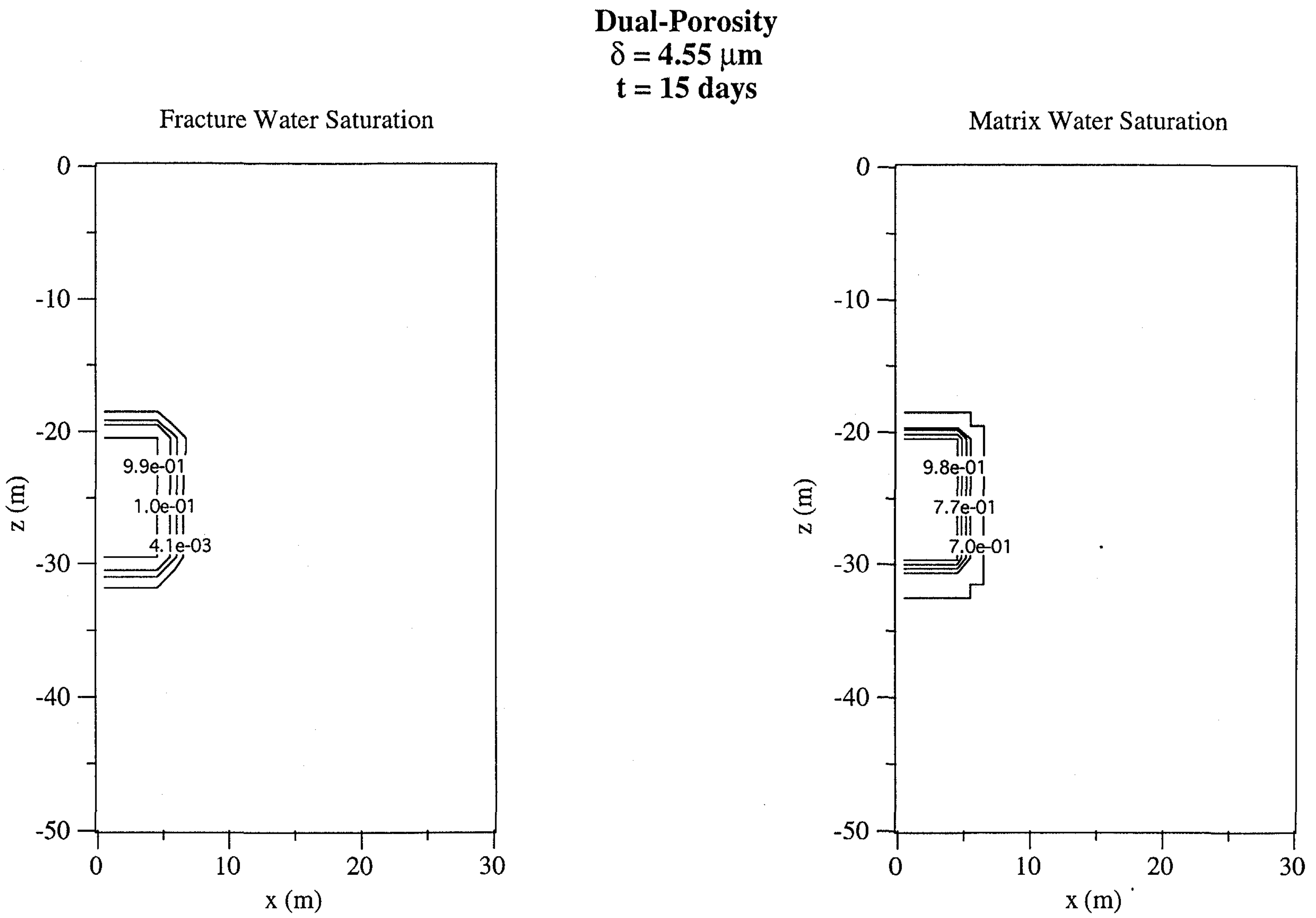

Figure 5.4-1. Water saturation contours in the fracture and matrix elements of TSw2 during flooding of the ESF tunnel using the dual-porosity model. The fracture aperture is 4.55 μm and the time is 15 days.

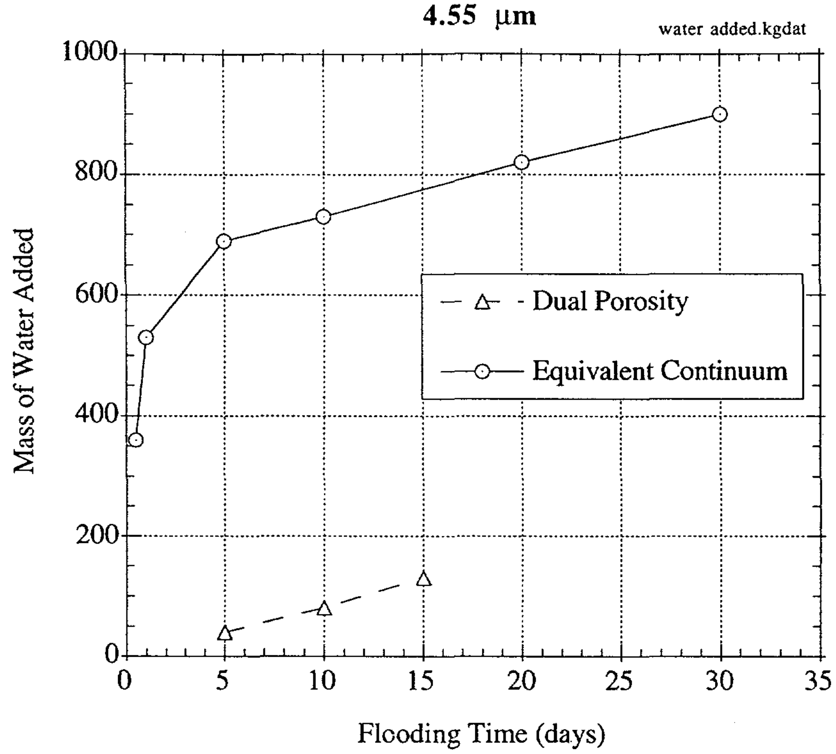

Figure 5.4-2. Plot of water flux into the TSw2 from the saturated tunnel using dual-porosity and equivalent continuum TOUGH2 models. The fracture aperture size is 4.55 µm.

5.4.2 25 μm Simulations

Figure 5.4-3 shows the saturation contours at 30 days for the dual-porosity model using a fracture aperture of 25 μm. In this case the contours show that the larger fracture aperture sizes allowed gravity-driven drainage through the fractures and subsequent imbibition into the corresponding matrix elements. The equivalent continuum model also revealed gravity-driven drainage for this fracture aperture size as well, but the overall influx of water was greater as shown in Table 5.4-2.

Figure 5.4-4 shows the saturation contours at 30 days for the dual-permeability model using a fracture aperture of 25 μm. The results are very similar to the dual-porosity model except that the matrix saturations are slightly higher as a result of the direct imbibition from the saturated tunnel elements to the matrix elements. The amount of water added to the system in the dual permeability model is shown in Table 5.4-2, and the results are plotted in Figure 5.4-5. Figure 5.4-5 shows that the equivalent continuum model predicted more water imbibed into the system than either the dual porosity or dual permeability models.

5.4.3 Discussion

The discrepancy between the equivalent continuum model and the dual continuum models in predicting the amount of water imbibed into TSw2 is due, in part, to the value of the bulk permeability that was calculated for the different models. Recall that the fracture permeability used in the dual porosity and dual permeability models was scaled by the area ratio of the fracture aperture to matrix block size. In the equivalent continuum model, however, the bulk permeability was scaled by the fracture porosity as shown in Equation (5-3). Scaling by the fracture porosity is only appropriate if the fracture sets are uni-directional and in the direction of flow. In this study, we assumed the existence of three orthogonal fracture sets to calculate the fracture spacing. This resulted in a larger bulk permeability for the equivalent continuum model than the scaled fracture permeabilities of the dual porosity and dual permeability models. If the bulk permeability of the equivalent continuum model was calculated based on the area ratio of the fracture aperture to matrix block size, then the amount of water that imbibed into the system should be more similar among the three different models.

5.5 Summary

- Increasing the permeability of the composite material, whether through permeability relations for the fracture apertures or by increasing the aperture sizes, increased the influx of water from the saturated tunnel. The effects of gravity were more pronounced for aperture sizes greater than 10 μm (bulk permeabilities > 10^{-15} m^2).

- The 4.55 μm fracture aperture case was dominated by capillary imbibition in all models. Cases with fracture apertures of 25 μm or larger exhibited gravity drainage through the fractures.

- The dual porosity and dual permeability models produced similar results for the 25 μm fracture aperture case. Primary influx was apparently through the fractures followed by imbibition into the matrix.

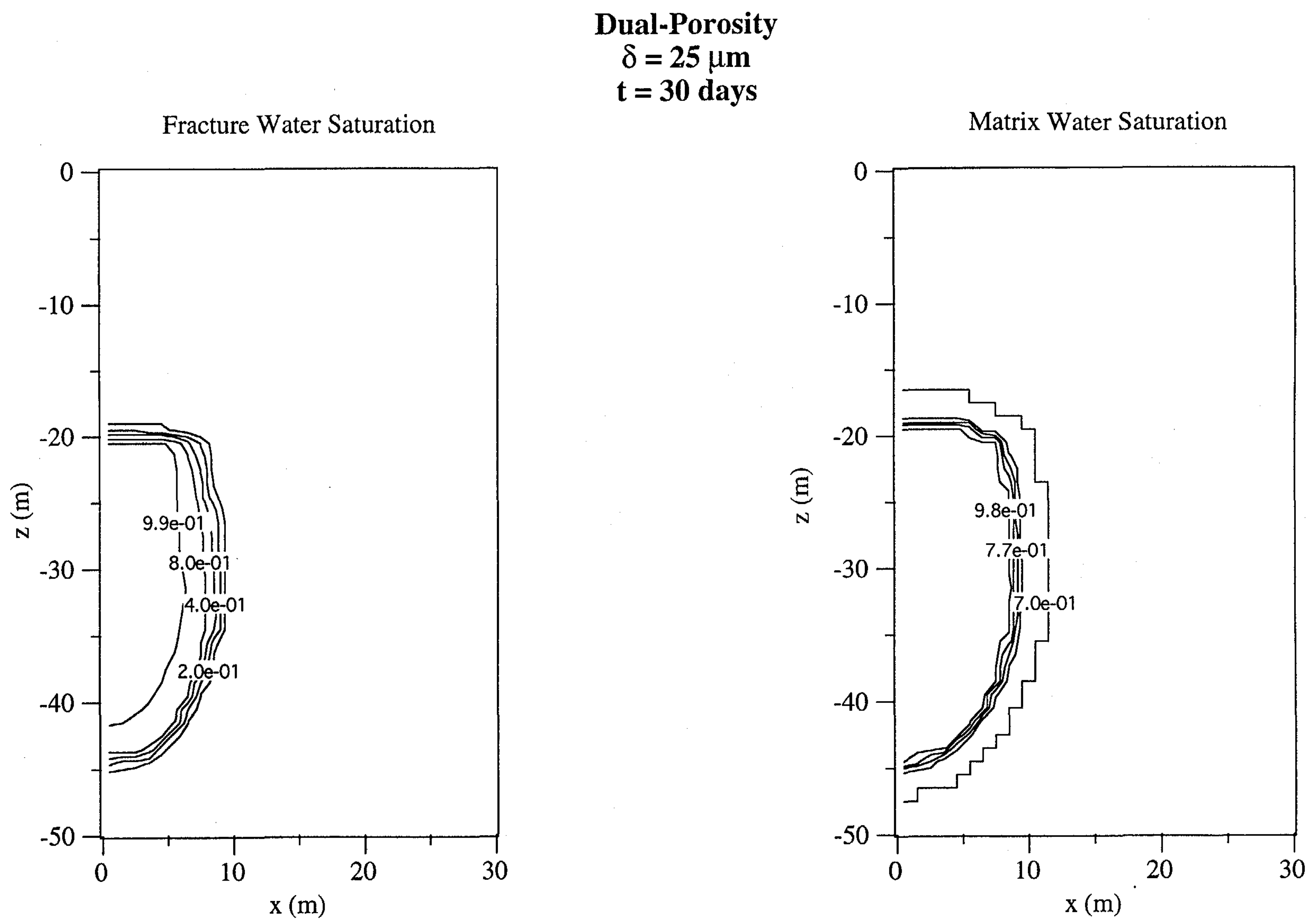

Figure 5.4-3. Water saturation contours in the fracture and matrix elements of TSw2 during flooding of the ESF tunnel using the dual-porosity model. The fracture aperture is 25 μm and the time is 30 days.

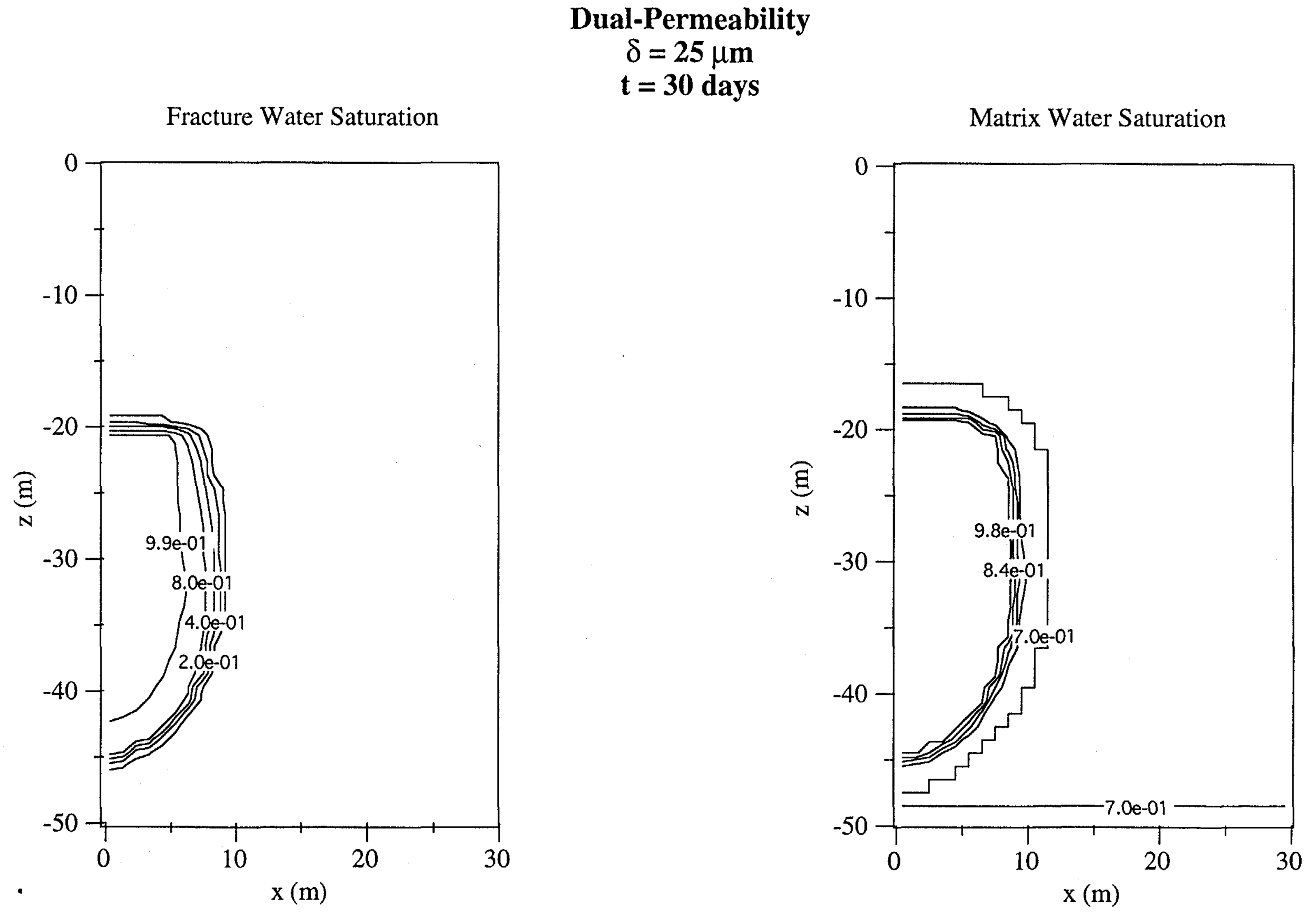

Figure 5.4-4. Water saturation contours in the fracture and matrix elements of TSw2 during flooding of the ESF tunnel using the dual-permeability model. The fracture aperture is 25 μm and the time is 30 days.

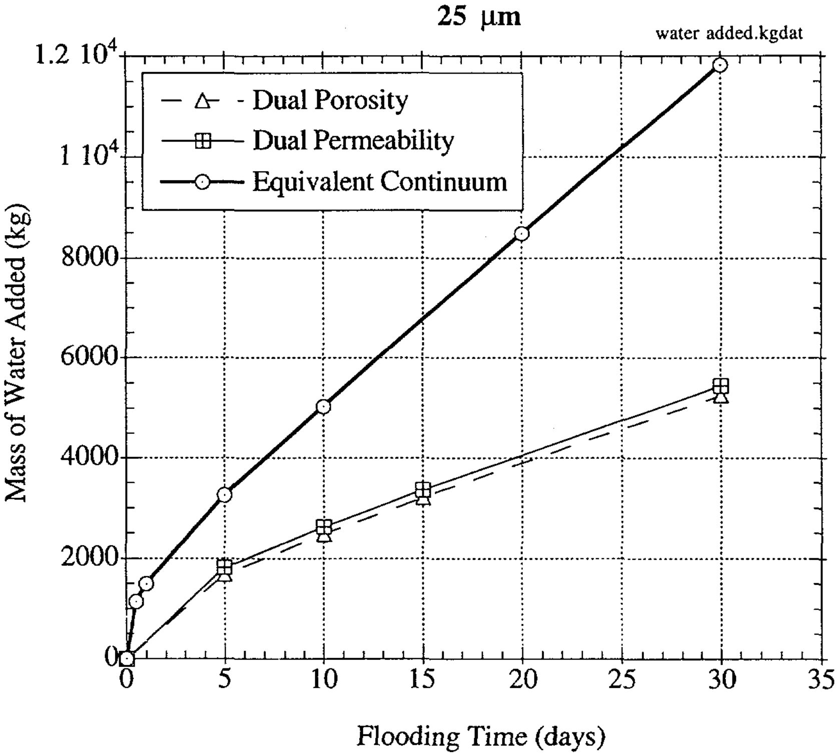

Figure 5.4-5. Plot of water flux into the TSw2 from the saturated tunnel using dual-porosity and equivalent continuum TOUGH2 models. The fracture aperture size is 25 μm.

- The characteristic curves of the fractures and matrix were held constant even though the fracture aperture size was changed. Future sensitivity analyses should consider changes in characteristic curves with changes in fracture apertures.

- The characteristic curves that were used in this study were from Klavetter and Peters (1986). In their studies the relative permeabilities were derived from capillary pressure constraints. Relative permeabilities obtained from gravity driven flow should be considered in future studies.

6.0 Sensitivity of the Evaluation of Underground Water Movement to Modeling of Rock Drying Effects Due to Ventilation

(Ho, Dunn)

6.1 Introduction

In Dunn and Sobolik (1993), ventilation through the ESF tunnel was simulated for 100 years using the single-phase flow code NORIA-SP. The result was that water was removed from the Topopah Spring welded unit (TSw2) surrounding the ESF tunnel. Ventilation simulations were performed for in situ conditions as well as for conditions following 30 days of flooding in the ESF tunnel. Kelvin's equation was used in those studies to relate the relative humidity near the tunnel wall (assumed to be 90%) to a capillary pressure, which was then used as a boundary condition for the ventilation simulations. Thus, the 'drying' of the surrounding rock was actually a capillary-driven liquid imbibition process to the tunnel walls. In this study, a more physically realistic model of vapor-phase diffusion is used for the ventilation process. Sensitivity analyses are performed to determine the effects of relative humidity of the tunnel, tortuosity of the rock, and fracture aperture size on the removal of water from TSw2 during ventilation using the equivalent continuum model.

6.2 Alternative Conceptual Models of Ventilation and Drying

In previous studies by Dunn and Sobolik (1993), Sobolik et al. (1991), and Hopkins et al. (1987), ventilation was modeled with a single-phase flow code by relating the relative humidity of a boundary to a capillary pressure. The equation relating capillary head to temperature and relative humidity is given by Kelvin's equation as follows:

$$\psi = -(RT/g) \ln (\phi/100) \tag{6-1}$$

where ψ is the capillary head, R is the gas constant for water vapor, T is the temperature in Kelvin, g is the gravitational constant, and ϕ is the percent relative humidity. The capillary head determined in Equation (6-1) is a potential used in the single-phase flow models to determine liquid-phase flow towards the boundary where the relative humidity is specified.

In this study, ventilation and drying is modeled by vapor-phase diffusion using the multiphase flow code TOUGH2 (Pruess, 1991). The relative humidity of the tunnel corresponds to a particular mass fraction of air, which is fixed for the tunnel elements in TOUGH2. Water vapor will therefore diffuse towards the tunnel elements if the vapor-phase concentration is greater in the surrounding elements. The diffusion coefficient for vapor-phase diffusion in porous media is given by the following relation:

$$D_{va} = \tau \phi S_g \frac{D_{va}^o}{P} \left(\frac{T + 273.15}{273.15} \right)^{\theta} \tag{6-2}$$

where D_{va} is the effective vapor-air diffusion coefficient, $D^o{}_{va}$ is the molecular vapor-air diffusion coefficient (=2.13x10^{-5} m^2/s at P=1 bar, T=0°C), P is the gas pressure (bar), τ is the tortuosity, ϕ is the porosity, S_g is the gas-phase saturation, T is the temperature (°C), and θ is a material parameter =1.80 (Vargaftik, 1975). Therefore, the molecular diffusion coefficient is modified to account for changing gas phase saturations and tortuosities.

In addition, the liquid relative permeability of the tunnel elements is set to zero so that water can only enter the tunnel by vapor-phase diffusion. In other words, the tunnel acts as a capillary barrier to liquid-phase flow. Therefore, the amount of water that is removed by vapor-phase diffusion to the tunnel depends on the relative humidity of the tunnel, the gas-phase tortuosity of the surrounding rock, and the initial saturation distribution. A sensitivity analysis of these parameters will be performed in the following sections in addition to a general comparison of the two different ventilation models.

6.3 General Behavior of the Vapor-Phase Diffusion Model

The general behavior of the vapor-phase diffusion model and its comparison with the single-phase flow model presented in Dunn and Sobolik (1993) are given in this section. In Dunn and Sobolik (1993), two venting simulations were presented with different initial saturations distributions. The first simulation considered venting after 30 days of flooding of the ESF tunnel. The second simulation considered venting with the TSw2 at in situ conditions. In this section only the first simulation will be replicated for comparison.

The computational model that is used here is similar to the mesh shown in Figure 5.2-2 (except that only one primary mesh is used for the equivalent continuum model). The grid is 30 m wide by 50 m high (each element was 1 m by 1 m), and only half of the tunnel is modeled due to symmetry. The rock properties and two-phase characteristic curve parameters are given in Tables 5.2-1 and 5.4-1 for the equivalent continuum model with an assumed fracture aperture and density of 4.55 μm and 40 fracture/m^3.

The initial saturation of the TSw2 is assumed to result from 30 days of flooding in the ESF tunnel (see Chapter 5). The relative humidity of the tunnel is maintained at 90% (air mass fraction = 0.987). The initial liquid saturation along a horizontal transect through the middle of the ESF tunnel is shown in Figure 6.3-1. In addition, the liquid saturations along this transect following 6 months, 5 years, and 100 years of ventilation via vapor-phase diffusion to the tunnel are also shown in Figure 6.3-1. The higher liquid saturations near the tunnel are seen to decrease over time as the liquid spreads outward into the TSw2 unit. In addition, vapor-phase transport into the tunnel also contributes to the diminishing liquid saturations near the tunnel. Figure 6.3-2 shows the liquid saturation contours during this ventilation simulation.

Figure 6.3-3 shows the liquid-phase velocities during the ventilation stage. Note that the liquid continues to spread outward from the tunnel for long periods of time. However, the velocity of the liquid diminishes greatly with time as the liquid saturation gradients decrease as shown in Figure 6.3-1. Note also that there is no liquid flow into the tunnel, but Figure 6.3-4 shows that gas-phase advection occurs near the tunnel. This is due to the hydrostatic pressure distribution established in

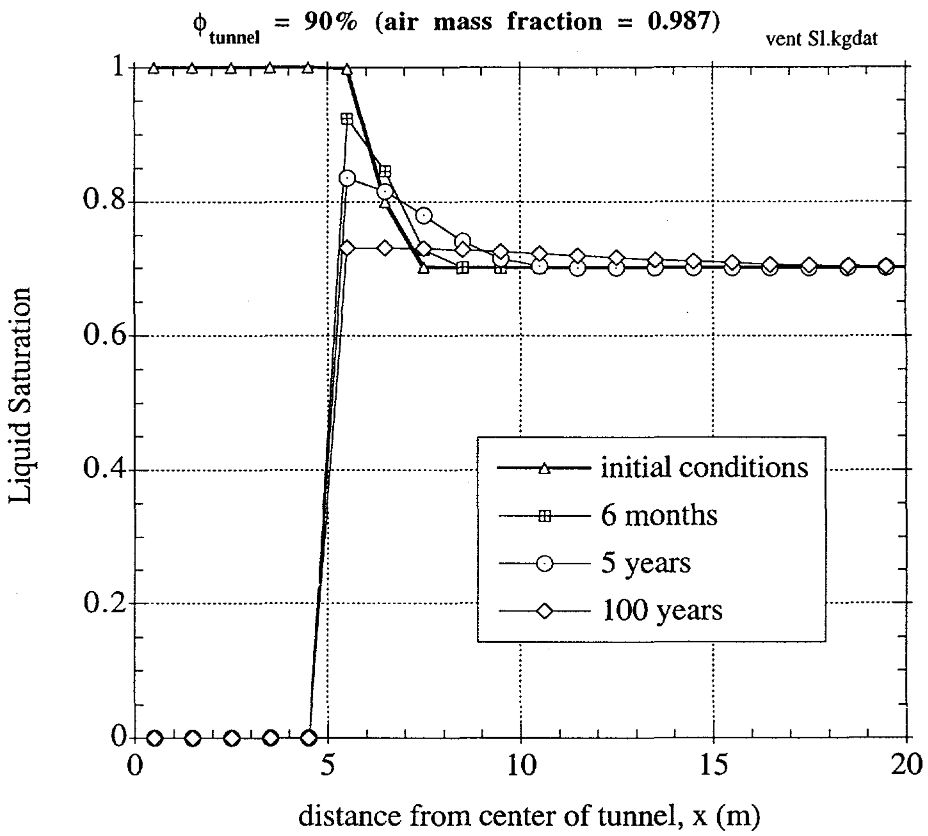

Figure 6.3-1. Liquid saturations along a horizontal transect through the ESF tunnel during ventilation via vapor-phase diffusion. The initial saturation distribution is the result of 30 days of completely saturated conditions in the tunnel. The relative humidity of the air in the tunnel was maintained at 90%.

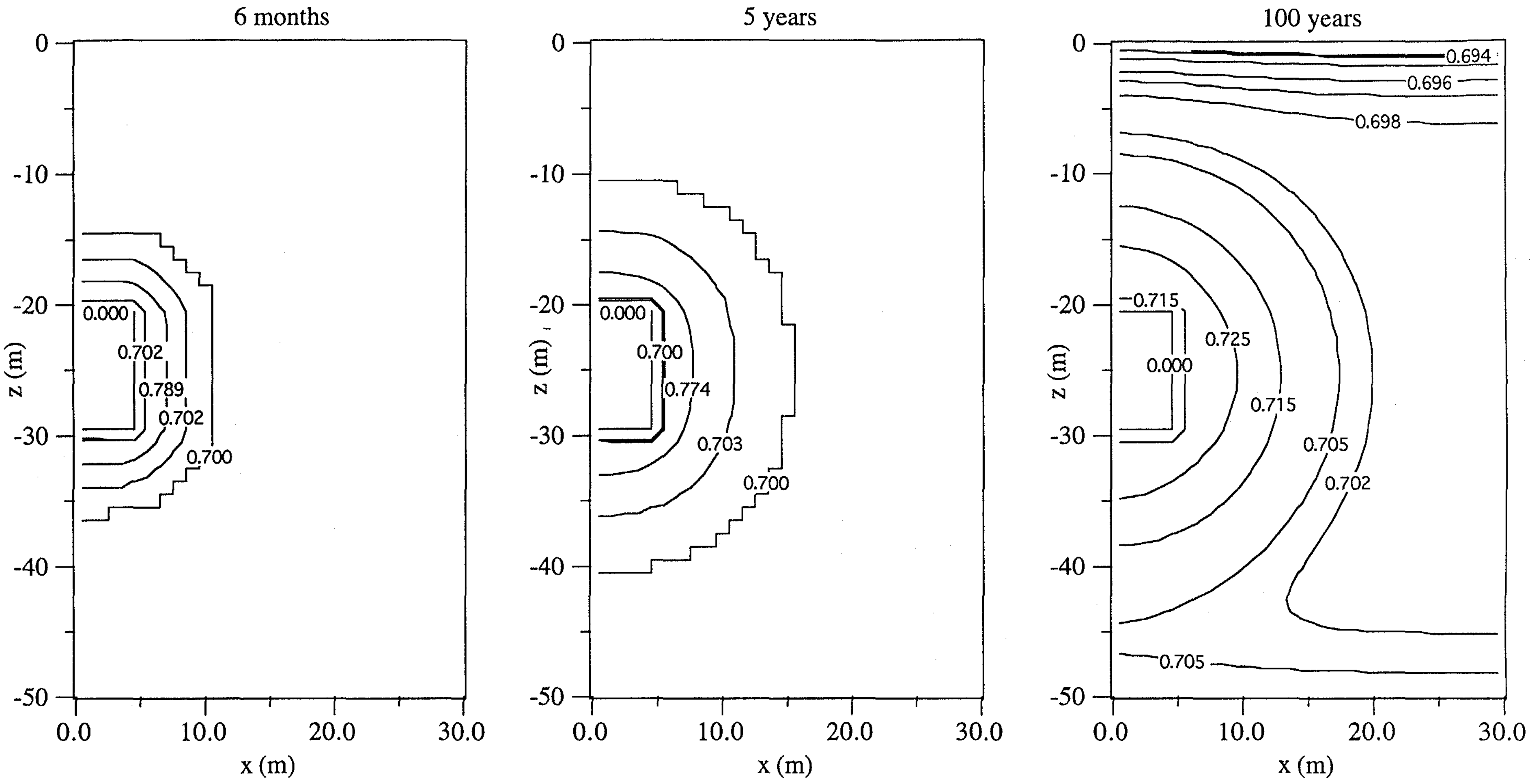

Figure 6.3-2. Liquid saturation contours in TSW2 following 6 months, 5 years, and 100 years of ventilation in the tunnel. The relative humidity in the tunnel was assumed to be 90% (air mass fraction = 0.987).

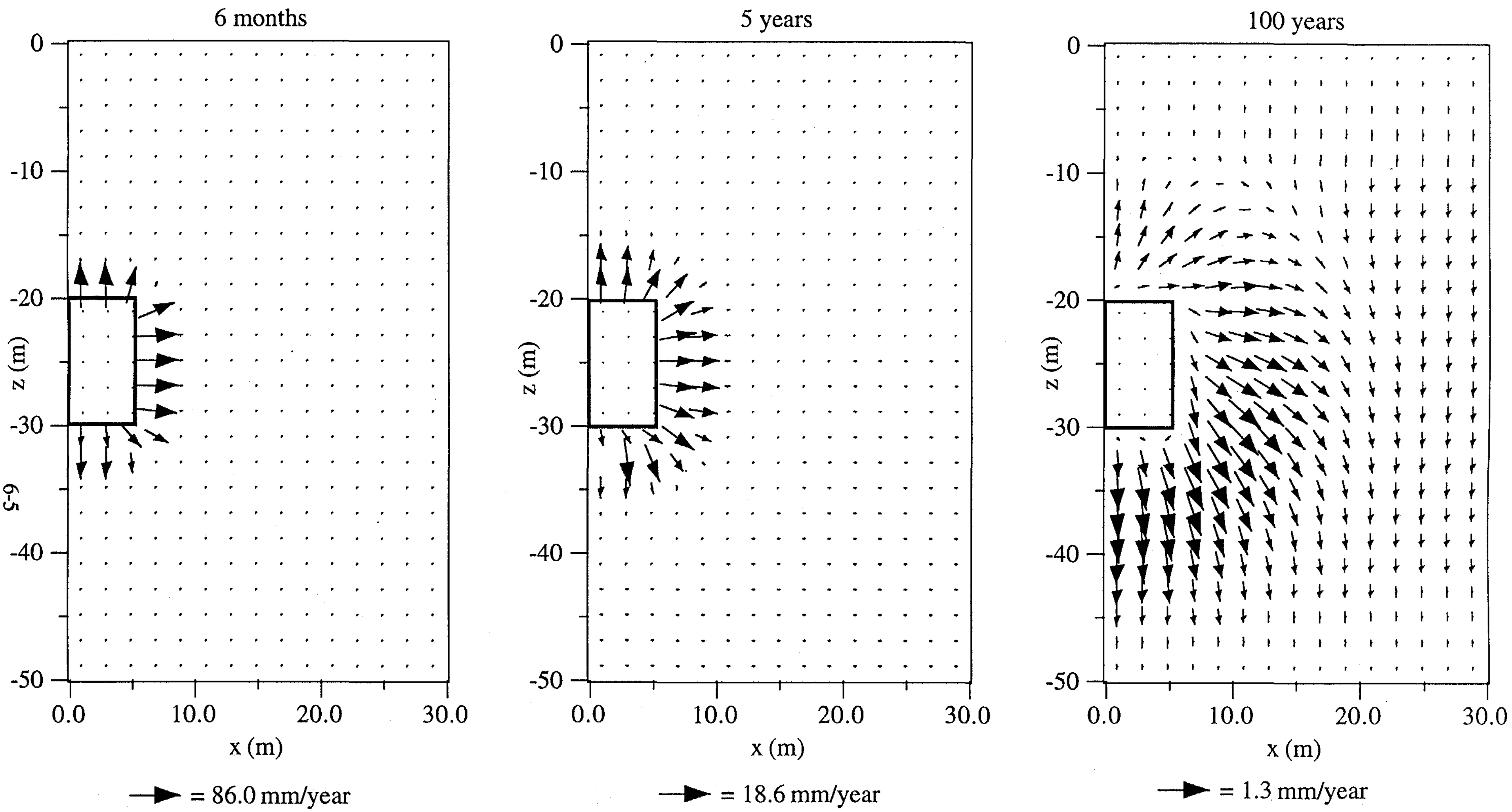

Figure 6.3-3. TOUGH2 simulations of liquid-phase velocities in TSW2 following 6 months, 5 years, and 100 years of ventilation in the tunnel (outlined in bold). The relative humidity in the tunnel was assumed to be 90% (air mass fraction = 0.987).

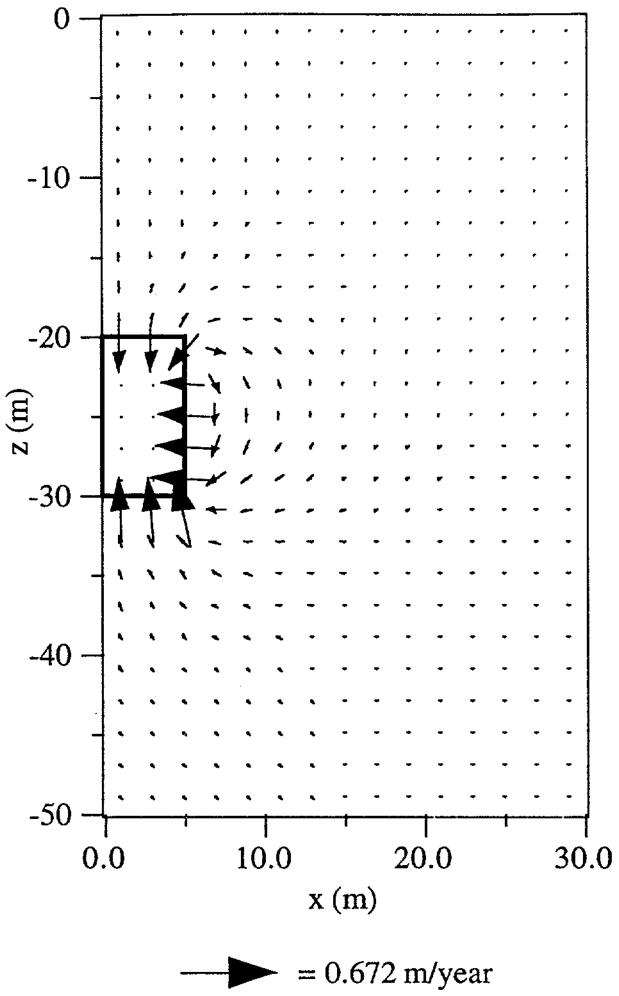

Figure 6.3-4. TOUGH2 simulations of gas-phase velocities in TSW2 following 100 years of ventilation in the tunnel (outlined in bold). The relative humidity in the tunnel was assumed to be 90% (air mass fraction = 0.987).

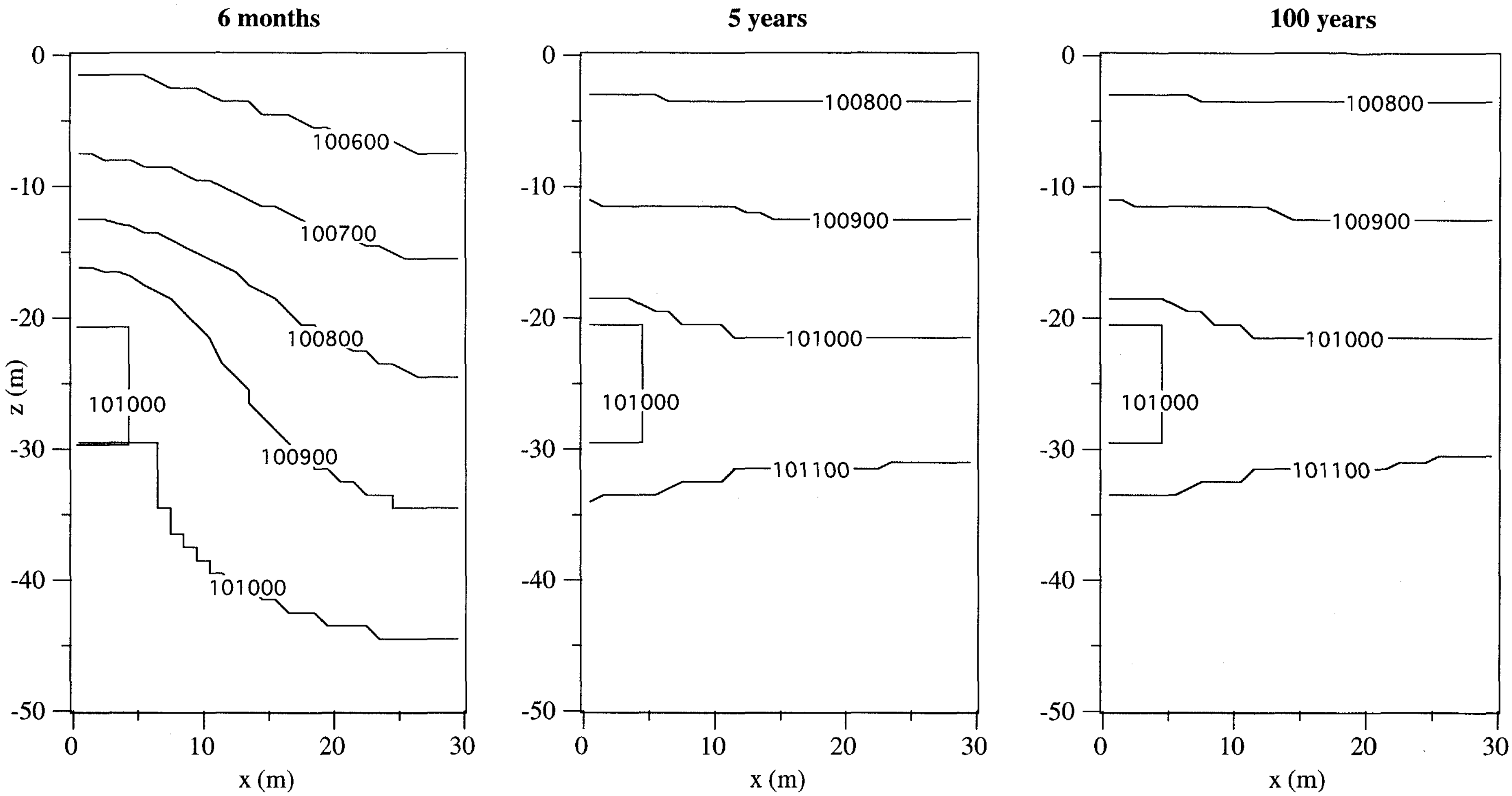

Figure 6.3-5. Gas pressures in TSw2 after 6 months, 5 years, and 100 years of venting. The relative humidity of the tunnel was assumed to be 90%, and the tortuosity was assumed to be 0.1.

xvapor.vent.cnvs

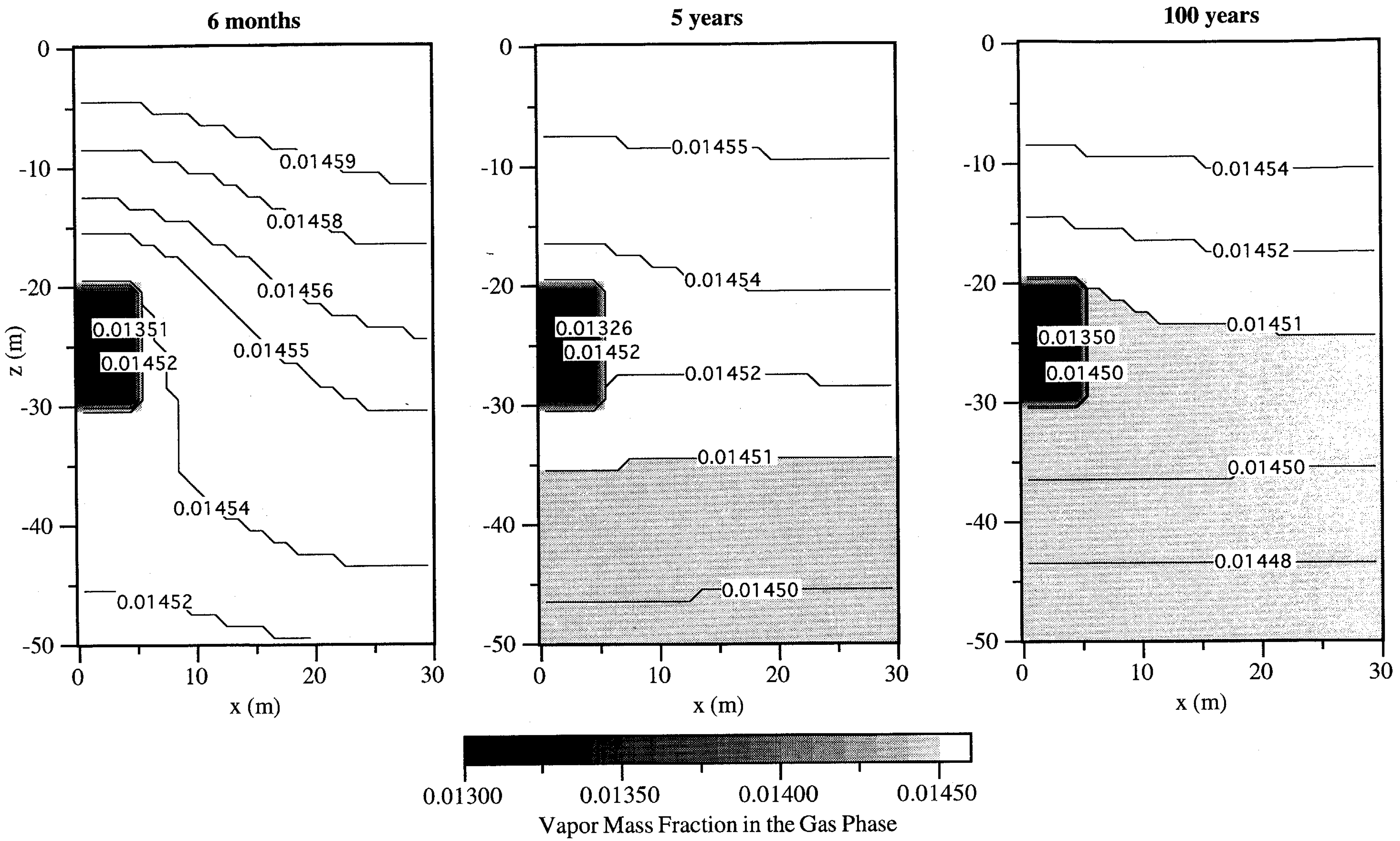

Figure 6.3-6. Vapor mass fractions in TSw2 after 6 months, 5 years, and 100 years of venting. The relative humidity of the tunnel was assumed to be 90%, and the tortuosity was assumed to be 0.1.

xvapor.vent.cnvs

the system and the imposed pressure (1.01×10^5 Pa) of the tunnel elements as shown in Figure 6.3-5. Gravity forces also play a role in the simulated gas-phase advection. In addition to advection, water vapor is also diffused towards the tunnel as indicated by the vapor mass fraction contours shown in Figure 6.3-6. The vapor mass fraction gradients are the driving potential for vapor phase diffusion, and Figure 6.3-6 shows that the direction of diffusion near the tunnel is always into the tunnel. The contribution of water migration towards the tunnel resulting from vapor phase diffusion relative to vapor phase advection is not quantified, but section 6.4 shows that vapor phase diffusion is significant in this case through sensitivity analyses.

Overall, the liquid saturation contours shown in Figure 6.3-2 are qualitatively similar to those presented by Dunn and Sobolik (p.10, 1993). However, a comparison of the liquid saturations near the tunnel reveal that the amount of water removed by vapor-phase diffusion is less than the single-phase flow model.

6.4 The Effect of Relative Humidity of the Tunnel on Ventilation Using Vapor Phase Diffusion

In the previous simulation, the relative humidity of the tunnel was assumed to be fixed at 90%. Results showed that after 100 years of venting, the liquid saturation near the tunnel did not decrease below saturation levels that were present before the flooding scenario. However, in Dunn and Sobolik (1993), liquid saturations near the tunnel were seen to decrease significantly as a result of 100 years of venting using the single-phase flow model.

Since the relative humidity in the tunnel is uncertain, a sensitivity analysis was performed using the TOUGH2 model to determine if a lower relative humidity would account for the reduced liquid saturations observed by the NORIA-SP model in the vicinity of the tunnel. Figure 6.4-1 shows the liquid saturations vs. distance from the center of the ESF tunnel in TSw2 at various times and at three different relative humidities of the tunnel. Note that reducing the relative humidity of the tunnel elements increases the vapor phase diffusion into the tunnel due to the higher concentration gradients, thereby lowering the liquid saturations near the tunnel at any given time. However, the reduction in liquid saturation is small compared to that observed by Dunn and Sobolik (1993). In fact, the liquid saturation profiles are very similar for various relative humidities ranging between 0% and 90% as shown in Figure 6.4-1. Further studies need to be performed to assess the relatively insensitive behavior of the water removal to the humidity of the tunnel.

6.5 The Effect of Tortuosity on Ventilation Using Vapor-Phase Diffusion

Results of this study reported thus far have shown that vapor-phase diffusion has not been effective in removing significant amounts of water from TSw2 as compared to results presented by Dunn and Sobolik (1993). However, no sensitivity analyses have been performed on the vapor-phase tortuosity, which in previous simulations has been assumed to be fixed at 0.1. The purpose here is to replicate the ventilation simulations using a range of vapor-phase tortuosities to assess the effects on the removal of water from TSw2 by vapor-phase diffusion.

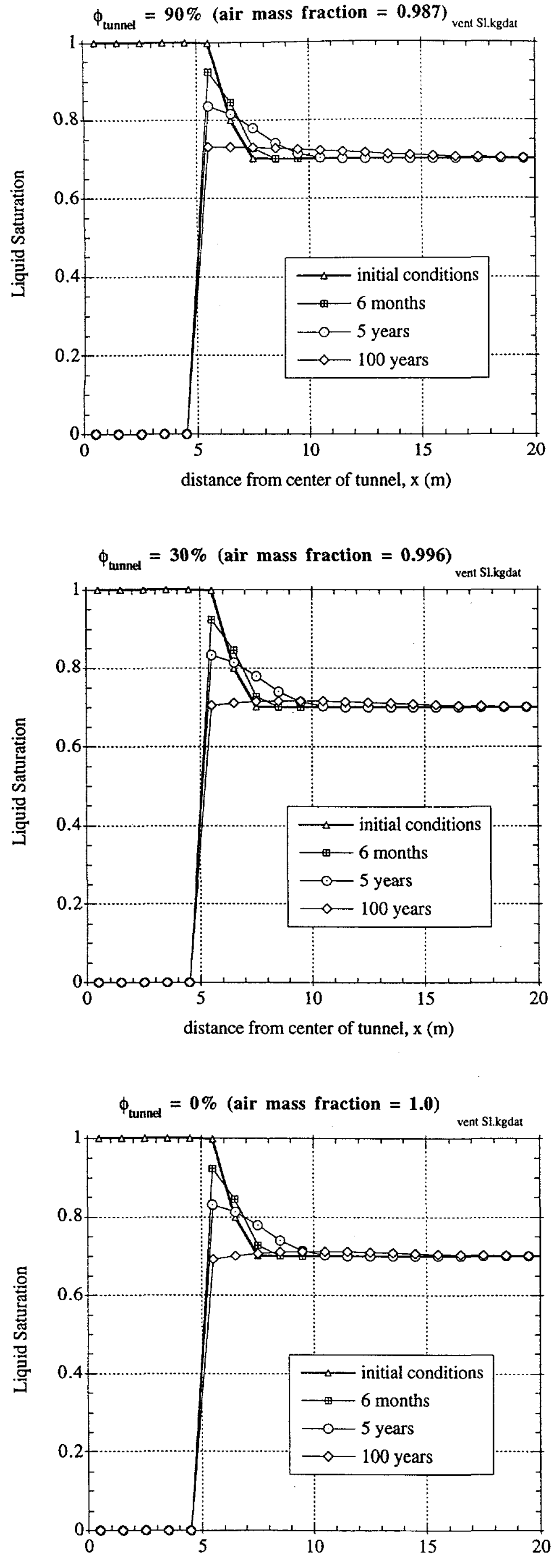

Figure 6.4-1. TOUGH2 liquid saturation distributions along a horizontal transect through the tunnel in TSw2 at various times and relative humidities during ventilation in the tunnel. Ventilation began after 30 days of completely saturated conditions in the tunnel.

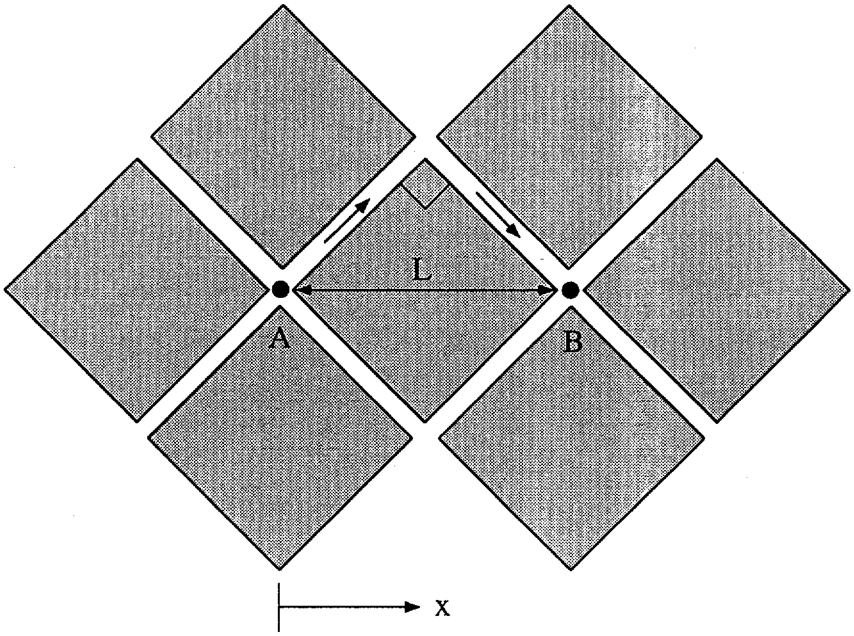

Figure 6.5-1. Tortuous path taken by a gas particle diffusing through a porous medium from point A to point B. The actual distance traversed by the particle is L $\sqrt{2}$ while the linear distance in the x-direction is only L.

The tortuosity coefficient, τ, defined in Equation (6-2) is the ratio of the linear to actual distance a gas particle must travel while diffusing through the porous medium. For example, Figure 6.5-1 shows a two-dimensional representation of a simplified porous medium. For a gas particle to travel from point A to point B, it must traverse an actual distance equal to $L\sqrt{2}$. However, the linear distance it traveled in the x-direction is only equal to L. Thus, the tortuosity coefficient as defined in Equation 1 is equal to $1/\sqrt{2}$ or 0.707.

Since the actual path taken by a gas particle in tuff at moderate to high liquid saturation levels is expected to be more tortuous than the path shown in Figure 6.5-1, the tortuosity coefficient defined in Equation (6-2) was set to 0.1 for the previous ventilation simulations (this implied that the actual path taken by a gas particle was ten times as long as the linear distance traveled). This value may be arguably small, so additional simulations were performed to investigate ventilation effects when the vapor-phase tortuosity coefficient was set to 0.5 and 1.0. Note that a tortuosity coefficient of 1.0 is an upper bound that implies pure molecular diffusion with no interference from a porous medium.

Figure 6.5-2 shows the liquid saturation distribution along a horizontal transect in TSw2 after 100 years of ventilation in the ESF tunnel (relative humidity of the tunnel = 0%). The initial saturation of TSw2 was assumed to be uniform at 0.7. Figure 6.5-2 shows that an increase in the tortuosity coefficient (implying less tortuous diffusion paths) significantly increases the drying effect in the tuff surrounding the tunnel. Using a tortuosity value of 1.0 causes the liquid saturation to decrease nearly 40% in the element nearest the tunnel.

Figure 6.5-3 also shows the liquid saturation distribution along a horizontal transect in TSw2 following 100 years of ventilation in the ESF tunnel with a relative humidity of 0%. In this case, however, the initial liquid saturation distribution was assumed to be the result of 30 days of prior flooding in the ESF tunnel. Figure 6.5-3 shows that the higher tortuosity coefficients again yield greater drying in the regions near the tunnel.

Since the actual tortuosity is uncertain, a reasonable estimate should be used for the tortuosity coefficient defined in Equation (6-2). Values between 0.1 and 0.5 seem reasonable for partially saturated tuff. Pruess (1987) has used a value of 0.25 to represent the tortuosity coefficient in tuffaceous materials. However, the ventilation of TSw2 appears to be quite sensitive to the tortuosity during the time scales of this study. Therefore, future analyses should consider using experimentally determined tortuosities or a model of the vapor-phase tortuosity as a function of gas-phase saturation and porosity such as the Millington model (1959):

$$\tau = \phi_t^{1/3} S_g^{7/3} \qquad (6\text{-}3)$$

where ϕ_t is the total porosity and S_g is the gas phase saturation.

In addition, Pruess (1991) has cited studies in which the combination of the tortuosity, the porosity, and the gas saturation ($\beta = \tau\ \phi\ Sg$) have been postulated as being constant and on the order of one due to enhanced diffusion effects caused by evaporation and condensation across islands of liquid between solid particles. TOUGH2 has the capability of assigning a constant value to this group of parameters. Future studies should consider assessing the effect of this enhanced diffusion coefficient on ventilation of TSw2.

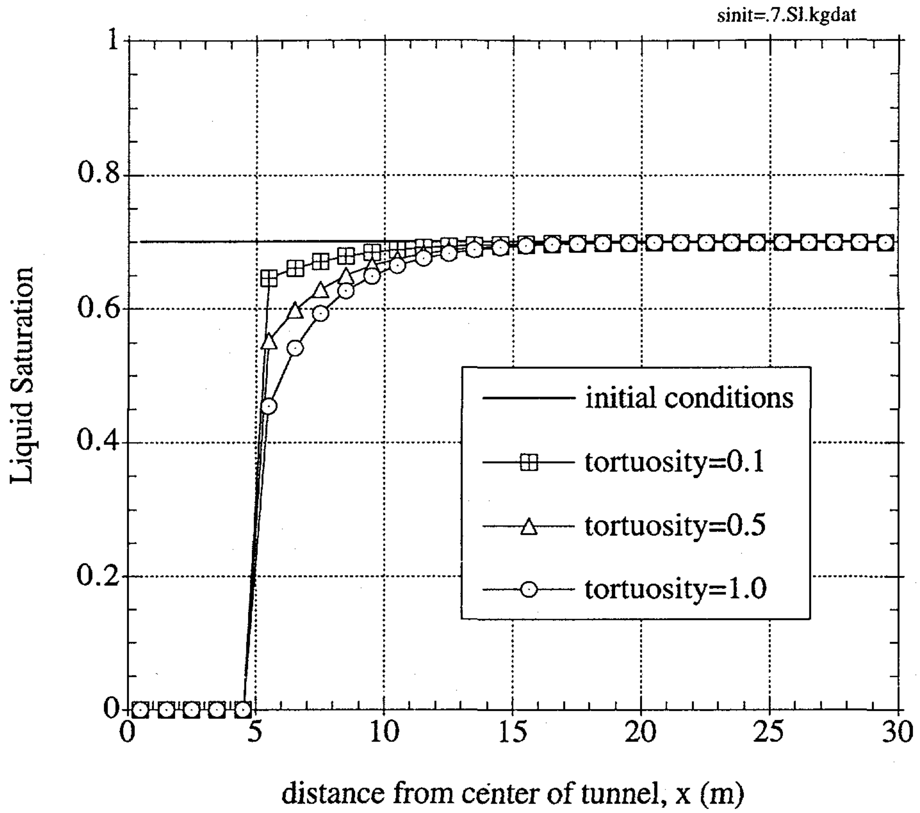

Figure 6.5-2. Liquid saturation distribution along a horizontal transect through the ESF tunnel in TSw2 after 100 years of ventilation in the tunnel (relative humidity in the tunnel=0%) for various vapor-phase tortuosities in TSw2. The initial liquid saturation is 0.7 everywhere in TSw2. The parameters used in TOUGH2 were taken from Dunn and Sobolik (1993).

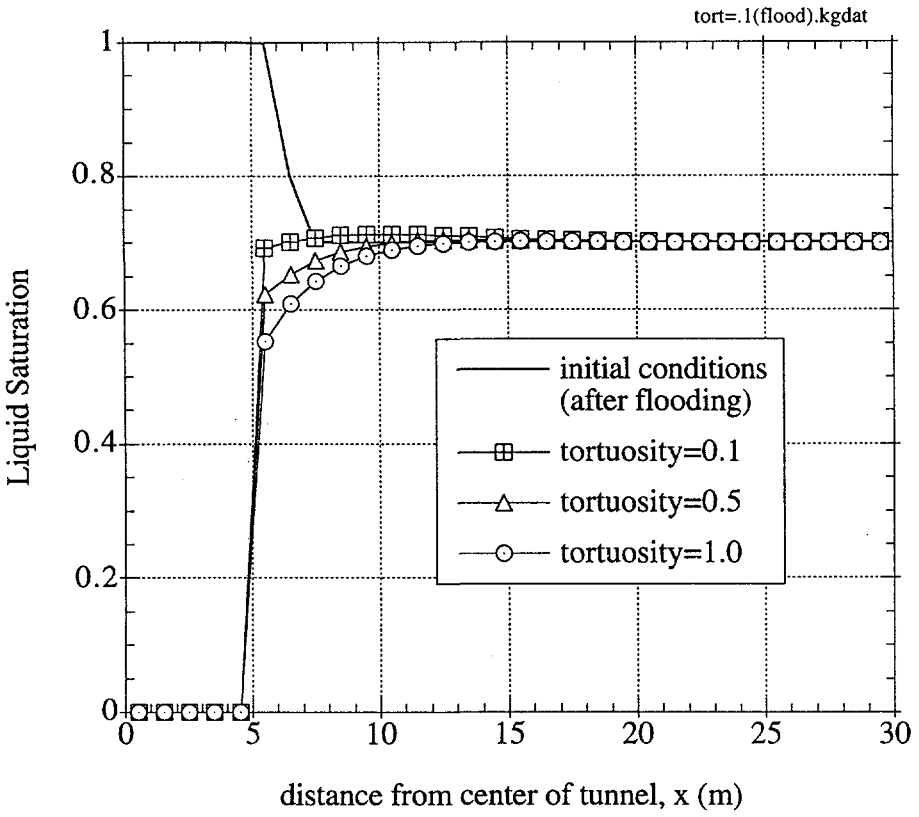

Figure 6.5-3. Liquid saturation distribution along a horizontal transect through the ESF tunnel in TSw2 after 100 years of ventilation in the tunnel (relative humidity in the tunnel=0%) for various vapor-phase tortuosities in TSw2. The initial liquid saturation distribution resulted from 30 days of completely saturated conditions in the tunnel. The parameters used in TOUGH2 were taken from Dunn and Sobolik (1993).

6.6 The Effect of Fracture Aperture on Ventilation using Vapor-phase Diffusion

A set of simulations was run to examine the effect of fracture aperture on the drying of previously wetted TSw2 wall rock. Reported here are results from three example apertures, 4.55, 18 and 25 microns. For these simulations the air mass fraction for the tunnel elements of the mesh shown in Figure 5.3-1 was set to 1.0 to represent a relative humidity of 0% to maximize the drying effect due to the relative humidity of the tunnel air. To maximize the drying effect due to tortuosity, the tortuosity was set at 0.5, the upper edge of the reasonable range for partially saturated tuff as discussed in section 6.5. The initial saturation distributions for these simulations were taken from the saturation distributions after 30 days of saturated tunnel boundary elements, the subject of section 5.3. The specific distributions used as initial conditions for these simulations are the t = 30 days members of Figure 5.3-2, Figure 5.3-4, and Figure 5.3-5. Rock porosity and permeability properties are the 4.55μm, 18μm, and 25μm entries in Table 5.3-1.

TOUGH2 was instructed to print results from ventilation simulations at 0.5, 5, 10, and 100 years. Figure 6.6-1 shows saturation at these time steps for the TSw2 with 4.55 micron fractures. As shown in Figure 5.3-2 the water imbibed into the side walls was held tightly in the vicinity of the tunnel. Figure 6.6-1 shows the migration of water both into and out of the TSw2 over the first 10 years of ventilation. The steeper gradients, due to the diffusion and escape of vapor into the tunnel, to the tunnel side of the saturation swell causes a release of water from the tunnel wall rock. Table 6.6-1 shows this amount to be 1110 kg of water per meter of half tunnel over the 100 years of the simulation. Comparing the 1110 kg loss of water with the quantity of water imbibed during the 30 days of saturated tunnel surface from Table 5.3-2, there is a net loss of 220 kg per meter of half tunnel.

Table 6.6-1 A summary of water removed from the tunnel wall rock in each of the three cases of 4.55micron, 18micron, and 25micron fractures in TSw2

aperture (μm)	ϕ_f	k_f	ϕ_b	k_b	Water removed in 100 years (kg)	Water added in 30 days (kg)	Net water gain (or loss) (kg)
4.55	1.8×10^{-4}	1.7×10^{-12}	.1102	3.158×10^{-16}	1,110	890	(220)
18	7.2×10^{-4}	2.7×10^{-11}	.1106	1.94×10^{-14}	2,040	5480	3440
25	1.0×10^{-3}	5.2×10^{-11}	.1109	5.2×10^{-14}	810	11820	11010

For the 18 micron fractured TSw2. Figure 6.6-2 shows the saturation contours for the same time intervals. The larger fractures apparently allow greater release of water and greater drying of the rock in the vicinity of the tunnel. Gravity apparently has pulled some of the imbibed water downward, out of the influence of the dryer rock in the vicinity of the tunnel. Table 6.6-1 shows a release of 2040 kg of water per meter of half tunnel while Table 5.3-2 indicates that 5480 kg of water per meter were imbibed for a net gain to the rock of 3440 kg of water per meter of half tunnel. It is speculated that no matter how long ventilation proceeds, some of the water that entered the rock during flooding will not be removed by diffusion to the tunnel.

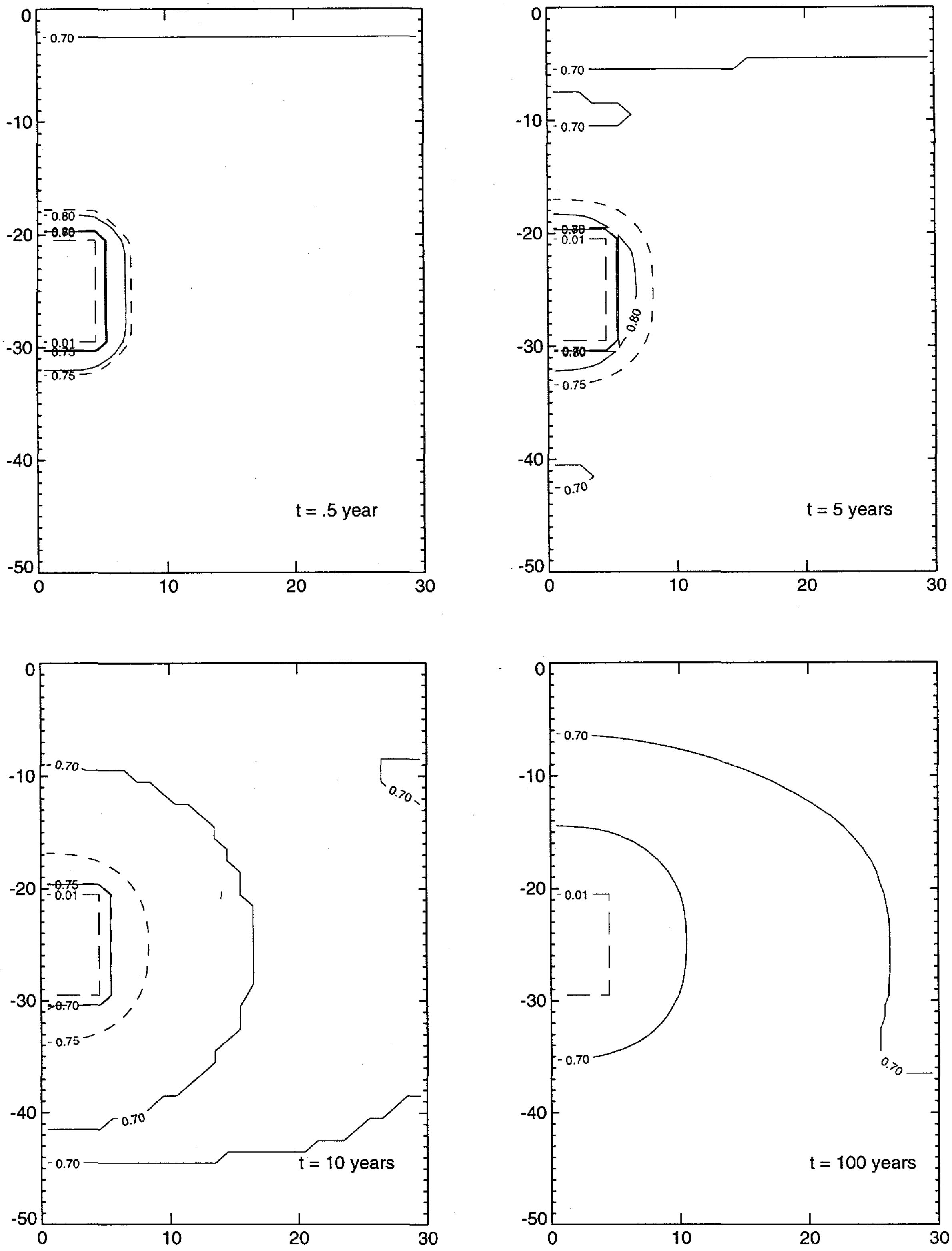

Figure 6.6-1 Saturation history during ventilation of the 4.55 micron fractured TSw2. Horizontal scale is distance from tunnel center. $\tau = .5$, relative humidity = 0%.

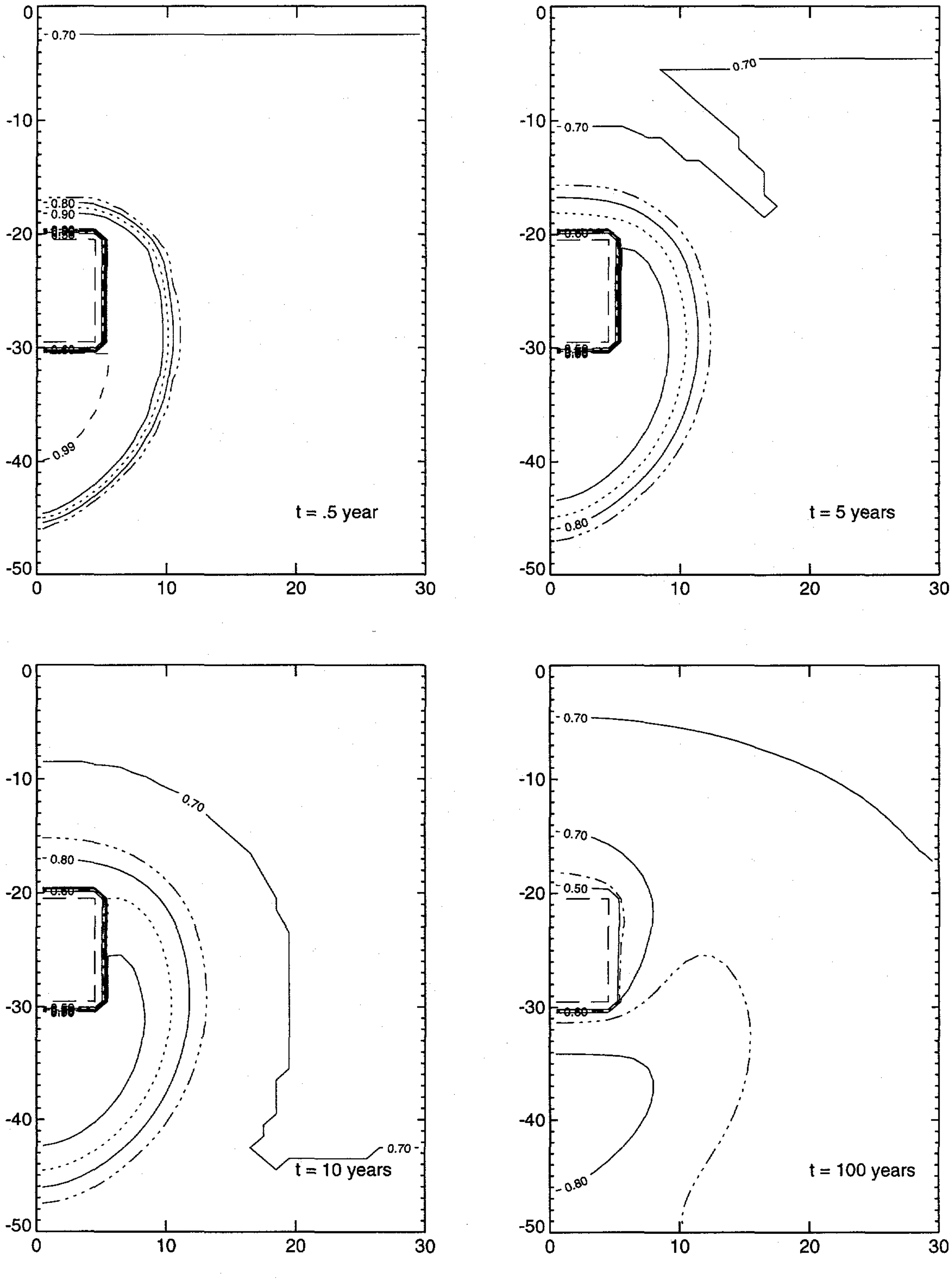

Figure 6.6-2 Saturation history during ventilation of 18 micron fractured TSw2. $\tau = .5$, relative humidity = 0%.

The results for the 25 micron fractured case indicate that the balance of forces is not exactly the same in the case of larger fractures. Figure 6.6-3 is the saturation contour history for 100 years of ventilation. Table 6.6-1 shows that of the 11820 kg of water added per meter of half tunnel during the flood only 810 kg of water was removed during 100 years of ventilation. The large quantity of water imbibed into the rock and pulled by gravity out of the influence of ventilation is consistent with the overall results of this study; however, elevated saturation did remain in the proximity of the tunnel for the full 100 years for the 25 micron case, so the smaller amount of water removed by ventilation was cause for further investigation. The explanation for this discrepancy can be postulated by referring to the gas phase velocity vectors shown in Figure 6.6-4. In the 18 micron case, the gas phase velocity vectors are pointing towards the tunnel along each of the tunnel boundaries. However, in the 25 micron case, the gas phase velocity vectors are seen to be pointing away from the tunnel along the top boundary, indicating that vapor phase diffusion towards the tunnel was not occurring along that boundary. In this case, gas movement due to advection appears to dominate over vapor phase diffusion, causing higher pressure gas in the tunnel to advect towards lower pressure regions above the tunnel despite the opposing gradient of vapor phase diffusion towards the tunnel (recall that the tunnel was maintained at a constant pressure of 0.1 MPa, while the surrounding rock at the beginning of ventilation had a hydrostatic gas pressure that was greater than 0.1 MPa below the tunnel and less than 0.1 MPa above the tunnel).

In both the 18 and 25 micron cases, higher pressure gas directly below the tunnel was also advected towards the tunnel, enhancing the movement of gas towards the tunnel from below as shown in Figure 6.6-4. These plots reveal that both vapor phase diffusion and gas phase advection contributed to the bulk gas phase movement around the tunnel. In the 25 micron case, the permeability of the system was high enough to allow gas phase advection to dominate vapor phase diffusion along the top boundary of the tunnel. In the 18 micron case, the permeability was low enough so that advection was small compared to vapor phase diffusion. In order to confirm these assertions, future studies should set the gas phase relative permeability to zero to determine the sole contribution of vapor phase diffusion to gas phase movement.

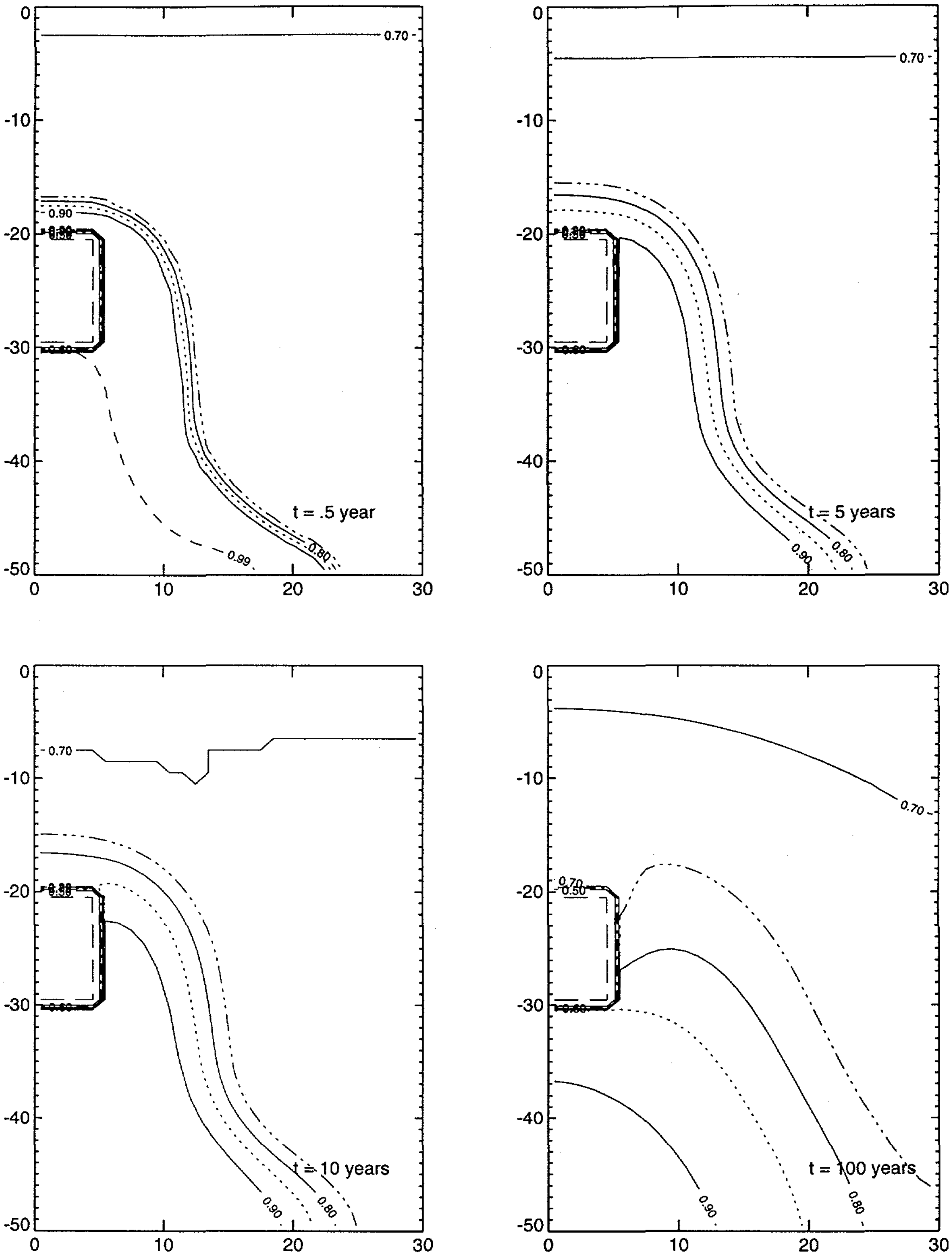

Figure 6.6-3 Saturation history of the ventilation case of TSw2 with $\tau = .5$, humidity = 0%, and fracture aperture = 25 microns.

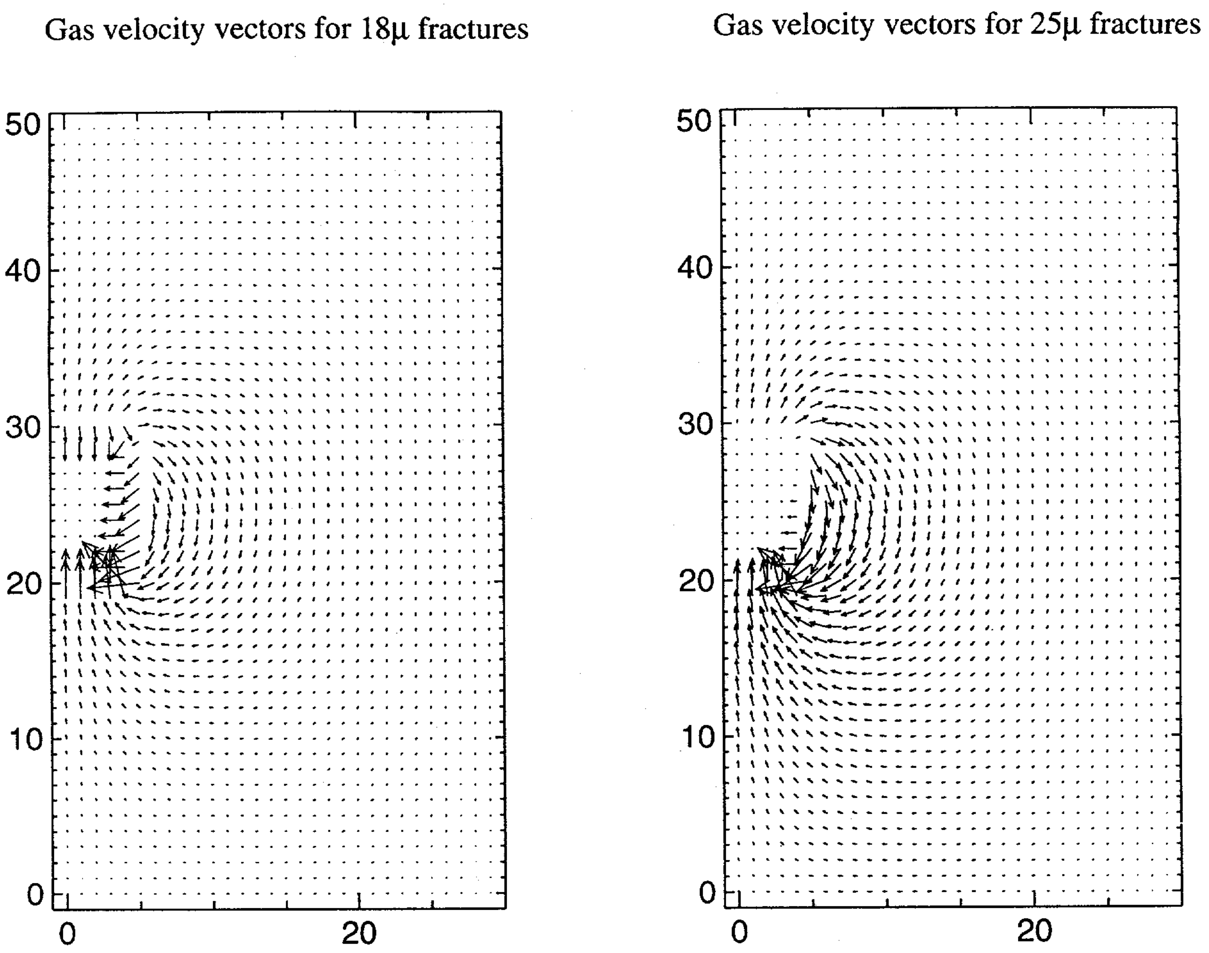

Figure 6.6-4 Velocity vectors of the gas phase in fractured TSw2 at 100 years of ventilation. It is hypothesized that vapor phase diffusion dominates the 18μ case and advection dominates the 25μ case.

6.7 Summary

- Ventilation was simulated in TOUGH2 using vapor-phase diffusion to the ESF tunnel. The tunnel was maintained at a constant relative humidity and acted as a capillary barrier to liquid flow. The equivalent continuum model was used in all cases.

- Comparison between the vapor-diffusion model and the single-phase liquid flow model for ventilation resulted in qualitatively similar drying fronts during venting. However, less water was removed by vapor-phase diffusion.

- The ventilation was relatively insensitive to changes in the relative humidity of the tunnel.

- Ventilation was sensitive to changes in the tortuosity used for TSw2. A model such as Millington (1959) for the tortuosity is suggested.

- Ventilation and subsequent drying using the vapor diffusion model could depend on both gas phase advection (driven by pressure gradients) and vapor phase diffusion (driven by vapor phase concentration gradients). For larger fracture apertures (> 18 μm), it is postulated that the permeability of the system was large enough to allow gas phase advection to dominate over vapor phase diffusion, reducing the amount of water removed by vapor phase diffusion towards the tunnel.

7.0 Conclusions

The purpose of ESF PA Analysis 14 was to estimate the sensitivity of hydrological PA analyses used to evaluate potential impacts on waste isolation to the selection of several parameters, and to assess the effect of this sensitivity on the recommendations provided by previous PA analyses. Calculations were performed to evaluate sensitivity to four parameters:

- Sensitivity of Water Movement to Characterization of **PTn Hydraulic Parameters**
- Sensitivity of Water Movement to **Heterogeneity of Material Properties**
- Sensitivity of Water Movement to **Fracture/Matrix Characterization**
- Sensitivity of Underground Water Movement to Modeling of Rock Drying Effects Due to **Ventilation**

The results of these calculations were evaluated as to their potential impact on ESF design, construction, and operations. Conclusions drawn from these calculations were compared to those drawn from ESF PA Analyses 3 (Sobolik and Fewell, 1992), 12 (Sobolik and Fewell, 1993), and 13 (Dunn and Sobolik, 1993). Additional recommendations for inclusion in Appendix I of the Exploratory Studies Facility Design Requirements Document (ESFDR) (DOE, 1993b) were derived from these comparisons.

7.1 PTn Hydraulic Parameters

The calculations performed for ESF PA Analyses 3, 12, and 13 utilized a set of homogeneous material hydrological properties for the nonwelded Paintbrush Tuff unit (PTn) which has been used for many Yucca Mountain hydrological analyses. Due to the highly variable nature of the PTn and recent sets of measured hydrological data, calculations from those analyses were repeated using several different sets of homogeneous properties for PTn. Calculations performed to model the movement of surficially applied water (replicating ESF Analyses 3 and 12) showed little significant difference in the amounts of infiltrated water and the vertical and lateral spread of the wetting front, both at early (5 years) and late (10,000 years) times. On the other hand, calculations performed to model the movement of water applied underground in the PTn section of the North Ramp of the ESF (replicating ESF Analysis 13) displayed a strong sensitivity to bulk hydraulic conductivity for both the amount of infiltrated water and the vertical and lateral movement of the wetting front. Materials used to represent PTn similar to bedded tuff and highly fractured tuff were shown to be especially vulnerable to imbibing large amounts of water. Because of the large distance between the PTn section of tunnel and the potential repository horizon, and the expected system of vertical faults occurring between the two which could act as a barrier to lateral flow, there is no anticipated impact to waste isolation; however, the recommendation derived from ESF Analysis 13 cautioning about allowing the ponding of water in the PTn is reiterated.

7.2 Heterogeneity of Material Properties

Calculations were performed to model the surficial application of water on road surfaces (replicating ESF Analysis 12) using heterogeneous material hydrological properties. These properties were derived from geostatistical calculations using measured data from several boreholes in and around Yucca Mountain as conditional data. The hydrological calculations showed a very high sensitivity of the degree of infiltration and migration of the water to the distribution of properties at the near surface (alluvium and welded Tiva Canyon units). Some sets of calculations had considerable numerical problems, indicating the sensitivity of the computational code to pressure and conductivity gradients and grid generation. The primary results of these calculations were the identification of several site characterization and analytical methodology issues; no recommendations for the ESF design were identified.

7.3 Fracture/Matrix Characterization

Previous calculations performed for ESF Analysis 13 estimated the migration of water used in underground activities in the Topopah Spring welded unit (TSw). Those calculations were performed using the code NORIA-SP, which employs an equivalent continuum model (ECM) approach to the interaction of flow between fractures and matrix. Sensitivity calculations were performed using the TOUGH2 code and employing three different flow models: the ECM; the dual porosity model, for which flow between matrix elements may only occur through fractures; and the dual permeability model, for which matrix, fracture, and matrix-to-fracture flow are all evaluated. Additionally, water flow was evaluated for different rock conditions; that is, fracture apertures ranging from 4.5 to 100 μm were modeled. Similarities and differences between the fracture/matrix models are noted in the Chapter 5. All three models indicated that, given a ponded condition in the tunnel, for fracture apertures geater than or equal to 25 μm, significant water infiltration may occur, and the flow of that water would be gravity-driven. The results of the analysis indicate that ponding of the water in the ESF tunnel, particularly in the Topopah Spring section of tunnel in the repository block, should not be allowed. These results strongly support the recommendation made under ESF Analysis 13 regarding the most immediate-as-possible removal of excess water from the ESF; this recommendation is restated to include the results of ESF Analysis 14.

7.4 Ventilation

Calculations performed previously for ESF Analysis 13 evaluated the potential capability of ventilation to remove water added to the in situ rock during ESF construction and operations. The ventilation model used for those calculations was an empirically based model equating the suction pressure at the surface of the wall to a function of the relative humidity of the ventilating air. New calculations were performed for ESF Analysis 14 using the TOUGH2 code, the ECM flow model, and a vapor-diffusion model requiring values for relative humidity of the ventilating air stream and vapor-phase tortuosity of the matrix. Calculations simulating the effects of ventilation from in situ conditions indicated little sensitivity to the relative humidity of the air, but significant sensitivity to the value of tortuosity used over a range of physically-reasonable values. Calculations simulating the removal of water after a tunnel-flooding event by ventilation were performed using a mid-range tortuosity value and varying the fracture aperture from 4.5 μm to 25 μm. The results indicate that ventilation will remove most or all added water within one radius of the tunnel walls in cases where the fracture apertures are small. For cases where large apertures exist, only water relatively close to the tunnel walls will be removed. Ventilation and subsequent drying was found to depend on both gas advection (driven by pressure gradients) and vapor phase diffusion (driven by vapor phase concentration gradients). For larger fracture apertures (>18 μm), the permeability of the system was large enough to allow gas phase advection to dominate over vapor phase diffusion, reducing the amount of water removed by vapor phase diffusion towards the tunnel. These results do not suggest additional recommendations to Appendix I, but they do strongly support the following recommendation regarding the removal of ponds in the tunnel and the recommendation from ESF Analysis 13 regarding the monitoring of moisture removal by ventilation.

7.5 Recommendations for the ESFDR

The results stated above had little effect on previous recommendations made to the ESFDR by previous analyses. The recommendation regarding the no allowance of a pooled water condition in the ESF tunnel from ESF Analysis 12 was reiterated by this analysis. Pooled water on the tunnel floor will continue to infiltrate the rock as long as the two are in contact. Furthermore, these sensitivity studies indicate a connected fracture system with apertures of 25 μm or greater in the Topopah Spring section of the tunnel could create a preferential pathway for water flow to the Calico Hills units, which could impact waste isolation capabilities. For these reasons, during construction and operation of the ESF excess water should be removed to preclude adding unnecessary water to the ESF tunnel wall rock. Water should not be allowed to puddle, pond or stand on the floors of the tunnels at any time, and it is suggested that a readily available water pickup system be accessible to immediately pick up any standing water which might collect during the construction or operation phase of the ESF.

7.6 General Recommendations for Future Performance Assessment Analyses

Several general recommendations can be made for the advancement of the state-of-the-art of future performance assessment analyses (including postclosure, total system, and those used to determine site suitability). Performance assessment analyses are an iterative process requiring reinvestigation given new site data, new information on the in situ physical processes, and improved or enhanced numerical models. These advancements require the gathering of field and site data, as well as performing numerical experiments in parallel with these activities.

One requirement for future ESF and total system PA analyses is the need for site data on the spatial distribution of alluvium, including thicknesses, porosities, pore size or grain size distribution (including correlation of that distribution to location and depth), and hydraulic conductivity. Site test data regarding water infiltration and evaporation from alluvial soils would also provide much needed support to the performance of postclosure PA analyses. Much of the current work being performed by USGS and SNL will meet these needs, although there is still some effort required to establish how much information is enough.

As illustrated in Chapter 4, information and capabilities which would greatly enhance the understanding of flow through welded tuffs, such as TCw and TSw, include the further development of flow models such as dual permeability, more definitive fracture information (conductivity, moisture retention properties), and particularly a greater understanding of how to properly scale data measure from core-size samples to the size of computational grid cells.

Several activities can be initiated that combine laboratory and numerical experiments to investigate and improve existing models to better evaluate the coupled physical processes thought to exist at Yucca Mountain. One activity should be to perform numerical and laboratory experiments to establish the adequacy of the ventilation model used in Chapter 6, and perhaps extend its applicability by adding heat and convection (i.e., amount of drying due to varying the volume and speed of air used for ventilating). These activities are important to do soon to determine before the majority of tunnel construction is completed if there are any measures that need to be taken to mitigate potential impacts on waste isolation. YMP participants should continue developing the capability to perform two-dimensional flow analyses using several different flow models (dual porosity, dual permeability, etc.) as quality-affecting performance assessment analyses. In addition, there should be continuing development of the capability to perform two-dimensional flow analyses using heterogeneous material property data based on site measurements and geostatistics as quality-affecting performance assessment analyses.

8.0 Limitations and Assumptions

The validity of the results of this analysis depends on the assumptions underlying the conceptual model of flow and the methods used to produce material property input data. This section contains a list of the assumptions and a discussion of the potential errors in the calculations if these assumptions are invalid. Omitted is the fundamental question of the applicability of Darcy's law and Richards' equation -- capillary-bundle theory in general -- to the modeling of unsaturated flow through relatively impermeable rock.

8.1 Boundary Conditions (Ambient Infiltration, Evapotranspiration, and Water Application)

A potential limitation on the validity of this analysis is the way in which the moisture influx and efflux processes are modeled by the boundary conditions imposed in the calculations. The ambient evapotranspiration (ET) environment is modeled in this analysis by the time-averaged and areally-averaged infiltration rate of 0.01 mm/yr. However, the conceptual models for ET processes at Yucca Mountain, both for the usual climatic conditions as well for episodic events such as flooding or surficial watering, are not well developed, and sufficient data do not yet exist to develop these models with confidence. A better understanding of surface infiltration processes, including fracture flow at the surface, evapotranspiration, and runoff phenomena, will be required before the uncertainties of water movement analysis can be decreased. In addition, surficial and underground water application is modeled in this analysis as a continuous process, not as an activity that occurs periodically as would be expected; this modeling could result in an overprediction of the amount of water infiltrating the surface and the range of water movement from the wetted surface.

8.2 Quantity and Scaling of Site Material Hydrological Data

As has been stated earlier in the report, the results of these calculations are sensitive to the hydrological properties used for each material. The existence of stratigraphic and material property data from several boreholes around Yucca Mountain provide a foundation for using geostatistics to produce a 2-D or 3-D model of the mountain. Two particularly important information needs for performance assessment calculations are material property and topographic data for alluvium, and fracture property information for welded tuffs. Currently available data on the spatial distribution of alluvium, including thicknesses, porosities, pore size or grain size distribution (including correlation of that distribution to location and depth), and hydraulic conductivity, is sparse and of questionable quality, and both factors make geostatistical modeling of near-surface stratigraphy difficult. Site test data regarding water infiltration and evaporation from alluvial soils would also provide much needed support to the performance of postclosure and total system PA analyses. Much of the current work being performed by USGS and SNL will meet these needs, although there is still some effort required to establish how much information is enough. The results of Chapter 5 and 6 demonstrate the importance of fracture characterization in assessing the performance implications of underground activities; this topic is discussed further in the next section.

The other assumption that affects the results of this analysis is the upscaling of material properties measured on the core scale to computational grid cells many meters in height and width. The calculations in Chapter 4 indicate that the current method of volumetric averaging of properties from a geostatistical to a computational grid tends to wash out the steepness of moisture retention curves. Several laboratory experiments in their infancy at SNL have also indicated that the values obtained in measurements taken from core samples can vary dramatically based, for example, on the size of the tip on an air hose[4]. A greater understanding of appropriate scaling methods is essential for future credible performance assessment analyses.

8.3 Modeling Uncertainties (Fracture Characteristics, Anisotropy, and Hysteresis)

Geologic units (e.g., the Tiva Canyon welded tuffs) are modeled as a single matrix material and a single fracture material. It is known that fracture properties such as apertures, spacing, and orientation, from samples within a geologic unit can vary greatly (e.g., Peters et al., 1984). It is unknown what effect this variation would have on fluid flow or the analysis thereof. Furthermore, the traditional method used for estimating the conductivity of a particular fracture is based on the theoretical flow between two parallel plates; this assumption has not yet been fully tested for its appropriateness for modeling flow in fractured tuffs. For this particular analysis, variations in fracture properties and connectivity in moderately saturated, nonporous regions (such as TCw and TSw) may have large effects on the vertical and horizontal dispersion of water. If these regions are vertically connected, groundwater travel time could be shortened. If they are horizontally connected, lateral dispersion of flow could be enhanced.

Another simplifying assumption used in these calculations is that of isotropic hydraulic conductivity ($K_{xx}=K_{zz}$) at each point throughout the geologic units. There is much data in professional hydrology literature that indicates a higher degree of anisotropy ($K_{xx}/K_{zz} > 1$) for hydraulic conductivity in soils as the saturation level decreases. This anisotropy in soils tends to favor horizontal movement of water. If this sort of anisotropy exists in the alluvium at Yucca Mountain, it could mean that the estimates given in this report for distances of lateral movement of water from roads and ponds might be less conservative than stated. Furthermore, the assumption of isotropic hydraulic conductivity could cause the influence of down dip to be underestimated (e.g., in the calculations in Soboli and Fewell, 1993). However, Flint and Flint (1990) found no evidence of small-scale anisotropy in the nonwelded tuff samples that they tested.

A third simplifying assumption is the neglect of hysteresis in the modeling of the moisture retention and relative conductivity curves. Most of the early data used for Yucca Mountain analyses were based on data taken during the drying phase. The meaning of hysteresis as it relates to performance assessment is not very well understood at this point, and the feasibility of first measuring and then modeling wetting phase phenomena is far from trivial.

8.4 Conceptual Model for Fluid Flow

Three conceptual models for fluid flow were used in this analysis. The equivalent continuum (or composite-porosity) model used in these calculations treats the matrix and the fractures as an equivalent porous medium; the pressure heads in the matrix and the fractures at any given location are assumed equal. The dual porosity model is essentially a fracture-flow-only model. The dual

---

[4] These experiments are being conducted by Vince Tidwell at Sandia National Laboratories; the results cited here are preliminary.

permeability model allows two coexistent continua, matrix and fractures, with flow occurring in either continuum or from one to the other.

Other flow models have been proposed for Yucca Mountain. For example, the weeps-and-seeps model has been used in total-system performance assessment calculations (Wilson et al., 1994); it assumes that flow is confined to limited regions down connected fracture networks. If the weeps-and-seeps model is applicable to flow at Yucca Mountain, the result would be that a great deal of the surface water could flow directly to the water table within a few years. Such short travel times imply that surface water might not affect the repository: first, the matrix would have little time to saturate, and second, the water would be gone before the repository would be sealed. Discrete fracture models, which would have fractures explicitly located at various locations within a matrix, may be the most physically realistic but is also currently the most difficult to use to produce credible PA analyses. In addition, fast pathways such as faults, boreholes, and new or widened fractures created by construction could either act as preferential pathways that could affect repository performance, or prevent adverse effects by routing water away from the potential repository or acting as a barrier to water flow, depending on their orientation with respect to the proposed repository horizon. These features have not yet been explicitly added to any of the available flow models.

8.5 Computational Model for Estimating Fluid Flow

To adequately determine the suitability of the Yucca Mountain site as a location for a permanent nuclear waste repository, and for the potential licensing of such a facility, performance assessment analyses must become increasingly more sophisticated, both in terms of their use of site-based material property and stratigraphic data and the physically-realistic modeling of the coupled processes that govern radionuclide transport. Most postclosure performance assessment analyses to this point have been performed with codes that model simplified concepts of the in situ processes: NORIA-SP (liquid water only, isothermal, equivalent continuum model), TOSPAC (Dudley et al., 1988) (one-dimensional, isothermal). The studies described in this report make the first use of TOUGH2 to include multi-phase, multi-component flow (water and air), and different models for fracture/matrix interaction. TOUGH2 and other flow codes such as FEHM (Zyvoloski et al., 1992) should be used to further enhance performance assessment capabilities. Activities that combine laboratory and numerical experiments should be used to better evaluate the coupled physical processes thought to exist at Yucca Mountain. Such processes would include the effects of heat on ventilation, dryout, and gaseous and aqueous flow processes; the effect of ESF construction on the size and connectivity of fractures and the creation of new fractures; the additional change to fractures based on thermal expansion processes; and the geochemical effects of these process on sorptivity, fracture aperture sizes, and the release of in situ water from the zeolites, to name a few. Performance assessment analyses are an iterative process, and the enhancement of codes such as TOUGH2 and FEHM to include coupled processes and more complete site data will provide better confidence for determining site suitability and appropriateness for licensing.

9.0 References

Barenblatt, G. I., I. P. Zheltov, and I. N. Kochina, 1960. "Basic Concepts in the Theory of Seepage of Homogeneous Liquids in Fissured Rocks Strata," Journal of Applied Mathematics and Mechanics (USSR), Vol. 24, No. 5, pp. 1286-1303.

Barnard, R. W., and H. A. Dockery, editors, 1991. Technical Summary of the Performance Assessment Calculational Exercises for 1990 (PACE-90), Vol. 1: 'Nominal Configuration' Hydrogeologic Parameters and Calculational Results, SAND90-2726, Sandia National Laboratories, Albuquerque, New Mexico.

Barnard, R. W., M. L. Wilson, H. A. Dockery, J. H. Gauthier, P. G. Kaplan, R. R. Eaton, F. W. Bingham, and T. H. Robey, 1992. TSPA 1991: An Initial Total-System Performance Assessment for Yucca Mountain, SAND91-2795, Sandia National Laboratories, Albuquerque, New Mexico.

Bentley, C.B., J.H. Robinson, and R.W. Spengler, 1983. Geohydrologic Data for Test Well USW H-5, Yucca Mountain Area, Nye County, Nevada, USGS/OFR-83-853, U.S. Geological Survey, Denver, Colorado.

Brooks, R. H., and A. T. Corey, 1964. Hydraulic Properties of Porous Media, Hydrology Paper No. 3, Colorado State University , Civil Engineering Department, Fort Collins, Colorado, 27 pp.

Campbell, G.S., 1985. Soil Physics with Basic: Transport Models for Soil-Plant Systems, Elsevier, New York, New York.

Deutsch, C.V., and A.G. Journel, 1992. GSLIB: Geostatistical Software Library and User's Guide, Oxford University Press, New York.

DOE-YMP, 1993a. See U.S. Department of Energy, 1993a.

DOE-YMP, 1993b. See U.S. Department of Energy, 1993b.

Dudley, A. L., R. R. Peters, M. S. Tierney, E. A. Klavetter, J. H. Gauthier, and M. L. Wilson, 1988. Total System Performance Assessment Code (TOSPAC) Volume 1: Physical and Mathematical Bases, SAND85-0002, Sandia National Laboratories, Albuquerque, New Mexico.

Dunn, E., and S. R. Sobolik, 1993. Evaluation of the Effects of Underground Water Usage and Spillage in the Exploratory Studies Facility, SAND93-1182, Sandia National Laboratories, Albuquerque, New Mexico.

Fewell, M.E., S.R. Sobolik, and J.H. Gauthier, 1992. Estimation of the Limitations for Surficial Water Addition Above a Potential High Level Radioactive Waste Repository at Yucca Mountain, Nevada, SAND91-0790, Sandia National Laboratories, Albuquerque, New Mexico.

Flint, L. E., and A. L. Flint, 1990. Preliminary Permeability and Water-Retention Data for Nonwelded and Bedded Tuff Samples, Yucca Mountain Area, Nye County, Nevada, USGS/OFR 90-569, U.S. Geological Survey, Denver, Colorado.

Freeze, R. A., and J. A. Cherry, 1979. Groundwater, Prentice-Hall, Inc., Englewood Cliffs, New Jersey, p. 74.

Hopkins, P.L., R.R. Eaton, and S. Sinnock, 1987. Effect of Drift Ventilation on Repository Hydrology and Resulting Solute Transport Implications, SAND86-1571, Sandia National Laboratories, Albuquerque, New Mexico.

Hopkins, P. L., N. E. Bixler, and R. R. Eaton, 1991. NORIA-SP - A Finite Element Computer Program for Analyzing Liquid Water Transport in Porous Media, SAND90-2542, Sandia National Laboratories, Albuquerque, New Mexico.

Klavetter, E. A., and R. R. Peters, 1986. Estimation of Hydrologic Properties of An Unsaturated, Fractured Rock Mass, SAND84-2642, Sandia National Laboratories, Albuquerque, New Mexico.

Kume, J., and D.P. Hammermeister, 1990. Geohydrologic Data from Test Hole USW UZ-7, Yucca Mountain Area, Nye County, Nevada, USGS/OFR-88-465, U.S. Geologic Survey, Denver, Colorado.

Lobmeyer, D.H., M.S. Whitfield, Jr., R.G. Lahoud, and L. Bruckheimer, 1983. Geohydrologic Data for Test Well UE-25b No. 1, evada Test Site, Nye County, Nevada, USGS/OFR-83-855, U.S. Geological Survey, Denver, Colorado, and Fenix and Scisson, Inc., Mercury, Nevada.

Millington, R. J., 1959. "Gas Diffusion in Porous Media," Science, Vol. 130, pp.100-102.

Nelson, P.H., D.C. Muller, U. Schimschal, and J.E. Kibler, 1991. Geophysical Logs and Core Measurements from Forty Boreholes at Yucca Mountain, Nevada, Geophysical Investigations Map USGS-MAP-GP-1001, U.S. Geological Survey, Denver, Colorado.

Odeh, A. S., 1965. "Unsteady-State Behavior of Naturally Fractured Reservoirs," Society of Petroleum Engineers Journal., Vol. 5, pp. 60-65.

Ortiz, T.S., R.L. Williams, F.B. Nimick, B.C. Whittet, and D.L. South, 1985. A Three-Dimensional Model of Reference Thermal/Mechanical and Hydrological Stratigraphy at Yucca Mountain, Southern Nevada, SAND84-1076, Sandia National Laboratories, Albuquerque, New Mexico.

Peters, R. R., and E. A. Klavetter, 1988. "A Continuum Model for Water Movement in an Unsaturated Fractured Rock Mass," Water Resources Research, Vol. 24, No. 3, pp. 416-430, March 1988.

Peters, R. R., E. A. Klavetter, I. J. Hall, S. C. Blair, P. R. Heller, and G. W. Gee, 1984. Fracture and Matrix Hydrologic Characteristics of Tuffaceous Materials from Yucca Mountain, Nye County, Nevada, SAND84-1471, Sandia National Laboratories, Albuquerque, New Mexico.

Pruess, K., 1983. GMINC-A Mesh Generator for Flow Simulations in Fractured Reservoirs, LBL-15227, Lawrence Berkeley Laboratory, Berkeley, California.

Pruess, K., 1987. TOUGH User's Guide, LBL-20700, NUREG/CR-4645, Lawrence Berkeley Laboratory, Berkeley, California.

Pruess, K., 1991. TOUGH2-A General-Purpose Numerical Simulator for Multiphase Fluid and Heat Flow, LBL-29400, Lawrence Berkeley Laboratory, Berkeley, California.

Pruess, K., and T. N. Narasimhan, 1985. "A Practical Method for Modeling Fluid and Heat Flow in Fractured Porous Media," Society of Petroleum Engineers Journal, Vol. 25, No. 1, pp. 14-26.

Robey, T. H., 1994. Development of Models for Fast Fluid Pathways Through Unsaturated Heterogeneous Porous Media, SAND93-7109, Sandia National Laboratories, Albuquerque, New Mexico.

Schenker, A. R., D. C. Guerin, T. H. Robey, C.A. Rautman, and R.W. Barnard, 1995. Stochastic Hydrogeologic Units and Hydrogeologic Properties Development for Total Systems Performance Assessments, SAND94-0244, Sandia National Laboratories, Albuquerque, New Mexico.

SNL (Sandia National Laboratories), 1994. *ESF PA Analysis #14 -- Sensitivity of ESF Hydrological Analyses to Variations in Ventilation Models, Conceptual Models, and Material Properties*, Work Agreement WA-0089, Rev. 01, Sandia National Laboratories, Albuquerque, New Mexico.

Sobolik, S. R., M. E. Fewell, and R. R. Eaton, 1991. Movement of Shaft and Drift Construction Water in Yucca Mountain, Nevada -- An Extended Study, SAND91-0791, Sandia National Laboratories, Albuquerque, New Mexico.

Sobolik, S. R., and M. E. Fewell, 1992. Estimation of the Impact of Water Movement from Sewage and Settling Ponds Near a Potential High Level Radioactive Waste Repository in Yucca Mountain, Nevada, SAND91-0792, Sandia National Laboratories, Albuquerque, New Mexico.

Sobolik, S. R., and M. E. Fewell, 1993. Estimations of the Extent of Migration of Surficially Applied Water for Various Surface Conditions Near the Potential Repository Perimeter, SAND92-2248, Sandia National Laboratories, Albuquerque, New Mexico. (NNA.931110.0040)

Spengler, R.W., D.C. Muller, and R.B. Livermore, 1979. Preliminary Report on the Geology and Geophysics of Drill Hole UE25a-1, Yucca Mountain, Nevada Test Site, USGS/OFR-79-1244, U.S. Geological Survey, Denver, Colorado.

Spengler, R.W., and J.G. Rosenbaum, 1980. Preliminary Interpretations of Geologic Results Obtained from Boreholes UE25a-4, -5, -6, and -7, Yucca Mountain, Nevada Test Site, USGS/OFR-80-929, U.S. Geological Survey, Reston, Virginia.

Spengler, R.W., M.P. Chornack, D.C. Muller, and J.E. Kibler, 1984. Stratigraphic and Structural Characteristics of Volcanic Rocks in Core Hole USW G-4, Yucca Mountain, Nye County, Nevada, USGS/OFR-84-789, U.S. Geological Survey, Denver, Colorado.

U.S. Department of Energy, 1988. "Core Photographs of USW G-4," PAN AM-DNA Photo, Negative No. W 088 through W 195, U.S. Department of Energy, Mercury, Nevada.

U.S. Department of Energy, 1988. "Core Photographs of UE25a#1," PAN AM-DNA Photo, Negative No. W 217 through W 301, U.S. Department of Energy, Mercury, Nevada.

U.S. Department of Energy, 1988. "Core Photographs of UE25b-1H," PAN AM-DNA Photo, Negative No. W 800 through W 883, U.S. Department of Energy, Mercury, Nevada.

U.S. Department of Energy, 1988. "Core Photographs of UE25a#5," PAN AM-DNA Photo, Negative No. W 1448 through W 1461, U.S. Department of Energy, Mercury, Nevada.

U.S. Department of Energy, 1988. "Core Photographs of UE25a#6," PAN AM-DNA Photo, Negative No. W 1482 through W 1493, U.S. Department of Energy, Mercury, Nevada.

U.S. Department of Energy, 1988. "Core Photographs of UE25a#4," PAN AM-DNA Photo, Negative No. W 1530 through W 1545, U.S. Department of Energy, Mercury, Nevada.

U.S. Department of Energy, 1988. "Yucca Mountain Site Project Atlas," YMP/88-21, U.S. Department of Energy, Las Vegas, Nevada.

U.S. Department of Energy, 1989. "Core Photographs of UE25a#7," PAN AM-DNA Photo, Negative No. W 1560 through W 1592, U.S. Department of Energy, Mercury, Nevada.

U.S. Department of Energy, Yucca Mountain Site Characterization Project (DOE-YMP), 1993a. Reference Information Base (RIB), Rev. 0, YMP/93-02, Las Vegas, Nevada.

U.S. Department of Energy, Yucca Mountain Site Characterization Project (DOE-YMP), 1993b. Yucca Mountain Site Characterization Project Exploratory Studies Facility Design Requirements Document, Rev. 0, YMP/CM-0019, July 14, 1993, Las Vegas, Nevada.

van Genuchten, M., 1980. "A Closed-Form Equation for Predicting the Hydraulic Conductivity of Unsaturated Soils," Soil Science Society of America Journal., Vol. 44, No. 5, pp. 892- 898.

Vargaftik, N.B., 1975. Tables on the Thermophysical Properties of Liquids and Gases, 2nd ed., Hemisphere Publishing Corp., Washington, D.C., distributed by Halsted Press, New York.

Voss, C., 1992, Letter to T. Robey, SNL, Subject: Additional Data for Yucca Mountain Test Case - Attachment 3: USW UZN-53 Core Data, dated October 30, 1992, Golder Associates, Redmond, Washington. (MOL.19941021.0002)

Warren, J. E. and P. J. Root, 1963. "The Behavior of Naturally Fractured Reservoirs," Society of Petroleum Engineers Journal, Vol. 3, No. 5, pp. 245-255.

Whitfield, M.S., Jr., W. Thordarson, and E.P. Eshom, 1984. Geohydrologic and Drill-Hole Data for Test Well USW H-4, Yucca Mountain, Nye County, Nevada, USGS/OFR-84-449, U.S. Geological Survey, Denver, Colorado.

Wilson, M. L. et al., 1994. Total-System Performance Assessment for Yucca Mountain - SNL Second Iteration (TSPA-1993), SAND93-2675, Sandia National Laboratories, Albuquerque, New Mexico.

Zyvoloski, G., Z. Dash, and S. Kelkar, 1992. FEHMN 1.0: Finite Element Heat and Mass Transfer Code, LA-12062-MS, Rev. 1, Los Alamos National Laboratory, Los Alamos, New Mexico.

APPENDIX A: Stratigraphic and Hydraulic Parameters Used For the Analyses

Table A.1. Definition of Hydrologic Units (Ortiz et al., 1985)

CFUn -- Upper Crater Flat nonwelded, zeolitized unit
PPw -- Prow Pass welded unit
CHnz -- Zeolitized Calico Hills nonwelded unit (CHn3z, CHn2z, CHn1z)
CHnv -- Vitric Calico Hills nonwelded unit (CHn3v, CHn2v, CHn1v)
TSw3 (also TSbv) --
Basal Vitrophyre of the Topopah Spring welded unit
TSw2 -- Topopah Spring welded unit (The potential repository unit)
TSw1 -- Topopah Spring welded unit
PTn -- Paintbrush nonwelded unit
TCw -- Tiva Canyon welded unit
UO -- Undifferentiated Overburden (alluvium)

Table A.2. UE-25a #1 Stratigraphy Used for Previous ESF Performance Assessment Analyses

(Ref: Sobolik and Fewell, 1992; Sobolik and Fewell, 1993)
Nevada State Plane Coordinates (feet): E.566,350, N.764,900

Material Designation	Elevation (m) Bottom	Top
Water Table		730.6
CHnz	730.6	798
TSw3	798	815
TSw2	815	871
TSw1	871	1115
PTn	1115	1140
TCw	1140	1190
Alluvium	1190	1199

Table A.3. Alluvium Hydrogeologic Properties as Used by Previous ESF Performance Assessment Analyses

(Ref: Sobolik and Fewell, 1992; Sobolik and Fewell, 1993)

Porosity	Matrix Saturated Hydraulic Conductivity (m/s)	Residual Saturation	α (1/m)	β	Bulk-Rock Compressibility (1/m)
0.32	5.00×10^{-7}	0.3	0.423	2.06	0

Fracture porosity, none 0
Fracture compressibility, 1/m 0

Table A.4. Hydrogeologic Properties Used for Previous ESF Performance Assessment Analyses

(Ref: Klavetter and Peters, 1986)

Matrix Properties

Unit	Porosity	Saturated Hydraulic Conductivity (m/s)	Residual Saturation	α (1/m)	ß	Bulk-Rock Compressibility (1/m)	Sample
CHnz	0.28	2.00×10^{-11}	0.11	0.00308	1.602	2.60×10^{-6}	G4-11
CHnv	0.46	2.70×10^{-7}	0.041	0.0160	3.872	3.90×10^{-6}	GU3-14
TSw3	0.07	1.50×10^{-12}	0.08	0.00441	2.058	5.80×10^{-7}	GU3-11
TSw2	0.11	1.90×10^{-11}	0.08	0.00567	1.798	5.80×10^{-7}	G4-6
TSw1	0.11	1.90×10^{-11}	0.08	0.00567	1.798	1.20×10^{-6}	G4-6
PTn	0.40	3.90×10^{-7}	0.10	0.015	6.872	8.20×10^{-6}	GU3-7
TCw	0.08	9.70×10^{-12}	0.002	0.00821	1.558	6.20×10^{-7}	G4-1

Fracture Properties

Unit	Porosity	Saturated Hydraulic Conductivity (m/s)	Residual Saturation	α (1/m)	ß	Fracture Compress-ibility (1/m)	Sample
CHnz	4.60×10^{-5}	2.00×10^{-4}	0.0395	1.2851	4.23	2.80×10^{-8}	G4-4F
CHnv	4.60×10^{-5}	2.00×10^{-4}	0.0395	1.2851	4.23	2.80×10^{-8}	G4-4F
TSw3	4.30×10^{-5}	1.60×10^{-5}	0.0395	1.2851	4.23	2.10×10^{-8}	G4-2F
TSw2	1.80×10^{-4}	1.75×10^{-5}	0.0395	1.2851	4.23	1.20×10^{-7}	G4-2F
TSw1	4.10×10^{-5}	2.20×10^{-5}	0.0395	1.2851	4.23	5.60×10^{-8}	G4-2F
PTn	2.70×10^{-5}	6.10×10^{-4}	0.0395	1.2851	4.23	1.90×10^{-7}	G4-3F
TCw	1.40×10^{-4}	3.80×10^{-5}	0.0395	1.2851	4.23	1.32×10^{-6}	G4-2F

APPENDIX B: Borehole Stratigraphic Log Data Used for Calculations Involving Heterogeneous Material Properties

Table B.1. UE25 a#1 Stratigraphic Log Data

```
# GROUNDWATER TRAVEL TIME 93/94 #
# UE25a-1 STRATIGRAPHY DCG/LATA #
# Coordinates: (DOE, 1988, YMP/88-21) E-566350.0 N-764900.2 ft #
 172615.06 233130.20 # m #
# Ground Elevation: 1199.02 m (3934.0 ft) MSL (DOE, 1988, YMP/88-21) #
# Sources: Litholog-Spengler et al, 1979, USGS-OFR-79-1244; Geophysical log-Nelson et al., 1991, USGS-MAP-
GP-1001, UE25a-1 core photographs, Neg. Nos. W217-W301 #

# Elev. Strat  Depth Depth  Stratigraphic Unit: lithology (methods) #
# (m)    ID     (m)   (ft) #

  1199.0  3 #   0.0    0.0  Alluvium (litholog, low GR) #
  1189.9  1 #   9.1   30.0  Tiva: densely welded-devitrified (litholog, photolog, >GR, smooth-CAL) #
  1146.3  1 #  52.7  173.0  Tiva: moderately welded-? (litholog, photolog, <GR, NNL-spike, MS-spike) #
  1139.6  2 #  59.4  195.0  Tiva: non & partially welded-argillized (litholog, photolog, >CAL, <GR) #
  1132.9  2 #  66.1  217.0  Bedded Tuff: nonwelded-argillized (litholog, photolog, >CAL, <GR, <NNL, <MS) #
  1116.7  2 #  82.3  270.0  Topopah Sp.: nonwelded-vitric (litholog, photolog, <CAL, >NNL) #
  1115.0  1 #  84.0  275.6  Topopah Sp.(caprock): moderately & densely welded-vitric (litholog, photolog, <CAL,
low-PORCN, hi-DBDCN & GDCN) #
  1109.4  1 #  89.6  294.0  Topopah Sp.: moderately to densely welded-devitrified (litholog, photolog, <CAL,
>GR, >NNL, <<MS) #
   814.3  1 # 384.7 1262.2  Topopah Sp.: moderately to densely welded-vitric (litholog, photolog, GR-spike,
<NNL) #
   811.0  5 # 388.0 1273.0  Topopah Sp.: densely welded-vitrophyre (litholog, photolog, low-CAL, hi-DBC, NNL-
spike) #
   797.5  3 # 401.5 1317.3  Topopah Sp.: non & partially welded-devitrified (litholog, photolog, <<DBC) #
   783.3  4 # 415.7 1364.0  Calico Hills & bedded tuff: nonwelded-zeolitic (litholog, photolog, >CAL, <DBC,
>NNL) #
   639.5  2 # 559.5 1835.7  Prow Pass: non to partially welded-devitified (litholog, photolog, >SP, stable DBC &
PVEL) #
   604.7  5 # 594.3 1950.0  Prow Pass: moderately welded-devitrified (litholog, photolog, <SP, >DBC, >PVEL,
>R-SN, >R-LN, >NNL) #
   585.1  2 # 613.9 2014.2  Prow Pass: partially welded-devitrified (litholog, photolog, >SP, <DBC, <PVEL, <R-
SN, <R-LN, <NNL) #
   556.0  5 # 643.0 2109.7  Prow Pass: moderately welded-vitric (litholog, photolog, <SP, >DBC, >PVEL, >R-SN,
<R-LN, >NNL) #
   552.2  2 # 646.8 2122.2  Prow Pass: partially welded-devitrified (litholog, photolog, >SP, <DBC, <PVEL, <R-
SN, >R-LN, <NNL) #
   501.6  2 # 697.4 2288.2  Prow Pass: non to partially welded-zeolitic (litholog, photolog, >SP, >DBC, <R-SN,
<R-LN, >NNL) #
   487.9  3 # 711.1 2333.2  Bullfrog: partially to moderately welded-devitrified (litholog, photolog, >GR, <SP,
<PVEL, >R-SN, <R-LN, >NNL) #
   436.8 -1 # 762.2 2500.6  Bottom #
```

Table B.2. UE25 a#4 Stratigraphic Log Data

```
# GROUNDWATER TRAVEL TIME 93/94 #
# UE 25a-4 STRATIGRAPHY DCG/LATA #
# Coordinates: E-564471.6 N-767971.6 ft (DOE, 1988, YMP/88-21) #
 172042.5 234066.3 # m #
# Ground El. 1249.8 m (4100.70 ft) MSL (DOE, 1988, YMP/88-21) #
# Sources: litholog-Spengler and Rosenbaum, 1980, USGS-OFR-80-929; geophysics-Nelson et al., 1991, USGS-MAP-GP-1001; UE25a-4 core photographs, neg. no's W1535 - W1445 #

# Alt.   ID Depth Depth  Stratigraphic Unit: lithology (methods) #
# (m)       (m)   (ft) #

 1249.8 3 #  0.0   0.0 Alluvium (litholog, hiCAL-erratic, lowDBC, lowENP) #
 1240.7 1 #  9.1  30.0 Tiva: moderately to densely welded-devitrified (litholog, <SP, >GR, <<CAL, >DBC, >R-SN & LN, >ENP) #
 1212.9 2 # 36.9 121.0 Tiva: partially to nonwelded-vitric (litholog, photolog, >CALspike, RILDspike, ENPspike) #
 1203.9 2 # 45.9 150.6 Bedded Tuff: nonwelded-vitric (litholog, GRspike, DBCspike, RILDspike, ENPspike) #
 1203.3 2 # 46.5 152.5 Yucca Mtn.: nonwelded-vitric (litholog, photolog, >GR, <DBC, >RILD, >ENP) #
 1195.2 2 # 54.6 179.0 Bedded Tuff: nonwelded-vitric (litholog, photolog, slight>CAL, GRspike, DBCspikes, >RILD) #
 1191.6 2 # 58.2 191.0 Pah Canyon: nonwelded-vitric, some argillic (litholog, photolog, <CAL, <GR, <DBC, >RILD, <ENP) #
 1166.1 2 # 83.7 274.6 Bedded Tuff: nonwelded-vitric (litholog, >CAL, <GR, >DBC, <RILD, <R-SN & LN, MSspike) #
 1164.5 2 # 85.3 280.0 Topopah Sp.: non & partially welded-vitric (litholog, photolog, >CAL, <GR, <DBC, <R-SN & LN, <ENP, MSspike) #
 1153.2 1 # 96.6 317.0 Topopah Sp.: welded-vitrophyre (litholog, photolog, <CAL, >GR, >>DBC, >RILD, >R-SN & LN, >MS) #
 1152.3 1 # 97.5 320.0 Topopah Sp.: moderately & densely welded-devitrified (litholog, photolog, GRspike, hiDBC, RILDspike, <ENP, <MS) #
 1097.4 -1 # 152.4 500.0 Bottom #
```

Table B.3. UE25 a#5 Stratigraphic Log Data

```
# GROUNDWATER TRAVEL TIME 93/94 #
# UE25a-5 STRATIGRAPHY DCG/LATA #
# Coordinates: E-564755.1 N-766956.4 ft (DOE, 1988, YMP/88-21) #
 172129.0  233756.9 # m #
# Ground El. 1236.4 m (4056.50 ft) MSL (DOE, 1988, YMP/88-21) #
# Sources: lithology-Spengler and Rosenbaum, 1980, USGS-OFR-80-929; Geophysics-Nelson et al., 1991, USGS-MAP-GP-1001; UE25a-5 core photographs, neg. no's W1448 - W1461 #

# Elev. ID  Depth  Depth  Stratigraphic Unit: lithology (methods) #
# (m)        (m)   (ft)#

 1236.4  3 #  0.0    0.0  Alluvium (litholog, erraticCAL, lowDBC, lowENP, lowMS) #
 1209.0  1 #  27.4   90.0  Tiva: densely welded-devitrified (litholog, photolog, lowCAL-deflects lower @ 118', highDBC) #
 1197.4  2 #  39.0  128.0  Tiva: non to partially welded-vitric (litholog, photolog, >CAL, >GR, <DBC, <RILD, <ENP) #
 1194.2  2 #  42.2  138.5  Yucca Mtn.: nonwelded-vitric (litholog, photolog, >CAL, <GR, <DBC, <RILD, MSspike) #
 1185.5  2 #  50.9  167.0  Bedded Tuff: nonwelded-vitric (litholog, photolog, <CAL, >GR, <SP, >DBC, >RILD, slight>ENP, <MS) #
 1179.9  2 #  56.5  185.4  Pah Canyon: nonwelded-vitric (litholog, photolog, >GR, <DBC, >RILD, >ENP, <MS) #
 1166.4  2 #  70.0  229.7  Bedded Tuff: nonwelded-vitric (litholog, photolog, <GR, >SP, >DBC, <RILD, <R-SN & LN, <MS) #
 1164.1  2 #  72.3  237.2  Topopah Sp.: nonwelded-vitric (litholog,>GR, <SP, <DBC, >RILD, >R-SN & LN, >ENP, <MS) #
 1154.7  2 #  81.7  268.0  Topopah Sp.: nonwelded-moderately welded-vitric (litholog, photolog, slight>CAL, >GR, <SP, >>DBC, >RILD, >R-SN & LN, >ENP, >MS) #
 1152.0  5 #  84.4  277.0  Topopah Sp.: densely welded-vitrophyre (litholog, photolog, slight<CAL, <GR, >SP, >>DBC, >RILD, > R-SN & LN, >ENP, >MS) #
 1151.4  1 #  85.0  279.0  Topopah Sp.: densely welded-devitrified (litholog, photolog, CALspike, <GR, >SP, <DBC, >RILD, >R-SN & LN, <ENP, <<MS) #
 1088.0 -1 # 148.4  487.0  Bottom #
```

Table B.4. UE25 a#6 Stratigraphic Log Data

GROUNDWATER TRAVEL TIME 93/94
UE25a-6 STRATIGRAPHY DCG/LATA
Coordinates: E-564500.7 N-765899.5 ft (DOE, 1988, YMP/88-21)
172051.4 233434.8 # m #
Ground El. 1235.3 m (4052.90 ft) MSL (DOE, 1988, YMP/88-21)
Sources: litholog-Spengler and Rosenbaum, 1980, USGS-OFR-80-929; Geopyhsics-Nelson et al., 1991, USGS-MAP-GP-1001; UE25a-6 core photographs, neg. no's W1842 - W1493

Elev. ID Depth Depth Stratigraphic Unit: lithology (methods)
(m) (m) (ft)

1235.3 3 # 0.0 0.0 Alluvium (litholog, lowGR, lowENP) #
1229.2 1 # 6.1 20.0 Tiva: densely & moderately welded-devitrified (litholog, photolog, >GR, mod-hiDBC, mod-hiRILD, lowIP & MS) #
1203.9 1 # 31.4 103.0 Tiva: partially to moderately welded-devitrified (litholog, photolog, <CAL, <GR, hiSP, <DBC, <RILD, <R-SN & LN, <ENP, <MS) #
1197.8 2 # 37.5 123.0 Tiva: non to partially welded-vitric (litholog, photolog, >CAL, <GR, <DBC, <RILD, >R-SN, <ENP, >MS, <IP) #
1191.3 2 # 44.0 144.4 Bedded Tuff:nonwelded-argillic (litholog, photolog, >CAL, <GR, >SP, >DBC, >RILD, >R-SN, >ENP, >MP, >MS) #
1189.8 2 # 45.5 149.3 Yucca Mtn. mbr.: nonwelded-vitric (litholog, photolog, <CAL, >GR, >SP, <DBC, >RILD, >R-SN, >ENP, <MS, >IP) #
1183.7 2 # 51.6 169.3 Bedded Tuff: nonwelded-vitric (litholog, <CAL, <GR, >SP, <DBC, >RILD, >R-SN, <ENP, >MS, <IP) #
1177.9 2 # 57.4 188.3 Pah Canyon & bedded tuff.: nonwelded-vitric (litholog, photolog, <CAL, <SP, <GR, >DBC, <RILD, >R-SN, <ENP, >MS, <IP) #
1166.1 2 # 69.2 227.0 Topopah Sp.: non to/& partially welded vitric (litholog, photolog, <CAL, >GR, <SP, >DBC, >RILD, >R-SN & LN, >ENP, <MS, >IP) #
1161.6 5 # 73.7 241.8 Topopah Sp.: densely welded-vitrophyre (litholog, photolog, <CAL, >GR, <SP, >>DBC, >RILD, >R-SN & LN, >>ENP, <IP, >MS) #
1160.3 1 # 75.0 246.0 Topopah Sp.: densely welded-devitrified (litholog, photolog, <CAL, >GR, <SP, slight<DBC, >RILD, >R-SN & LN, <IP, <MS) #
1082.9 -1 # 152.4 500.0 Bottom #

Table B.5. UE25 a#7 Stratigraphic Log Data

```
# GROUNDWATER TRAVEL TIME 93/94 #
# UE25a-7 STRATIGRAPHY DCG/LATA #
# Coordinates: E-565468.5 N-766249.9 (DOE, 1988, YMP/88-21) #
 172346.4  233541.6 # m #
# Ground El. 1220.5 m (4004.60 ft) MSL (DOE, 1988, YMP/88-21) #
# Sources: litholog-Spengler and Rosenbaum, 1980, USGS-OFR-80-929; Geophysics-Nelson et al., 1991, USGS-
MAP-GP-1001; UE25a-7 core photographs, neg. no's W1560 - W1592 #

# Alt.  ID  Depth  Depth  Stratigraphic Unit: lithology (methods) #
# (m)        (m)    (ft) #

 1220.5  6 #   0.0    0.0  Alluvium (litholog, photolog, hiCAL, low-erraticDBC, lowENP, lowMS) #
 1173.9  1 #  46.6  153.0  Tiva: densely welded-devitrified (litholog, photolog, <CAL, <GR, >DBC, <RILD, <R-
SN & LN, <ENP, >MS, <IP) #
 1167.6  2 #  52.9  173.6  Tiva: partially to nonwelded-vitric (litholog, photolog, <CAL, >GR, >SP, <DBC,
<RILD, <R-SN & LN, <ENP, >MS, <IP) #
 1162.6  2 #  57.9  190.0  Bedded Tuff: nonwelded-argillic (litholog, photolog, GP stratigraphic breaks obscure
logs) #
 1161.3  2 #  59.2  194.2  Yucca Mtn. mbr.: nonwelded-vitric (litholog, slight>CAL, <GR, >SP, <DBC, <RILD,
<R-SN, >R-LN, <ENP, <MS) #
 1155.6  2 #  64.9  213.0  Bedded Tuff: nonwelded-vitric (litholog, photolog, slight>CAL, <GR, >SP, <DBC, R's
crowded, can't read) #
 1153.4  2 #  67.1  220.2  Pah Canyon mbr.: nonwelded-vitric (litholog, slight>CAL, <GR, >SP, <DBC, <RILD,
<R-SN & LN, <ENP, >MS) #
 1139.5  2 #  81.0  265.8  Bedded Tuff: nonwelded-argillic (litholog, photolog, >CAL, >GR, >SP, >DBC, <RILD,
<R-SN & LN, >ENP, >MS, <IP) #
 1137.4  2 #  83.1  272.7  Topopah Sp.: partially & nonwelded-vitric (litholog. photolog, <CAL, <GR, >SP,
<DBC, >RILD, >R-SN & LN, <MS, <IP) #
 1127.7  5 #  92.8  304.5  Topopah Sp.: densely welded-vitrophyre (litholog, photolog, smoothCAL, >>GR, <SP,
>>DBC, >RILD, >R-SN & LN, >>ENP, >NNL, >>MS, >>IP) #
 1126.6  1 #  93.9  308.0  Topopah Sp.: densely & moderately welded-devitrified (litholog, photolog, smoothCAL,
>GR, <SP, slight<DBC, >RILD, >R-SN & LN, <IP, <MS) #
 1068.1  1 # 152.4  500.0  Topopah Sp.: densely welded (lowCAL, bottom of lithologic description) #
 1008.1  1 # 212.4  697.0  Topopah Sp.: welded-?? (USW G-4 GP & lithologs, photolog, smoothCAL, <GR, >SP,
>R-SN & LN, <<NNL) #
  954.1  1 # 266.4  874.0  Topopah Sp.: moderately welded?? (USW G-4 GP & lithologs, photolog, <GR, <SP, <R-
SN & LN, <NNL) #
  915.1 -1 # 305.4 1002.0  bottom of geophysics #
```

Table B.6. UE25 b#1 Stratigraphic Log Data

GROUNDWATER TRAVEL TIME 93/94 DCG/LATA
UE25b-1 STRATIGRAPHY
Coordinates: E-566416.4 N-765243.4 ft. (DOE, 1988, YMP/88-21)
172635.3 233234.8 # m #
Ground Elevation: 1200.5 m (3939.00 ft) MSL (DOE, 1988, YMP/88-21)
Sources: litholog-Lobmeyer et al., 1983, USGS-OFR-83-855; GP logs-Nelson et al., 1991, USGS-MAP-GP-1001; UE25b-1H core photographs, neg. no's W801-W883

# Elev. (m)	ID	Depth (m)	Depth (ft)#	Stratigraphic Unit: lithology (methods) #
1200.5	3 #	0.0	0.0	Alluvium (litholog, erratic CAL) #
1154.8	1 #	45.7	149.9	Tiva: densely welded (litholog, <CAL) #
1136.5	2 #	64.0	210.0	Tiva: partially to nonwelded-vitric (litholog, slight>CAL) #
1127.4	2 #	73.1	239.8	Pah Canyon & Bedded Tuffs: nonwelded-vitric (litholog, erratic CAL) #
1116.7	1 #	83.8	275.0	Topopah Sp.: densely welded-vitrophyre (litholog, slight>CAL) #
1115.2	1 #	85.3	279.9	Topopah Sp.: densely welded-devitrified (litholog, photolog, <CAL, >K, >Th) #
805.8	5 #	394.7	1295.0	Topopah Sp.: densely welded-vitrophyre (litholog, <CAL, >DBC, <ENPspike, <RILDspike) #
795.1	3 #	405.4	1330.0	Topopah Sp.: moderately to partially welded-vitric (litholog, slight>CAL, <DBC, <ENP) #
792.1	3 #	408.4	1340.0	Topopah Sp.: ?partially welded?-?vitric? (>CAL, <<DBCspike, >>RILD, ENPstable, >U) #
789.0	4 #	411.5	1350.0	Bedded Tuff: nonwelded-altered-?zeolitic? (litholog, >SP, >DBC, >K, <RILD, >ENP) #
778.3	4 #	422.2	1385.2	Calico Hills & bedded tuff: nonwelded-zeolitic (litholog, photolog from 1571 ft. & below to 1591 ft., <SP, slight<DBC, <RILD, <K) #
630.8	2 #	569.7	1869.2	Prow Pass: non to/& partially welded-zeolitic & devitrified (litholog, photolog from 1900 ft. & below, >SP, >DBC, >PVEL, <RILD, <R-SN, <K) #
599.5	5 #	601.0	1972.0	Prow Pass: partially to moderately welded-devitrified (litholog, photolog, <CAL, >DBC, <NBC, >PVEL, >RILD, >R-SN, <FLOW) #
577.3	2 #	623.2	2044.7	Prow Pass: partially to/& nonwelded-devitrified (litholog, photolog, >CAL, <SP, <DBC, >NBC, <PVEL, <RILD, <R-SN, <K) #
549.8	5 #	650.7	2135.0	Prow Pass: partially to moderately welded-devitrified (litholog, photolog, <CAL, >SP, >DBC, <NBC, >PVEL, >SVEL, >RILD, >R-SN) #
520.7	2 #	679.8	2230.4	Prow Pass & Bedded Tuff: non & partially welded-devitrified & zeolitic (litholog, photolog, <DBC, >NBC, <PVEL, <SVEL, <RILD, <R-SN) #
480.8	3 #	719.7	2361.3	Bullfrog: non & partially welded-devitrified & vapor phase alt. (litholog, photolog, slight>CAL, <SVEL, <PVEL, >RILD, >R-SN) #
408.7	1 #	791.8	2598.0	Bullfrog: moderately welded-devitrified (litholog, photolog, slight>CAL, >SP, slight>PVEL & SVEL, >K, <FLOW) #
352.3	3 #	848.2	2783.0	Bullfrog & Bedded Tuff: partially to/& nonwelded-zeolitic (slightly argillic) (litholog, photolog, <<SP, <DBC, >NBC, SVEL & PVELspikes, <RILD, <R-SN, <K) #
321.9	-1 #	878.6	2882.7	Tram: non to partially welded-zeolitic (litholog, photolog, >SP, slight>DBC, <SVEL & PVEL, <RILD & R-SN) #

Table B.7. USW G-4 Stratigraphic Log Data

```
# GROUNDWATER TRAVEL TIME 94 #
# USW G-4 STRATIGRAPHY DCG/LATA #
# Coordinates: (DOE, 1988, YMP/88-21) 563081.6 765807.1 ft #
   171618.9 233406.6  # m #
# Dirt Pad El. 4166.90 ft, 1270.0 m (DOE, 1988, YMP/88-21) #
# Sources: Litholog-Spengler et al., 1984, USGS-OFR-84-789, Geophysics-Nelson et al., 1991, USGS-MAP-GP-
1001, USW G-4 core photographs, neg. number's W088-W195 #

#Elev.  ID   Depth  Depth  Stratigraphic Unit: lithology (methods) #
#(m)         (m)    (ft) #
1270.0  3  #   0.0    0.0  Alluvium: (litholog) #
1260.9  1  #   9.1   30.0  Tiva: mod. & densely welded-devitrified (litholog, photolog, hiSP, low CAL, hiDBC,
hiGRAV,  lowNNL,>K, >Th) #
1241.0  2  #  29.0   95.0  Tiva & Bedded Tuff: moderately, partially & nonwelded-vitric (litholog, photolog,
>CAL1 & CAL2, <<DBC, >NBC <NNL,<all resistivities) #
        #               PICK CHANGED FROM TSPA-93, BASED ON POROSITIES & GP #
1218.7  2  #  51.3  168.3  Pah Canyon: nonwelded-vitric (litholog, photolog, >CAL, >SP, <DBC, <GRAV, >K,
<Th) #
1212.7  2  #  57.3  188.0  Bedded Tuff: nonwelded-vitric & vitrophyric (litholog, photolog, hiCAL, <DBC,
<GRAV, <NNL, <K, <Th) #
1200.5  2  #  69.5  228.0  Topopah Sp.: nonwelded-vitric (litholog, photolog, <CAL,<SP,>GRAV, >DBC, >NNL,
>K, >Th) #
1197.2  1  #  72.8  239.0  Topopah Sp.: densely welded-vitrophyre (litholog, photolog,  >DBC, >GRAV, <NNL,
<K, >Th) #
1196.0  1  #  74.0  242.8  Topopah Sp.: densely welded(caprock)-devitrified (litholog, photolog, <CAL, <SP,
>DBC,>GRAV, >NNL, >K, >Th ) #
1189.1  1  #  80.9  265.4  Topopah Sp.: mod. to densely welded-vapor phase x-stalliztion (litholog, photolog,
<DBC, <GRAV, <NNL, >K) #
1185.3  1  #  84.7  278.0  Topopah Sp.: moderately to densely welded (caprock)-devitrified (litholog, photolog,
<CAL, <SP, <DBC, <GRAV, <NNL, >K) #
1184.7  2  #  85.3  280.0  Topopah Sp.: non to partially welded- vapor phase x-stalliztion (litholog, photolog,
<CAL, >SP,>DBC, >NNL, >K) #
1183.3  1  #  86.7  284.5  Topopah Sp.: mod. to densely welded-devitrified (litholog, photolog, >DBC, >NNL, >K,
>TH) #
 875.9  1  # 394.1 1293.0  Topopah Sp.: mod. to densely welded-argillic & zeolitic(?) (litholog, photolog, <CAL,
>DBC, <K) #
 868.7  5  # 401.3 1316.7  Topopah Sp.: densely welded-vitrophyre (litholog, photolog, >CAL, >DBC, >NNL, >K)
#
 859.9  3  # 410.1 1345.5  Topopah Sp.: moderately welded-vitric (litholog, photolog, <CAL, <DBC, >NNL, <K)
#
 854.2  3  # 415.8 1364.3  Topopah Sp.: partially welded-vitric (litholog INDICATES "WELDING DECREASES
DOWNWARD FROM 412.6 m," PHOTOLOG IND. WELDING TO 1364.3 ft (415.8 m), #
        #               GP BASED ON PHOTOLOG PICK, >CAL, <DBC, <NNL, <K, >U, <Th) #
 850.1  3  # 419.9 1377.7  Topopah Sp.: partially welded-zeolitic &  vitric (litholog, photolog, >CAL, <GRAV,
<DBC) #
 841.2  4  # 428.8 1407.0  Topopah Sp./Bedded Tuff: nonwelded-zeolitic (litholog, photolog, <GRAV, <DBC,
<RILD) #
 840.4  4  # 429.6 1409.5  Calico Hills: nonwelded-vitric (slightly zeolitic) (litholog, photolog, DBC, <GRAV,
>RILD, >K, >Th) #
 835.8  4  # 434.2 1424.6  Calico Hills: nonwelded-zeolitic (litholog, photolog, <CAL, >DBC, <RILD) #
 733.2  2  # 536.8 1761.2  Prow Pass: nonwelded-zeolitic (litholog, photolog, >CAL1, <TC, <DBG, <GRAV,
>RILD, >SN, <NNL, Kspike) #
```

728.2 2 # 541.8 1777.6 Prow Pass: nonwelded-devitrified (slightly zeolitic & argillic) (litholog, photolog, >RILD, >SN, <K, <Th) #

723.7 2 # 546.3 1792.4 Prow Pass: nonwelded-vapor phase x-stallization-argillic (litholog, photolog, >TC, <NBC, >GRAV, <DBC, <PVEL, >RILD, >SN, >NNL, >>K) #

700.1 5 # 569.9 1869.8 Prow Pass: partially welded ([welding] "inc. from unit above")-devitrified (litholog, ind. part. welding, GP ind. mod weldeing by >GRAV, >DBC) #

674.3 2 # 595.7 1954.5 Prow Pass: non to partially welded-devitrified & zeolitic (litholog, photolog, CALspike, TCspike, SPspike, <DBC, <NBC, <DBC, <RILD, <SN, <K) #

588.0 2 # 682.0 2237.6 Prow Pass/Bedded Tuff: nonwelded-zeolitic (litholog, photolog, >CAL, >TC, >PVEL, >K) #

586.0 3 # 684.0 2244.2 Bullfrog: partially welded- devitrified (litholog, photolog, <CAL, <TC, <DBC, <NBC, <DBC, <PVEL, >RILD, >SN, >NNL, >K) #

547.7 1 # 722.3 2370.0 Bullfrog: moderately welded-devitrified (litholog, photolog, slight<CAL, >DBC, <RILD, <SN) #

539.2 3 # 730.8 2397.8 Bullfrog: non & partially welded-devitrified (litholog, photolog, >CAL, <TC, <DBC, <PVEL,<K) #

490.1 1 # 779.9 2559.0 Bullfrog: moderately to densely welded-devitrified (litholog, photolog indicates mod.-dens. welded @ 2559-correlates w/GP, <CAL, >TC, >GRAV, >DBC, >PVEL, >SVEL, >SN, >K) #

453.1 3 # 816.9 2680.2 Bullfrog: partially welded-argillic (litholog, photolog, >CAL, >TC, <GRAV, <DBC, >NBC, <PVEL, <RILD, <SN, <NNL, <K) #

448.4 3 # 821.6 2695.7 Bullfrog: non & partially welded-zeolitic (litholog, photolog, <CAL, >TC, >DBC, >PVEL, <NNL, <K) #

436.9 3 # 833.1 2733.4 Bullfrog/Bedded Tuff: nonwelded-argillic & zeolitic (litholog, photolog, >TC, >GRAV, >DBC, >SVEL, <RILD, <SN, >K) #

430.1 -1 # 839.9 2755.7 Tram: nonwelded-devitrified (litholog, photolog, <TC, <DBC, <GRAV, >RILD, >SN, <NNL, <K) #

Table B.8. USW H-4 Stratigraphic Log Data

```
# GROUNDWATER TRAVEL TIME 94 #
# USW H-4 STRATIGRAPHY DCG/LATA #
# Coordinates: E-563911.1 N-761643.6 ft., Dirt pad elev. 4096.5 ft, 1248.6 m (DOE, 1988, YMP/88-21) COLLAR
EL. USED IN TSPA-93, 4097.64 #
    171871.7 232137.6 # m #
# Sources: litholog-Whitfield et al., 1984, USGS-OFR-84-449; Geophysics-Nelson et al., 1991, USGS-MAP-GP-
1001;#

# Elev.  ID  Depth  Depth  Stratigraphic Unit: lithology (methods) #
# (m)        (m)    (ft) #
1248.6 1 #   0.0    0.0 Land Surface, Tiva Canyon welded (litholog) #
1195.6 2 #  53.0  174.0 Bedded Tuff, Tiva & Paintbrush: nonwelded and partly to moderatly welded-vitric
(litholog, <DBC, <CAL, <RILD) #
1172.8 1 #  76.8  252.0 Topopah Sp.: densely and moderatly welded-?? (litholog, >DBC, >RILD) #
 887.4 5 # 361.2 1185.0 Topopah Sp.: [densely?] welded-vitrophyre (litholog, >CAL, <RILD, <ENP,<K,Th&U) #
 877.7 3 # 370.9 1217.0 Topopah Sp.: partly and nonwelded-vitric (litholog, <RILD, <ENP) #
 848.7 4 # 399.9 1312.0 Calico Hills: nonwelded and partly welded-zeolitic (litholog, >DBC, <RILD, <ENP) #
 768.5 4 # 480.1 1575.2 BEDDED TUFF: NONWELDED-ZEOLITIC? (LITHOLOG, >CAL, <TC, >DBC,
<RILD, >ENP, <U, <Th) #
 752.7 2 # 495.9 1627.0 PROW PASS: NOWELDED-ZEOLITIC (LITHOLOG, <DBC, >TC, >CAL, >RILD) #
 748.8 2 # 499.8 1640.0 Prow Pass: partly welded-DEVITRIFIED (litholog, >DBC, >RILD, ENPspike) #
 743.8 2 # 504.8 1656.2 Prow Pass: partly welded-devitrified, SLIGHTLY ZEOLOTIC? (litholog, >DBC, >RILD,
ENPspike)#
 652.7 2 # 595.9 1955.0 Prow Pass: partly welded-HIGHLY ZEOLITIC? (litholog, <CAL, >DBC, >R-LN&SN,
>Th&U) #
 558.8 2 # 689.8 2263.2 BEDDED TUFF: nonwelded-zeolitic (litholog, >R-LN&SN, >K, >DBC) #
 555.2 3 # 693.4 2275.0 Bullfrog: PARTLY welded (litholog, <CAL, >DBC, >R-SN&LN) #
 486.6 1 # 762.0 2500.0 BULLFROG: MODERATLY TO DENSELY WELDED-ZEOLITIC? (LITHOLOG,
<CAL, >TCspike, >DBC, <NBC, >R-LN & SN, Kspike, >U & Th, MAGZspike) #
 460.7 3 # 787.9 2585.1 BULLFROG: NON TO PARTLY WELDED-DEVITIFIED (LITHOLOG, >CAL, >SP,
<DBC, >NBC, <R-LN &SN, >MAGZ) #
 442.7 3 # 805.9 2644.2 BEDDED TUFF: NONWELDED-DEVITRIFIED (LITHOLOG, <CAL, >DBC, <NBC,
<PVEL, <R-SN & LN, >K, >Th, >MAGZ) #
 436.6 -1 # 812.0 2664.2 Tram #
```

Table B.9. USW H-5 Stratigraphic Log Data

```
# GROUNDWATER TRAVEL TIME 1994 #
# USW H-5 Stratigraphy #
#Coordinates: E-558908.7 N-766634.3 ft, elev. 4850.80 ft (DOE, 1988, YMP/88-21) #
 170347.1 233658.7 #m#
#Sources:  Lithologic Log of Drill Hole USW  H-5" Table  1  from USGS, 1983, USGS-OFR-83-853; Plate 12
and Figures 4, 10, 12,  13, #
# and 14 from Nelson et al. 1991, USGS-MAP-GP-1001 #

#Elev.   ID   Depth   Depth  Stratigraphy #
# (m)           (m)    (ft) #

1478.5   1  #   0.0    0.0  Tiva Canyon:  welded, lithologic log, ash flow, densely welded, devitrified. Geophysical
log, density high, #
         #              resistivity moderately high, potassium plateau. #
1353.6   2  #  124.9  409.8  Paintbrush and top 25 ft. Topopah Springs: nonwelded, lithologic log, bedded, ash-
fall or flow nonwelded, #
         #              vitric, geophysical log density decreases, resistivity decreases to moderate level, epithermal
neutron #
         #              stabilizes at low value, potassium low, total magnetic field plateau. #
1305.4   1  #  173.1  568.0  Topopah Spring:  welded, lithologic log, ashflow densely welded, devitrified;
geophysical log, density very #
         #              hashy but uniform, epithermal neutron uniform. #
 996.3   5  #  482.2 1582.0  Topopah Spring:  vitrophyre, lithologic log, ash flow densely welded vitrophere;
geophysical log, DBC changes #
         #              character, smoother, higher density, resistivity characterization changes-higher value. Both
resistivity and  #
         #              epithermal neutron show kick to lower values just above welded to vitric interface, could be
indication of #
         #              paleo weathered zone. #
 974.1   3  #  504.4 1655.0  Bottom 170 ft. of Topopah Spring below vitrophere and Calico Hills:  vitric, lithologic
log, first 55.45 ft. #
         #              Topopah Spring ashflow tuff, below Calico Hills, ash flow vitric; geophysical log, density log
decreases, character change. #
 905.5   4  #  573.0 1880.0  Calico Hills:  zeolitic, lithologic log, ash fall (?) zeolitic. Geophysical log, increase in
density (DBC),#
         #              decrease in resistivity, total count, spectral gamma decreases. #
 885.7   2  #  592.8 1945.0  Prow Pass: nonwelded vitric. Lithologic log, ashflow; geophysical log, decrease in
density and total #
         #              magnetic field, slight increase in resistivity. #
 877.8   5  #  600.7 1971.0  Prow Pass partially welded, devitrified.  Lithologic log, ashflow, devitrified. #
 830.8   2  #  647.7 2125.0  Lower Prow Pass: nonwelded, zeolitic (lithologic log, ash flow, zeolitized;
geophysical log, total count spectural #
         #              gamma shows dip, short rise followed by low swing in compensated borehole density) #
 788.7   1  #  689.8 2263.2  Bullfrog Member:  partially to mod welded, devitrified.  Lithologic log, ashflow.
Geophysical log, compensated #
         #              borehole density signal changes character, loses smoothness, resistivity increases. #
 651.6   3  #  826.9 2713.0  bedded tuff. Lithologic log, reworked. Geophysical log only slight indications in
resistivity; quick peak then dip. #
 642.7  -1  #  835.8 2742.3  Tram  #
```

Table B.10. USW UZN-53 Stratigraphic Log Data

```
# GROUNDWATER TRAVEL TIME 94 #
# USW UZN-53 STRATIGRAPHY DCG/LATA #
# Coordinates (T. Robey, Flint data) E-564236.86 N-760095.86 ft #
    171971.0 231665.9 # m #
# Ground El. 4055.64 ft. 1236.1 m. (T. Robey, Flint data) #
# Sources: Letter to T. Robey (SNL), from C. Voss (Golder Associates, Inc.), #
# Re: "Additional Data for Yucca Mountain Test Case," dated October 30, 1992, USW UZN-54 litholog #

# Elev   ID  Depth  Depth  Stratigraphic Unit: lithology (methods) #
#  (m)        (m)    (ft) #

 1236.1  3 #  0.0    0.0  Alluvium (assumed) #
 1235.3  1 #  0.8    2.6  Tiva: welded-lower lithophysal/hackely (litholog, personal comm. w/L. Flint, Dec., 1992)
#
 1221.6  1 # 14.5   47.5  Tiva: welded-hackely (litholog) #
 1211.7  1 # 24.4   80.1  Tiva: welded-columnar (litholog) #
 1193.4  1 # 42.7  140.1  Tiva: WELDED[MODERATLY WELDED?, BASED ON POROSITIES]-columnar
(litholog) #
 1189.5  2 # 46.6  152.8  Paintbrush: non-moderatly welded shardy base (litholog, USW UZN-54 litholog) #
 1180.6  2 # 55.5  182.0  Bedded Tuff: nonwelded (litholog) #
 1168.6  2 # 67.5  221.5  Topopah Sp.: nonwelded (litholog) #
 1166.0  1 # 70.1  230.0  Topopah Sp.: welded caprock (litholog, USW UZN-54 litholog) #
 1165.0 -1 # 71.1  233.4  bottom #
```

Table B.11. USW NRG-6 Stratigraphic Log Data

```
# GROUNDWATER TRAVEL TIME #
# USW NRG-6 STRATIGRAPHY #
# Source: Geslin, J. and T. Moyer, 18 November 1993, "Graphical Lithologic Log of Borehole USW NRG-6,"
USGS/SAIC, Field Operations #

#               Coordinates            Elev. #
#Feet        564187.2      766726.3     4093.2 #
#Meters #      171955.9      233686.8    # 1247.5 #

#Elev.  ID   Depth  Depth  Stratigraphic Unit: lithology #
#(m)         (m)    (ft)   #

1247.5  1 #   0.0     0.0  Tiva: moderately to densely welded-devitrified, X-stal poor lower lithophysal zone #
1230.8  1 #  16.8    55.0  Tiva: moderately to densely welded-devitrified, X-stal poor lower nonlithophysal zone #
1206.4  1 #  41.1   135.0  Tiva: moderately to densely welded-altered, X-stal poor vitric zone (135.3 - 158.8) #
1201.8  2 #  45.8   150.2  Tiva: non to partially welded-vitric #
1199.2  2 #  48.3   158.6  Bedded Tuffs: nonwelded-vitric #
1194.2  2 #  53.3   174.9  Pah Canyon: partially welded-vitric, glassy to vapor-phase-altered matrix #
1180.2  2 #  67.3   220.8  Bedded Tuffs: nonwelded-vitric and altered #
1172.4  2 #  75.2   246.7  Topopah Sp: non to partially welded-vitric and altered, X-stal rich vitric zone (267.7-
263.2) #
1170.0  1 #  77.6   254.5  Topopah Sp: moderately welded-vitrc #
1168.4  5 #  79.2   259.8  Topopah Sp: moderately to densely welded-vitrophyre #
1167.3  1 #  80.2   263.2  Topopah Sp: partially to moderately welded-devitrified, X-stal rich nonlithophysal zone
(263.2 - 429.0) #
        #                  [based on prior & simular logs, this unit is welded is considered as a moderately to densely
welded] #
1116.8  1 #  130.8  429.0  Topopah Sp: moderately to densely welded-devitrified, x-stal rich lithophysal zone
(429.0 - 465.5) #
1105.7  1 #  141.9  465.5  Topopah Sp: moderately to densely welded-devitrified, X-stal poor upper lithophysal
zone (465.5 - 713.0) #
1030.2  1 #  217.3  713.0  Topopah Sp: moderately to densely welded-devitrified, X-stal poor mid. nonlithophysal
zone ( 713.0 - 810.0) #
1000.7  1 #  246.9  810.0  Topopah Sp: moderately to densely welded-devitrified, X-stal poor lower lithophysal
zone (810.0 - 1100.0 TD) #
 912.3 -1 #  335.3 1100.0  Bottom #
```

Table B.12. USW UZ-16 Stratigraphic Log Data

```
# GROUNDWATER TRAVEL TIME 94 DCG/LATA #
# USW UZ-16 STRATIGRAPHY #
# Sources: Buesch, D. C., 20 May 1993, "Graphical Lithologic Log of Borehole UZ-16," Version 1, USGS, Las Vegas, NV #
#        Voss, C., June 5, 1992, "USW UZ-16 Lab Measurements on Preserved Core," #
#                Coordinates          Elev.  #
#feet        564857.5     760535.2     4001.0 #
#meters #    172160.2     231799.8     # 1219.4 #

#Elev.  ID    Depth  Depth  Stratigraphy: lithology #
#(m)          (m)    (ft)   #

1219.4  3 #    0.0     0.0  Alluvium #
1207.3  1 #   12.1    39.7  Tiva: moderate to densely welded-devitrified #
1196.6  1 #   22.9    75.0  Tiva: moderate to densely welded-devitrified, hackly zone #
1190.9  1 #   28.5    93.5  Tiva: moderate to densely welded-devitrified, columnar zone #
1176.5  2 #   42.9   140.8  Tiva: partly welded-devitrified #
1171.4  2 #   48.1   157.7  Tiva: nonwelded-vitric #
1170.5  2 #   49.0   160.7  Bedded Tuff #
1168.9  2 #   50.6   165.9  Yucca Mtn.: nonwelded #
1166.1  2 #   53.3   175.0  Bedded Tuff #
1164.5  2 #   54.9   180.2  Pah Canyon: nonwelded #
1161.9  2 #   57.5   188.8  Topopah Sp: bedded tuff-vitric? #
1155.5  2 #   63.9   209.7  Topopah Sp: non and moderately welded-vitric #
1149.3  5 #   70.2   230.3  Topopah Sp: [densely] welded-vitrophyre #
1146.6  1 #   72.8   238.9  Topopah Sp:moderate to densely welded, x-stal rich nonlithophysal #
1110.4  1 #  109.1   357.8  Topopah Sp: moderate to densely welded, x-stal rich lithophysal #
1106.4  1 #  113.1   371.0  Topopah Sp: moderate to densely welded, x-stal poor upper lithophysal zone (nonlithophysal 371 to 396 ft.) #
1052.1  1 #  167.3   549.0  Topopah Sp: moderate to densely welded, x-stal poor middle nonlithophysal zone #
1009.1  1 #  210.3   690.0  Topopah Sp: moderate to densely welded, x-stal poor lower lithophysal zone (transition w. rare lithophysae 669 to 690 ft) #
 940.6  1 #  278.9   915.0  Topopah Sp: moderate to densely welded, x-stal poor nonlithophysal zone #
 880.8  1 #  338.7  1111.2  Topopah Sp: moderate to densely welded, x-stal poor vitric (vitrophyre) zone #
 864.3  3 #  355.1  1165.2  Topopah Sp: non to partially welded-devitified #
 853.3  4 #  366.1  1201.3  Calico Hills: nonwelded-zeolitic #
 766.8  2 #  452.6  1485.0  Prow Pass: non to partially welded-[zeolitic, Voss, C., June 5, 1992] #
 737.1  5 #  482.4  1582.6  Prow Pass: partial to moderately welded-[devitrified & zeolitic, Voss, C. June 5, 1992] #
 717.8  2 #  501.7  1646.0  Prow Pass: non to partly welded-[zeolitic, Voss, C., June 5, 1992] #
 705.5 -1 #  513.9  1686.2  Bottom #
```

Table B.13. USW WT-2 Stratigraphic Log Data

```
# GROUNDWATER TRAVEL TIME 1994 DCG/ARS/LATA #
# USW WT-2 Stratigraphy #
# Coordinates E-561923.6 N-760660.5 ft, casing el. 4269.70 ft (1301.3 m) (DOE, 1988, YMP88/21) #
 171266.0 231838.0 #m#
# General Comment: Due to no lithologic log for USW WT-2, hole was evaluated by using geophysical log #
# for WT-2 and comparing both the geophysical and lithologic logs for USW H-4 for units below 81.7 m and #
# relating the geophysical information between the two holes. For units above 81.7 m, the litholog from USW UZ-7
#
# provided the "picks" between units #

# References: For WT-2, USGS OFR-86-46, Muller & Kibler, 1985. USW H-4 from USGS Map GP-1001: USW
UZ-7 from Kume and #
# For USW UZ-7, Kume and Hammermeister, 1990, USGS-OFR-88-465; Geophysics, Nelson et. al., 1991
Lithologic log for H-4 from ..................#

#Elev  ID   Depth  Depth  Stratigraphic Unit: lithology (methods) #
#(m)        (m)    (ft) #

1301.3  1  #  0.0    0.0  Tiva: densely and moderately welded (UZ-7 litholog, geophysical log, caliper, density
high, seismic velocity, 2-3K m/s #
1259.3  2  #  42.0  137.8  Tiva: partilly to nonwelded-vitric (UZ-7 litholog indicates 7.2 m of unit, GP log from
WT-2: <CAL, >DBC, >ENP) #
1252.1  2  #  49.2  161.4  Bedded Tuffs: nonwelded-vitric (UZ-7 litholog indicates 5.9 m of unit, #
1246.2  2  #  55.1  180.8  Pah Canyon: nonwelded-vitric (UZ-7 litholog indicates 4.4 m of unit, GP log from WT-
2: short spike in TC, <RILD, >ENP, <K, Uspike) #
1241.8  2  #  59.5  195.2  Bedded Tuff: nonwelded, moderate to slight induration-vitric (UZ-7 litholog indicates
22.2 m of unit, GP log from WT-2: >CAL, <TC, #
        #              <DBC, <RDIEL, <RILD, <<ENP, >DIEL) #
1219.6  2  #  81.7  268.0  Topopah Springs non welded, vitric, as above, similar non welded sequence #
1216.0  1  #  85.3  280.0  Topopah Springs densely - mod welded, devitrified, geophysical log, resistivity mod
high, character of density trace; very variable & spikey #
 938.6  5  # 362.7 1190.0  Topopah Springs vitrophyre, geophysical log, caliper - hole becomes larger in diameter,
contrary to expected trend, but is similar to H-4. #
        #              Resistivity increases, epithermal neutron increases #
 927.0  3  # 374.3 1228.0  Topopah Springs part. - non welded, vitric, geophysical log, general decrease in density
and epithermal neutron #
 904.5  4  # 396.8 1302.0  Calico Hills non - partially welded, devitrified & zeolitized, geophysical log, resistivity
decreases, dielectric constant increases. #
        #              epithermal neutron decreases, density decreases #
 815.2  2  # 486.1 1595.0  Prow Pass non welded, zeolitized and devitrified, geophysical log, high resistivity first
100 feet sequence, resistivity decreases on down #
 673.4 -1  # 627.9 2060.0  Bottom #
```

APPENDIX C: Borehole Material Property Data Used for Calculations Involving Heterogeneous Material Properties

The beta distribution and linear regression information plotted in the figures in the appendix and used for heterogeneous calculations was developed for Schenker et al. (1995), Wilson et al. (1994), and Robey (1994).

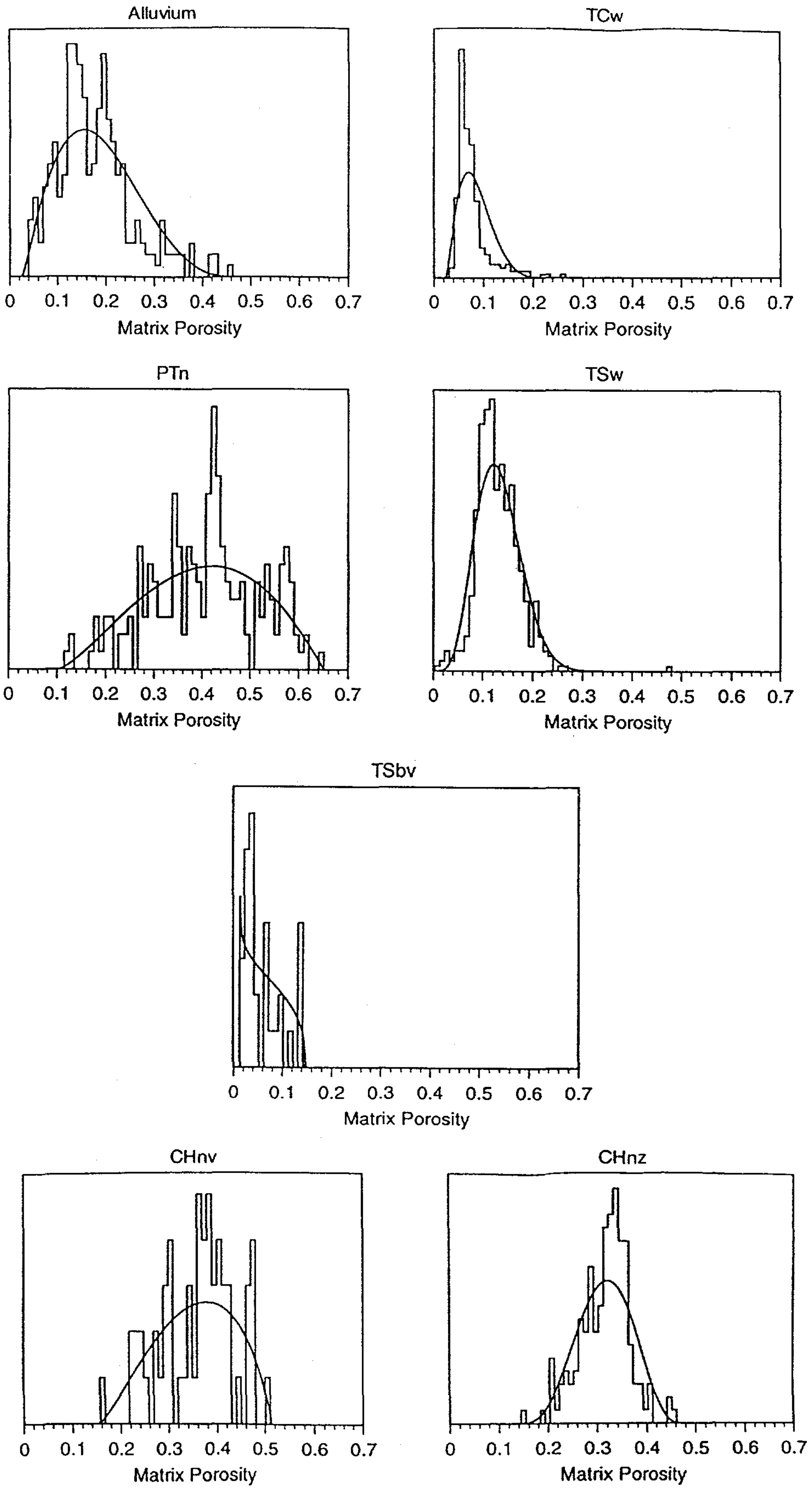

Figure C.1: Beta Distributions and Histograms of Porosity Data Used for Heterogeneous Property Calculations

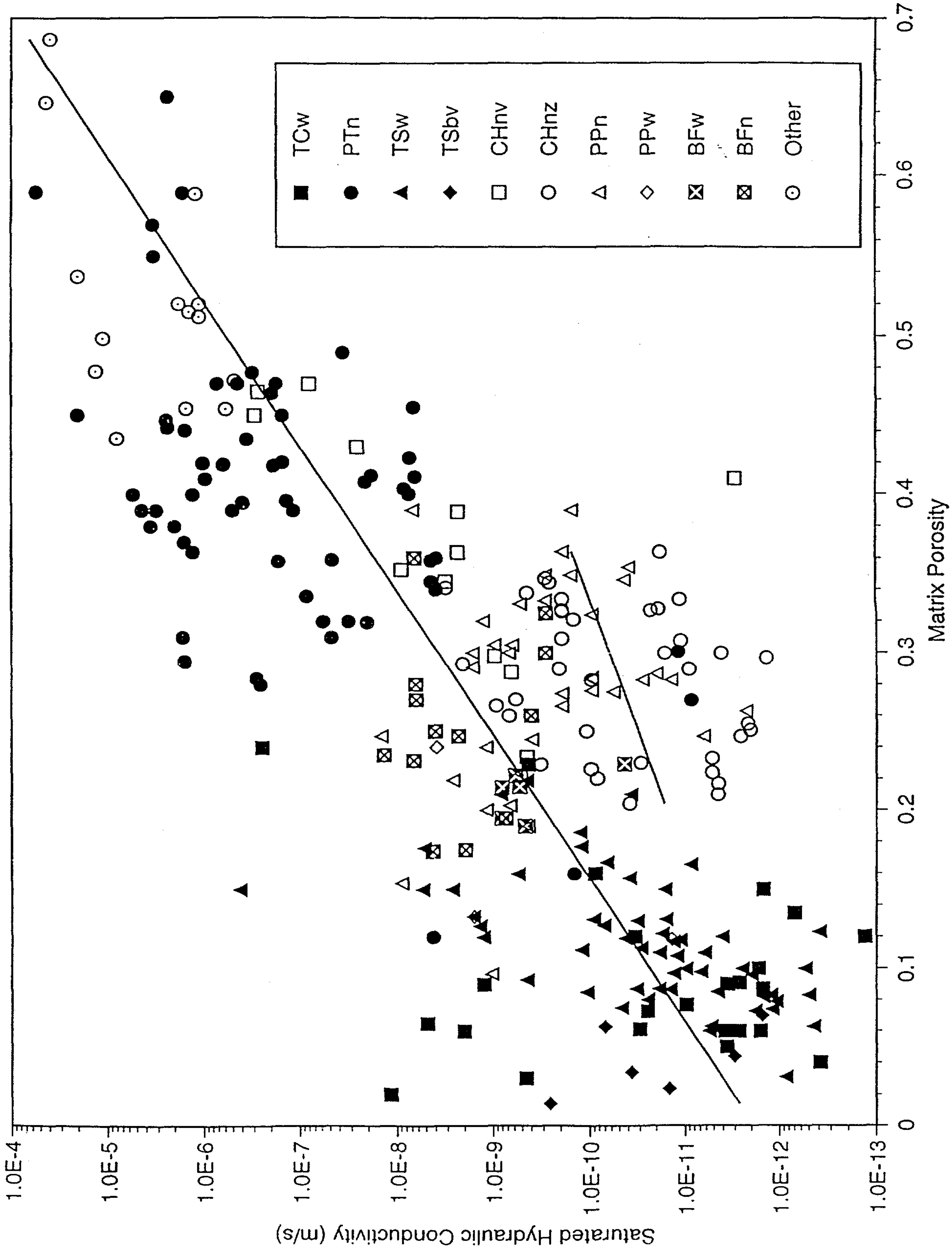

Figure C.2: Linear Regressions of Saturated Hydraulic Conductivity as a Function of Porosity

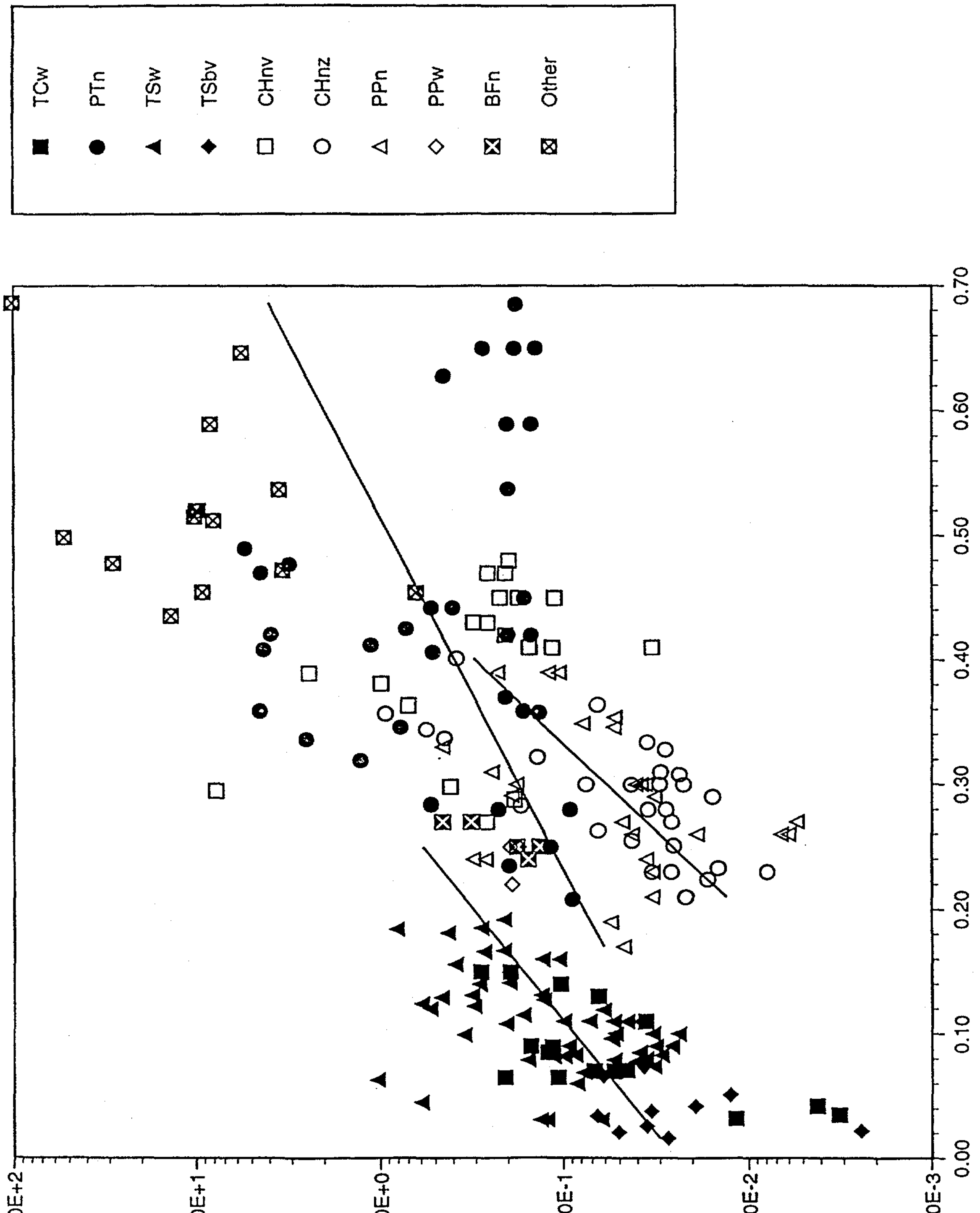

Figure C.3: Linear regressions of Average Pore Size as a Function of Porosity .

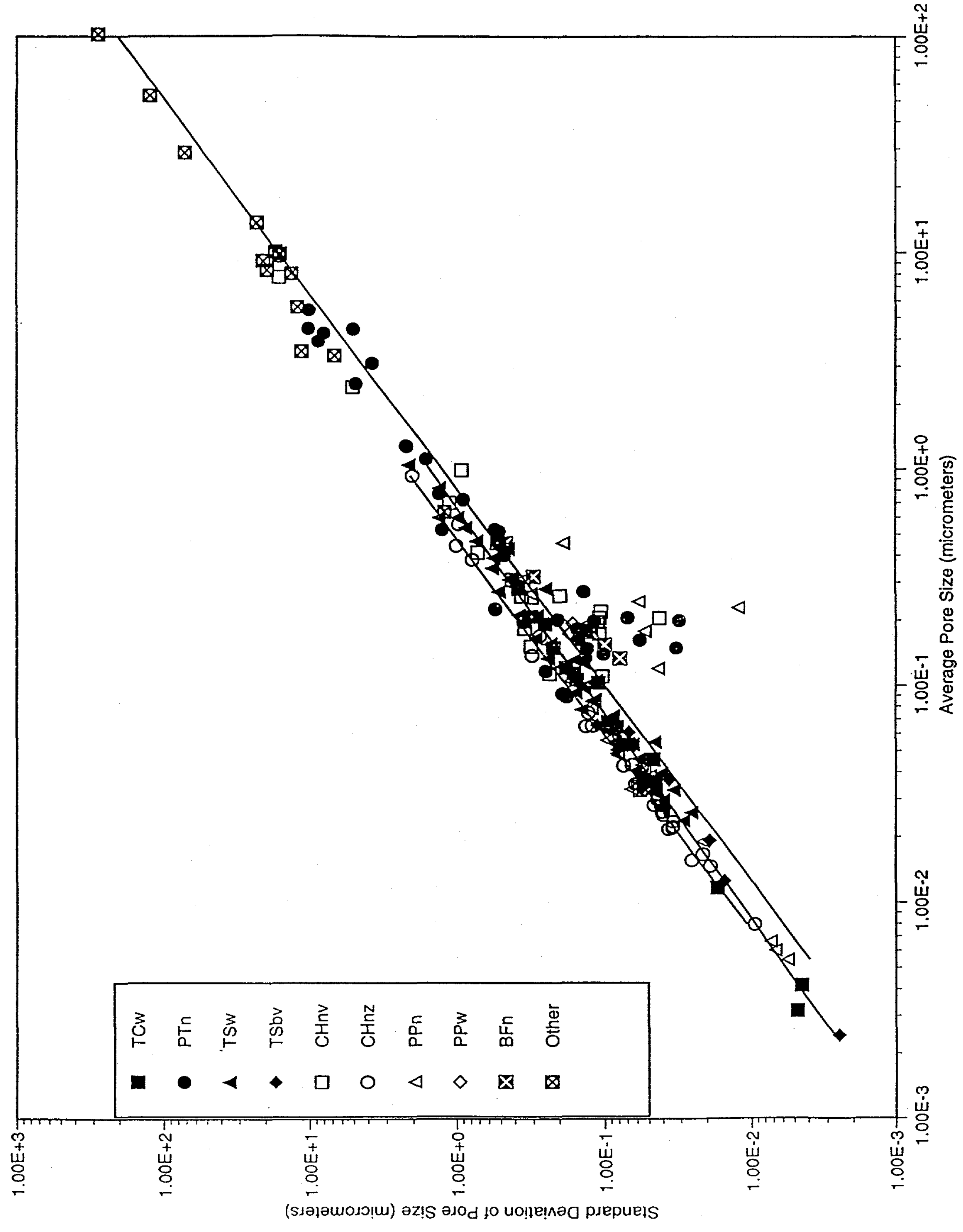

Figure C.4: Linear Regressions of the Standard Deviation of Pore Size as a Function of the Average Pore Size

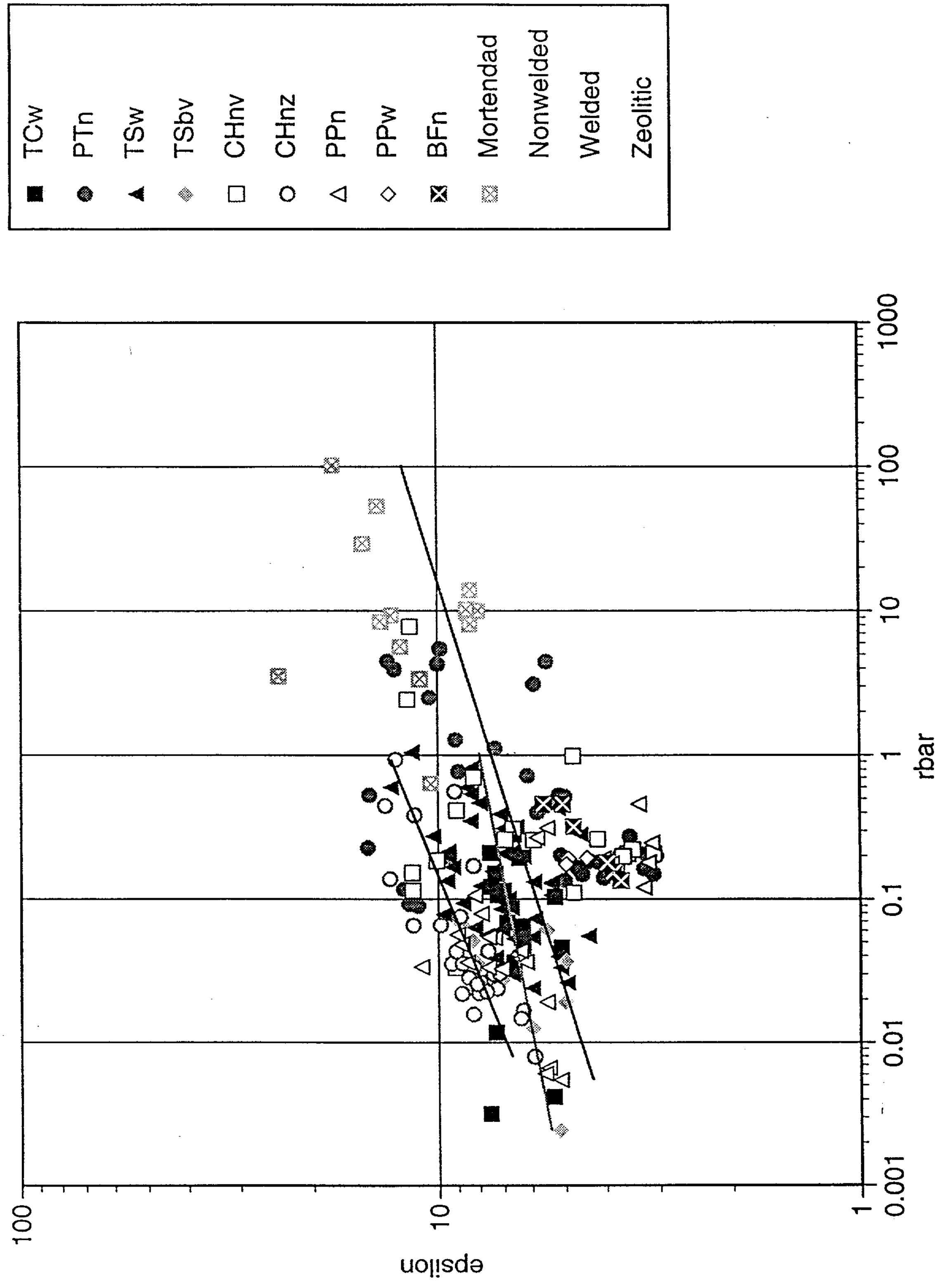

Figure C.5: Linear Regressions of the Brooks Corey Constant as a Function of the Average Pore Size

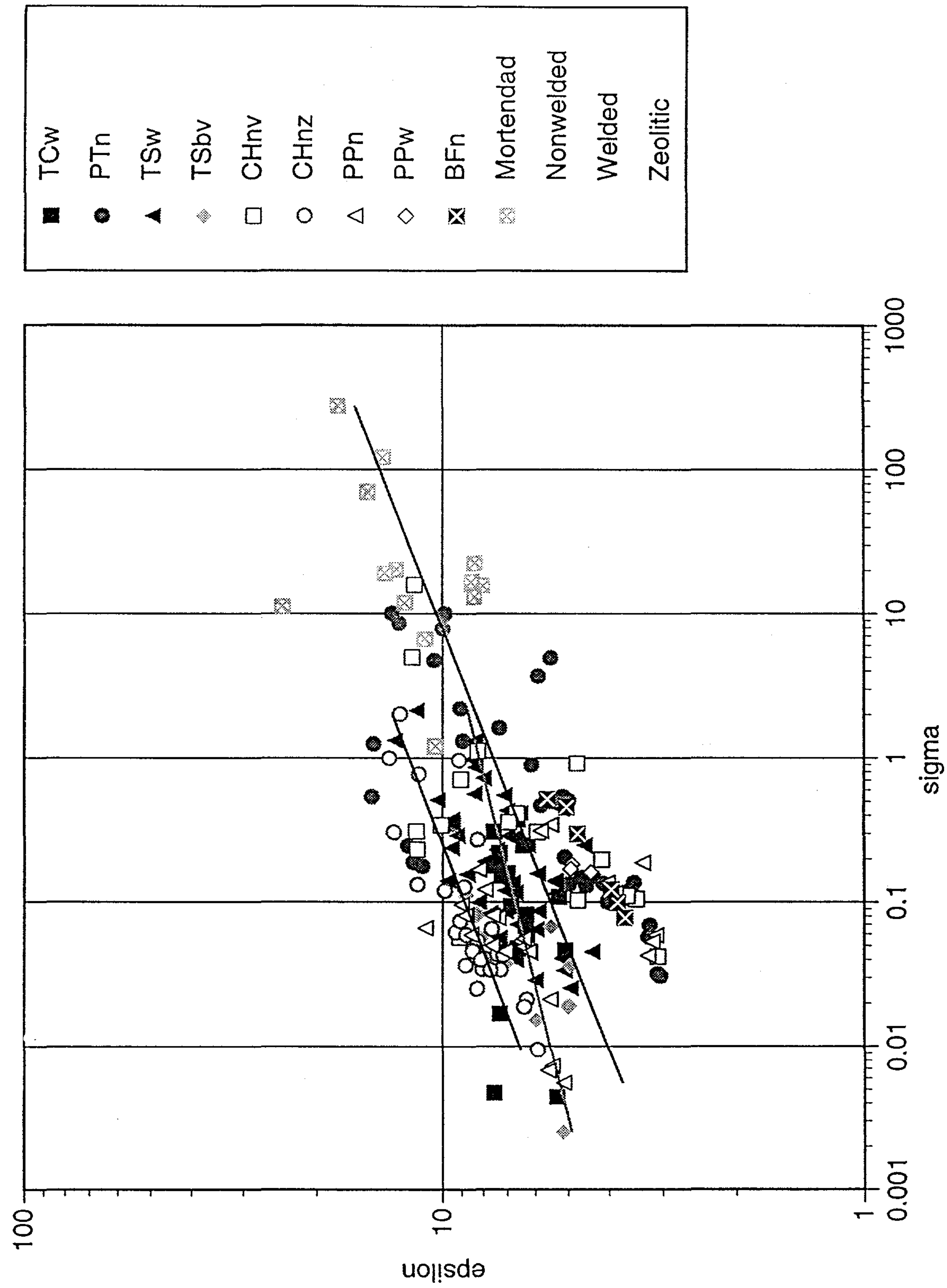

Figure C.6: Linear Regressions of the Brooks Corey Constant as a Function of the Standard Deviation of the Pore Size

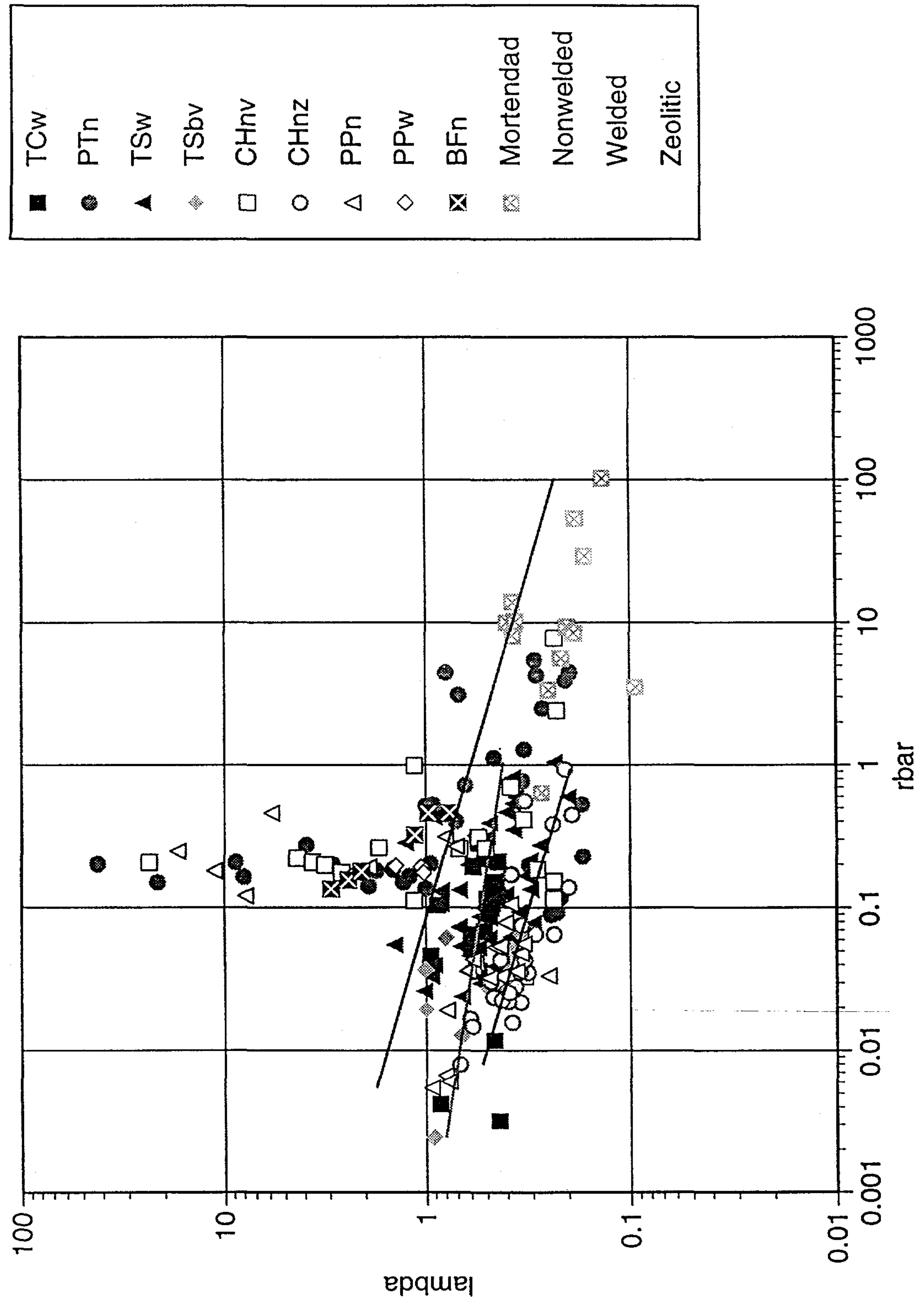

Figure C.7: Linear Regressions of the Pore Size Distribution as a Function of the Average Pore Size

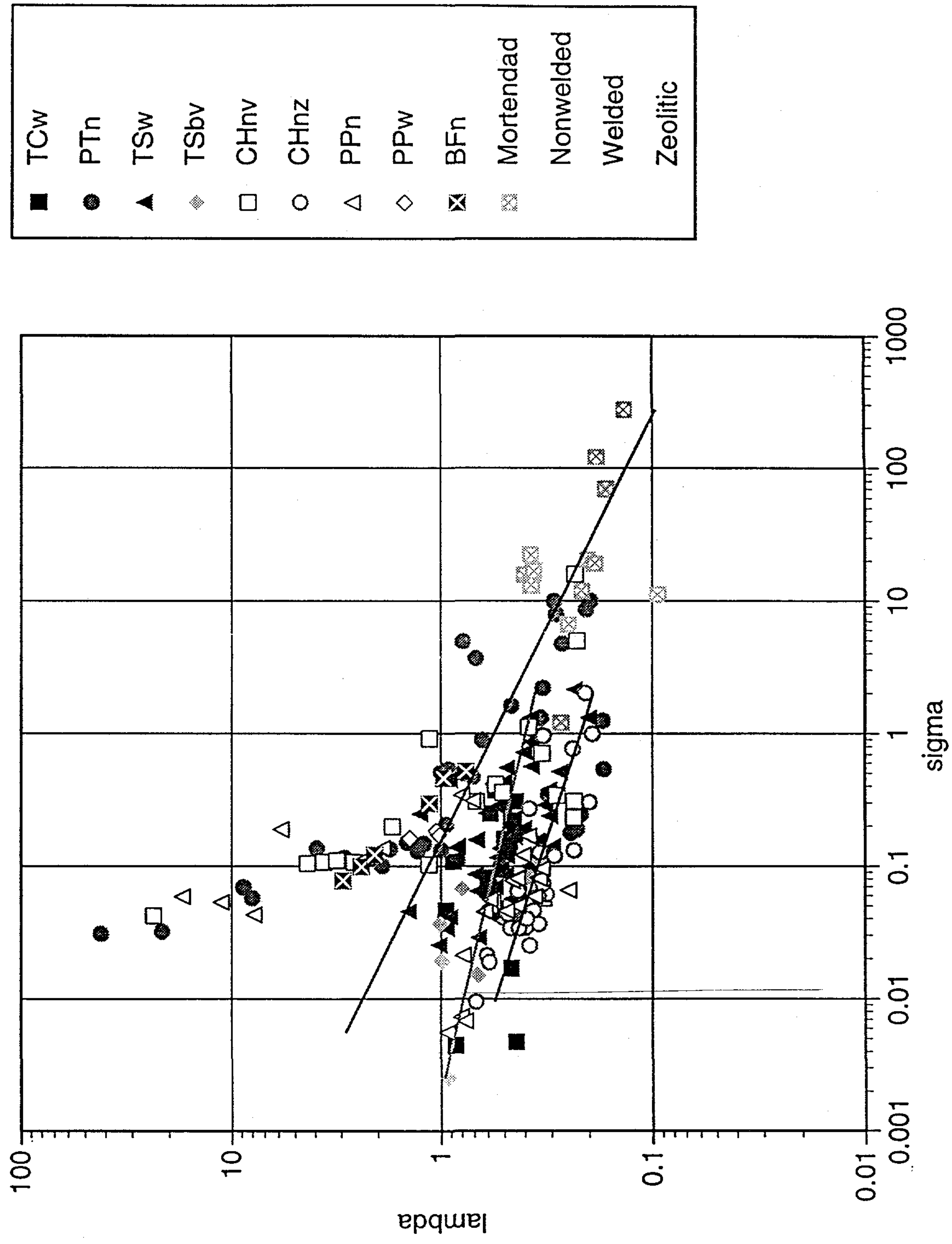

Figure C.8: Linear Regressions of the Pore Size Distribution as a Function of the Standard Deviation of the Pore Size

APPENDIX D

Reference Information Base and Geographic Nodal Information Study and Evaluation System

This report uses no information from the Reference Information Base.

This report contains no candidate information for inclusion in the Reference Information Base.

This report contains no candidate information for the Geographic Nodal Information Study and Evaluation System.

YUCCA MOUNTAIN SITE CHARACTERIZATION PROJECT
SAND94-0779 DISTRIBUTION LIST

1 D. A. Dreyfus (RW-1)
Director
OCRWM
US Department of Energy
1000 Independence Avenue SW
Washington, DC 20585

1 L. H. Barrett (RW-2)
Acting Deputy Director
OCRWM
US Department of Energy
1000 Independence Avenue SW
Washington, DC 20585

1 S. Rousso (RW-40)
Office of Storage and Transportation
OCRWM
US Department of Energy
1000 Independence Avenue SW
Washington, DC 20585

1 R. A. Milner (RW-30)
Office of Program Management
and Integration
OCRWM
US Department of Energy
1000 Independence Avenue SW
Washington, DC 20585

1 D. R. Elle, Director
Environmental Protection Division
DOE Nevada Field Office
US Department of Energy
P.O. Box 98518
Las Vegas, NV 89193-8518

1 T. Wood (RW-14)
Contract Management Division
OCRWM
US Department of Energy
1000 Independence Avenue SW
Washington, DC 20585

4 Victoria F. Reich, Librarian
Nuclear Waste Technical Review Board
1100 Wilson Blvd., Suite 910
Arlington, VA 22209

1 Wesley Barnes, Project Manager
Yucca Mountain Site Characterization
Office
US Department of Energy
P.O. Box 98608–MS 523
Las Vegas, NV 89193-8608

1 Director, Public Affairs Office
c/o Technical Information Resource Center
DOE Nevada Operations Office
US Department of Energy
P.O. Box 98518
Las Vegas, NV 89193-8518

8 Technical Information Officer
DOE Nevada Operations Office
US Department of Energy
P.O. Box 98518
Las Vegas, NV 89193-8518

1 J. R. Dyer, Deputy Project Manager
Yucca Mountain Site Characterization Office
US Department of Energy
P.O. Box 98608 -- MS 523
Las Vegas, NV 89193-88608

1 M. C. Brady
Laboratory Lead for YMP
M&O/Sandia National Laboratories
1261 Town Center Drive
Bldg. 4, Room 421A
Las Vegas, NV 89134

1 J. A. Canepa
Laboratory Lead for YMP
EES-13, Mail Stop J521
M&O/Los Alamos National Laboratory
P.O. Box 1663
Los Alamos, NM 87545

1 Repository Licensing & Quality
Assurance
Project Directorate
Division of Waste Management, MS T7J-9
US NRC
Washington, DC 20555

1 Senior Project Manager for Yucca
Mountain
Repository Project Branch
Division of Waste Management, MS T7J-9
US NRC
Washington, DC 20555

1 NRC Document Control Desk
Division of Waste Management, MS T7J-9
US NRC
Washington, DC 20555

1 Chad Glenn
NRC Site Representative
301 E Stewart Avenue, Room 203
Las Vegas, NV 89101

1 Center for Nuclear Waste
Regulatory Analyses
Southwest Research Institute
6220 Culebra Road
Drawer 28510
San Antonio, TX 78284

2 W. L. Clarke
Laboratory Lead for YMP
M&O/ Lawrence Livermore Nat'l Lab
P.O. Box 808 (L-51)
Livermore, CA 94550

1 Robert W. Craig
Acting Technical Project Officer/YMP
US Geological Survey
101 Convention Center Drive, Suite P-110
Las Vegas, NV 89109

1 J. S. Stuckless, Chief
Geologic Studies Program
MS 425
Yucca Mountain Project Branch
US Geological Survey
P.O. Box 25046
Denver, CO 80225

1 L. D. Foust
Technical Project Officer for YMP
TRW Environmental Safety Systems
101 Convention Center Drive
Suite P-110
Las Vegas, NV 89109

1 A. L. Flint
U. S. Geological Survey
MS 721
P. O. Box 327
Mercury, NV 89023

1 Robert L. Strickler
Vice President & General Manager
TRW Environmental Safety Systems, Inc.
2650 Park Tower Dr.
Vienna, VA 22180

1 Jim Krulik, Geology Manager
US Bureau of Reclamation
Code D-8322
P.O. Box 25007
Denver, CO 80225-0007

1 B. T. Brady
Records Specialist
US Geological Survey
MS 421
P.O. Box 25046
Denver, CO 80225

1 M. D. Voegele
Deputy of Technical Operations
M&O/SAIC
101 Convention Center Drive
Suite P-110
Las Vegas, NV 89109

2 A. T. Tamura
Science and Technology Division
OSTI
US Department of Energy
P.O. Box 62
Oak Ridge, TN 37831

1 P. J. Weeden, Acting Director
Nuclear Radiation Assessment Div.
US EPA
Environmental Monitoring Sys. Lab
P.O. Box 93478
Las Vegas, NV 89193-3478

1 John Fordham, Deputy Director
Water Resources Center
Desert Research Institute
P.O. Box 60220
Reno, NV 89506

1 The Honorable Jim Regan
Chairman
Churchill County Board of
Commissioners
10 W. Williams Avenue
Fallon, NV 89406

1 R. R. Loux
Executive Director
Agency for Nuclear Projects
State of Nevada
Evergreen Center, Suite 252
1802 N. Carson Street
Carson City, NV 89710

1 Brad R. Mettam
Inyo County Yucca Mountain
Repository Assessment Office
P. O. Drawer L
Independence, CA 93526

1 Vernon E. Poe
Office of Nuclear Projects
Mineral County
P.O. Box 1600
Hawthorne, NV 89415

1 Les W. Bradshaw
Program Manager
Nye County Nuclear Waste Repository
Project Office
P.O. Box 1767
Tonopah, NV 89049

1 Florindo Mariani
White Pine County Coordinator
P. O. Box 135
Ely, NV 89301

1 Tammy Manzini
Lander County Yucca Mountain
Information Officer
P.O. Box 10
Austin, NV 89310

1 Jason Pitts
Lincoln County Nuclear Waste
Program Manager
P. O. Box 158
Pioche, NV 89043

1 Dennis Bechtel, Coordinator
Nuclear Waste Division
Clark County Dept. of Comprehensive
Planning
P.O. Box 55171
Las Vegas, NV 89155-1751

1 Juanita D. Hoffman
Nuclear Waste Repository
Oversight Program
Esmeralda County
P.O. Box 490
Goldfield, NV 89013

1 Sandy Green
Yucca Mountain Information Office
Eureka County
P.O. Box 714
Eureka, NV 89316

1 Economic Development Dept.
City of Las Vegas
400 E. Stewart Avenue
Las Vegas, NV 89101

1 Community Planning & Development
City of North Las Vegas
P.O. Box 4086
North Las Vegas, NV 89030

2 Librarian
YMP Research & Study Center
101 Convention Center Drive, Suite P-110
Las Vegas, NV 89109

1 Library Acquisitions
Argonne National Laboratory
Building 203, Room CE-111
9700 S. Cass Avenue
Argonne, IL 60439

1 Glenn Van Roekel
Manager, City of Caliente
P.O. Box 158
Caliente, NV 89008

1 G. S. Bodvarsson
Head, Nuclear Waste Department
Lawrence Berkeley National Laboratory
1 Cyclotron Road, MS 50E
Berkeley, CA 94720

1 Steve Hanauer (RW-2)
OCRWM
U. S. Department of Energy
1000 Independence Ave.
Washington, DC 20585

	MS	
1	1324	P. R. Davies, 6115
5	1324	C. K. Ho, 6115
1	1326	H. Dockery, 6851
1	1326	N. Francis, 6851
1	1326	T. H. Robey, 6851 (c/o H. Dockery)
1	1325	L. S. Costin, 6852
5	1325	E. Dunn, 6852 (c/o L. S. Costin)
1	1325	N. D. Brodsky, 6852
1	1325	R. E. Finley, 6852
1	1325	R. E. Price, 6852
1	1325	E. E. Ryder, 6852
5	1325	S. R. Sobolik, 6852
5	1325	W. T. Cruz, 6852 (c/o S. R. Sobolik)
2	1330	B. Pierson, 6811 100/12547/SAND94-0779/QA
20	1330	WMT Library, 6752
1	9018	Central Technical Files, 8523-2
5	0899	Technical Library, 4414
2	0619	Review and Approval Desk, 12630, For DOE/OSTI

*U.S. GOVERNMENT PRINTING OFFICE 1996-0-774-030/20032